Time-delay interferometric ranging for LISA

Statistical analysis of bias-free ranging
using laser noise minimization

Von der QUEST-Leibniz-Forschungsschule
der Gottfried Wilhelm Leibniz Universität Hannover
zur Erlangung des Grades

DOKTOR DER NATURWISSENSCHAFTEN
– Dr. rer. nat. –

genehmigte Dissertation
von

M. Sc.
Martin Benedikt Staab

2023

Referent	Apl. Prof. Dr. Gerhard Heinzel Institut für Gravitationsphysik, Leibniz Universität Hannover
Korreferent	Prof. Dr. Graham Woan School of Physics and Astronomy, University of Glasgow
Korreferent	Maître de Conférences Dr. Hubert Halloin Astroparticule et Cosmologie, Université de Paris
Tag der Promotion	26.10.2023

Für meinen Opa,
der mich von klein auf für Technik begeistert hat.

Abstract

The Laser Interferometer Space Antenna (LISA) is a future ESA-led space-based observatory to explore the gravitational universe in the frequency band between 10^{-4} Hz and 1 Hz. LISA implements picometer-precise inter-satellite ranging to measure tiny ripples in spacetime induced by gravitational waves (GWs). However, the single-link measurements are dominated by laser frequency noise, which is about nine orders of magnitude larger than the GW signals. Therefore, in post-processing, the time-delay interferometry (TDI) algorithm is used to synthesize virtual equal-arm interferometers to suppress laser frequency noise.

In this work we identify several laser frequency noise coupling channels that limit the performance of TDI. First, the on-board processing, which is used to decimate the sampling rate from tens of megahertz down to the telemetry rate of a few hertz, requires careful design. Appropriate anti-aliasing filters must be implemented to mitigate folding of laser noise power into the observation band. Furthermore, the flatness of these filters is important to limit the impact of the flexing-filtering effect. We demonstrate that this effect can be effectively reduced by using compensation filters on ground. Second, the post-processing delays applied in TDI are subject to interpolation and ranging errors. We study these laser and timing noise residuals analytically and perform simulations to validate the models numerically. Our findings have direct implications for the design of the LISA instrument as we identify the instrumental parameters that are essential for successful laser noise suppression and provide methods for designing appropriate filters for the on-board processing.

In addition, we discuss a dedicated ranging processing pipeline that produces high-precision range estimates that are the input for TDI by combining the sideband and pseudo-random noise (PRN) ranges. We show in this thesis that biases in the PRN measurements limit the laser noise suppression performance. Therefore, we propose time-delay interferometric ranging (TDI-R) as a third ranging sensor to estimate bias-free ranges that can be used to calibrate the biases in the PRN measurements. We present a thorough statistical study of TDI-R to evaluate its performance. Therefore, we formulate the likelihood function of the interferometric data and use the Fisher information formalism to find a lower bound on the estimation variance of the inter-satellite ranges. We find that the ranging uncertainty is proportional to the inverse of the integration time and the ratio of secondary noise power, that limits the interferometric readout, to the laser noise power. To validate our findings we implement prototype TDI-R pipelines and perform numerical simulations. We show that we are able to formulate optimal estimators of the unbiased range that reach the Cramér-Rao lower bound previously expressed analytically. The developed TDI-R pipeline will be integrated into the ranging processing pipeline to perform consistency checks and ensure well-calibrated inter-satellite ranges.

Keywords: Gravitational waves, LISA, Time-Delay Interferometry

Kurzzusammenfassung

Die Laser Interferometer Space Antenna (LISA) ist eine Mission der europäischen Weltraumagentur (ESA) zur Detektion von Gravitationswellen im Frequenzbereich zwischen 10^{-4} Hz und 1 Hz. Gravitationswellen induzieren relative Abstandsänderungen, die LISA mithilfe von Laserinterferometrie mit Picometerpräzision misst. Ein großes Problem hierbei ist das Frequenzrauschen der Laser. Um dieses zu unterdrücken, ist es notwendig, mithilfe eines Algorithmus namens TDI (engl. time-delay interferometry), virtuelle Interferometer mit gleichlangen Armen zu konstruieren, wie z.B. das klassische Michelson-Interferometer.

In dieser Arbeit untersuchen wir die Performanz von TDI unter realistischen Bedingungen und identifizieren verschiedene Kopplungsmechanismen des Laserfrequenzrauschens. Als erstes betrachten wir die Datenverarbeitung an Bord der Satelliten, die benötigt wird, um die Abtastrate der interferometrischen Messungen zu reduzieren. Hierfür sind Anti-Alias-Filter vorgesehen, die der Faltung von Laserrauschleistung in das Beobachtungsband vorbeugen. Außerdem wirkt sich die Ebenheit der Filter auf die Effektivität von TDI aus (engl. flexing-filtering-effect). Dieser Effekt ist bereits in der Literatur beschrieben und wir demonstrieren in dieser Arbeit die Möglichkeit, ihn mithilfe von Kompensationsfiltern effektiv zu reduzieren. Als zweites betrachten wir Kopplungsmechanismen von Laserfrequenzrauschen im TDI-Algorithmus selbst. Fehler in der Interpolation der interferometrischen Messungen und Ungenauigkeiten in den absoluten Abstandsmessungen zwischen den Satelliten führen ebenfalls zu einer unzureichenden Reduzierung des Laserfrequenzrauschens. Wir beschreiben die oben genannten Kopplungsmechanismen analytisch und validieren die zugrundeliegenden Modelle mithilfe von numerischen Simulationen. Das tiefere Verständnis dieser Residuen ermöglicht es uns, geeignete instrumentelle Parameter zu wählen, die von hoher Relevanz für das Missionsdesign von LISA sind.

Des Weiteren beschäftigen wir uns in dieser Arbeit mit der möglichst genauen Bestimmung der absoluten Abständen zwischen den Satelliten, die für den TDI Algorithmus erforderlich sind. Hierfür werden die Abstandsinformationen aus den Seitenbändern und der PRN-Modulation (engl. pseudo-random noise) kombiniert. Wir zeigen, dass die PRN-Messung von systematischen Verzerrungen betroffen ist, die zu Laserrauschresiduen in den TDI-Variablen führen. Um diesen Fehler zu korrigieren, schlagen wir als zusätzliche Abstandsmessung TDI-Ranging (TDI-R) vor. TDI-R ist zwar ungenauer, aber frei von systematischen Verzerrungen und kann daher zur Kalibrierung der PRN-Messungen herangezogen werden. Wir präsentieren in dieser Arbeit eine ausführliche statistische Studie, um die Performanz von TDI-R zu charakterisieren. Dafür formulieren wir die Likelihood-Funktion der interferometrischen Messungen und berechnen die Fisher-Informationsmatrix, um die theoretisch mögliche untere Grenze der Schätzvarianz zu finden. Diese verhält sich invers proportional zur Integrationszeit und dem Verhältnis von Sekundärrauschleistung, die die interferometrische Messung fundamental limitiert, und Laserrauschleistung. Zusätzlich validieren wir die analytische untere Grenze der Schätzvarianz mithilfe von numerischen Simulationen und zeigen damit, dass unsere Implementierung von TDI-R optimal ist. Der entwickelte TDI-R-Algorithmus wird Teil der Datenverarbeitungspipeline sein und Konsistenzprüfungen und Kalibrierung der primären Abstandsmessmethoden ermöglichen.

Schlagwörter: Gravitationswellen, LISA, Time-Delay Interferometry

Acknowledgements

I would like to take a moment and express my deep gratitude to everyone who supported me during the past four years. This journey was fun, but also challenging for me and I was extremely lucky to be surrounded by many wonderful people. I would like to express special thanks at least to some of you.

First and foremost, I would like to thank my supervisors Gerhard Heinzel and Antoine Petiteau. You were always available for me to ask questions and discuss my progress with you. Furthermore, you provided me with essential guidance and directions that have shaped my research. You have placed trust in my abilities and allowed me freedom to explore my own ideas and avenues. I also would like to thank my co-examiners Graham Woan and Hubert Halloin for readily and happily agreeing to review the manuscript and providing valuable input, and Birgit Ohlendorf, who did an exceptional job in navigating me through the modalities of graduating.

Jean-Baptiste and Olaf, thank you for all the invaluable lessons you have taught me from the very first day of my PhD. It was a great pleasure learning from you and working with you. Olaf, thank you for teaching me the arts of time-delay interferometry. You have always endured all my insisting questions with infinite patience. Jean-Baptiste, thank you for teaching me how to write beautiful and functional Python code, but also for all other valuable personal advice you gave me along the way.

I would like to thank Jan Lautenschläger for providing his wonderful artwork presented in fig. 1.1. Furthermore, I am grateful to everyone who improved the quality of the thesis by proofreading it and providing helpful comments.

Next, I would like to thank the entire Space Interferometry group for welcoming me and providing a vibrant and constructive environment. Thank you for all the interesting conversations we had, for playing board games, and being good friends. Also, our daily excursions to Mensa were definitely one of my personal highlights.

Lastly, I want to thank my friends and family who have always believed in me and encouraged me to push on. Especially, during the very last weeks of my thesis writing you have helped me to keep my sanity and supported me in every way possible. I am also thankful to Rasmus for welcoming me into his flat and for sharing the fun times we had in the past four years.

Contents

List of Figures

List of Acronyms

ACF auto-correlation function

ADC analog-to-digital converter

ASD amplitude spectral density

CSD cross spectral density

DPLL digital phase-locked loop

EMRI extreme mass-ratio inspiral

ESA European Space Agency

FIM Fisher information matrix

FIR finite impulse response

GRACE-FO Gravity Recovery and Climate Experiment follow-on

GRS gravitational reference sensor

GW gravitational wave

LIGO Laser Interferometer Gravitational-Wave Observatory

LISA Laser Interferometer Space Antenna

LTI linear time-invariant

MBH massive black hole

MOSA movable optical sub-assembly

PRN pseudo-random noise

PSD power spectral density

PTA pulsar timing array

RMS root mean square

TCB barycentric coordinate time

TDI time-delay interferometry

TDI-R time-delay interferometric ranging

TM test mass

USO ultra-stable oscillator

Table 1: Table of symbols and notation used in the manuscript.

Symbol	Unit	Description
c	$\mathrm{m\,s^{-1}}$	Speed of light in vacuum ($299\,792\,458\,\mathrm{m\,s^{-1}}$)
ϕ	cycles	General phase of a system (e.g. laser, clock or beatnote)
ν	Hz	Instantaneous frequency, defined as time derivative of the phase $\dot{\phi}(t)$
ν_0	Hz	Central laser frequency, nominally 281.6 THz
L	m	Physical arm length of interferometer
x^o	$[x]$	Slow varying (out-of-band) offsets of quantity $x(t)$
x^ϵ	$[x]$	Fast (in-band) fluctuations of quantity $x(t)$
ϕ^{c}_{ij}	cycles	Carrier phase of laser ij
ϕ^{m}_{ij}	cycles	Optical phase modulation of laser ij
$\phi^{\mathrm{usb/lsb}}_{ij}$	cycles	Upper or lower sideband phase of laser ij
$\mathbf{S}$	-	Decimation stage operator (includes anti-aliasing and decimation)
$\mathbf{F}$	-	Filtering operator
$\mathbf{S}_{M\downarrow}$	-	Decimation operator (where M denotes the decimation factor)
T_s	s	Sampling time, defined as time interval between samples
f_s	Hz	Sampling frequency, defined as $\frac{1}{T_s}$
f_n	Hz	Nyquist frequency, defined as half the sampling frequency
$\bar{x}$	$[x]$	Signal $x(t)$ passed through the decimation stage
$\mathbf{T}^a_b$	-	Time reference frame transformation operator (from b to a)
t	s	Barycentric coordinate time (global time reference frame)[1]
τ_i	s	Proper time on spacecraft i (includes relativistic effects)
$\delta\tau_i$	s	Deviation of proper time on spacecraft i from TCB
$\hat{\tau}_i$	s	Onboard time on spacecraft i (includes clock imperfections)
$\delta\hat{\tau}_i$	s	Deviation of on-board timer from proper time on spacecraft i
$\mathbf{D}_{ij}$	-	Delay operator, applies propagation delay $d_{ij}(t)$ from spacecraft j to i
$\bar{\mathbf{D}}_{ij}$	-	Delay operator, applies decimated propagation delay $\mathbf{S}d_{ij}(t)$
$\mathcal{D}_{ij}$	-	Post-processing delay operator, applies to discrete data
$\hat{\mathbf{D}}_{ij}$	-	Delay operator, applies estimated delay $\hat{d}_{ij}(t)$
$\hat{\mathcal{D}}_{ij}$	-	Post-processing delay operator, applies estimated delay $\hat{d}_{ij}(t)$
$\hat{\bar{\mathcal{D}}}_{ij}$	-	Post-processing delay operator, applies estimated and decimated delay $\hat{\bar{d}}_{ij}(t)$
$R_x(\tau)$	$[x]^2$	Auto-correlation function of quantity $x(t)$
$S_x(f)$	$[x]^2/\mathrm{Hz}$	Power spectral density of quantity $x(t)$, defined as Fourier transform of $R_x(\tau)$
$\sqrt{S_x(f)}$	$[x]/\sqrt{\mathrm{Hz}}$	Amplitude spectral density of quantity $x(t)$, defined as square-root of PSD
o_{ij}	Hz	Megahertz-frequency offset from nominal laser frequency of laser ij
p_{ij}	cycles	Laser phase noise of laser ij
q_i	s	Timing jitter of clock i
M_{ij}	s	Modulation noise on MOSA ij
H_{ij}	s	Path length variation (in units of seconds) along link ij caused by a GW
N^{ob}_{ij}	s	Path length noise (in units of seconds) on optical bench ij
N^{ro}_{ij}	s	Equivalent path length noise (in units of seconds) due to readout noise
N^{bl}_{ij}	s	Equivalent path length noise (in units of seconds) due to backlink fiber noise
N^{δ}_{ij}	s	Path length noise (in units of seconds) due to acceleration noise of the TM
B_{ij}	s	Ranging bias of the PRN measurement
N^{R}_{ij}	s	Ranging noise of the PRN measurement
$\mathrm{E}\{X\}$	$[X]$	Expected value of random variable X
$\mathrm{Var}\{X\}$	$[X]$	Variance of random variable X, defined as $\mathrm{E}\left\{(X-\mathrm{E}\{X\})^2\right\}$

[1] The symbol t is often used as the "muted" variable for time dependent functions in which case it can represent the evolution of time in any time reference frame (not just the TCB).

Chapter 1

Introduction

Gravitational waves (GWs) are tiny perturbations of the metric tensor that defines the structure of spacetime. They are emitted by heavy masses that are accelerated; most commonly in binary system, where two compact objects revolve around each other. Due to the radiation of gravitational energy, such compact binary systems lose angular momentum over time, and therefore their orbital distance shrinks and the orbital period decreases. This enabled Taylor (1994) to perform the first indirect detection of GWs using radio observations of a system consisting of a pulsar and another neutron star. The loss of angular momentum over time was perfectly consistent with Einstein's theory of general relativity, so he concluded that the binary system must radiate energy in form of GWs. This initial proof of the existence of GWs led to the construction of the first ground-based detectors.

1.1 Gravitational Wave Detection

GW astronomy is a new and fast moving field that opens up new windows for observing the most energetic events in the Universe. In 2015, the Laser Interferometer Gravitational-Wave Observatory (LIGO) announced the first direct detection of GWs emitted by a stellar-mass black hole merger. Shortly after, many more compact binary coalescences were added to the catalogue (Abbott et al., 2019; Abbott et al., 2021), among them, the first multi-messenger observation of a binary neutron star inspiral (Abbott et al., 2017). Recently, pulsar timing array (PTA) collaborations around the world reported strong evidence for an isotropic stochastic GW background at nanohertz-frequencies (Reardon et al., 2023; Agazie et al., 2023; EPTA Collaboration et al., 2023; Xu et al., 2023). This leaves a wide unexplored GW landscape between PTAs and ground-based detectors ultimately limited below a few hertz by seismic and Newtonian noise. The Laser Interferometer Space Antenna (LISA) (Amaro-Seoane et al., 2017) is a space mission selected by ESA as the third large mission in the Cosmic Visions program themed "The Gravitational Universe" to fill-in parts of the gap left by PTAs and ground-based detectors. It will be sensitive between 0.1 mHz and 1 Hz. Moving the detector to space allows for much larger baselines and provides a much more quiet environment for the test masses that serve as inertial references for the relative length measurement.

Stable references in time and translation are the fundamental ingredients to probe the ripples in spacetime caused by GWs. Figure 1.1 shows the most basic detector design consisting of two stations at different locations hosting clocks that are synchronized via an optical link. The transferred clock reading is sensitive to the differential effect of time dilation at the two stations and to the travel time the light takes to traverse the space between stations. Both effects depend on the spacetime metric that is disturbed by the GW. It is possible to form a ranging and timing observable from the remote clock comparison (Reynaud et al., 2008). The advantage of this procedure is that the ranging observable is rejecting timing noise of the clocks while the timing observable is less sensitive to spurious motion of the stations. Laser interferometers like

Figure 1.1: Artistic illustration of a single baseline GW detector composed of two stations carrying clocks that are synchronized via an optical link. The blue fabric, the clocks sit, represents the spacetime that is perturbed by the passing of GWs. Due to the local spacetime metric at the stations the clocks tick at different rates, thus accumulating different readings. Furthermore, the light travel time between the stations is modulated by the GWs. Those two effects are the fundamental principles to detect GW.

LIGO or LISA rely on ranging by realizing equal-arm Michelson interferometers to measure GW as frequency standards are not mature enough to be sensitive in the timing observable.

1.1.1 Laser interferometry for GW detection

A laser interferometer is a device to detect tiny changes in relative distance measurements. As the laser light is coherent over many cycles it effectively acts as a very precise measuring stick. Laser interferometers are used on ground and in space to perform ranging experiments, e.g., lunar ranging and other geodesy experiments.

The first laser ranging interferometer in space is currently flying on the Gravity Recovery and Climate Experiment follow-on (GRACE-FO) mission (Abich et al., 2019). It consists of two spacecraft on the same near polar orbit with a separation of 200 km. Laser interferometers constantly track the inter-satellite range that is modulated by the Earth's gravity field. The instrument has reached precisions of tens of $200\,\mathrm{pm}/\sqrt{\mathrm{Hz}}$.

In the following, we explain the basic working principle of a Michelson interferometer (see fig. 1.2). This type of interferometer is used in all operational ground-based observatories, like LIGO. It is constructed from a laser source, a beam splitter, two end-mirrors that serve as test masses (TMs) and a photodiode detecting the interference pattern.

For simplicity, we model the laser beam as a plane wave propagating along the beam axis neglecting its transversal profile (which is usually assumed to be Gaussian). Thus the electric field vector at the longitudinal coordinate z and time t is given as

$$\boldsymbol{E}(z,t) = \boldsymbol{E}_0 \cdot \cos\big(2\pi\phi(z,t)\big). \tag{1.1}$$

Here $\boldsymbol{E}_0$ denotes the field amplitude and $\phi(z,t)$ the phase of the laser light (in cycles). For

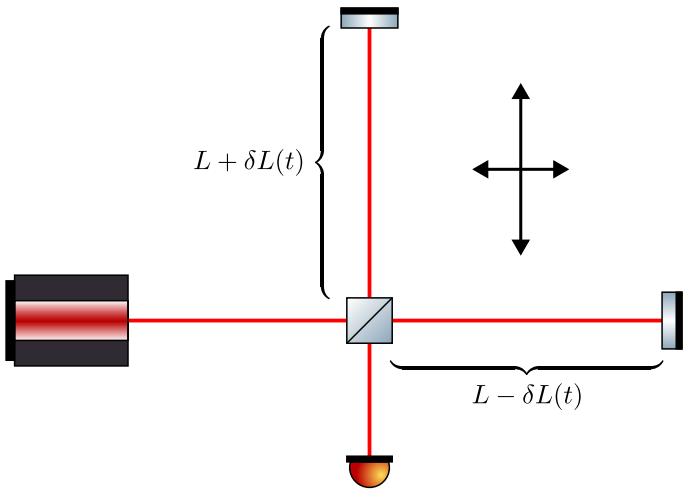

Figure 1.2: Illustration of a basic equal-arm Michelson interferometer setup.

monochromatic light and propagation in vacuum the laser phase is given as

$$\phi(x,t) = \nu_0 \cdot \left(t - \frac{z}{c}\right) + \phi_0. \tag{1.2}$$

The laser phase is quickly increasing quantity (in space and time) with terahertz optical frequencies.

In a Michelson interferometer a laser beam is emitted by the laser source and split into two identical copies[1] at the beam splitter. Both beams traverse the arms reflecting off the end-mirrors of the interferometer and recombine again to interfere at the output port of the interferometer.

A plus-polarized GW traveling perpendicular to the interferometer stretches one arm by $\delta L(t)$ while compressing the other one by the same amount. Therefore, after the round-trip though the arms the phases of the beams have evolved differently. The phases at recombination read

$$\phi_1(t) = \nu_0 \cdot \left(2\frac{L + \delta L(t)}{c} - t\right) \tag{1.3a}$$

$$\phi_2(t) = \nu_0 \cdot \left(2\frac{L - \delta L(t)}{c} - t\right) \tag{1.3b}$$

The photodetector at the output port measures the intensity of the incident light which is proportional to the square of the superposition of the electric fields. The terahertz-oscillations of the intensity are much too fast for the photodiodes bandwidth. Therefore, it effectively acts as a low-pass filter rejecting oscillating components at the optical frequency of the laser. This is indicated in the equation below by the angular brackets.

$$I(t) \propto \left\langle \big(E_1(t) + E_2(t)\big)^2 \right\rangle = \left\langle E_1^2(t)\right\rangle + \left\langle E_2^2(t)\right\rangle + 2\left\langle E_1(t) \cdot E_2(t)\right\rangle \tag{1.4}$$

The first two contributions are the individual intensities of the beams. They oscillate at twice the optical frequency and, therefore, they yield a constant photocurrent. The cross term can be

[1] This is not exactly true as the beam that is transmitted at the beam splitter picks up extra phase $\frac{\pi}{2}$. However, transmitted and reflected beam switch roles after traversing the arms and, hence, are in phase again at the output port of the interferometer.

rewritten by using the trigonometric identity $\cos(\alpha)\cos(\beta) = \frac{\cos(\alpha+\beta)+\cos(\alpha-\beta)}{2}$.

$$\left\langle E_{1/2}^2(t)\right\rangle = E_0^2\left\langle \cos^2\left(2\pi i\phi_{1/2}(t)\right)\right\rangle \simeq \frac{E_0^2}{2} \tag{1.5}$$

$$\left\langle E_1(t)\cdot E_2(t)\right\rangle = E_0^2\left\langle \cos\left(2\pi\phi_1(t)\right)\cdot\cos\left(2\pi\phi_2(t)\right)\right\rangle \tag{1.6}$$

$$= \frac{E_0^2}{2}\left\langle \cos\left(2\pi(\phi_1(t)+\phi_2(t))\right) + \cos\left(2\pi(\phi_1(t)-\phi_2(t))\right)\right\rangle \tag{1.7}$$

$$\simeq \frac{E_0^2}{2}\left(\frac{1}{2} + \cos\left(2\pi(\phi_1(t)-\phi_2(t))\right)\right) \tag{1.8}$$

As we will see below the cosine function of the differential phase $\delta\phi(t) = \phi_1(t) - \phi_2(t)$ survives the detector as its evolution in time is driven by the Doppler shift caused by the GW. Therefore, we find for the total measured intensity[2]

$$I(t) \propto E_0^2 \cdot \left(1 + \cos\left(2\pi(\phi_1(t)-\phi_2(t))\right)\right). \tag{1.9}$$

Throughout the manuscript we call $\delta\phi(t)$ the phase of the beatnote formed by the two beams recombining at the beam splitter. It can be extracted from eq. (1.9) by a dedicated device, a phasemeter.

Plugging in the phases calculated in eq. (1.3) the beatnote phase is indeed sensitive to the disturbance $\delta L(t)$ that is caused by the GW. We find

$$\delta\phi(t) = 4\nu_0 \cdot \frac{\delta L(t)}{c}. \tag{1.10}$$

1.2 The Laser Interferometer Space Antenna

The Laser Interferometer Space Antenna is a future space observatory led by the European Space Agency that will start observing GWs in the late 2030s (Amaro-Seoane et al., 2017). It will be sensitive in the 10^{-4} Hz to 1 Hz frequency band and thus opening up a complementary window for GW astronomy between PTAs and ground-based observatories, like LIGO.

In this section we give a brief description of the LISA mission parameters. We start off by taking a closer look at the high-level measurement principle and then discuss the catalogue of GW sources LISA is expected (or even guaranteed) to detect. Ultimately, we describe the individual components that are relevant for appropriately model the LISA measurements that are further used in this thesis to demonstrate the performance of the instrument.

1.2.1 The LISA constellation

LISA consists of three satellites flying in formation and constantly exchanging laser beams to realize picometer-precise ranging. The three spacecraft are placed in heliocentric orbits trailing the earth by approximately 20° (see fig. 1.3). Each orbit is tilted towards the ecliptic such that the satellites form an almost equilateral triangle with arm length of 2.5 million kilometer. The plane defined by the triangle is inclined towards the ecliptic by 60° and its normal vector stays aligned towards the sun. Furthermore, during the course of a year the constellation performs its typical cartwheel motion, enabling LISA to resolve the sky location of individual sources. As the antenna pattern sweeps across the sky the signal is modulated by the time-dependent instrument response and picks up a characteristic Doppler signature.

The LISA mission relies on picometer-precise ranging measurements along the 2.5 million kilometer arms to pick up GW strains of the order of 10^{-21}. As the frequency standard on board the LISA spacecraft are only 10^{-13} stable(see LISA Performance Working Group (2021) for the

[2]Here, we assume an ideal contrast of one.

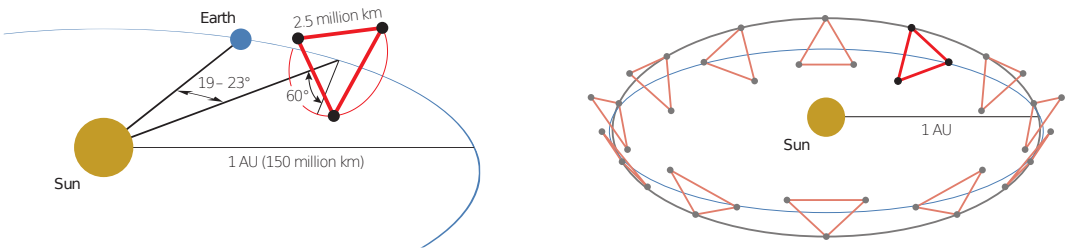

Figure 1.3: Orbital trajectory of the LISA constellation. The LISA spacecraft are depicted by black dots and are separated by 2.5 Gm. They form an (almost) equilateral triangle that is performing a cart-wheel motion around the sun (right panel). Taken from Amaro-Seoane et al. (2017).

allocated stability of clocks and lasers), measurement of the differential effect of time dilation is far out of reach. To be insensitive to timing jitter of the local frequency reference (i.e. the laser source) LISA realizes equal arm interferometers that effectively reject laser noise. This technique is already implemented in today's ground-based GW detectors that all implement equal-arm Michelson interferometers.

Constructing an equal-arm Michelson interferometer with the dimensions of LISA in space is extremely difficult. As the end-stations of the interferometer are not rigidly connected to the central station, they will drift around with relative line-of-sight velocities of up to a few tens of meters per second. Furthermore, the beams strongly diverge when propagating between the spacecraft such that the light intensity is reduced by a factor 10^{10} (Amaro-Seoane et al., 2017). Therefore, it is rather impractical to back-reflect them at the end-stations to form a beatnote at the center-station which would diminish the light power by another factor of 10^{10} rendering the beam immeasurable. The solution is to detect the "one-way links" that compare local with distant laser light that has traveled along the link. In post-processing the six resulting measurements can be combined in an algorithm called time-delay interferometry that synthesizes arbitrary virtual interferometers (see section 3.1.2). The ultimate goal of time-delay interferometry (TDI) is to seek interferometers with sufficiently equal arms to suppress laser noise to acceptable levels. At the same time the sensitivity for GW signals must be preserved.

1.2.2 LISA Sources

The LISA band is richly populated with a multitude of astrophysical GW sources (Amaro-Seoane et al., 2023). Figure 1.4 provides an overview showing the characteristic strain of the various source types and at which frequencies they emit. The most abundant source type for LISA is represented by millions of compact galactic binaries (Nissanke et al., 2012) indicated as light blue dots. The black and blue lines represent black hole binaries as observed by ground based detector already today. LISA will observe them in their early inspiral phase and be able to predict their merger. In general, compact binary systems consist of stellar remnants, i.e. white dwarfs, neutron stars or stellar-mass black holes. As they revolve around each other in a close orbit they emit a virtually monochromatic signal at twice the orbital frequency. As a result they lose orbital momentum and slowly spiral into each other. Out of all compact galactic binaries only roughly a thousand will be loud enough and, therefore, resolvable by LISA. The remaining binaries will blend into a foreground hum that is indistinguishable from a stochastic signal (Amaro-Seoane et al., 2023; Sesana, 2016; Périgois et al., 2021). It is represented by the grey area in fig. 1.4 and limits the detector sensitivity at millihertz-frequencies. Compact binaries also facilitate a great opportunity for multi-messenger astronomy as they can be observed in the optical, UV and x-ray spectrum (Gaia Collaboration et al., 2018; Brown et al., 2020; Stella et al., 1987). This puts LISA in a unique position as those electromagnetic surveys include "guaranteed sources" (also dubbed "verification binaries") that will be detected after only a few

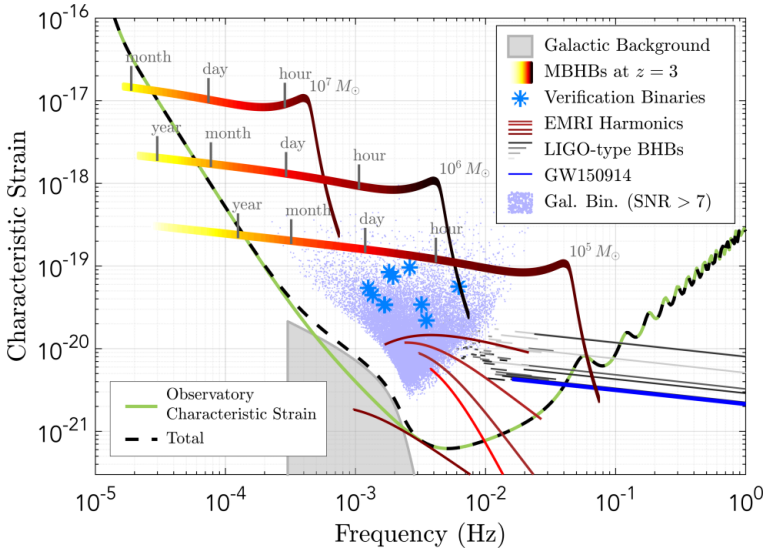

Figure 1.4: Overview of expected LISA sources (see text for detailed explanation) taken from Amaro-Seoane et al. (2017).

weeks to month (Stroeer and Vecchio, 2006). Those are indicated with blue asterisk in fig. 1.4.

Another class of binary sources are massive black hole (MBH) binaries with component masses ranging from 10^3 to $10^7 M_\odot$. MBHs reside in the center of most galaxies (Kormendy and Ho, 2013) and were recently observed directly by the Event Horizon Telescope (Akiyama, 2019). Their origin is assumed to be twofold; some MBH must have already existed at early cosmic times (Bañados et al., 2014), others may have formed via successive merger events (Fakhouri et al., 2010). With LISA it will be possible to detect GW signals from MBH binaries out to redshifts $z \sim 20$, thus, will help us to drastically improve our understanding of their formation and growth across cosmic ages. Depending on their components masses they will sweep across the LISA band in their final stages of inspiraling and finally merge. Figure 1.4 shows three examples at $z = 3$ of different masses as the thick lines changing color from yellow to dark red. The vertical ticks mark the time to merger. Current estimates of the observed merger rates are highly uncertain and predict 1 to 100 detection per year (Sesana et al., 2005; Amaro-Seoane et al., 2023).

The MBHs hosted in the center of most galaxies also form another type of binary system with stellar-mass compact objects, so-called extreme mass-ratio inspirals. Radio observations of our own galactic center have revealed a highly dynamic environment where the central MBH is surrounded by a cluster of stars on highly eccentric orbits (Genzel et al., 2010) suggesting the existence of extreme mass-ratio inspirals (EMRIs). The name stems from the fact that the involved masses differ by many orders of magnitude. Common mass-ratios range from 10^{-8} to 10^{-5}. A sub class is represented by intermediate mass-ratio inspirals which describe systems consisting of an intermediate-mass black hole either inspiraling into a MBH or stellar-mass compact objects revolving around it with typical mass-ratios below 10^{-5}. These systems hold a myriad of exciting science cases (Amaro Seoane, 2021). The orbits of lighter component around the central black hole are highly eccentric and dynamic. These characteristics can be viewed in fig. 1.4 as the five red lines. The signal of a single EMRI is not just a chirping sinusoid but has higher harmonic content due to the elliptic orbit. As a consequence EMRIs probe different regimes of spacetime curvature along its orbital phase. However, the GW emission is strongest in the highly relativistic regime where the companions are closest reaching velocities of a few percent of the speed of light.

The final class of anticipated GW signals are broadband stochastic GW backgrounds. They can be either of astrophysical or cosmological origin. The former stems from abundant popu-

lations of compact binaries at various redshifts (Schneider et al., 2001; Rosado, 2011). Their virtually monochromatic signals spectrally overlap and are indistinguishable from noise. However, the most prominent background source for LISA will be the combined signal coming from millions of detached white dwarf binaries from our own galaxy (Nelemans et al., 2001). An estimate of their expected spectral strain is shown in fig. 1.4 as the grey shaded area. Due to the stochastic nature of the background it behaves as instrumental noise and impacts the LISA sensitivity at millihertz-frequencies. The second possible origin of a stochastic GW in the LISA band are cosmological processes, e.g. a first-order phase transition in the very early universe (Caprini et al., 2016) or primordial black holes (García-Bellido et al., 2016). The detection of stochastic background is especially difficult as they can easily be confused with instrumental noise. Therefore, traditionally to distinguish signal from measurement noise the data taken by several detectors is cross-correlated to filter out the signal that is common among them. As shown in section 3.1, LISA can be understood as two Michelson interferometers rotated by 45° against each other and a third "null"-channel that is insensitive to GW and thus acts as a monitor for instrumental noise (Flauger et al., 2021).

1.2.3 Time reference frames

Exact timing plays a crucial role for the discrete sampling of the LISA measurements and data processing on ground. The measurements are represented by megahertz-beatnotes that contain tiny GW induced Doppler shifts. Tracking of the beatnote phase at microcycle-precision requires ultra stable clocks. In section 1.2.4 we will see that the clocks that will be implemented in LISA drift apart by many seconds over the mission time. Therefore, the measurements taken on the spacecraft must be resynchronized to a well-defined reference frame prior to handing the data over to data analysis.

To better understand the various effects determining the spacecraft on-board time, we introduce the various time reference frames relevant to model the LISA measurement chain and properly design effective data processing algorithms. We indicate the time scale a physical quantity x is defined in by a superscript. For the global time scale barycentric coordinate time (TCB) we choose t, for the spacecraft proper and on-board clock times we use τ_i and $\hat{\tau}_i$, respectively. Here the index $i = 1, 2, 3$ denotes the spacecraft. Furthermore we introduce the operator $\mathbf{T}^b_a$ that transforms a variable $x^b(t)$ given in time scale b to time scale a, i.e.,

$$x^a(t) = \mathbf{T}^a_b x^b(t). \tag{1.11}$$

Here, the variable t is used as the "muted variable". It does not define the reference frame of the measurement (we could also call it τ) but only indicates the time of evaluation in the reference frame given by the superscript.

The barycentric coordinate time

The TCB is a well-defined global time reference frame to describe events in the solar system (Kaplan, 2006). It places a perfect clock in the barycenter of the solar system neglecting relativistic effects due to its gravitational potential, therefore realizing a coordinate time in a "mass-less" universe with a well-defined origin.

For LISA this time frame is relevant to describe effects that apply to the full constellation. Examples are the individual orbital trajectories of the three satellites or the effect of a passing GW. It represents the time reference frame in which astrophysical events are usually described, like solar system ephemerides or the emission of GWs.

The spacecraft proper time

To describe any physics that happens inside the spacecraft it is convenient to define the spacecraft proper time as a co-moving observer would experience it. In general, this time scale differs for

each LISA spacecraft and drifts apart by a few milliseconds over the course of the mission (Bayle et al., 2022b). In our modeling we use it to describe all local physical processes, e.g., the evolution of the laser and ultra-stable oscillator (USO) phases or path length noises due to moving optics.

As the spacecraft proper time is related to the TCB we define the transformation of a physical quantity x^t expressed in the TCB into the spacecraft proper time by

$$x^{\tau_i}(t) = \mathbf{T}_t^{\tau_i} x^t(t) = x^t(t^{\tau_i}(t)) = x^t(t + \delta t_i(t)) \tag{1.12}$$

where we have introduced the operator $\mathbf{T}_t^{\tau_i}$ that effectively shifts the time argument t by the deviation $\delta t_i(t)$ of the TCB with respect to the spacecraft proper time on spacecraft i (Hees et al., 2014).

The spacecraft on-board time

As opposed to the spacecraft proper time the spacecraft on-board time includes technical imperfections of the real clock. The properties of real clocks are characterized by their Allan deviations which expresses the frequency stability over a certain integration time. A thorough study of various space qualified clocks can be found in Hartwig (2021).

Analogously to eq. (1.12) we can define the transformation of an on-board physical quantity $x^{\tau_i}(t)$ into the on-board clock frame. We use this operation to model time-stamping of all LISA measurements.

$$x^{\hat{\tau}_i}(t) = \mathbf{T}_{\tau_i}^{\hat{\tau}_i} x^{\tau_i}(t) = x^{\tau_i}(\tau_i^{\hat{\tau}_i}(t)) = x^{\tau_i}(t + \delta\tau_i(t)) \tag{1.13}$$

Here, $\delta\tau_i(t)$ denotes the time difference between the spacecraft proper time and the spacecraft on-board time as it is observed by the clock.

1.2.4 Instrument overview

In this section we want to give an overview of the LISA instrument. Here, we mainly discuss the space segment, i.e., the satellites, that host the interferometric detection system.

As discussed in section 1.2.1 the fundamental measurement principle of LISA is to monitor tiny relative distance changes between the satellites that are induced by GW radiation with picometer-precision. Therefore, the interferometric detection system must be built such that it does not introduce spurious path-length noise that buries the GW signals.

In what follows, we discuss the various subcomponents that make up the detection system and discuss their critical stability parameters. Each spacecraft hosts two identical MOSAs that facilitates all components required for the optical interferometry. They are attached to a hinge to be able to follow the far spacecraft with the telescope as the opening angle of the triangle changes slightly over time. Figure 1.5 shows a sketch of a single MOSA.

As we will see, the sensitivity of LISA is mainly limited by two classes of noises. Spurious accelerations of the TMs at low frequencies and readout noise of the interferometric detection system at high frequencies. The level and temporal correlation properties of the noise sources is characterized by their power spectral density (PSD) or amplitude spectral density (ASD) (the square-root of the former). They are intimately connected to the auto-correlation function and represent the spectral content of the noise (for more details see section 1.3). This is relevant for determining the signal-to-noise ratio of a GW signal. The spectral components of the latter only compete with the spectral components of the noise at the same frequency. Therefore, the signal-to-noise ratio of a monochromatic signal is dependent on the signal's frequency. This gives rise to the characteristic strain shown in fig. 1.4 which defines the detectors sensitivity and takes into account instrumental noises and the average detector response (Moore et al., 2015).

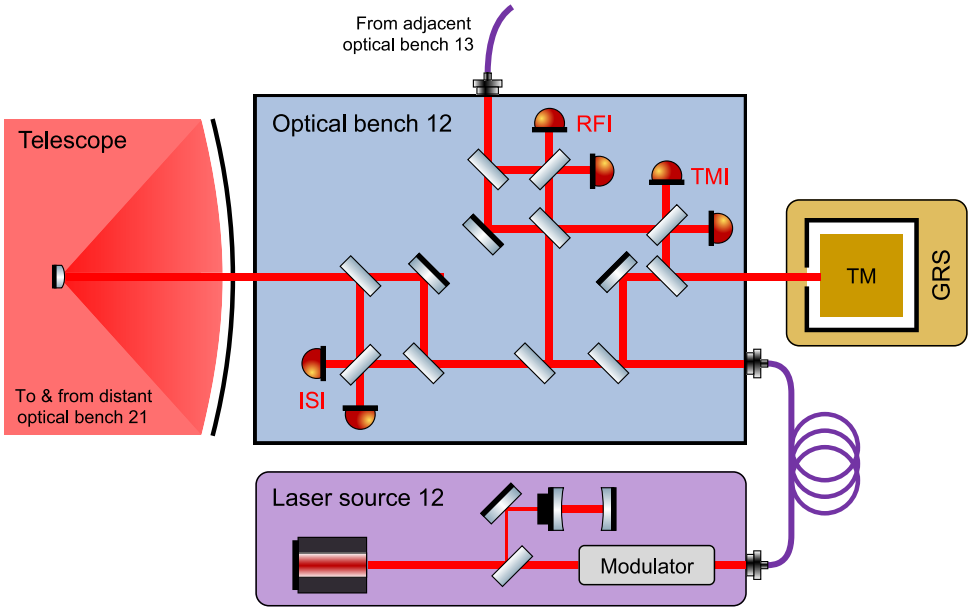

Figure 1.5: Overview of the interferometric readout on a single MOSA. Each MOSA hosts a laser source, an optical bench, a telescope and a GRS. Adjacent MOSAs are connected via the backlink fiber to exchange light. The three different beams are ultimately combined in the inter-spacecraft interferometer (ISI), the test-mass interferometer (TMI) and the reference interferometer (RFI). Taken from Wissel et al. (2023) with permission from the author.

Geodesic reference sensor

Effective GW detection requires a very quiet environment. In on-ground observatories this is achieved by suspending mirrors as pendulum masses that strongly decouple them from ground-motion. Space, on the other hand, is naturally very quiet as any free-falling objects simply follow their geodetics. However, even the inner solar system is not quiet enough to allow for GW detection. The solar wind will shake the satellites and spoil the picometer-precise relative length measurements. The solution to this is to implement a so-called GRS which tracks any non-gravitational forces on the spacecraft. This yields geodetic references that are much closer to "free-fall" than the spacecraft itself.

The GRS is inherited from the LISA pathfinder mission and is constructed from an Au-Pt TM (cube of side length 46 mm) placed inside a vacuum housing that is vented to space to reduce the residual gas pressure further. The latter shields the TM from any external disturbances and such serves as free-falling inertial reference for the range measurement. Moreover, the GRS housing is equipped with electrodes that exert electrostatic forces to control the position of the TM and ultra-violet lamps to discharge it. As the two TMs on adjacent MOSAs follow slightly different geodesic they would drift apart over time. It can be shown that it is sufficient to only control the position of the TMs in y and z direction and leave the (sensitive) x direction untouched.

The TM interferometer reads out the longitudinal position of the TM (see fig. 1.5). The inertial stability of the TM is limited by residual gas pressure in the GRS housing which is of the order of a few micropascal. Upon impact, residual gas molecules transfer tiny momenta to the TM. The performance of the GRS was extensively tested in the LISA pathfinder mission not just fulfilling the mission requirements but even exceeding the requirements set for the LISA mission (Armano et al., 2016; Armano et al., 2018). Those are given by

$$\sqrt{S_{\mathrm{tm}}(f)} = (2\pi f)^{-2} \cdot 3\,\mathrm{fm/s^2/\sqrt{Hz}} \cdot \sqrt{1 + \left(\frac{0.4\,\mathrm{mHz}}{f}\right)^2} \cdot \sqrt{1 + \left(\frac{f}{8\,\mathrm{mHz}}\right)^4}. \tag{1.14}$$

The factor of $(2\pi f)^{-2}$ converts the requirement (Amaro-Seoane et al., 2017) from acceleration units to displacement units for easier comparison later. We plot the requirement curve in fig. 1.6.

Interferometric readout system

As demonstrated in section 1.1.1 laser interferometers are a sensitive tool to measure the relative path-length difference in an equal-arm Michelson interferometer. All operational ground-based interferometers use such a setup to sense GWs. For LISA it is impossible to directly construct an equal-arm interferometer in space for two reasons. First, after propagating a laser beam from one spacecraft to the other the beam diverges and only a few hundreds of picowatts out of the few watts originally emitted. Back-reflecting the beam would attenuate the power by the same factor and would render it immeasurable. Second, the LISA triangle is not perfectly equilateral. Due to the orbital dynamics governing the trajectory of the satellites the arms of the constellation are time-dependent and differ by a few percent.

As a solution LISA implements the so called split-interferometry design which leads to three interferometers per MOSA as shown in fig. 1.5. The TM to TM measurement is performed in parts. Locally, the TM interferometer measures the TM position with respect to the MOSA. Then, the inter-spacecraft interferometer performs a measurement between the local and the distant MOSAs. To relate adjacent lasers via the backlink fiber the reference interferometer is implemented. The dominating noise in each interferometer is now presented by laser frequency noise. The origin of this noise is the jitter of the laser frequency around its central value. In this manuscript we assume a level of[3]

$$\sqrt{S_{\dot{p}}(f)} = 30\,\mathrm{Hz}/\sqrt{\mathrm{Hz}}. \tag{1.15}$$

Converted to displacement units the level reads $5\,\mathrm{mm}/\sqrt{\mathrm{Hz}}$ at 1 mHz which strongly violates the targeted picometer-precision by nine orders of magnitude. The solution is to combine the three interferometers in the TDI algorithm discussed in section 3.2 to form virtual equal-arm interferometers that effectively suppress laser noise.

After laser noise suppression the performance of the interferometric readout is limited by several other effective displacements noises. Even though all optical components in the path of the beams are rigidly fixed to the optical bench they are subject to tiny movements due to, e.g., temperature fluctuations or vibrations of the telescope. Those result in path-length noises that couple similar to a GW to the central laser frequency and produce an additional phase contribution

$$\phi(t - N^{\mathrm{ob}}(t)) \simeq \phi(t) - N^{\mathrm{ob}}(t) \cdot \nu(t). \tag{1.16}$$

Similarly, the propagation of the adjacent beam through the backlink adds phase noise to the beam due to scattering centers in the fiber (Fleddermann et al., 2018; Max Rohr et al., 2020).

Another major contribution is photon shot noise which mainly depends on the power level of the interfering beams. Quadrant photodiodes are used to detect the megahertz beatnote formed by the interfering beams. Due to the low power level of the distant beam (hundreds of picowatts) the dominant unsuppressed noise in the inter-spacecraft interferometer is shot noise at a level of roughly $6\,\mathrm{pm}/\sqrt{\mathrm{Hz}}$ (Bayle and Hartwig, 2023).

Overall, the LISA noise budget allows for $10\,\mathrm{pm}\sqrt{\mathrm{Hz}}$ of effective displacement noise in the interferometric detection system. The LISA performance model keeps track of the individual contribution and allocates part of the budget to each. To account for the fact that residual force noise on the TMs is dominating the noise budget at frequencies below a few millihertz, the white

[3]Here, for simplicity, we omit the commonly assumed noise shape function that amplifies the noise power at frequencies below 2 mHz.

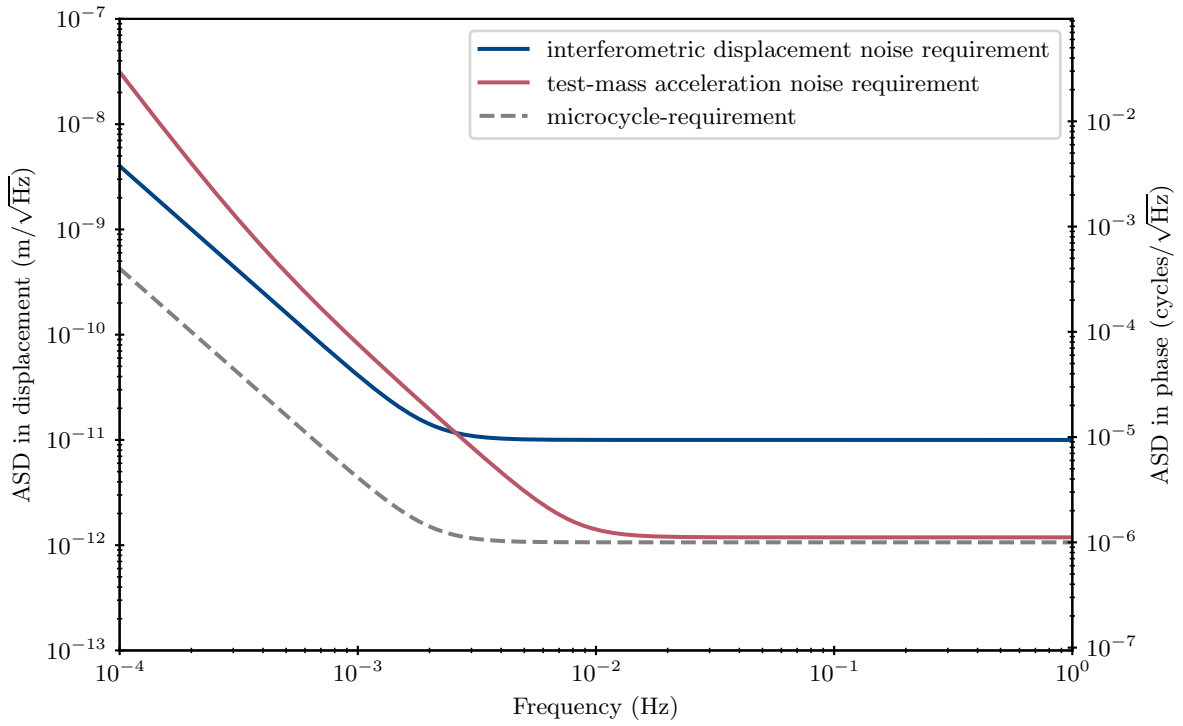

Figure 1.6: Comparison of various requirement curves. In blue the requirement of displacement noise in the interferometric readout system is shown. The acceleration noise requirement on the TM (converted to displacement units) is plotted in red. The grey dashed line indicates the microcycle-requirement that serves as a benchmark.

noise budget of $10\,\mathrm{pm}/\sqrt{\mathrm{Hz}}$ is relaxed as

$$\sqrt{S_{\mathrm{ifo}}(f)} = 10\,\mathrm{pm}/\sqrt{\mathrm{Hz}} \cdot \sqrt{1 + \left(\frac{2\,\mathrm{mHz}}{f}\right)^4}. \tag{1.17}$$

We plot the requirement in fig. 1.6. We observe that the relaxation has the desired effect. The requirement curve for interferometric displacement noise stays below the requirement for TM acceleration noise.

As a benchmark to judge the relevance of a noise source disturbing the measurements we define the picometer (displacement units) or equivalently the microcycle (phase units) requirement. They denote the same thing and only differ by the unit they are expressed in. To convert from displacement units to phase units we have to divide by the nominal laser wavelength $\lambda_0 = 1064\,\mathrm{nm}$.

$$\sqrt{S^{\mathrm{req}}_{\delta\phi}(f)} = 1\,\mu\mathrm{cycle}/\sqrt{\mathrm{Hz}} \cdot \sqrt{1 + \left(\frac{2\,\mathrm{mHz}}{f}\right)^4} \tag{1.18}$$

Again, we add it to the graph in fig. 1.6 to compare it to the other requirement. The rationale behind it is a factor ten below the other curves and therefore virtually negligible. It would take 100 uncorrelated noise sources with a level of $1\,\mathrm{pm}/\sqrt{\mathrm{Hz}}$ each to add up to a level of $10\,\mathrm{pm}/\sqrt{\mathrm{Hz}}$.

Onboard clock and frequency distribution system

Each LISA spacecraft houses a single USO that serves as a unique clock to drive all on-board electronics. Furthermore, the on-board timer is derived from this clock which is used to accurately time-stamp all measurement. Time-stamping can be modeled as shifting the time argument of

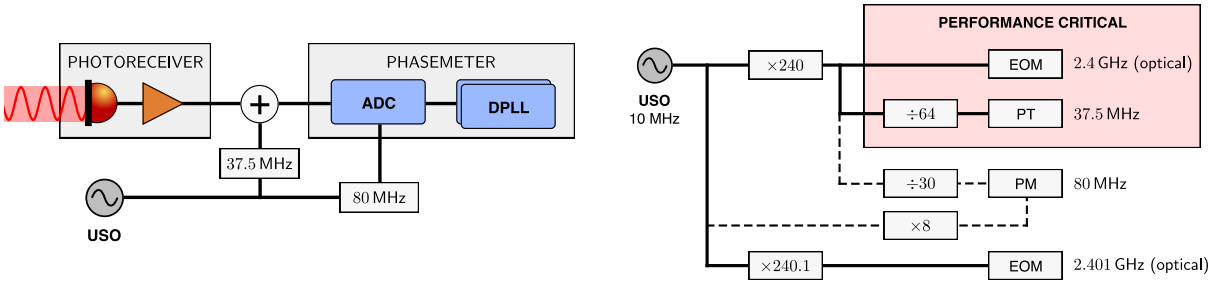

Figure 1.7: Distribution of the clock signal of the USO. The left panel represents the injection of the pilot tone into the phase readout of the photoreceiver. The phasemeter's ADC digitally samples the sinusoidal beatnote and extracts its phase. The right panel shows how the various frequencies required in LISA are derived from the 10 MHz clock. For more details see the text. Adapted from Bayle and Hartwig (2023) with permission from the author.

the beatnote phase φ by the timing jitter q of the clock.

$$\varphi(t + q(t)) = \nu \cdot (t + q(t)) = \varphi(t) + \nu \cdot q(t) \tag{1.19}$$

In this calculation we assume that the derivative of the beatnote phase, the beatnote frequency ν, is constant. The timing-jitter couples proportionally with the beatnote frequency which is of the order of 20 MHz. To fulfill the microcycle-requirement we need a clock timing stability of $50\,\mathrm{fs}/\sqrt{\mathrm{Hz}}$.

$$\sqrt{S_q} \cdot 20\,\mathrm{MHz} \lesssim 1\,\mu\mathrm{cycle}/\sqrt{\mathrm{Hz}} \tag{1.20}$$

However, with current state-of-the-art space-qualified clocks this cannot be achieved. The baseline design of LISA foresees a temperature-stabilized quartz oscillator with a timing precision of

$$\sqrt{S_q(f)} = 10^{-14}\,\mathrm{s}/\sqrt{\mathrm{Hz}} \cdot \left(\frac{f}{\mathrm{Hz}}\right)^{-\frac{3}{2}}. \tag{1.21}$$

This level of timing jitter results in a phase noise level of approximately $6\,\mathrm{mcycles}/\sqrt{\mathrm{Hz}}$ at 1 mHz which strongly violates the microcycle-requirement. The solution to this problem is to distribute the clock signals among the satellites and measure it differentially in an auxiliary channel. This is achieved by modulating sidebands on the laser beam via electro-optic modulators.

In addition to the timing jitter of the clock the ADC is subject to sampling jitter. For mitigation a 37.5 MHz pilot tone is injected in the readout of the photodetectors before digitally sampling the signals (see left panel of fig. 1.7). After sampling it at the phasemeter rate of 80 MHz it provides a timing reference to correct all phase readouts. This procedure is called pilot tone correction.

The right panel of fig. 1.7 shows the distribution of the 10 MHz[4] clock signal to the different subcomponents. For sideband modulation it is upconverted to 2.4 GHz and 2.401 GHz for left-handed and right-handed MOSAs, respectively. The 2.4 GHz signal is then downconverted again by a factor of 32 to derive the 37.5 MHz pilot tone. The 80 MHz phasemeter clock can be either derived directly from the 10 MHz clock signal or from the 2.4 GHz signal.

Critical for performance is a stable phase relation between the optical 2.4 GHz phase modulation and the pilot tone. The latter indirectly defines the timing of the sampling procedure via pilot tone correction and is therefore the relevant timing reference for each spacecraft. The sidebands are read out in the inter-spacecraft and reference interferometers to synchronize the carrier-carrier beatnote measurements with femtosecond-precision. Here, the stability of the sideband modulation on right-handed MOSAs is secondary as it can be related to the sideband

[4]This has been recently changed to $3 \cdot 2^{24}\,\mathrm{Hz} \simeq 50.3\,\mathrm{MHz}$. However, the particular choice of the USO frequency does not change the general principle of the conversion chain, so we stick with the 10 MHz clock in this manuscript

modulation on left-handed MOSAs via the sideband-sideband beatnote measured locally by the reference interferometer. Furthermore, the phase stability of the 80 MHz phasemeter clock is also not performance critical as it is accounted for by the pilot tone correction.

Any deviation of the phase of the optical 2.4 GHz signal from the pilot tone due to errors in the downconversion or the phase modulation is described by modulation noise. The current best estimate of modulation noise in terms of timing jitter is given by the LISA Performance Working Group (2021) as

$$\sqrt{S_M(f)} = 8.3 \times 10^{-15}\,\mathrm{s}/\sqrt{\mathrm{Hz}} \cdot \left(\frac{f}{\mathrm{Hz}}\right)^{-2/3}. \tag{1.22}$$

For the optical phase modulation error on right-handed MOSAs we assume a level that is ten times higher to account for the "larger" separation from the pilot tone in the frequency conversion chain (see fig. 1.7). However, as we will later show this can be mitigated by the ranging processing algorithm presented in section 3.2.4.

1.3 Time Series Analysis of Stochastic Signals

In this manuscript, we make extensive use of the notation of spectral densities of stochastic processes. Therefore, in this section, we give a brief overview of the definitions and methods we use to derive analytical expressions for those. Stochastic processes are, as the term "stochastic" suggest, random processes that cannot be predicted. However, we can define "ensemble quantities" that describe the temporal correlation properties of a random process. The most basic random process is represented by the white Gaussian random process. For any distinct times t_1 and t_2 the values the random process $x(t)$ takes are uncorrelated. We write

$$\mathrm{E}\{x(t_1) \cdot x(t_2)\} = 0. \tag{1.23}$$

Here, $\mathrm{E}\{\cdot\}$ denotes the ensemble average which expresses the mean value over many independent realisations of the process. This property does not apply to all random processes. Any random process of finite bandwidth is indeed correlated in time which can be described by the auto-correlation function (ACF). For zero mean random processes $x(t)$ the ACF is defined as

$$\mathrm{ACF}\{x(t)\}(\tau) = \mathrm{E}\{x(t) \cdot x(t+\tau)\}. \tag{1.24}$$

In this definition of the ACF, we require that the random process $x(t)$ is *stationary* which implies that the statistical properties of the process are independent of absolute time t and only the relative displacement τ is relevant. Evaluating the ACF at $\tau = 0$ yields the variance or power of the process.

The PSD views the frequency content of the ACF in the Fourier domain. The PSD is defined as the Fourier transform of the ACF.

$$\mathrm{PSD}\{x(t)\}(f) = \int_{\mathbb{R}} \mathrm{ACF}\{x(t)\}(\tau) \cdot e^{-2\pi i f \tau}\,\mathrm{d}\tau \tag{1.25}$$

It indeed represents a density function as the integral over all frequencies yields the total power of the signal $\int_{\mathbb{R}} \mathrm{PSD}\{x(t)\}(f)\,\mathrm{d}f = \mathrm{ACF}\{x(t)\}(0)$. As the ACF is a real function of even symmetry the PSD inherits the same properties. Therefore, it is customary to only consider positive Fourier frequencies f and "discard" negative frequencies. This gives rise to the *one-sided* PSD which is defined only for positive frequencies and equals to twice the *two-sided* PSD to account for the negative frequencies in the density function. In the remainder of this document, we implicitly mean the *one-sided* PSD if we discuss spectral densities and make use of the symbol $S_x(f) = 2 \cdot \mathrm{PSD}\{x(t)\}(f)$.

Next, let us discuss the effect of linear time-invariant (LTI) systems on a stochastic process. A system is called LTI if its properties are constant over time and it reacts linearly to any input such that the result of the input $x(t) = x_1(t) + x_2(t)$ equals to the sum of the results of the individual inputs. We write

$$\mathbf{F}\big(x_1(t) + x_2(t)\big) = \mathbf{F}x_1(t) + \mathbf{F}x_2(t). \tag{1.26}$$

Here, we have introduce the operator $\mathbf{F}$ that maps the input $x(t)$ to the output $y(t)$ of an LTI system. This can be described by convolving the impulse response $h(t)$ of the system with the input. Formally we have

$$y(t) = \mathbf{F}x(t) = \int_{\mathbb{R}} h(\tau)x(t-\tau)\,\mathrm{d}t. \tag{1.27}$$

The output $y(t)$ of the system is again a random process with a modified PSD. Using eq. (1.24), eq. (1.25) and common Fourier transformation rules, we find that the PSD of $y(t)$ equals to the PSD of $x(t)$ multiplied by the magnitude square of the Fourier transform of the impulse response $\tilde{h}(f)$.

$$S_y(f) = \tilde{\mathbf{F}}S_x(f) = |\tilde{h}(f)|^2 \cdot S_x(f). \tag{1.28}$$

The latter is also called the transfer function of the system. Here, $\tilde{\mathbf{F}}$ denotes the effect of the operation on the PSD, which is a simple multiplication for LTI systems.

In the data analysis presented in chapters 3 and 4 we operate on discretely sampled data. To apply the formalism introduced above we use the Whittaker-Shannon interpolation formula given in Oppenheim et al. (1999) as

$$x(t) = \sum_{n=-\infty}^{\infty} \mathrm{sinc}(f_s t - n) \cdot x_n. \tag{1.29}$$

It perfectly reconstructs the continuous-time representation from the discrete samples. Here, the sinc-function is defined as $\mathrm{sinc}(x) = \frac{\sin(\pi x)}{\pi x}$. Furthermore, this identity only holds for signals $x(t)$ that are band-limited up to the Nyquist frequency which is given by $\frac{f_s}{2}$.

Next, let us define the effect of a finite impulse response (FIR) filter on a discretely sampled time series x_n. The operation is described by the discrete convolution of the finite length FIR filter kernel h_n with the data

$$y_n = \sum_m h_m x_{n-m}. \tag{1.30}$$

Then, we use eq. (1.29) to represent this operation in continuous time. It is trivial to show that

$$y(t) = \int_{\mathbb{R}} \underbrace{\sum_m h_m \delta(\tau - mT_s)}_{h(\tau)}\, x(t-\tau)\,\mathrm{d}t, \tag{1.31}$$

where $\delta(t)$ denotes the Dirac-delta function. In the equation above we have identified the impulse response $h(\tau)$ of the FIR filter operation which can be used to calculate the transfer function.

Another operation we require for the modeling of the LISA on-board processing is decimation which describes the reduction of the sampling rate by an integer factor M. Decimation is implemented by skipping every M-th sample in the time series. Formally we have

$$y_n = x_{M \cdot n}. \tag{1.32}$$

In appendix B we show that this process cannot be represented by an LTI system. As a consequence, a transfer function does not exist for this operation but instead the PSD of $y(t)$ is given

by folding so-called aliases into the new band which is limited up to the new Nyquist rate. From eq. (B.13) we derive the following expression for the one-sided PSD

$$S_y(f) = \tilde{\mathbf{S}}_{M\downarrow} S_x(f) = \mathrm{rect}\left(\frac{f}{f_s}\right) \sum_{n=0}^{M-1} S_x^{(n)}(f). \tag{1.33}$$

Here, $\tilde{\mathbf{S}}_{M\downarrow} S_x(f)$ is a shorthand notation representing the action of the decimation operator in Fourier space on the PSD of $x(t)$ and the rectangular function is defined to be equal to zero for $|f| > f_n$ and equal to one for $|f| < f_n$ such that the decimated signal is band-limited up to the new Nyquist rate f_n which is defined as half the sampling rate f_s after decimation. Finally, the n^{th} alias, $S_x^{(n)}(f)$, on the right-hand-side of eq. (1.33), is given by

$$S_x^{(n)}(f) = \begin{cases} S_x\big(nf_n + f\big) & \text{if } n \text{ is even,} \\ S_x\big((n+1)f_n - f\big) & \text{if } n \text{ is odd.} \end{cases} \tag{1.34}$$

Equations (1.33) and (1.34) highlight the typical folding into band of any spectral component that resides at frequencies higher than the new Nyquist rate (up to the highest frequency Mf_n, which corresponds to the Nyquist rate before decimation). This result is also presented in Staab et al. (2023b).

1.4 Outline

This thesis is structured as follows. In chapter 2 we present the detailed modeling of the LISA measurement that serves as a basis for the remaining chapters. We introduce the basic measurement principle of LISA; performing inter-satellite ranging with picometer-precision using laser interferometry. To understand what limits the ranging performance we explain the coupling mechanisms of various instrumental noises. Most relevant in this context are laser frequency noise and timing jitter of the clocks. They completely dominate the single-link measurements and cover up any GW signals.

The solution is presented in chapter 3 which discusses the TDI algorithm that can be used to synthesizes virtual equal-arm interferometers. Those are (almost) immune to laser frequency noise and clock timing jitter. Prior to TDI the various ranging sensors have to be "fused" in a dedicated ranging processing pipeline to form accurate, high-precision estimates of the pseudo-ranges that are required as an input for TDI. Then, we investigate the various coupling channels of laser and timing noise residuals in the TDI combinations. We find that biases of a few meters in the pseudo-random noise (PRN) ranges limit the laser noise suppression in TDI.

To calibrate those biases we propose to use time-delay interferometric ranging (TDI-R) which is a bias-free ranging method for LISA. We present a detailed statistical analysis of TDI-R in chapter 4 using the Fisher information formalism and present analytical lower bounds on the estimation variance of the ranges.

Finally, we conclude in chapter 5. We discuss the implications of this thesis for the LISA mission and point out avenues for future work.

Chapter 2

Instrumental Modeling

In this section we explain the model behind the LISA measurements that we analyze in the remaining chapters. Bayle and Hartwig (2023) give a concise overview of the modeling used in state-of-the-art LISA simulators, like LISA Instrument (Bayle et al., 2022a) and LISANode. We only reproduce the model in phase units here as frequency units are straight-forward to derive by taking the time derivative.

Stable frequency standards are the core components of the LISA mission. As explained in section 1.2.4 lasers and clocks are used to perform inter-satellite ranging with picometer precision and timing of the measurement chain. Even though lasers and clocks have very different requirement they both can be described by the same formalism. Therefore, the main task of LISA modeling is to represent the phase evolution of each frequency standard appropriately. In general, frequency standards are very stable oscillators with an initial phase $\phi_0 = \phi(t_0)$ and a nominal frequency ν_0. Thus, their ideal phase evolution, according to the local proper time, is given by

$$\phi_0 + \nu_0 \cdot (t - t_0). \tag{2.1}$$

However, in reality, the real frequency of the oscillator is different from the nominal one and their exact timing is subject to noise. We describe any deviations from the nominal phase in terms of timing deviations $x(t)$. The real phase is then modeled as

$$\phi(t) = \phi_0 + \nu_0 \cdot (t + x(t) - t_0). \tag{2.2}$$

Conceptually and numerically it is appropriate to split up the timing deviations $x(t)$ into a large but slowly varying component and small in-band fluctuations.

$$x(t) = x^o(t) + x^\epsilon(t) \tag{2.3a}$$
$$y(t) = y^o(t) + y^\epsilon(t) \tag{2.3b}$$

Here, we also define the fractional frequency deviations $y(t) = \dot{x}(t)$ that represent the relative frequency shifts with respect to the nominal frequency. Slow drifts in this variable capture effects like Doppler shifts in the laser beams or systematic clock offsets that vary over time scales of a few months. For the frequency standards used in LISA, $y^o(t)$ is of the order of 10^{-7}, which accumulates to a timing deviation of a few seconds over the mission of ten years. On the other hand, in-band timing fluctuations $x^\epsilon(t)$ account for much less. For example, the LISA lasers have a fractional frequency stability in terms of ASD of $\sqrt{S_y} = 10^{-13}\,1/\sqrt{\text{Hz}}$. This results in an in-band noise root mean square (RMS) of[1]

$$\sqrt{\int_{10^{-4}\,\text{Hz}}^{1\,\text{Hz}} \frac{S_y}{(2\pi f)^2}\,\mathrm{d}f} \approx 1.6 \times 10^{-12}\,\text{s}. \tag{2.4}$$

[1] For this order-of-magnitude calculation, we neglect again the noise shape function that amplifies the power at frequencies below 2 mHz.

Therefore, the timing deviations accumulated by the slow drifts is around 12 orders of magnitude higher than the timing fluctuations caused by in-band noise. To appropriately describe both quantities we model the slow varying fractional frequency shifts $y^o(t)$ and in-band timing fluctuation $x^\epsilon(t)$ in separate variables and express the total timing deviations as

$$x(t) = \int_{t_0}^{t} y^o(t')\,\mathrm{d}t' + x^\epsilon(t). \tag{2.5}$$

Consequently, the total phase of a frequency standard can be described by two scalars, the initial phase ϕ_0 and the nominal frequency ν_0, and two time series, the out-of-band fractional frequency deviations $y^o(t)$ and the in-band timing fluctuations $x^\epsilon(t)$.

$$\phi(t) = \phi_0 + \nu_0 \cdot \int_{t_0}^{t} \big(1 + y^o(t')\big)\,\mathrm{d}t' + \nu_0 \cdot x^\epsilon(t) \tag{2.6}$$

In the following section we will explain the contents of the main LISA measurements which are the beatnote phases of the three interferometers and the PRN ranges. We start off by describing the model of the laser beams. Besides the main carrier phase it also contains sidebands that are used to transfer the clock signals and spacecraft timers for absolute ranging. Ultimately, the beatnote phase measurements and PRN ranges are discretely sampled according to the spacecraft timers and decimated down to the telemetry rate of 4 Hz.

2.1 Laser Beam

As already introduced in section 1.1.1, we describe laser beams in the plane-wave approximation. The electric field at some fixed point along the beam axis is given as

$$E(t) = E_0 \cdot \cos\big(2\pi\phi(t)\big), \tag{2.7}$$

where E_0 denotes its amplitude and $\phi(t)$ determines the time-dependent phase of the laser, which quickly accumulates due to the terahertz optical frequency. Furthermore, we assume that the laser propagates in vacuum at the speed of light without suffering from dispersion.

For our studies we assume E_0 to be constant and therefore irrelevant to the final beatnote measurement. However, in general, the beatnote phase tracked by the phasemeter is sensitive to fluctuations in the absolute laser power. This coupling is called relative-intensity noise and is further detailed in Wissel et al. (2023).

The relevant quantity for modeling the beatnotes are the six laser phases. They encode the evolution of the carrier phase, the upper and lower sideband phase and the reading of the local timer. For simpler modeling we keep track of each quantity in a separate variable.

Following this decomposition the laser carrier phase at the source without any modulations can be described by using eq. (2.6),

$$\begin{aligned} \phi^{\mathrm{c}}_{ij}(t) &= \phi^{\mathrm{c}}_{0,ij} + \nu_0 \cdot (t - t_0 + x^{\mathrm{c}}_{ij}(t)) && (2.8)\\ &= \phi^{\mathrm{c}}_{0,ij} + \int_{t_0}^{t} \big(\nu_0 + \underbrace{\nu_0 \cdot y^{\mathrm{c}}_{ij}(t')}_{o_{ij}(t')}\big)\,\mathrm{d}t' + \underbrace{\nu_0 \cdot x^{\mathrm{c},\epsilon}_{ij}(t)}_{p_{ij}(t)}. && (2.9) \end{aligned}$$

Here, we have identified the slowly varying megahertz-offsets $o_{ij}(t)$ and the laser frequency noise $p_{ij}(t)$.

2.1.1 Pseudo-random noise modulation

LISA implements absolute ranging by modulating a pseudo-random noise code onto the laser beam (Esteban Delgado, 2012). This code is read out by the phasemeter on the distant spacecraft

and correlated with a local copy to infer the propagation delay between the satellites. In essence, this allows to compare the timer of the emitting and receiving spacecraft at the events when the beams were emitted and received, respectively. To simplify the modeling we directly compare the readings of the timers which are defined as

$$\hat{\tau}_i(t) = \hat{\tau}_{0,i} + \int_{t_0}^{t} 1 + y_i^{\mathrm{uso},o}(t')\,\mathrm{d}t' + \underbrace{x_i^{\epsilon}(t)}_{q_i(t)}. \tag{2.10}$$

They are derived from the pilot tone and therefore inherit the properties of the USO. Here, $y_i^{\mathrm{uso},o}(t')$ describes any slow varying fractional frequency drifts of the clock and $q_i(t)$ any in-band timing jitter. To allow the timers to be started at an arbitrary time we introduce the initial timer reading $\hat{\tau}_{0,i}$ at time t_0. For more convenient modeling we rewrite eq. (2.10) in terms of the nominal spacecraft proper time and timer deviations

$$\hat{\tau}_i(t) = t + \delta\hat{\tau}_i(t). \tag{2.11}$$

The timer deviations collect large drifts and small fluctuations. To retain numerical precision in the small variable we decompose $\delta\hat{\tau}_i(t)$ into $\delta\hat{\tau}_i^o(t)$ and $\delta\hat{\tau}_i^{\epsilon}(t)$. They are related to the quantities in eq. (2.10) as

$$\delta\hat{\tau}_i^o(t) = \hat{\tau}_{0,i} - t_0 + \int_{t_0}^{t} y_i^{\mathrm{uso},o}(t')\,\mathrm{d}t' \tag{2.12}$$

$$\delta\hat{\tau}_i^{\epsilon}(t) = q_i(t). \tag{2.13}$$

2.1.2 Sideband modulation

For clock noise transfer, the local clock is phase-modulated onto the laser carrier phase. The modulation phase $\phi_{ij}^{\mathrm{m}}(t)$ is derived from the megahertz clock signal which is upconverted to a few gigahertz. We can therefore model the total phase of the signal as

$$\phi_{ij}^{\mathrm{m}}(t) = \phi_{0,ij}^{\mathrm{m}} + \nu_{0,ij}^{\mathrm{m}} \cdot \int_{t_0}^{t} 1 + y_i^{\mathrm{uso},o}(t')\,\mathrm{d}t' + \nu_{0,ij}^{\mathrm{m}} \cdot \big(q_i(t) + M_{ij}(t)\big). \tag{2.14}$$

Additionally to the timing jitter of the clocks $q_i(t)$, we account for any extra noise that adds in the modulation chain by the modulation noise $M_{ij}(t)$. The modulation frequency $\nu_{0,ij}^{\mathrm{m}}$ on left-handed and right-handed MOSAs are 2.4 GHz and 2.401 GHz, respectively. The 1 MHz difference between left-handed and right-handed MOSAs is needed to allow separation of the carrier-carrier and sideband-sideband beatnotes.

The modulation phase is then fed to an electro-optical modulator that modulates the phase of the electric field that passes through the device. We can formally describe this process by augmenting eq. (2.7) with a modulation term,

$$E(t) = E_0 \cdot \cos\big(2\pi\phi^{\mathrm{c}}(t) + m\cos(2\pi\phi^{\mathrm{m}}(t))\big). \tag{2.15}$$

For LISA, the modulation index m is about 0.15 , and thus sufficiently small to truncate the Jacobi-Anger expansion after the linear term and rewrite this expression as

$$E(t) \simeq E_0 \cdot \cos\big(2\pi\phi^{\mathrm{c}}(t)\big) - E_0 \cdot \frac{m}{2}\sin\big(2\pi\phi^{\mathrm{lsb}}(t)\big) - E_0 \cdot \frac{m}{2}\sin\big(2\pi\phi^{\mathrm{usb}}(t)\big). \tag{2.16}$$

We note that the modulated laser beam is represented by a superposition of three frequencies, the carrier and the lower and upper sidebands. The phase of the latter is defined as

$$\phi_{ij}^{\mathrm{usb/lsb}}(t) = \phi_{ij}^{\mathrm{c}}(t) \pm \phi_{ij}^{\mathrm{m}}(t). \tag{2.17}$$

The term sideband comes from the fact that they oscillate at a nominal frequency of $\nu_{0,ij}^{\mathrm{usb/lsb}} = \nu_0^{\mathrm{c}} \pm \nu_{0,ij}^{\mathrm{m}}$.

2.1.3 Free-space propagation

In the next step, we propagate the variables defined above through free space. This is required to transport the laser beams from the laser source to the photodiodes. We can model propagation of an arbitrary phase $\phi(t)$ as a time-delay by $d(t)$. This is possible since the wavefronts travel at constant rate; the speed of light. We split this delay up into a large slowly drifting quantity $d^o(t)$ and small in-band fluctuations $d^\epsilon(t)$. The out-of-band component captures the slowly evolving inter-spacecraft light travel times due to orbital dynamics or (almost) constant optical path-lengths on the optical benches. The in-band component describes path length noises due to the instability of components on the optical bench that limit the relative length measurement by LISA, but also the effect of GWs on the travel time.

Let us observe the effect of a time-delay on an arbitrary phase $\phi(t)$ as it is given in eq. (2.6).

$$\phi(t - d(t)) = \phi_0 + \nu_0 \cdot \int_{t_0}^{t-d(t)} 1 + y^o(t')\,\mathrm{d}t' + \nu_0 \cdot x^\epsilon\big(t - d(t)\big) \tag{2.18}$$

$$\simeq \phi_0 + \nu_0 \cdot \int_{t_0}^{t-d^o(t)} 1 + y^o(t')\,\mathrm{d}t' - d^\epsilon(t) \cdot \nu_0 \cdot \big(1 + y^o(t - d^o(t))\big) + \nu_0 \cdot x^\epsilon\big(t - d^o(t)\big) \tag{2.19}$$

$$= \phi_0 - \nu_0 \cdot \int_{t_0 - d^o(t)}^{t_0} 1 + y^o(t')\,\mathrm{d}t' + \nu_0 \cdot \int_{t_0}^{t} \big(1 - \dot{d}^o(t')\big) \cdot \big(1 + y^o(t' - d^o(t'))\big)\,\mathrm{d}t' + \nu_0 \cdot \big(x^\epsilon\big(t - d^o(t)\big) - d^\epsilon(t) \cdot \big(1 + y^o(t - d^o(t))\big)\big) \tag{2.20}$$

In the second line we expand the integral to first order in the small quantity $d_\epsilon(t)$. Furthermore, the effect of the later on the time-delay of the already small quantity $x^\epsilon(t)$ can be neglected. Finally, we perform the substitution $t' \to t' - d^o(t')$ and collect the following terms. We find a modified initial phase offset

$$\phi_0 - \nu_0 \cdot \int_{t_0 - d^o(t)}^{t_0} 1 + y^o(t')\,\mathrm{d}t', \tag{2.21}$$

the Doppler shifted and delayed out-of-band fractional frequency

$$\big(1 - \dot{d}^o(t)\big) \cdot \big(1 + y^o(t - d^o(t))\big), \tag{2.22}$$

and the effective timing jitter of the delayed phase

$$x^\epsilon\big(t - d^o(t)\big) - d^\epsilon(t) \cdot \big(1 + y^o(t - d^o(t))\big), \tag{2.23}$$

that consists of the origin delayed timing jitter and the coupling of the small in-band delay fluctuations to the delayed out-of-band fractional frequency. The modified initial phase offset and the Doppler shift are illustrated in fig. 2.1.

We recover equivalent expressions for the description of the laser phase including sideband modulation as reported in the literature (Bayle and Hartwig, 2023). In addition, we explicitly model the effect of the initial phase ϕ_0 in lasers and clocks.

In the following we will make extensive use of the notion of delay operators which are defined as

$$\mathbf{D}x(t) = x\big(t - d(t)\big). \tag{2.24}$$

The delay operator $\mathbf{D}$ effectively delays the argument of an arbitrary time-dependent function $x(t)$ by the value $d(t)$.

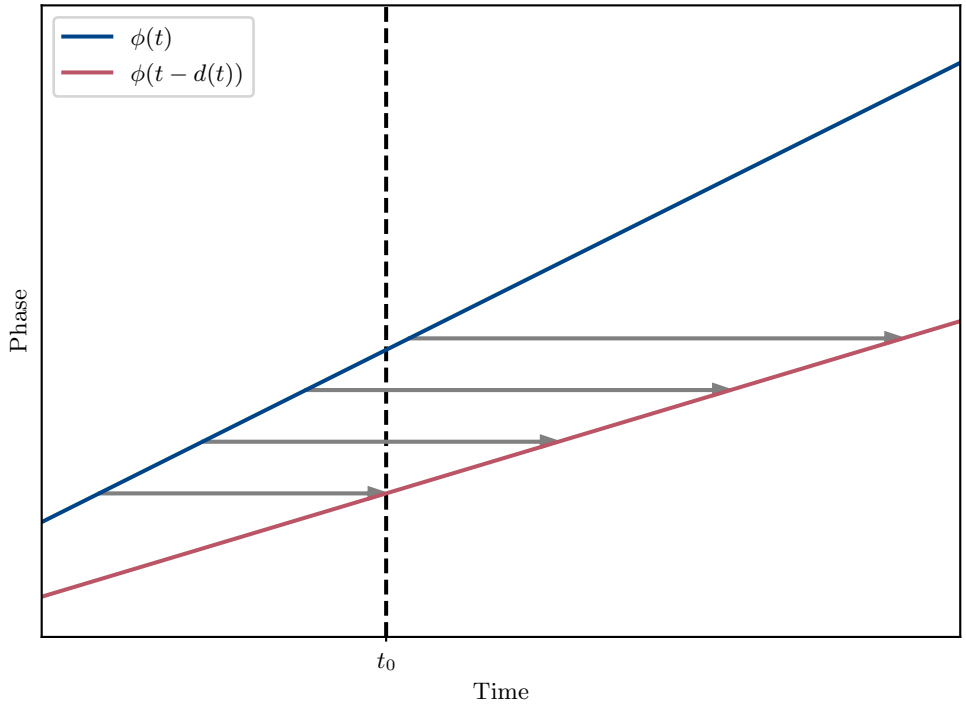

Figure 2.1: Illustration of total phase propagation by applying an arbitrary time-dependent time-delay $d(t)$ that models beam propagation between the spacecraft. The blue and red lines represent the origin phase and propagated phase, respectively. The grey arrows indicate the time-shifting operation which leads to a reduction of the phase offset and a smaller effective slope (Doppler shift). The effect of the much smaller in-band component of the time-delay is not resolved in the picture.

2.2 Interferometry

Each MOSA hosts three interferometers combining beams from the local laser, the adjacent laser and the distant laser. The mixing of the beams in each interferometer generates three beatnotes that are in the bandwidth of the photodetector: the carrier-carrier beatnote and the two sideband beatnotes. Each of those beatnote phases is tracked by an individual digital phase-locked loop (DPLL).

Constant optical path lengths on the optical benches are assumed to be zero[2]. Therefore, we only model the in-band optical path-length noise that is caused by various effects, like thermal expansion due to temperature fluctuations. Furthermore, upon detection on the photodiodes, readout noise enters the beatnote measurements. It is made up of photon shot noise and electronic noise of the readout chain.

At the time of writing, the LISA simulators do not implement the non-inertial motion of the spacecraft[3] or MOSA translational jitter. The modeling of the spacecraft dynamics is quite sophisticated as it includes a control loop that adjusts the spacecraft position to follow the TMs and suppress the influence of external disturbances (Inchauspé et al., 2022). For now we assume that the optical benches follow perfect geodesics such that the test-mass interferometer only senses the residual acceleration noise shaking the TMs. Furthermore, we account for translational MOSA jitter and spacecraft motion in TDI (see section 3.2.1).

The reference and TM interferometers combine beams from adjacent MOSAs. The so-called backlink fiber is used to optically connect the two optical benches. Propagation through the fiber introduces phase noise, which we call backlink noise.

As explained in section 1.1.1, interfering two laser beams at optical frequencies and detecting the time-dependent power of the superposition is equivalent to mixing the two frequencies. The readout chain is only sensitive to the difference frequency that we call *beatnote*. The beatnote frequency is always interpreted as positive by the phasemeter that tracks its phase. In our modeling we implicitly assume that the sign ambiguity can be resolved, as the signs can be inferred from the frequency plan. Furthermore, the phasemeter only tracks the phase up to an integer cycle, such that it reads

$$\varphi(t) = \phi_1(t) - \phi_2(t) + n, \tag{2.25}$$

where $n \in \mathbb{Z}$ is constant but unknown and resets at any interruption. Interestingly, we will see later that the transfer function of TDI has a vanishing response to carrier beatnote measurements and laser phases at d.c. thus it removes any constant offsets. Therefore, the modeling of the laser initial phase and carrier beatnote phase ambiguity is not required.

2.2.1 Carrier beatnotes

The three carrier beatnotes are produced by beating the carrier phases of two beams against each other. They represent the main science measurements of LISA and are later processed through TDI to produce the final observables. Apart from the overwhelming laser noise that is suppressed in TDI, they contain the GW signal, other path-length noises and test-mass acceleration noise that ultimately limit the sensitivity of the detector.

Inter-spacecraft interferometer

The inter-spacecraft interferometer interferes the distant beam with the local beam. Below we express the optical path length both beams have to travel from the laser source to the

[2] In reality they are not because of the path lengths between components on the optical bench. However, if they are matched for each interferometer they do not impact the laser noise suppression in TDI as, in the end, they represent a simple group delay of a few ns

[3] This feature is already available in the simulation tool LISANode which is not used in this thesis.

interferometer.

$$d_{\mathrm{isi}_{ij}\leftarrow\phi_{ji}}(t) = d^o_{ij}(t) + H_{ij}(t) + N^{\mathrm{ob,isi}_{ij}\leftarrow\phi_{ji}}_{ij}(t) \tag{2.26a}$$

$$d_{\mathrm{isi}_{ij}\leftarrow\phi_{ij}}(t) = N^{\mathrm{ob,isi}_{ij}\leftarrow\phi_{ij}}_{ij}(t) \tag{2.26b}$$

The distant beam experiences the inter-spacecraft propagation delay that consists of large out-of-band component $d^o_{ij}(t)$ that is driven by orbital dynamics and the tiny fluctuations $H_{ij}(t)$ caused by a passing GW. Additionally, it collects any optical path-length noises. The local laser only experiences the latter.

Let us make use of eqs. (2.9) and (2.20) to express the total phase of the inter-spacecraft beatnote. For better readability we drop the explicit time-dependence.

$$\mathrm{isi}^{\mathrm{c}}_{ij} = \mathbf{D}_{\mathrm{isi}_{ij}\leftarrow\phi_{ji}}\phi^{\mathrm{c}}_{ji} - \mathbf{D}_{\mathrm{isi}_{ij}\leftarrow\phi_{ij}}\phi^{\mathrm{c}}_{ij} + N^{\mathrm{ro,isi^c}}_{ij} \tag{2.27}$$

$$\begin{aligned}\simeq \mathrm{isi}^{\mathrm{c}}_{0,ij} &+ \int_{t_0}^{t} \dot{\mathbf{D}}^o_{ij} o_{ji} - o_{ij} - \dot{d}^o_{ij}\cdot\nu_0\,\mathrm{d}t' + \mathbf{D}^o_{ij}p_{ji} - p_{ij} \\ &- \left(H_{ij} + N^{\mathrm{ob,isi}_{ij}\leftarrow\phi_{ji}}_{ij}\right)\cdot\left(\nu_0 + \mathbf{D}^o_{ij}o_{ji}\right) + N^{\mathrm{ob,isi}_{ij}\leftarrow\phi_{ij}}_{ij}\cdot\left(\nu_0 + o_{ij}\right) + N^{\mathrm{ro,isi^c}}_{ij}.\end{aligned} \tag{2.28}$$

For the reason stated above we omit specifying the initial phase $\mathrm{isi}_{0,ij}$. The offset frequency of the beatnote is now of the order of megahertz as the central laser frequency ν_0 drops out. As small fluctuations, we collect the differential laser phase noise, the GW and optical path-length noises coupling to the associated carrier frequencies and readout noise.

Reference interferometer

The reference interferometer mixes the adjacent beam and the local beam. Their respective optical path lengths are entirely made up of optical path-length noises.

$$d_{\mathrm{rfi}_{ij}\leftarrow\phi_{ik}}(t) = N^{\mathrm{bl},ij\leftarrow ik}_{ij}(t) + N^{\mathrm{ob,rfi}_{ij}\leftarrow\phi_{ik}}_{ij}(t) \tag{2.29a}$$

$$d_{\mathrm{rfi}_{ij}\leftarrow\phi_{ij}}(t) = N^{\mathrm{ob,rfi}_{ij}\leftarrow\phi_{ij}}_{ij}(t) \tag{2.29b}$$

As the adjacent beam is connected via the backlink fiber it additionally picks up backlink noise. Ideally, this noise is identical for counter-propagating beams such that it cancels in TDI (see section 3.2.2) but in practice, we do expect some non-reciprocity of the fiber backlink.

The resulting beatnote phase has the following form.

$$\mathrm{rfi}^{\mathrm{c}}_{ij}(t) = \mathbf{D}_{\mathrm{rfi}_{ij}\leftarrow\phi_{ik}}\phi^{\mathrm{c}}_{ik} - \mathbf{D}_{\mathrm{rfi}_{ij}\leftarrow\phi_{ij}}\phi^{\mathrm{c}}_{ij} + N^{\mathrm{ro,rfi^c}}_{ij} \tag{2.30}$$

$$\begin{aligned}\simeq \mathrm{rfi}^{\mathrm{c}}_{0,ij} &+ \int_{t_0}^{t} o_{ik} - o_{ij}\,\mathrm{d}t' + p_{ik} - p_{ij} - \left(N^{\mathrm{bl},ij\leftarrow ik}_{ij} + N^{\mathrm{ob,rfi}_{ij}\leftarrow\phi_{ik}}_{ij}\right)\cdot\left(\nu_0 + o_{ik}\right) \\ &+ N^{\mathrm{ob,rfi}_{ij}\leftarrow\phi_{ij}}_{ij}\cdot\left(\nu_0 + o_{ij}\right) + N^{\mathrm{ro,rfi^c}}_{ij}.\end{aligned} \tag{2.31}$$

Test-mass interferometer

Similar to the reference interferometer, the TM interferometer interferes the adjacent beam and the local beam. However, the local beam is bounced off the TM and therefore senses the spurious test-mass acceleration noise $N^{\delta}_{ij}(t)$.

$$d_{\mathrm{tmi}_{ij}\leftarrow\phi_{ik}}(t) = N^{\mathrm{bl},ij\leftarrow ik}_{ij}(t) + N^{\mathrm{ob,tmi}_{ij}\leftarrow\phi_{ik}}_{ij}(t), \tag{2.32a}$$

$$d_{\mathrm{tmi}_{ij}\leftarrow\phi_{ij}}(t) = 2N^{\delta}_{ij}(t) + N^{\mathrm{ob,rfi}_{ij}\leftarrow\phi_{ij}}_{ij}(t). \tag{2.32b}$$

It is counted twice as the beam travels forth and back along the additional path length produced by the motion of the TM.

The resulting beatnote phase reads

$$\mathrm{tmi}^{\mathrm{c}}_{ij}(t) = \mathbf{D}_{\mathrm{tmi}_{ij}\leftarrow\phi_{ik}}\phi^{\mathrm{c}}_{ik} - \mathbf{D}_{\mathrm{tmi}_{ij}\leftarrow\phi_{ij}}\phi^{\mathrm{c}}_{ij} + N^{\mathrm{ro},\mathrm{tmi}^{\mathrm{c}}}_{ij} \tag{2.33}$$

$$\begin{aligned}\simeq \mathrm{tmi}^{\mathrm{c}}_{0,ij} + \int_{t_0}^{t} o_{ik} - o_{ij}\,\mathrm{d}t' + p_{ik} - p_{ij} - \left(N^{\mathrm{bl},ij\leftarrow ik}_{ij} + N^{\mathrm{ob},\mathrm{tmi}_{ij}\leftarrow\phi_{ik}}_{ij}\right)\cdot\left(\nu_0 + o_{ik}\right)\\ + \left(2N^{\delta}_{ij} + N^{\mathrm{ob},\mathrm{tmi}_{ij}\leftarrow\phi_{ij}}_{ij}\right)\cdot\left(\nu_0 + o_{ij}\right) + N^{\mathrm{ro},\mathrm{tmi}^{\mathrm{c}}}_{ij}.\end{aligned} \tag{2.34}$$

The results for the carrier beatnote phases are consistent with the existing literature (Bayle and Hartwig, 2023). The only differences are that we account for the offset frequencies o_{ij} of the lasers for the coupling of in-band path-length fluctuations and that we explicitly model the initial phase of the interferometers.

2.2.2 Sideband beatnotes

The sideband beatnotes are produced by beating the sideband phases against each other. They are defined in eq. (2.17) and contain the sum or difference (upper and lower sideband) of the carrier phase ϕ^{c}_{ij} and the phase modulation ϕ^{m}_{ij}. We model the phase readout of the sideband beatnotes in a feed-forward configuration. This means that the sideband DPLL receives the carrier beatnote phase and uses it to offset its error point. As a result, the phase register only accumulates any additional phase to the carrier phase.

To read out the lower and upper sidebands individually LISA implements two separate DPLLs. Both signals in principle track the same quantity but have independent readout noise. Furthermore, they experience slightly different Doppler shifts due to their different absolute frequency in the beam ($\nu^{\mathrm{c}}_0 \pm \nu^{\mathrm{m}}_0$). Therefore, we propose that the phase readouts of the upper and lower sidebands are merged on board to avoid sending redundant data and relax the data budget. However, the exact merging procedure must be able to detect whether the upper or lower sideband beatnote is degraded to minimize the technical noise in the combined product.

Let us explain the contents of the sideband beatnote using the example of the inter-spacecraft interferometer. To model the feed-forward readout we subtract the carrier beatnote. The upper and lower sidebands are then given by

$$\mathrm{isi}^{\mathrm{usb/lsb}}_{ij}(t) = \mathbf{D}_{\mathrm{isi}_{ij}\leftarrow\phi_{ji}}\left(\phi^{\mathrm{c}}_{ji} \pm \phi^{\mathrm{m}}_{ji}\right) - \mathbf{D}_{\mathrm{isi}_{ij}\leftarrow\phi_{ij}}\left(\phi^{\mathrm{c}}_{ij} \pm \phi^{\mathrm{m}}_{ij}\right) + N^{\mathrm{ro},\mathrm{isi}^{\mathrm{usb/lsb}}}_{ij} - \mathrm{isi}^{\mathrm{c}}_{ij} \tag{2.35}$$

$$= \pm\left(\mathbf{D}_{\mathrm{isi}_{ij}\leftarrow\phi_{ji}}\phi^{\mathrm{m}}_{ji} - \mathbf{D}_{\mathrm{isi}_{ij}\leftarrow\phi_{ij}}\phi^{\mathrm{m}}_{ij}\right) + N^{\mathrm{ro},\mathrm{isi}^{\mathrm{usb/lsb}}}_{ij} - N^{\mathrm{ro},\mathrm{isi}^{\mathrm{c}}}_{ij}. \tag{2.36}$$

Here, we use the definition of the sideband phases in eq. (2.17) and the carrier beatnote in eq. (2.28). After subtraction, the sideband beatnotes inherit the readout noise of the carrier beatnotes. However, we notice that it is common mode for the upper and lower sideband beatnotes while the phase modulation that contains the clock information is differential mode. We therefore consider in the following the combined sideband signal as

$$\mathrm{isi}^{\mathrm{sb}}_{ij}(t) = \frac{\mathrm{isi}^{\mathrm{usb}}_{ij} - \mathrm{isi}^{\mathrm{lsb}}_{ij}}{2} \tag{2.37}$$

$$= \mathbf{D}_{\mathrm{isi}_{ij}\leftarrow\phi_{ji}}\phi^{\mathrm{m}}_{ji} - \mathbf{D}_{\mathrm{isi}_{ij}\leftarrow\phi_{ij}}\phi^{\mathrm{m}}_{ij} + \underbrace{\frac{N^{\mathrm{ro},\mathrm{isi}^{\mathrm{usb}}}_{ij} - N^{\mathrm{ro},\mathrm{isi}^{\mathrm{lsb}}}_{ij}}{2}}_{N^{\mathrm{ro},\mathrm{isi}^{\mathrm{sb}}}_{ij}} \tag{2.38}$$

$$\begin{aligned}= \mathrm{isi}^{\mathrm{sb}}_{0,ij} + \int_{t_0}^{t} \nu^{\mathrm{m}}_{0,ji} - \nu^{\mathrm{m}}_{0,ij} - d^{o}_{ij}\cdot\nu^{\mathrm{m}}_{0,ji} + \nu^{\mathrm{m}}_{0,ji}(1 - \dot{d}^{o}_{ij})\mathbf{D}^{o}_{ij}y^{\mathrm{uso},o}_{j} - \nu^{\mathrm{m}}_{0,ij}y^{\mathrm{uso},o}_{i}\,\mathrm{d}t'\\ + \nu^{\mathrm{m}}_{0,ji}\mathbf{D}^{o}_{ij}\left(q_j + M_{ji}\right) - \nu^{\mathrm{m}}_{0,ij}\left(q_i + M_{ij}\right) + N^{\mathrm{ro},\mathrm{isi}^{\mathrm{sb}}}_{ij}.\end{aligned} \tag{2.39}$$

The carrier beatnote readout noise cancels and the inherent sideband beatnote readout noise is reduced by a factor $\sqrt{2}$ in amplitude. In the last line we plugin the definition of the phase

modulation (see eq. (2.14)). We neglect the coupling of path-length noises to the gigahertz modulation frequency as they are much smaller than the picometer readout noise ($N^{\mathrm{ob}} \cdot \nu_0^{\mathrm{m}} \ll N^{\mathrm{ro,ifo^{sb}}}$). Furthermore, we find that the sideband beatnote beats at nominal frequency of $\nu_{0,ji}^{\mathrm{m}} - \nu_{0,ij}^{\mathrm{m}} = \pm 1\,\mathrm{MHz}$ and tracks the differential clock information contaminated by modulation noise and readout noise.

The reference and TM interferometer sideband beatnotes are defined similarly and compare adjacent phase modulations on the same spacecraft. We derive

$$\begin{aligned}\mathrm{ifo}_{ij}^{\mathrm{sb}}(t) = \mathrm{ifo}_{0,ij}^{\mathrm{sb}} + \int_{t_0}^{t} \nu_{0,ik}^{\mathrm{m}} - \nu_{0,ij}^{\mathrm{m}} + \nu_{0,ik}^{\mathrm{m}} y_i^{\mathrm{uso},o} - \nu_{0,ij}^{\mathrm{m}} y_i^{\mathrm{uso},o}\,\mathrm{d}t' \\ + \nu_{0,ik}^{\mathrm{m}}\big(q_i + M_{ik}\big) - \nu_{0,ij}^{\mathrm{m}}\big(q_i + M_{ij}\big) + N_{ij}^{\mathrm{ro,ifo^{sb}}}.\end{aligned} \tag{2.40}$$

As they measure the same quantity, we use the placeholder ifo_{ij}, which can either be replaced by rfi_{ij} or tmi_{ij}. As we will later see, this measurement tracks the differential modulation noise on adjacent MOSAs and can be used to remove the dominant modulation noise terms.

2.2.3 Absolute ranging

An absolute ranging measurement is achieved in LISA by modulation of a PRN code on the carrier. It is read out by the phasemeter and correlated with a local copy in a delay-locked loop to infer the time shift between the codes. As the codes have a finite length corresponding to a few hundred kilometers, the delay measurement is ambiguous and can only be determined up to an integer multiple of the code length. However, this ambiguity can easily be resolved on ground using position and synchronization information of the spacecraft obtained from ground-based observations.

We model this measurement as the difference of spacecraft timers $\hat{\tau}_i$ as those drive the timing of the modulation and extraction of the codes. The six PRN ranges compare the local timer with the distant timer that has propagated along the link

$$R_{ij}(t) = \hat{\tau}_i(t) - \mathbf{D}_{ij}\hat{\tau}_j(t) + B_{ij} + N_{ij}^R(t). \tag{2.41}$$

To account for noise in the readout process we add a generic ranging noise term to it with a typical RMS amplitude of 1 m at 4 Hz. Furthermore, the PRN range is potentially biased due to various sources of group delays. Most of those are calibrated on ground prior to launch but might drift over the mission time. We assume that typical values for the residual bias B_{ij} are of the order of meters.

We plug in the model for the timer given in eq. (2.11) and arrive at

$$R_{ij}(t) = \delta\hat{\tau}_i(t) - \mathbf{D}_{ij}\delta\hat{\tau}_j(t) + d_{ij}^o(t) + B_{ij} + N_{ij}^R(t). \tag{2.42}$$

Here, we can clearly see that the PRN range is a pseudo-range, as differential clock information is entangled with the inter-spacecraft distance. We neglect any coupling to path-length noises or GW signals (picometer) as they are much smaller than the ranging noise.

2.3 Sampling and Onboard Processing

All LISA measurements defined above are encoded in the differential phase of two interfering laser beam as they arrive at the photodetector. As already mentioned, DPLLs in the phasemeters are employed to read out the different components of the beatnote phase (carrier-carrier, sideband-sideband beatnotes and PRN range). Prior to this, the continuous-time analog signals need to be converted to discrete-time digital signals. To appropriately capture beatnote frequencies up to 25 MHz, the DPLLs run at 80 MHz. Finally, several decimation stages are used to decimate down to the telemetry rate of 4 Hz.

2.3.1 Sampling by the on-board clock

We model the process of signal sampling as transforming the time reference frame of the measurements from the spacecraft proper time to the spacecraft on-board time as it is dictated by the spacecraft timer. Therefore, we apply the following transformation to all beatnote phases

$$\phi^{\hat{\tau}_i}(t) = \mathbf{T}^{\hat{\tau}_i}_{\tau_i}\phi^{\tau_i}(t) = \phi^{\tau_i}\big(\tau_i^{\hat{\tau}_i}(t)\big), \tag{2.43}$$

which requires the reading of the spacecraft proper time $\tau_i^{\hat{\tau}_i}(t)$ according to the spacecraft on-board time. However, we currently only model the "inverse" quantity $\hat{\tau}_i^{\tau_i}(t)$. To calculate it, we evaluate eq. (2.11) at time $\tau_i^{\hat{\tau}_i}(\tau)$, which gives

$$t = \hat{\tau}_i^{\tau_i}\big(\tau_i^{\hat{\tau}_i}(t)\big) = \tau_i^{\hat{\tau}_i}(t) + \delta\hat{\tau}_i\big(\tau_i^{\hat{\tau}_i}(t)\big), \tag{2.44}$$

where we also used that, trivially, $\hat{\tau}_i^{\tau_i}\big(\tau_i^{\hat{\tau}_i}(t)\big) = t$ (Bayle and Hartwig, 2023). This procedure provides an implicit definition of $\tau_i^{\hat{\tau}_i}(t)$. Again, to avoid large numbers we only calculate deviations of the spacecraft proper time from the on-board time $\delta\tau_i(t)$ and find

$$\delta\tau_i(t) = -\delta\hat{\tau}_i\big(t + \delta\tau_i(t)\big). \tag{2.45}$$

Generally, there exists no closed-form solution of this equation for arbitrary $\delta\hat{\tau}_i(t)$ so it must be solved numerically. This is achieved in an iterative fashion. As an initial guess we set $\delta\tau_i^{(0)}(t) = -\delta\hat{\tau}_i(t)$. Then we calculate more and more accurate estimates by following

$$\delta\tau_i^{(n+1)}(t) = -\delta\hat{\tau}_i\big(t + \delta\tau_i^{(n)}(t)\big), \tag{2.46}$$

until the solution has converged close enough for our purposes. If we like to retain numerical precision we can also operate on the decomposed timer deviations

$$\begin{aligned}\delta\tau_i^o(t) + \delta\tau_i^\epsilon(t) &= -\delta\hat{\tau}_i(t + \delta\tau_i(t)\big) && (2.47)\\ &\simeq -\delta\hat{\tau}_i\big(t + \delta\tau_i^o(t)\big) - \delta\tau_i^\epsilon(t)\cdot\delta\dot{\hat{\tau}}_i^o\big(t + \delta\tau_i^o(t)\big), && (2.48)\end{aligned}$$

which yields expressions for the slow drifts and small fluctuations of the deviation of the proper time from the on-board time. We identify

$$\begin{aligned}\delta\tau_i^o(t) &= -\delta\hat{\tau}_i^o\big(t + \delta\tau_i^o(t)\big), && (2.49a)\\ \delta\tau_i^\epsilon(t) &= -\frac{\delta\hat{\tau}_i^\epsilon\big(t + \delta\tau_i^o(t)\big)}{1 + \delta\dot{\hat{\tau}}_i^o\big(t + \delta\tau_i^o(t)\big)}. && (2.49b)\end{aligned}$$

Ultimately, we can use eq. (2.49) to describe signal sampling as defined in eq. (2.43).

$$\begin{aligned}\phi^{\hat{\tau}_i}(t) &= \phi^{\tau_i}\big(t + \delta\tau_i(t)\big) && (2.50)\\ &\simeq \phi^{\tau_i}\big(t + \delta\tau_i^o(t)\big) + \delta\tau_i^\epsilon(t)\cdot\nu^{\tau_i,o}\big(t + \delta\tau_i^o(t)\big) && (2.51)\\ &= \phi^{\tau_i}\big(t + \delta\tau_i^o(t)\big) - \frac{\delta\hat{\tau}_i^\epsilon\big(t + \delta\tau_i^o(t)\big)}{1 + \delta\dot{\hat{\tau}}_i^o\big(t + \delta\tau_i^o(t)\big)}\cdot\nu^{\tau_i,o}\big(t + \delta\tau_i^o(t)\big) && (2.52)\\ &= \mathbf{T}^{\tau_i,o}_{\hat{\tau}_i}\left(\phi^{\tau_i}(t) - \frac{\delta\hat{\tau}_i^\epsilon(t)}{1 + \delta\dot{\hat{\tau}}_i^o(t)}\cdot\nu^{\tau_i,o}(t)\right) && (2.53)\end{aligned}$$

In the last line we observe how the timing jitter of the clocks ($\delta\hat{\tau}_i^\epsilon(t) = q_i(t)$) couples to the megahertz-beatnote and enters the beatnote phase measurement.

2.3.2 Onboard processing

The phasemeter DPLLs output measurements of the beatnote phases and instantaneous frequencies at 80 MHz. This is required due to the megahertz-Doppler shifts that determine the absolute beatnote frequencies and therefore, the minimum rate of the DPLLs. However, LISA's sensitive band start below 1 Hz. To allow for some margin, the baseline design foresees a final sampling rate of 4 Hz that allows some headroom for appropriate filter design. Reducing the sampling rate by a factor of 2×10^7 is not a trivial task. It requires several stages of decimation. Each includes an anti-aliasing filter and a decimator that reduces the sampling rate by an integer factor by simply "skipping" samples. The filter removes all power at frequencies higher than the Nyquist rate after the decimator and ensures that aliasing does not contaminate the data irreversibly. The modeling of the filters and decimation is discussed in more detail in section 3.3.1.

Chapter 3

Time-delay Interferometry

Time-delay interferometry is a post-processing technique to suppress the overwhelming laser noise in the LISA interferometric measurements. This is achieved by time-shifting the latter and linearly combining them to cancel common laser noise terms. Tinto and Armstrong (1999) first proposed TDI for unequal-arm interferometers. As the two beams departing from the beam splitter traverse different path lengths (d_1 and d_2, respectively), upon recombination laser noise does not cancel perfectly. The solution to this is to read out both arms individually which yields two round-trip measurements

$$y_1(t) = p(t - d_1) - p(t) + H_1(t), \tag{3.1a}$$
$$y_2(t) = p(t - d_2) - p(t) + H_2(t). \tag{3.1b}$$

Here, $p(t)$ denotes laser phase noise and $H_1(t)$ and $H_2(t)$ represent the phase shifts induced by a passing GW in the arms of the interferometer. The goal of TDI is to find appropriate linear combinations of time-shifted versions of $y_1(t)$ and $y_2(t)$ that cancel out the laser phase noise. Tinto and Armstrong (1999) propose the following combination

$$X(t) = \big(y_1(t - d_2) - y_1(t)\big) - \big(y_2(t - d_1) - y_2(t)\big) \tag{3.2}$$
$$= \big(H_1(t - d_2) - H_1(t)\big) - \big(H_2(t - d_1) - H_2(t)\big). \tag{3.3}$$

As we can observe, all laser noise contributions drop out and the GW signal remains in the combination $X(t)$[1]. This TDI combination is commonly referred to as the first generation Michelson combination as it represents a Michelson interferometer where both arms are traversed twice by each beam to achieve equal path lengths.

3.1 TDI Combinations

3.1.1 Modeling laser beam propagation

The following sections make extensive use of time-shift operators. Therefore, before we set out to explain the various TDI combinations, we want to properly define this operations and discuss some of its properties. The time-delay operator $\mathbf{D}$ acts on a time series $\phi(t)$ by shifting its argument $t \to t - d(t)$. Formally, we write

$$\mathbf{D}\phi(t) = \phi(t - d(t)). \tag{3.4}$$

Here, $d(t)$ denotes a general time-dependent delay. In LISA time delays operations are used to model propagation of laser phases between spacecraft which is illustrated in fig. 3.1. The world lines of two spacecraft with non-zero relative velocity as viewed by an external observer at rest

[1] The GW signals enter as finite differences which approximate a time derivative at small frequencies.

are represented by the black lines. At time t_1 the first spacecraft emits a laser beam with phase $\phi_1(t_1)$. The laser beam travels towards the second spacecraft (represented by the blue arrow) and intersects its path at time t_2. There, the received phase must equal to the emitted phase $\phi(t_1)$. We define the delay

$$d(t_2) = t_2 - t_1 \tag{3.5}$$

to relate the time of emission t_1 and time of reception t_2. Therefore, for the received phase we can write $\phi_1(t_2 - d(t_2))$. We conclude that the delay operation defined in eq. (3.4) appropriately models propagation of the laser phase.

Conversely, we can define the "anti"-propagation of a laser beam. Conceptually, photons cannot only travel forwards in time but also backwards. While in the real world time is a constantly increasing quantity, post-processing of recorded data allows us to move in both directions; the past[2] and the future. An example is given in fig. 3.1 where the red arrow illustrates a laser beam traveling backwards in time. It is emitted on spacecraft 2 at time t_2 and received by spacecraft 1 at an earlier time t_1. These times can be related by the advancement

$$a(t_1) = t_2 - t_1. \tag{3.6}$$

In general, we define the advancement operator $\mathbf{A}$ as

$$\mathbf{A}\phi(t) = \phi(t + a(t)). \tag{3.7}$$

The delay $d(t)$ and advancement $a(t)$ are intimately connected. We note that their definition in eqs. (3.5) and (3.6) are almost identical but differ by the time they are evaluated at. Using both equations we can relate delays and advancements.

$$t_1 \overset{(3.5)}{=} t_2 - d(t_2) \overset{(3.6)}{=} t_1 + a(t_1) - d(t_1 + a(t_1)) \qquad \Rightarrow \qquad a(t) = d(t + a(t)) \tag{3.8a}$$

$$t_2 \overset{(3.6)}{=} t_1 + a(t_1) \overset{(3.5)}{=} t_2 - d(t_2) + a(t_2 - d(t_2)) \qquad \Rightarrow \qquad d(t) = a(t - d(t)) \tag{3.8b}$$

The resulting equations provide instructions on how to derived advancements from delays and vice versa. One difficulty is that in both cases the left-hand quantities are defined implicit as they also appear in the argument of the corresponding right-hand side quantity. This makes it impossible to write down a closed-form solution of either. However, for the special case of a linearly evolving delay we can explicitly state the solution for the advancement. It is given by

$$a(t) = \frac{d(t)}{1 - \dot{d}}\,. \tag{3.9}$$

The apparent singularity at $\dot{d} = 1$ is ruled out by special relativity that ensures $\dot{d} < 1$ as the spacecraft cannot move at superluminal speeds[3].

As one can already presume from fig. 3.1 delay and advancement are inverse operations. We can proof that by observing their successive action on ϕ.

$$\mathbf{AD}\phi(t) = \mathbf{A}\phi(t - d(t)) = \phi(t + a(t) - d(t + a(t))) \overset{(3.8a)}{=} \phi(t) \tag{3.10a}$$

$$\mathbf{DA}\phi(t) = \mathbf{D}\phi(t + a(t)) = \phi(t - d(t) + a(t - d(t))) \overset{(3.8b)}{=} \phi(t) \tag{3.10b}$$

We identify eq. (3.8) and conclude that $\mathbf{A}$ is indeed the inverse of $\mathbf{D}$ and vice versa.

[2] In the real world this is forbidden as it violates causality; the detection of a photon precedes its emission.

[3] Here, we assume that the rate of change of the delay is given by $\dot{d} = 1 - \frac{v_2 \pm 1}{v_1 \pm 1}$ where v_1 and v_2 denote the relative velocities of the spacecraft. The $\pm$ distinguishes between the two possible directions the laser beam is sent (represented by the light cone).

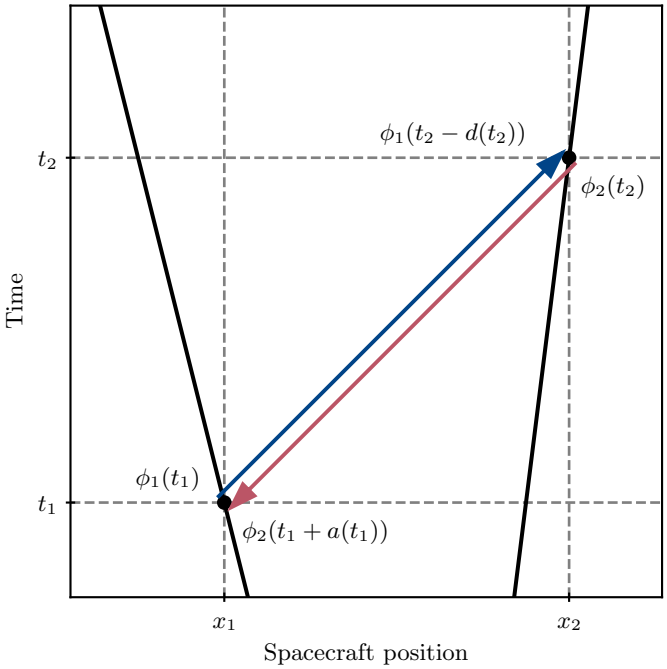

Figure 3.1: Spacetime diagram illustrating the propagation of laser beam from spacecraft 1 to spacecraft 2 (blue arrow) and the respective anti-propagation (red arrow). The black dots mark the events of emission and reception depending on the propagation direction (in time) of the beam.

3.1.2 Virtual interferometry

The aforementioned time-shift operators can be used to build up more complex beam paths. In LISA those form virtual equal-arm interferometers that suppress laser noise. To distinguish between the different links we label time-shift operators with two indices ij. Here, i denotes the index of the receiving and j the index of the emitting spacecraft. Following this, we have $\mathbf{D}_{ij}$ for propagation from spacecraft i to j and its inverse operation $\mathbf{A}_{ji}$ for anti-propagation the reverse path. As there are three LISA spacecraft ($i, j = 1, 2, 3$) we find six combinations of ij. In general, opposing time-shifts are not equivalent, e.g. $\mathbf{D}_{12} \neq \mathbf{D}_{21}$.

The fundamental building blocks for TDI combinations are the six one-way measurements that interfere distant beams with local beams. We define

$$\eta_{ij}(t) = \mathbf{D}_{ij}\phi_j(t) - \phi_i(t). \tag{3.11}$$

Figure 3.2 provides a representation of the one-link measurement $\eta_{12}(t)$. Here, the blue dot represents the emission time of the local beam (at coordinate time t) and the red dot followed by the red arrow the emission time of the distant beam (at time $t - d_{12}(t)$) and the propagation to the local spacecraft.

From the basic one-way measurements we can synthesize arbitrary two-beam interferometers. We require that both beams are emitted on and received by the same spacecraft. However, they are allowed to traverse different paths in between which makes them sensitive to GWs as the beams sense the differential strain along their paths.

$$X(t) = \mathbf{T}_{\mathrm{I}}\phi(t) - \mathbf{T}_{\mathrm{II}}\phi(t) \tag{3.12}$$

Here, $\mathbf{T}_{\mathrm{I}}$ and $\mathbf{T}_{\mathrm{II}}$ define the time-shifts that the beams experience along their round-trips. The roman numerals are to be replaced by a string of spacecraft indices defining the beam path. To

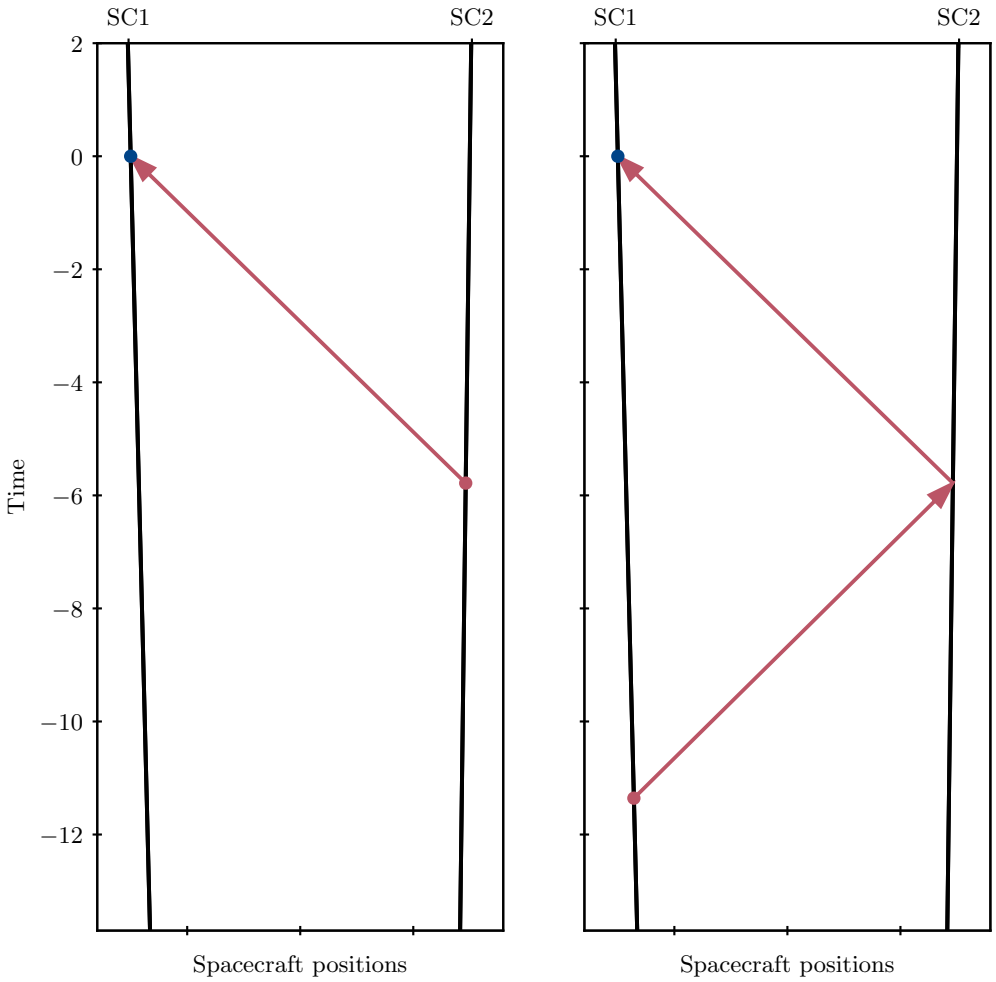

Figure 3.2: Illustration of the one-way measurement $\eta_{12}(t)$ and the round-trip variable $\eta_{1\leftarrow 2\leftarrow 1}(t)$.

indicate the direction of the time-shift we connect the spacecraft indices by arrows. Forward facing errors denote advancements and backward facing ones delays.

$$\mathbf{T}_{i\leftarrow j} \equiv \mathbf{D}_{ij} \tag{3.13}$$
$$\mathbf{T}_{i\rightarrow j} \equiv \mathbf{A}_{ij} \tag{3.14}$$

We can generally define time-shift operators representing arbitrary paths by nesting those basic operators. Here, we have to take care that the right-most index of the time-shift operator applied to the left is identical to the left-most index of the time-shift operator applied to the right. This assures that the total time-shift operator still represents a valid photon path. For example, the time-shift operation $\mathbf{T}_{i\leftarrow j}\mathbf{T}_{j\rightarrow k} = \mathbf{T}_{i\leftarrow j\rightarrow k}$ relates the event of emission at k and even of reception at i. The sequence of events happening in between is the following: A Photon is emitted on spacecraft k and propagates backwards in time to reach spacecraft j at an earlier time. Then, it is reflected towards spacecraft i where it is received after propagating forwards in time.

Constructing an arbitrary two-beam interferometer from the η variables is done in two steps. First, two round-trip variables η_{I} and η_{II} are computed. They represent interferometers with a long arm that defines the round-trip path I and II, respectively, and a short arm that is vanishing. We define two rules to recursively build them up from the six one-way measurements.

$$\mathbf{T}_{i\cdots j}\phi_j(t) - \phi_i(t) + \mathbf{T}_{i\cdots j}\eta_{jk}(t) = \mathbf{T}_{i\cdots j\leftarrow k}\phi_k(t) - \phi_i(t) \tag{3.15}$$
$$\mathbf{T}_{i\cdots j}\phi_j(t) - \phi_i(t) - \mathbf{T}_{i\cdots j\rightarrow k}\eta_{kj}(t) = \mathbf{T}_{i\cdots j\rightarrow k}\phi_k(t) - \phi_i(t) \tag{3.16}$$

We note that we can extend the long arm of an intermediary variable by a delay or advancement by adding or subtracting an appropriately time-shifted version of the one-way measurements. For illustration we draw the spacetime diagram for the round-trip variable $\eta_{1\leftarrow 2\leftarrow 1}$ in fig. 3.2 where the local beam (blue dot) is interfered with itself after taking a round-trip to the distance spacecraft 2 and back.

Finally, we take the difference of the two round-trip variables η_{I} and η_{II}. The contribution from the short arms cancels and we have successfully synthesized the interferometer given in eq. (3.12).

Generally speaking, there exists an infinite number of possible two-beam interferometers. We can construct round-trip beam paths of as many links as we like. Furthermore, we can combine any pair of round-trips to realize two-beam interferometers which increases the amount of possibilities further. Vallisneri (2005) conducts an exhaustive "brute force" search of interferometers involving up to 24 links. In a follow-on study Muratore et al. (2020) identifies combinations that were previously missed. We propose to explore the space of TDI methodologically by starting off with the very simplest interferometers and deriving more sophisticated combinations that fulfill certain conditions for laser noise suppression. We will extensively make use of the terminology introduced by Vallisneri (2005) and the indexing conventions used in Muratore et al. (2020).

Let us first consider the eight full round-trip paths around the constellation shown in the upper panel of fig. 3.3. Each arrow head represents an event of reception and each bullet an event of emission. Photons propagate forwards in time on solid lines and backwards on dashed lines. Using the six LISA symmetry transformations we find 48 different possibilities in total. By appending them we can construct any single-beam paths that start and end at the same spacecraft. The shortest of such paths just takes a two-link round trip to a neighboring spacecraft. As an example, in the second row of fig. 3.3 we depict the construction of the round-trip path $1 \leftarrow 2 \leftarrow 1$.

In the next step we combine the beams pairwise to form two-beam interferometers. The most common one is the Michelson variable X. We combine two beams that start at the local spacecraft and take a simple round-trip to the two distant spacecraft. Here, we have two options:

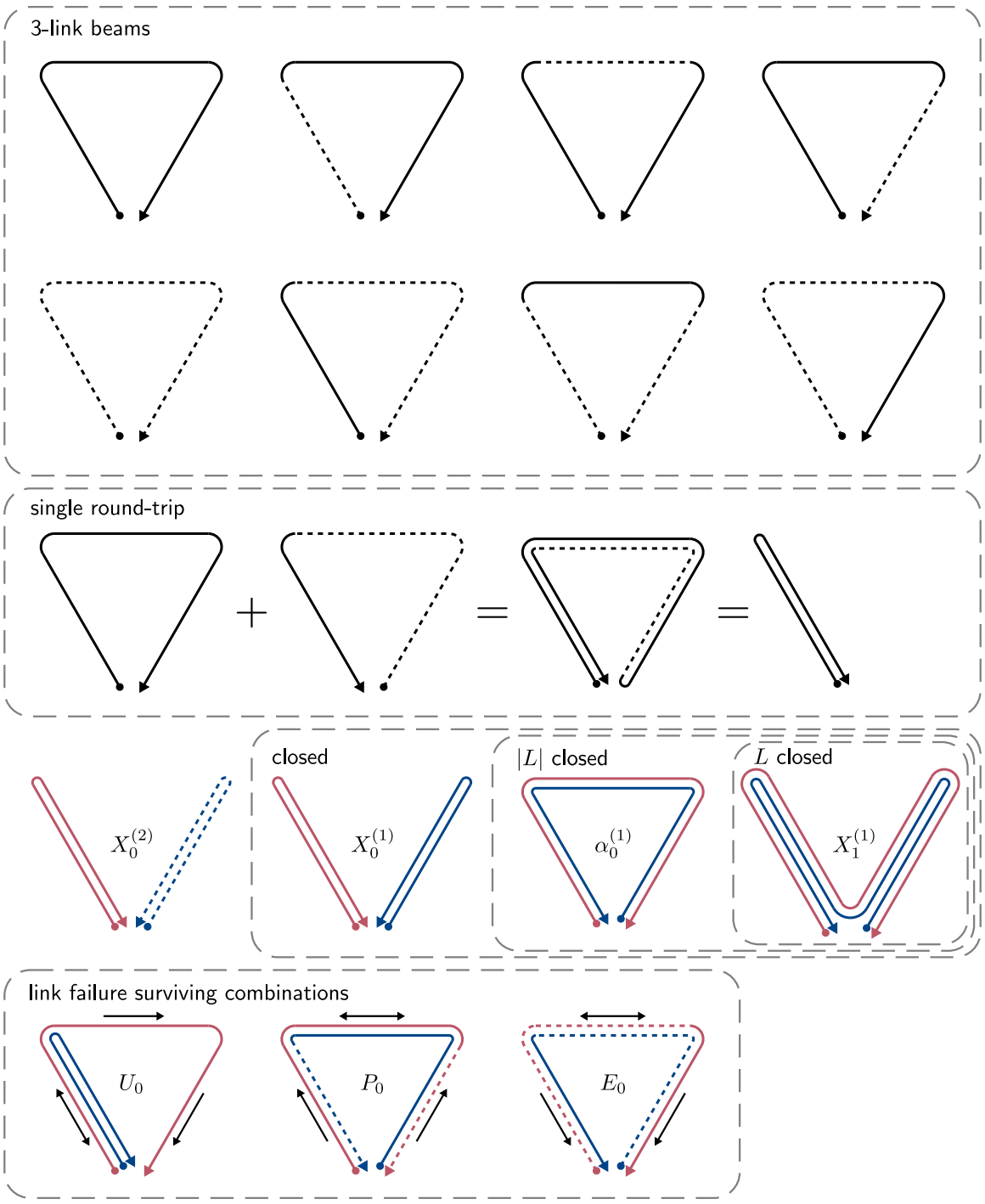

Figure 3.3: Overview of simple single beam paths and basic interferometers for the LISA constellation consisting of three stations. Dots indicate emission events, arrow heads reception events, solid lines propagation of photons and dashed lines "anti-propagation" which is defined as a photon traveling backwards in time. In the top panel we collect the eight possible beam paths to take a clockwise round-trip from the bottom spacecraft. In the second panel we demonstrate how to combine the basic 3-link beams to construct a round-trip beam to a neighboring spacecraft. The +-sign connects the emission event of the second beam with the reception event of the first. In the last two rows we present some simple interferometers with different properties. The black arrow for the link failure surviving combinations indicate the links involved.

Either both beams are traveling forwards/backwards in time or we alternate.

$$X_0^{(1)}(t) = \mathbf{T}_{1\leftarrow 3\leftarrow 1}\phi_1(t) - \mathbf{T}_{1\leftarrow 2\leftarrow 1}\phi_1(t) \tag{3.17a}$$

$$X_0^{(2)}(t) = \mathbf{T}_{1\rightarrow 3\rightarrow 1}\phi_1(t) - \mathbf{T}_{1\leftarrow 2\leftarrow 1}\phi_1(t) \tag{3.17b}$$

Here, $X_0^{(1)}$ represents the classical Michelson interferometer. It is said to be *closed* as for equal and constant arms the times of emission of the two beams coincides and therefore close the loop created by the two beams. In this setup laser noise cancels perfectly. On the other hand, combination $X_0^{(2)}$ is not closed as the times of emission of the beams is vastly different. Hence, this is not a laser noise suppressing combination. We illustrate the topology of both combinations in fig. 3.3.

From the three link beams we can readily construct Sagnac-type variables α. In those we combine two counter-propagating beams where we have many more choices as for the Michelson combinations. First, let us discuss two members that fulfill the $|L|$ *closed* property.

$$\alpha_0^{(1)}(t) = \mathbf{T}_{1\leftarrow 3\leftarrow 2\leftarrow 1}\phi_1(t) - \mathbf{D}_{1\leftarrow 2\leftarrow 3\leftarrow 1}\phi_1(t) \tag{3.18a}$$

$$\alpha_0^{(2)}(t) = \mathbf{T}_{1\rightarrow 3\leftarrow 2\leftarrow 1}\phi_1(t) - \mathbf{D}_{1\leftarrow 2\leftarrow 3\rightarrow 1}\phi_1(t) \tag{3.18b}$$

Combinations are called $|L|$ *closed* if the times of emission coincide for a static unequal arms and non-rotating constellation such that $d_{ij} = d_{ji}$. These combinations are sensitive to rotations of the LISA constellation as the beam traveling in the direction of rotation experiences a longer round-trip path. The reader can find a depiction of $\alpha_0^{(1)}$ in fig. 3.3. Further we show the standard first generation Michelson variable $X_1^{(1)}$ that is discussed later in this section.

Lastly, we want to discuss the class of the basic link failure combinations. They can be synthesized by two and three-link beam paths respecting that only four of the six links is used. In case of a link failure they present fall-back options. They complement the Michelson-type variables that are already only using four links. They can be categorised into three classes, the relay U, beacon P and monitor E combinations.

$$U_0(t) = \mathbf{T}_{1\leftarrow 2\leftarrow 1}\phi_1(t) - \mathbf{T}_{1\leftarrow 3\leftarrow 2\leftarrow 1}\phi_1(t) \tag{3.19a}$$

$$P_0(t) = \mathbf{T}_{1\rightarrow 2\leftarrow 3\leftarrow 1}\phi_1(t) - \mathbf{T}_{1\rightarrow 3\leftarrow 2\leftarrow 1}\phi_1(t) \tag{3.19b}$$

$$E_0(t) = \mathbf{T}_{1\leftarrow 2\rightarrow 3\rightarrow 1}\phi_1(t) - \mathbf{T}_{1\leftarrow 3\rightarrow 2\rightarrow 1}\phi_1(t) \tag{3.19c}$$

The names correspond to the specific function one of the spacecraft accepts. The links that are used are depicted in the last row of fig. 3.3 as black arrows. For the relay-type one satellite seems to transpond the beam. For the beacon and monitor-type the local spacecraft only emits or receives. It is easy to verify that those combinations are not closed and therefore have poor laser noise suppression capability.

Laser noise suppression performance of *closed* and $|L|$ *closed* combinations

Some of the TDI combinations defined above cancel laser noise for constant (and equal) arms. However, the LISA constellation will flex and rotate around its barycenter as the three spacecraft independently follow their respective heliocentric orbit. Consequently the light travel times between the satellites vary by a few percent and opposing arms, i.e., ij and ji, differ by about one millisecond. This is illustrated in fig. 3.4 where the light travel times along the six arms are shown assuming a realistic numerical orbit file provided by European Space Agency (ESA). The light travel time difference between opposing links is modulated by the movement of the constellation around the sun where two effects overlap. First, due to the orbital velocity of approximately $30\,\mathrm{km\,s^{-1}}$ the apparent distance for a photon traveling parallel to the orbit is extended by $d \cdot v$ which explains the consistent modulation shown in the lower panel of fig. 3.4. Second,

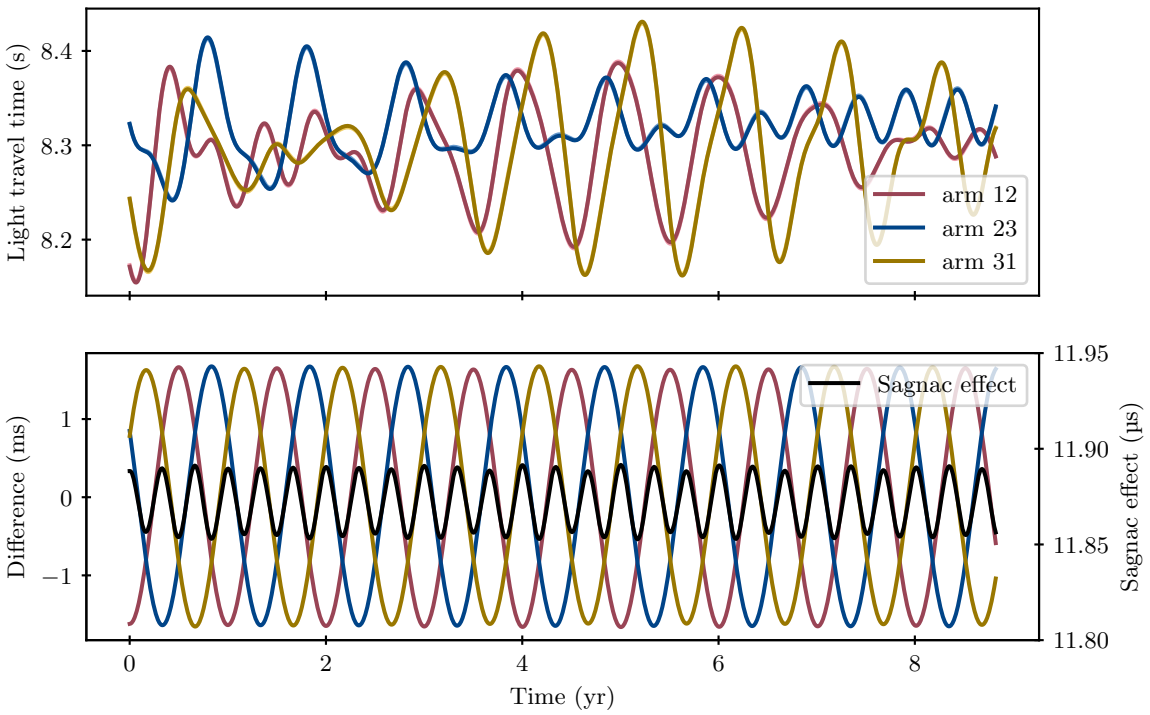

Figure 3.4: Evolution of light travel times between spacecraft for realistic LISA orbits (standard orbit file taken from Bayle et al. (2022b)). The upper panel shows the light travel times for the six arms (ascending indices in dark shade and descending in light shade). As opposing arms are difficult to distinguish we plot in the lower panel the difference, e.g., $d_{12}(t) - d_{21}(t)$, which follows a sinusoid with a period of once a year.

the characteristic cart-wheel motion of the LISA constellation superimposes a subdominant modulation with an amplitude of a few microseconds as the rotation velocity can be estimated to be of the order $200\,\mathrm{m\,s^{-1}}$.

To estimate the residual laser noise power due to the arm length mismatch between the two beams we use the approximation[4]

$$\sqrt{S_{\delta X}(f)} \simeq \Delta t \cdot \sqrt{S_{\dot{p}}(f)}, \tag{3.20}$$

where Δt denotes the difference between times of emission. We note that laser frequency noise couples proportional to mismatch Δt into the phase measurement.

Let us estimate the residual laser noise for the basic Michelson $X_0^{(1)}$ and Sagnac interferometers α_0 assuming a stabilized laser source with a white frequency noise of $30\,\mathrm{Hz}/\sqrt{\mathrm{Hz}}$. An arm length difference of 0.1 s in the basic Michelson interferometer amounts for a phase residual with an ASD of roughly $3\,\mathrm{cycles}/\sqrt{\mathrm{Hz}}$. As this violates the microcycle-requirement by many orders of magnitudes the basic Michelson combination is not a viable option for LISA. On the other hand, the Sagnac interferometer experiences an arm length mismatch of about 10 µs. In fig. 3.4 we plot in black the numerical value of

$$\big(d_{12}(t) + d_{23}(t) + d_{31}(t)\big) - \big(d_{13}(t) + d_{32}(t) + d_{21}(t)\big), \tag{3.21}$$

which approximately gives the arm length mismatch for the Sagnac combination α_0. As a result the residual laser noise in this combination stands at $300\,\mu\mathrm{cycles}/\sqrt{\mathrm{Hz}}$ which is still violating the

[4]This approximation holds in the limit of small δt. For large values much greater than the correlation time of the laser the residual power approaches the uncorrelated sum of two (apparently) independent laser sources, i.e., $S_{\delta X}(f) \to 2 \cdot S_p(f)$.

microcycle requirement by two orders of magnitude. Therefore, we must synthesize more sophisticated virtual interferometers that have arm length mismatches smaller than 30 ns according to eq. (3.20).

The generation of L *closed* and $\dot{L}$ *closed* combinations

Traditionally, TDI combinations are grouped into so called "generations". Above we have presented members of the zeroth generation (not closed), generation 0.5 (closed) and first generation ($|L|$ closed). As we have discussed above, inter-spacecraft distances differ by tens of thousands of kilometers and even light travel times sharing the same link deviate by a few milliseconds. Thus, in general we have to consider six unequal light travel times d_{ij}. This fact calls for L *closed* property which requires a combination to represent a closed loop for six constant but unequal arms. In the literature this property is referred to as modified TDI or generation 1.5.

We can conveniently generate combinations of this class by choosing two beam paths (I and II) and appending them in an alternating fashion[5]. The difference of the two beams represents a L closed combination X by definition.

$$X(t) = \mathbf{T}_{\mathrm{I}}\mathbf{T}_{\mathrm{II}}\phi(t) - \mathbf{T}_{\mathrm{II}}\mathbf{T}_{\mathrm{I}}\phi(t) = [\mathbf{T}_{\mathrm{I}}, \mathbf{T}_{\mathrm{II}}]\phi(t) \tag{3.22}$$

Here, we have introduced the commutator of time-shift operations. This provides us with the general recipe to turn a zeroth generation variable into its generation 1.5 counterpart. As an example, we consider the Michelson combinations defined in eq. (3.17).

$$X_1^{(1)}(t) = \mathbf{T}_{1\leftarrow 3\leftarrow 1\leftarrow 2\leftarrow 1}\phi_1(t) - \mathbf{T}_{1\leftarrow 2\leftarrow 1\leftarrow 3\leftarrow 1}\phi_1(t) \tag{3.23a}$$

$$X_1^{(2)}(t) = \mathbf{T}_{1\rightarrow 3\rightarrow 1\leftarrow 2\leftarrow 1}\phi_1(t) - \mathbf{T}_{1\leftarrow 2\leftarrow 1\rightarrow 3\rightarrow 1}\phi_1(t) \tag{3.23b}$$

Even though combination $X_0^{(2)}$ is not even closed, using the recipe in eq. (3.22) turns it into a L closed variable. Doing the same to the relay, beacon and monitor variables defined in eq. (3.19) recovers the original combinations reported in the literature (Tinto et al., 2004; Vallisneri, 2005). They are defined as

$$U_1(t) = \mathbf{T}_{1\leftarrow 2\leftarrow 1\leftarrow 3\leftarrow 2\leftarrow 1}\phi_1(t) - \mathbf{T}_{1\leftarrow 3\leftarrow 2\leftarrow 1\leftarrow 2\leftarrow 1}\phi_1(t) \tag{3.24a}$$

$$P_1(t) = \mathbf{T}_{1\rightarrow 2\leftarrow 3\leftarrow 2\leftarrow 1}\phi_1(t) - \mathbf{T}_{1\rightarrow 3\leftarrow 2\leftarrow 3\leftarrow 1}\phi_1(t) \tag{3.24b}$$

$$E_1(t) = \mathbf{T}_{1\leftarrow 2\rightarrow 3\rightarrow 2\rightarrow 1}\phi_1(t) - \mathbf{T}_{1\leftarrow 3\rightarrow 2\rightarrow 3\rightarrow 1}\phi_1(t) \tag{3.24c}$$

For the beacon P_1 and monitor E_1 combination we find the sections $3 \leftrightarrows 1 \rightleftarrows 3$ and $2 \leftrightarrows 1 \rightleftarrows 2$ in the beam paths (upper arrow for beacon, lower arrow for monitor). Those represent *null bigrams*, i.e., vanishing paths, and we strike them out. Therefore, U_1, P_1 and E_1 combinations represent an alternative set of three L closed variables that use eight links[6].

It can be shown that the difference in emission times of L closed combinations is of order $d \cdot \dot{d}$. To estimate the magnitude of higher order derivatives of the light travel time d we assume a sinusoidal modulation on top of the 8.3 s nominal value with an amplitude of 0.1 s and a characteristic frequency of once per year. This yields the relation

$$\left|\frac{\mathrm{d}^n}{\mathrm{d}t^n} d(t)\right| \simeq 0.1\,\mathrm{s} \cdot \left(2\pi \mathrm{yr}^{-1}\right)^n = \epsilon^n \cdot 0.1\,\mathrm{s}^{1-n}, \tag{3.25}$$

with $\epsilon = 2 \times 10^{-7}$. From this we follow that the rate of change of the light travel time is of the order of $2 \times 10^{-8}\,\mathrm{s\,s^{-1}}$. The difference in emission times for L closed combinations can then be estimates as 100 ns which still violates the 30 ns projection we have estimated before.

[5] In a recent publication Tinto and Dhurandhar (2023) refer to this as the "lifting" procedure.

[6] The relay combination U_1 seems to have ten links. However, the last time-shift $\mathbf{T}_{2\leftarrow 1}$ is common to both beams which makes it effectively an eight link combination

To improve on laser noise suppression even further we introduce the class of $\dot{L}$ closed variables. Members of this class are also called second generation variables. They take multiple round-trips to equalize the differences in the time-dependent light travel times of an orbiting LISA constellation (Shaddock et al., 2003; Cornish and Hellings, 2003). The exact condition for this property to be fulfilled can be taken from Vallisneri (2005). In short, a combination is called $\dot{L}$ *closed* if the beams represent a closed loop in the limit of small travel time derivatives. The "openness" Δt of the loop is of the order of $d \cdot \dot{d}^2$ and $d^2 \cdot \ddot{d}$ which is second order in ϵ and evaluates approximately to 300 fs. This results in a laser noise residual of $9\,\mathrm{ncycles}/\sqrt{\mathrm{Hz}}$ which is much smaller than the microcycle-requirement. Hence, second generation TDI is deemed sufficient for the LISA mission.

To construct $\dot{L}$ closed variables we can simply apply the recipe for L closed variables introduced in eq. (3.22).

$$X(t) = (\mathbf{T}_\mathrm{I}\mathbf{T}_\mathrm{II})(\mathbf{T}_\mathrm{II}\mathbf{T}_\mathrm{I})\phi(t) - (\mathbf{T}_\mathrm{II}\mathbf{T}_\mathrm{I})(\mathbf{T}_\mathrm{I}\mathbf{T}_\mathrm{II})\phi(t) = [\mathbf{T}_\mathrm{I}\mathbf{T}_\mathrm{II}, \mathbf{T}_\mathrm{II}\mathbf{T}_\mathrm{I}]\phi(t) = [[\mathbf{T}_\mathrm{I}, \mathbf{T}_\mathrm{II}], \mathbf{T}_\mathrm{II}\mathbf{T}_\mathrm{I}]\phi(t) \tag{3.26}$$

Interestingly, we recover a second order commutator that already hints towards the $\dot{L}$ closure property. As an example we explicitly state the differences in emission times for the classical Michelson combinations of increasing generation.

$$\begin{aligned}
\Delta t_{X_0}(t) &= \mathbf{D}_{131}t - \mathbf{D}_{121}t && (3.27)\\
&= d_{121}(t) - d_{131}(t), && (3.28)\\
\Delta t_{X_1}(t) &= [\mathbf{D}_{131}, \mathbf{D}_{121}]t && (3.29)\\
&= d_{121}(t) \cdot \dot{d}_{131}(t) - d_{131}(t) \cdot \dot{d}_{121}(t), && (3.30)\\
\Delta t_{X_2}(t) &= [[\mathbf{D}_{131}, \mathbf{D}_{121}], \mathbf{D}_{12131}]t && (3.31)\\
&= \big(d_{121}(t) \cdot \dot{d}_{131}(t) - d_{131}(t) \cdot \dot{d}_{121}(t)\big)\big(\dot{d}_{121}(t) + \dot{d}_{131}(t)\big) \\
&\quad - \big(d_{121}(t) + d_{131}(t)\big)\big(d_{121}(t) \cdot \ddot{d}_{131}(t) - d_{131}(t) \cdot \ddot{d}_{121}(t)\big), && (3.32)
\end{aligned}$$

which are of order $\mathcal{O}(\epsilon^0)$, $\mathcal{O}(\epsilon^1)$ and $\mathcal{O}(\epsilon^2)$, respectively. For this calculations we have come back to the notion of delay operators $\mathbf{D}_{ij}$ and also introduce the notation of contracted delays which are defined as $\mathbf{D}_{ijk} = \mathbf{D}_{ij}\mathbf{D}_{jk}$. We illustrate the beam paths in fig. 3.5 and visually demonstrate that the emission events become more simultaneous for increasing generation.

Practical considerations

Above we have presented how to construct various TDI combinations that suppress laser noise for realistic LISA setups. This begs the question whether there exists a set of combinations that is in some sense "complete". This is important as it is rather impractical to consider all possible (infinite amount) combinations at the same time.

From a naive algebraic point of view one would follow that a set of three combinations should span the entire laser noise free space. In TDI we seek linear combinations of the six one-way measurements η that cancel out laser noise. As there are only three lasers appearing in the system of equations it is overdetermined (6 measurements, 3 unknowns). We follow that there exists a linear transformation that transforms the six one-way measurements into a set of three laser noise free and three laser noise dominated variables which we discard (cf. section 4.3 and Armstrong et al. (1999) for more details).

Dhurandhar et al. (2002) demonstrate in a more rigorous algebraic study that this naive reasoning is incomplete. They show that for a static and non-rotating LISA constellation the space of laser noise free combinations is appropriately described by a module over polynomials in the three constant delays. They identify a minimum set of four generators that are required to

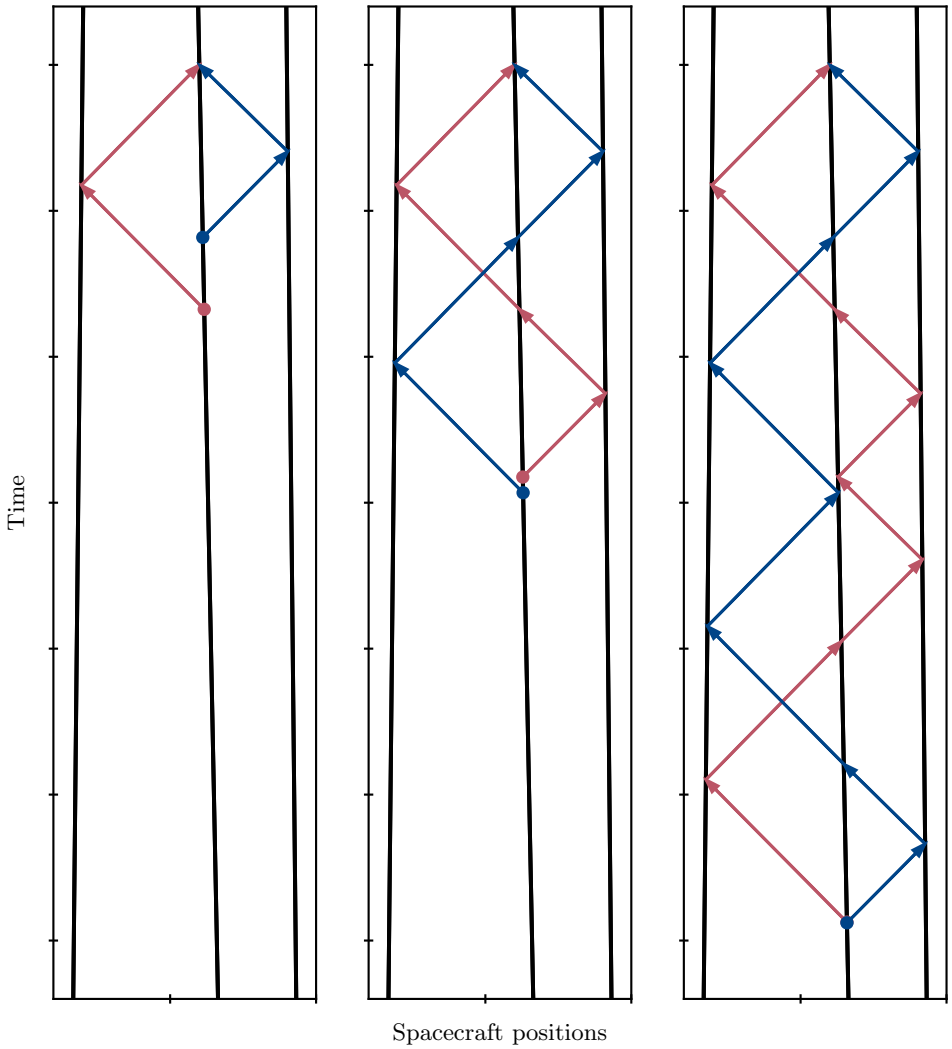

Figure 3.5: Spacetime diagrams of the Michelson variables of increasing generation. The dots indicate events of emission and arrows in red and blue the two beam paths. We represent the world lines of the three spacecraft as slightly slanted (non-zero relative velocity) black lines. The left most plot shows the "classical" Michelson interferometer where events of emission are clearly separated. For the first generation Michelson variable (center plot) the difference is reduced. Ultimately, for the second generation Michelson variable the events of emission of the two beams seems identical by eye.

span the entire space of laser noise free variables. We note that those four "basis" combinations are not independent as they can be related to each other up to a global delay polynomial. However, different generator exhibit different responses and most importantly insensitivities at characteristic Fourier frequencies towards GW signals. Those are the reason for requiring 4 generators for a "three dimensional" space as once those nulls are present in a combination they are irreducible. In a follow up study (Nayak and Vinet, 2004) they extend this approach to a rotating constellation which yields a total of six generators.

Finally, let us take the perspective of a data analyst. The three basic Michelson combinations redundantly measure the three GW strains along the arms[7]. We have

$$X(t) = H_3(t) - H_2(t) \tag{3.33}$$
$$Y(t) = H_1(t) - H_3(t) \tag{3.34}$$
$$Z(t) = H_2(t) - H_1(t) \tag{3.35}$$

where Y and Z represent Michelson interferometers centered on spacecraft 2 and 3, respectively and H_i denotes the GW signal projected on the link opposite to spacecraft i. We can transform this set of three combinations with similar properties into a set of two combinations that "concentrate" the GW signals and one that is completely insensitive (Cutler, 1998). The latter is simply given by the sum of the three Michelson combinations. Prince et al. (2002) present a technique to identify the optimal set of such combinations to maximize the signal-to-noise ratio of a GW signal uniformly distributed on the entire sky. They obtain the three combinations which can be equivalently defined from the Sagnac or Michelson variables as

$$A(t) = \frac{Z(t) - X(t)}{\sqrt{2}} \tag{3.36}$$
$$E(t) = \frac{X(t) - 2Y(t) + Z(t)}{\sqrt{6}} \tag{3.37}$$
$$T(t) = \frac{X(t) + Y(t) + Z(t)}{\sqrt{3}} \tag{3.38}$$

Here, A and E are sensitive to GW signals while T represents the null channel. In data analysis the latter is rather important as it serves as a noise monitor (Muratore et al., 2022) and helps distinguishing stochastic GWs from instrumental noise in the sensitive channels.

Generalizations of TDI

In standard TDI approach discussed above is well established by now (Tinto et al., 2023). However, there has been some ideas to generalize the standard method to transform the measurements to a set of observables that suppresses laser noise and is sensitive the GWs. The general idea is to use principal component analysis to identify the low variance components that represent laser noise suppressing variables (Romano and Woan, 2006; Baghi et al., 2021b; Baghi et al., 2021a; Baghi et al., 2023). This initial work is extended to setups assuming perfect knowledge of the light travel times (Vallisneri et al., 2021) and "fully data-driven" algorithms that even work without any prior knowledge on the laser noise content in the measurements.

3.2 TDI in Practice

In the split-interferometry setup of LISA, the fundamental one-way measurements η_{ij}, that compare laser phases from different spacecraft, are not readily available. They have to be constructed from the three interferometers introduced in section 1.2.4 and further detailed in

[7] Here, we assume a static, non-rotating constellation in the long wave length approximation such that a link produces the same GW response in both directions.

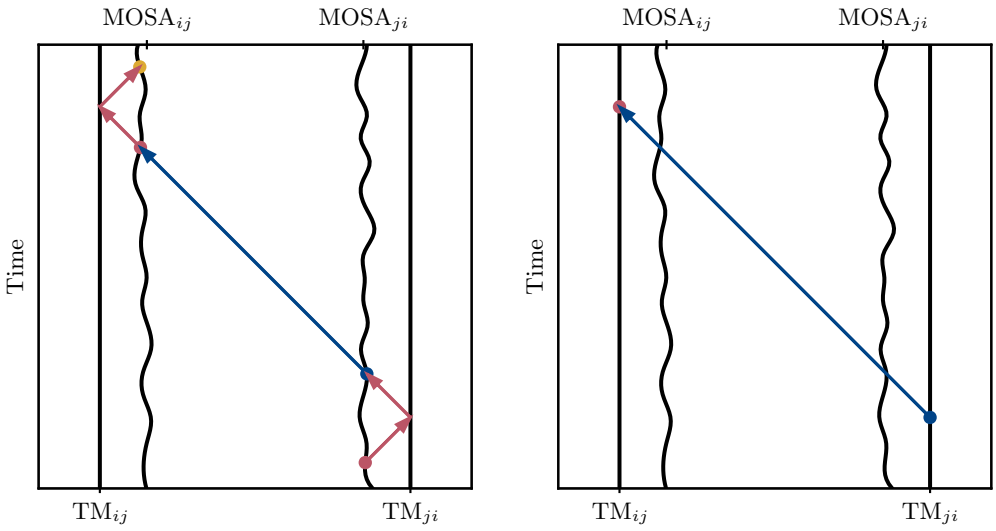

Figure 3.6: Illustration of MOSA jitter suppression. The wiggly and straight black lines represent the positions of the MOSAs and TMs, respectively. The left panel shows the inter-spacecraft interferometer formed by the blue beam in the red dot at the arrow head and the two TM interferometers formed by the red arrows and the blue and yellow dots at the corresponding error head. The right panel presents the MOSA jitter free variable ξ (see eq. (3.46)).

section 2.2.1. This is achieved in two steps: First, MOSA jitter is removed that affects the inter-spacecraft interferometer. As a second step, the information contained in the reference interferometer is used to cancel three of the six laser phases. This procedure yields six one-way measurements η that are free of MOSA jitter and refer to a single laser per spacecraft. We discuss both processing steps in more detail below.

3.2.1 Suppression of MOSA jitter

External disturbances in the space environment, like solar radiation pressure shake the spacecraft. Additionally the MOSAs that host the interferometers are not rigidly fixed to the spacecraft but need to independently move to point to the distant spacecraft. Therefore, they are also subject to displacement noises. To mitigate the effective movement of the MOSAs very quiet TMs are implemented to act as inertial reference points. Dedicated TM interferometers are implemented to track the longitudinal motion of the MOSAs with respect to the corresponding TM. This enables us to correct for it in post-processing (Estabrook et al., 2000).

As defined in eq. (2.34) the TM interferometer compares the same laser beams as the reference interferometer. However, the important difference is that the local beam probes the TM before interfering with the adjacent beam. Therefore, it picks up additional path length given by the round-trip from the MOSA to the TM. The round-trip delay $d_{\mathrm{MOSA}_{ij}\rightleftarrows\mathrm{TM}_{ij}}(t)$ is a small quantity as the spacecraft is actively controlled to follow the TM. Hence, we can develop the expression for the TM interferometer as

$$\mathrm{tmi}_{ij}(t) = \phi_{ik}(t) - \phi_{ij}(t - d_{\mathrm{MOSA}_{ij}\rightleftarrows\mathrm{TM}_{ij}}(t)) \tag{3.39}$$

$$\simeq \underbrace{\phi_{ik}(t) - \phi_{ij}(t)}_{\mathrm{rfi}_{ij}(t)} + d_{\mathrm{MOSA}_{ij}\rightleftarrows\mathrm{TM}_{ij}}(t) \cdot \nu^{o}_{ij}(t). \tag{3.40}$$

Here, we note two things. First, we recognize that indeed the TM interferometer tracks the same beatnote phase as the reference interferometer up to the additional phase contribution from the time-varying MOSA-TM-distance. Second, we realize that the round-trip path can be split up

into single contributions. Therefore, we write

$$d_{\mathrm{MOSA}_{ij}\leftarrow\mathrm{TM}_{ij}}(t) \simeq \frac{d_{\mathrm{MOSA}_{ij}\rightleftarrows\mathrm{TM}_{ij}}(t)}{2} \simeq d_{\mathrm{TM}_{ij}\leftarrow\mathrm{MOSA}_{ij}}(t) \tag{3.41}$$

We use these properties to virtually move the lasers and interferometers on top of the TMs (which is rather impractical in reality). This is illustrated in fig. 3.6. We construct the MOSA jitter free variable ξ in two steps. First, we subtract the TM interferometer from the reference interferometer to yield the following measurements

$$\frac{\mathrm{rfi}_{ij}(t) - \mathrm{tmi}_{ij}(t)}{2} \simeq -d_{\mathrm{MOSA}_{ij}\leftarrow\mathrm{TM}_{ij}}(t)\cdot\nu^o_{ij}(t) \simeq \mathbf{D}_{\mathrm{MOSA}_{ij}\leftarrow\mathrm{TM}_{ij}}\phi_{ij}(t) - \phi_{ij}(t), \tag{3.42a}$$

$$\simeq -d_{\mathrm{TM}_{ij}\leftarrow\mathrm{MOSA}_{ij}}(t)\cdot\nu^o_{ij}(t) \simeq \mathbf{D}_{\mathrm{TM}_{ij}\leftarrow\mathrm{MOSA}_{ij}}\phi_{ij}(t) - \phi_{ij}(t). \tag{3.42b}$$

In the next step, these two virtual interferometers are used to construct a TM-TM-measurement.

$$\xi_{ij}(t) = \frac{\mathrm{rfi}_{ij}(t) - \mathrm{tmi}_{ij}(t)}{2} + \mathbf{D}_{\mathrm{TM}_{ij}\leftarrow\mathrm{MOSA}_{ij}}\mathrm{isi}_{ij}(t) + \mathbf{D}_{\mathrm{TM}_{ij}\leftarrow\mathrm{MOSA}_{ji}}\frac{\mathrm{rfi}_{ji}(t) - \mathrm{tmi}_{ji}(t)}{2} \tag{3.43}$$

$$\begin{aligned}= {}& \mathbf{D}_{\mathrm{TM}_{ij}\leftarrow\mathrm{MOSA}_{ij}}\phi_{ij}(t) - \phi_{ij}(t) \\ & + \mathbf{D}_{\mathrm{TM}_{ij}\leftarrow\mathrm{MOSA}_{ji}}\phi_{ji}(t) - \mathbf{D}_{\mathrm{TM}_{ij}\leftarrow\mathrm{MOSA}_{ij}}\phi_{ij}(t) \\ & + \mathbf{D}_{\mathrm{TM}_{ij}\leftarrow\mathrm{TM}_{ji}}\phi_{ji}(t) - \mathbf{D}_{\mathrm{TM}_{ij}\leftarrow\mathrm{MOSA}_{ji}}\phi_{ji}(t)\end{aligned} \tag{3.44}$$

$$= \mathbf{D}_{\mathrm{TM}_{ij}\leftarrow\mathrm{TM}_{ji}}\phi_{ji}(t) - \phi_{ij}(t) \tag{3.45}$$

In practice, the local delay $d_{\mathrm{TM}_{ij}\leftarrow\mathrm{MOSA}_{ij}}$ is set to zero as it only couples weakly to the megahertz-beatnote frequency. Furthermore, for the same reasons, we use the "usual" propagation delay $\mathbf{D}_{ij}$ for the distant MOSA to local TM propagation.

$$\xi_{ij} = \mathrm{isi}_{ij}(t) + \frac{\mathrm{rfi}_{ij}(t) - \mathrm{tmi}_{ij}(t)}{2} + \mathbf{D}_{ij}\frac{\mathrm{rfi}_{ji}(t) - \mathrm{tmi}_{ji}(t)}{2} \tag{3.46}$$

With this we have successfully constructed the intermediary variable ξ that represents a virtual interferometer referenced to the (almost) inertial TMs (see right panel of fig. 3.6). Still at low frequencies the interferometric readout is limited by TM acceleration noise (ignoring primary noises).

3.2.2 Reduction to three lasers

The intermediary variables ξ given in eq. (3.46) almost resemble what we require as inputs for TDI. However, the one-way measurements used in eq. (3.11) is defined for a single laser source per spacecraft. In the following, we explain how to reduce the six laser source contained in ξ to only three.

The reference interferometer (see eq. (2.31)) relates the lasers on adjacent MOSAs via the backlink optical fiber. Consequently, we can use it to interchange adjacent laser phases in our expressions. This is convenient as we can replace all occurrences of lasers on right-handed MOSAs with their adjacent counterpart on left-handed MOSAs or vice versa. The common choice in the literature is to keep left-handed lasers and discard right-handed ones.

Before we can proceed, we need to reduce the fiber noise of the backlink. This is achieved by subtraction of adjacent reference interferometers. As the additional path length due to fiber noise is a small quantity we can develop the expressions up to first order and find

$$\frac{\mathrm{rfi}_{ik}(t) - \mathrm{rfi}_{ij}(t)}{2} = \left(\mathbf{D}_{\mathrm{MOSA}_{ik}\leftarrow\mathrm{MOSA}_{ij}}\phi_{ij}(t) - \phi_{ik}(t)\right) - \left(\mathbf{D}_{\mathrm{MOSA}_{ij}\leftarrow\mathrm{MOSA}_{ik}}\phi_{ik}(t) - \phi_{ij}(t)\right) \tag{3.47}$$

$$\simeq \phi_{ij}(t) - \phi_{ik}(t) + d_{\mathrm{MOSA}_{ik}\leftrightarrow\mathrm{MOSA}_{ij}}(t)\cdot\left(\nu^o_{ik}(t) - \nu^o_{ij}(t)\right) \tag{3.48}$$

$$\simeq \phi_{ij}(t) - \phi_{ik}(t). \tag{3.49}$$

Backlink fiber noise cancels under two conditions. First, the path length noise must be reciprocal, i.e., counter-propagating beams pick up the same small additional path length $d_{\mathrm{MOSA}_{ik}\leftrightarrow\mathrm{MOSA}_{ij}}$. Second, the wavelength of the laser beams must be identical as path length noises couple to the optical frequency of the lasers. This is approximately true as the optical frequencies only differ by a couple of megahertz and therefore the residual coupling of backlink noise is negligible.

Then, we use of the fiber-noise-suppressed interferometer in eq. (3.49) and reduce the six lasers to the three left-handed ones. We have to treat the intermediary variable ξ_{ij} differently for left-handed MOSAs and right-handed MOSAs. For $ij = 12, 23, 31$ (left-handed MOSAs) the distant laser has to be interchanged with its adjacent counterpart. We define

$$\begin{aligned}\eta_{ij}(t) &= \xi_{ij}(t) + \mathbf{D}_{ij}\frac{\mathrm{rfi}_{ji}(t) - \mathrm{rfi}_{jk}(t)}{2} && (3.50)\\ &= \mathbf{D}_{ij}\phi_{ji}(t) - \phi_{ij}(t) + \mathbf{D}_{ij}\big(\phi_{jk}(t) - \phi_{ji}(t)\big) && (3.51)\\ &= \mathbf{D}_{ij}\phi_{jk}(t) - \phi_{ij}(t). && (3.52)\end{aligned}$$

Equivalently for the indices $ij = 13, 32, 21$ (right-handed MOSAs) the local laser has to be replaced. We define

$$\begin{aligned}\eta_{ij}(t) &= \xi_{ij}(t) + \frac{\mathrm{rfi}_{ik}(t) - \mathrm{rfi}_{ij}(t)}{2} && (3.53)\\ &= \mathbf{D}_{ij}\phi_{ji}(t) - \phi_{ij}(t) + \phi_{ij}(t) - \phi_{ik}(t) && (3.54)\\ &= \mathbf{D}_{ij}\phi_{ji}(t) - \phi_{ik}(t). && (3.55)\end{aligned}$$

Consequently, the six intermediary variables η only contain three lasers and we can simplify the notation and write

$$\eta_{ij}(t) = \mathbf{D}_{ij}\phi_j(t) - \phi_i(t) \tag{3.56}$$

with $\phi_1 \equiv \phi_{12}$, $\phi_2 \equiv \phi_{23}$ and $\phi_3 \equiv \phi_{31}$.

3.2.3 Clock synchronization

All measurements aboard the satellites are taken according to the spacecraft on-board time (see sections 1.2.3 and 2.3.1). In order to perform data analysis the measurements need to be synchronized to a well-defined global reference time frame, e.g., TCB. This is required since astronomers use it to relate astrophysical events to the recorded LISA data. The on-board timers are expected to drift by several seconds over the mission duration. The current requirement on the knowledge of desynchronization to properly conduct parameter estimation is 0.1 ms.

LISA implements two measurements to keep track of the timer deviations. First, the spacecraft will send dedicated timing packets down to Earth that contain a reading of the on-board time at emission. This is combined with the orbital information from ground tracking to synchronize the on-board clocks to TCB with millisecond-accuracy. Second, the clock-sidebands realize a differential clock comparison that tracks the evolution of the clocks relative to each other with high precision. This information is used to properly synchronize the megahertz-beatnote measurements among the satellites.

Synchronizing the beatnote phases to TCB using the ground tracking information is impractical. As they are taken only once a day and are not precise enough to monitor the in-band clock timing jitter, clock noise remains in the beatnote phases. Therefore, as proposed by Hartwig et al. (2022) we first perform TDI in the time reference frames of the spacecraft timers and only in the very end synchronize the combinations to TCB. This order is convenient as TDI combinations naturally have a small beatnote frequency as compared to the few MHz of the original interferometric measurements. Furthermore, clock noise is suppressed in the TDI variable and therefore it is sufficient to make use of the out-of-band timer deviations from TCB to synchronize the variables.

We note that the very first publications on TDI all assume interferometric measurements that are synchronized to TCB and light travel times as an input to TDI. This scheme requires that clock synchronization and TDI are interchanged. In fact, the two steps are intimately connected as TDI itself can be regarded as the synchronization of the three spacecraft clocks to a single one (i.e. each combination receives two virtual laser beams on the same spacecraft according to the corresponding spacecraft clock). Therefore, one is free to choose any time reference frame per spacecraft (even fictional ones) and transform the six one-way measurement into that frame. However, the pseudo-ranges that are an input to TDI have to be corrected for the particular choice of time reference frames to ensure that TDI is appropriately synchronizing all one-way measurements to the respective "combination" reference time frame (i.e., the time-frame of the spacecraft that receives the two beams). A sensible and common choice is to synchronize the three spacecraft clocks to TCB. As a consequence, the six pseudo-ranges have to be corrected for the effect of the differential timer deviations such that they only account for the light travel time between the satellites. We now return to the first scheme described in the previous paragraph as it requires least processing steps as we take the one-way measurements and pseudo-ranges in the time reference frames they are originally taken in which eliminates the need of a re-synchronization step and correction of the pseudo-ranges.

Let us introduce some basic definitions that are relevant for the synchronization process. First, let us redefine the beatnote phases neglecting any path-length noises. Instead of first writing the laser phases ϕ_{ij}^{c} and phase modulations ϕ_{ij}^{m} in the spacecraft proper time and then transforming it to the spacecraft on-board time, we directly define the phases in the spacecraft on-board time and then account for the different time reference frames when propagating the beams. We yield the following models for the carrier-carrier and sideband-sideband beatnotes of the inter-spacecraft and reference interferometer

$$\mathrm{isi}_{ij}^{\mathrm{c/sb},\hat{\tau}_i}(t) = \mathbf{D}_{ij}^{\hat{\tau}_i}\phi_{ji}^{\mathrm{c/m},\hat{\tau}_j}(t) - \phi_{ij}^{\mathrm{c/m},\hat{\tau}_i}(t), \tag{3.57a}$$

$$\mathrm{rfi}_{ij}^{\mathrm{c/sb},\hat{\tau}_i}(t) = \phi_{ik}^{\mathrm{c/m},\hat{\tau}_i}(t) - \phi_{ij}^{\mathrm{c/m},\hat{\tau}_i}(t). \tag{3.57b}$$

Here, we have introduced the operator $\mathbf{D}_{ij}^{\hat{\tau}_i} = \mathbf{T}_{\tau_i}^{\hat{\tau}_i}\mathbf{D}_{ij}^{\tau_i}\mathbf{T}_{\hat{\tau}_j}^{\tau_j}$ where $d_{ij}^{\hat{\tau}_i}$ defines the *measured pseudo-range*. It accounts for the relativistic frame transformations, the propagation delay and time references transformations between the spacecraft on-board time and spacecraft proper time. The operator $\mathbf{D}_{ij}^{\tau_i}$ defines the *proper pseudo-range* which accounts for the time reference frame transformation between spacecraft proper times and the propagation delay between the spacecraft given by the light travel time as measured by an external observer. Moreover, in the equation above the phases $\phi_i^{\mathrm{c/m},\hat{\tau}_i}$ now evolve according to the spacecraft on-board time and thus clock effects enter.

$$\phi_{ij}^{\mathrm{c},\hat{\tau}_i}(t) = \mathbf{T}_{\tau_i}^{\hat{\tau}_i}\phi_{ij}^{\mathrm{c},\tau_i}(t) = \phi_{0,ij}^{\mathrm{c}} + \nu_{0,ij}^{\mathrm{c}} \cdot (t + \delta\tau_i(t) - t_0) + p_{ij}(t) \tag{3.58a}$$

$$\phi_{ij}^{\mathrm{m},\hat{\tau}_i}(t) = \mathbf{T}_{\tau_i}^{\hat{\tau}_i}\phi_{ij}^{\mathrm{c},\tau_i}(t) = \phi_{0,ij}^{\mathrm{m}} + \nu_{0,ij}^{\mathrm{m}} \cdot (t + M_{ij}(t) - t_0) \tag{3.58b}$$

We find that clock noise is entering the carrier phase as it couples to the terahertz-frequency of the laser. Its level is comparable to the level of laser phase noise. However, in the differential measurement of the interferometers clock noise becomes subdominant again as it is common to both beams and consequently couples via the megahertz-beatnote frequency. The modulation phase, on the other hand, simplifies as the clock related effects drop out. Intuitively, this makes sense as the spacecraft on-board time is by definition the time reference frame in which the clock has a constant rate. The phase modulation is only disturbed by modulation noise.

The one-way measurements $\eta_{ij}^{\hat{\tau}_i}$ recorded in the reference frame of the on-board timers can be constructed as presented above (using the measured pseudo-range as the propagation delay) and are modeled analogously as

$$\eta_{ij}^{\hat{\tau}_i}(t) = \mathbf{D}_{ij}^{\hat{\tau}_i}\phi_j^{\hat{\tau}_j}(t) - \phi_i^{\hat{\tau}_i}. \tag{3.59}$$

We note that eq. (3.59) has the same algebraic form as eq. (3.11) and therefore the total laser phase should be suppressed when performing TDI using the measured pseudo-ranges. As a result we obtain a virtual interferometer with round-trip delays calculated from nested pseudo-range delay operators. Those are defined as

$$\mathbf{D}^{\hat{\tau}_i}_{ij}\mathbf{D}^{\hat{\tau}_j}_{jk} = \mathbf{T}^{\hat{\tau}_i}_{\tau_i}\mathbf{D}^{\tau_i}_{ij}\underbrace{\mathbf{T}^{\tau_j}_{\hat{\tau}_j}\mathbf{T}^{\hat{\tau}_j}_{\tau_j}}_{\mathbb{1}}\mathbf{D}^{\tau_j}_{jk}\mathbf{T}^{\tau_k}_{\hat{\tau}_k} = \mathbf{T}^{\hat{\tau}_i}_{\tau_i}\mathbf{D}^{\tau_i}_{ijk}\mathbf{T}^{\tau_k}_{\hat{\tau}_k} = \mathbf{D}^{\hat{\tau}_i}_{ijk}, \tag{3.60}$$

and conveniently contract to an equivalent pseudo-range delay operator. We can use this property to demonstrate that any TDI combination $X^{\hat{\tau}_i}$ we obtain is indeed equivalent to the same combination X^{τ_i} given in the spacecraft proper time transformed to the spacecraft on-board time.

Let us discuss this for the example of the second generation Michelson combination X_2.

$$\begin{aligned} X^{\hat{\tau}_1}_2 &= [\mathbf{D}^{\hat{\tau}_1}_{13121}, \mathbf{D}^{\hat{\tau}_1}_{12131}]\phi^{\hat{\tau}_1}_1(t) && (3.61)\\ &= \mathbf{T}^{\hat{\tau}_1}_{\tau_1}\mathbf{D}^{\tau_1}_{131212131}\mathbf{T}^{\tau_1}_{\hat{\tau}_1}\phi^{\hat{\tau}_1}_1(t) - \mathbf{T}^{\hat{\tau}_1}_{\tau_1}\mathbf{D}^{\tau_1}_{121313121}\mathbf{T}^{\tau_1}_{\hat{\tau}_1}\phi^{\hat{\tau}_1}_1(t) && (3.62)\\ &= \mathbf{T}^{\hat{\tau}_1}_{\tau_1}\underbrace{[\mathbf{D}^{\tau_1}_{13121}, \mathbf{D}^{\tau_1}_{12131}]\phi^{\tau_1}_1(t)}_{X^{\tau_1}_2(t)}. && (3.63) \end{aligned}$$

By definition $X^{\tau_1}_2$ is free of clock noise as $\phi^{\tau_1}_1$ describes the laser phase evolution in the proper time frame that is only disturbed by laser noise. Furthermore, the virtual beatnote of $X^{\tau_1}_2$ is sub-millihertz[8]. Therefore, when performing the time reference frame transformation clock noise coupling is reduced by a factor 10^{10} compared to the usual mega-hertz beatnotes. In summary, TDI applied to total beatnote phases and measured pseudo-ranges timestamped according to their respective on-board time suppresses both laser and clock noise.

The resulting combination still needs to be synchronized to TCB. This is much easier to do as clock noise is already suppressed. Therefore, only the out-of-band component of the timer deviations from TCB is required which is measured by the ground station. The synchronization step hence reads

$$X^t(t) \simeq \mathbf{T}^{t,o}_{\hat{\tau}_i}X^{\hat{\tau}_i}(t). \tag{3.64}$$

3.2.4 Ranging processing

The main goal of the LISA instrument is to determine the inter-spacecraft ranges with high precision to measure the strain of a passing GW wave. To achieve that LISA implements the inter-spacecraft interferometer that is sensitive to the picometer path length changes. However, laser phase noise obstructs the signal. To mitigate it we build more complex virtual interferometers using TDI. This recovers the picometer-sensitivity of LISA (which applies now to the measurement of the length of the differential beam path of the virtual interferometer, not a single link). TDI relies on a independent absolute ranging estimate with an accuracy of approximately 10 m and noise lower than $30\,\mu\mathrm{m}/\sqrt{\mathrm{Hz}}$[9] (also see Tinto et al. (2003)).

The accuracy and precision of the independent estimate of the measured pseudo-range is realized with two auxiliary measurement; the PRN range and the sideband beatnotes. The PRN range is implemented by modulating a pseudo-random code on the laser beams which is read out and correlated with a local copy of the code at the receiving spacecraft and enables determination of the absolute range with meter-accuracy. However, the noise properties of this

[8] The beatnote frequency of a TDI combination is driven by the differential Doppler shift in the two virtual beams. For the second generation Michelson variable it is given by $\frac{\mathrm{d}}{\mathrm{d}t}\Delta t_{X_2}(t)\cdot\nu_0 \simeq \big(4d(\dot{d}_{121}\ddot{d}_{131} - \dot{d}_{131}\ddot{d}_{121}) + 2d(\dot{d}_{121}-\dot{d}_{131})(\ddot{d}_{121}+\ddot{d}_{131}) - 8d^2(\dddot{d}_{121} - \dddot{d}_{131})\big)\nu_0 < 1\,\mathrm{mHz}$ assuming approximately equal arms.

[9] Here, we assume a laser frequency noise level of $30\,\mathrm{Hz}/\sqrt{\mathrm{Hz}}$ and a beatnote frequency of 10 MHz. For more details see section 3.3.

measurement are insufficient with an ASD of roughly $1\,\mathrm{m}/\sqrt{\mathrm{Hz}}$. To achieve the micrometer-precision stated above LISA modulates the clock signals as gigahertz-sidebands on the carrier. Therefore, the sideband beatnotes realize a femtosecond-precise relative ranging measurement (with an unresolved ambiguity of 12.5 cm).

It is possible to combine the PRN range and sideband beatnotes to yield a high-accuracy, low-noise estimate. A simple scheme is presented by Hartwig et al. (2022) that we will discuss in the following. For optimal state estimation a Kalman-like filter can be applied (Reinhardt et al., 2023).

In the first step we reduce six phase modulations to only three. The reason for this is already discussed in section 3.2.4; the modulation noise on right-handed MOSAs has a ten-fold amplitude as compared to left-handed MOSAs. To remove the former we form the η intermediary variables for the sidebands beatnotes.

$$\eta^{\mathrm{sb}}_{ij}(t) = \mathbf{D}^{\hat{\tau}_i}_{ij}\phi^{\mathrm{m},\hat{\tau}_j}_{j}(t) - \phi^{\mathrm{m},\hat{\tau}_i}_{i}(t) \tag{3.65}$$

$$= \eta^{\mathrm{sb}}_{0,ij} + \nu^{\mathrm{m}}_{0} \cdot \left(\mathbf{D}^{\hat{\tau}_i}_{ij} M_j(t) - M_i(t) - d^{\hat{\tau}_i}_{ij}(t)\right) \tag{3.66}$$

Here, single-indexed quantities refer to left-handed MOSAs (and therefore $\nu^{\mathrm{m}}_{0} = \nu^{\mathrm{m}}_{0,i} = 2.4\,\mathrm{GHz}$). The constant phase offset $\eta^{\mathrm{sb}}_{0,ij}$ is dependent on the absolute phases of the USOs. Its exact value is irrelevant to us as we are primarily interested in the in-band noise properties that are given by the modulation noise contributions.

The PRN range in as given in the spacecraft on-board time can be derived from eq. (2.41) by applying the transformation given in eq. (2.43). It reads

$$R^{\hat{\tau}_i}_{ij}(t) = R^{\tau_i}_{ij}\left(\tau^{\hat{\tau}_i}_{i}(t)\right) = t - \mathbf{D}^{\hat{\tau}_i}_{ij} t + B_{ij} + N^{R}_{ij}(t) = d^{\hat{\tau}_i}_{ij}(t) + B_{ij} + N^{R}_{ij}(t), \tag{3.67}$$

and can be used to calibrate the constant in the sideband range. We determine the constant by taking the mean of the difference of the sideband range and the PRN range. Then, we subtract it from the sideband range itself

$$\hat{d}^{\hat{\tau}_i}_{ij}(t) = -\frac{\eta^{\mathrm{sb}}_{ij}(t)}{\nu^{\mathrm{m}}_{0}} - \mathrm{mean}\left\{-\frac{\eta^{\mathrm{sb}}_{ij}(t)}{\nu^{\mathrm{m}}_{0}} - R^{\hat{\tau}_i}_{ij}(t)\right\} \simeq d^{\hat{\tau}_i}_{ij}(t) + B_{ij} - \mathbf{D}^{\hat{\tau}_i}_{ij} M_j(t) + M_i(t). \tag{3.68}$$

The resulting estimate of the measured pseudo-range inherits the bias of the PRN range and the noise of the sideband range. The uncertainty of the determination of the constant can be estimated as $\sqrt{\frac{S^R_N}{T}}$ where T is the duration of the data. After only a couple of seconds the uncertainty drops below the dominant bias terms B_{ij} which is of the order of meters.

To further improve the ranging measurement one can extract the ranging information contained in the carrier-carrier beatnotes. The most dominant in-band contribution comes from the instability of the lasers' frequency and appears correlated among the beatnote phases. The TDI algorithm makes use of this property to suppress laser noise. As it reacts rather sensitive to errors in the ranges, one can use a technique called time-delay interferometric ranging (TDI-R) to infer them. Those estimates are by definition unbiased and can be used to validate and calibrate the PRN measurements. More details on TDI-R can be found in chapter 4.

3.2.5 TDI in units of frequency

A convenient quantity for describing the evolution of the beatnote phases is given by its derivative, the beatnote frequency. Over the whole mission duration it stays roughly constant and within the phasemeter's bandwidth (5 MHz to 25 MHz). A double precision float (approximately 16 digits of precision) is sufficient to numerically represent it as a 20 MHz beatnote frequency produces a noise floor with an amplitude of approximately $2\,\mathrm{nHz}/\sqrt{\mathrm{Hz}}$. We require that the numerical noise floor stays below the microcycle-requirement given in eq. (1.18) which takes its

minimum of $20\,\mathrm{nHz}/\sqrt{\mathrm{Hz}}$ at 2 mHz which results in a margin of one order of magnitude. On the other hand, the beatnote phase is a rapidly increasing quantity which requires a large number of significant digits to deal with its dynamical range. After a year the phase has accumulated approximately 10^{14} cycles and to meet the microcycle requirement we would need around 20 significant digits.

In principle, when converting from phase to frequency no information is lost apart from the initial phase of the beatnote. The total phase can be reconstructed by integrating the beatnote frequency and inferring the integration constant from some other measurement.

$$\phi(t) = \phi_0 + \int_0^t \nu(t')\,\mathrm{d}t' \tag{3.69}$$

The standard TDI combinations representing two-beam equal arm interferometers seem to be insensitive to the initial beatnote phase ϕ_0. They effectively act like differentiators at low frequencies as one-way measurements η_{ij} enter TDI combinations multiple times with different delays. As an example we consider the first generation Michelson variable X_1 where η_{13} enters as

$$(1 - \mathbf{D}_{121})\eta_{13}(t) = \int_{t_0}^{t} \dot{\eta}_{13}(t')\,\mathrm{d}t' + \int_{t_0}^{t-d_{121}(t)} \dot{\eta}_{13}(t')\,\mathrm{d}t' \tag{3.70}$$

$$= \int_{t_0}^{t} \underbrace{\dot{\eta}_{13}(t') + \big(1 - \dot{d}_{121}(t')\big)\dot{\eta}_{13}\big(t' - d_{121}(t')\big)}_{\dot{\eta}_{13}(t') + \dot{\mathbf{D}}_{121}\dot{\eta}_{13}(t')}\,\mathrm{d}t' - \int_{t_0 - d_{121}(t_0)}^{t_0} \dot{\eta}_{13}(t')\,\mathrm{d}t'. \tag{3.71}$$

We insert the definition of the beatnote phase and find that the initial phase drops out. Similarly, TDI combinations act like derivatives on the laser phase. Therefore, they are insensitive to the initial phase of the lasers.

Consequently, the computation of TDI combination in units of total phase should be possible from beatnote measurement given in frequency units as sketched in eq. (3.71). Here, we also introduce the Doppler delay operator $\dot{\mathbf{D}}$ that applies additional to the time-shift a multiplicative Doppler factor and is defined as

$$\dot{\mathbf{D}}\nu(t) = \big(1 - \dot{d}(t)\big)\nu(t - d(t)). \tag{3.72}$$

The additional last term in eq. (3.71) represents a constant phase offset and drops out if considering the TDI variable in frequency units.

3.3 Laser and Timing Noise Residuals

Onboard the spacecraft and in on-ground data processing laser noise and other timing noises enter the beatnote measurements through various channels (Staab et al., 2023b). We discuss the residuals due to the non-commutativity of the decimation stage and the delay operation (partially described in Bayle et al. (2019)) and the impact of ranging (Tinto et al., 2003) and interpolation errors arising in post-processed TDI (Shaddock et al., 2004).

3.3.1 On-board processing residuals

As discussed in section 2.3 decimation stages are used on board to reduce the data rate from 80 MHz down to 4 Hz. Those involve filters to mitigate aliasing, and decimators. In the following we will discuss how those operations give rise to residual laser noise.

In section 3.2 we have discussed several reduction steps that are needed to suppress laser and clock noise to the fundamental limit that is given by the arm-length mismatch. However, we

have left out the description of the on-board processing. Before telemetry, each measurement is passed through several stages of decimation that we denote by the operation $\mathbf{S}$. Therefore, the measurements relevant for laser noise suppression are given as

$$\overline{\mathrm{isi}}_{ij} = \mathbf{S}\big(\mathbf{D}_{ij}\phi_{ji} - \phi_{ij}\big), \tag{3.73a}$$
$$\overline{\mathrm{rfi}}_{ij} = \mathbf{S}\big(\phi_{ik} - \phi_{ij}\big). \tag{3.73b}$$

Here, we introduce the bar notation that indicates decimated measurements.

To carry out TDI we require precise measurements of the propagation delays between the satellites. Those are subject to the same decimation procedure such that we have only access to

$$\bar{d}_{ij} = \mathbf{S}d_{ij}. \tag{3.74}$$

We denote the corresponding delay operator by $\bar{\mathbf{D}}_{ij}$. Next, let us observe the effect of applying this operator two a generic decimated phase $\bar{\phi} = \mathbf{S}\phi$. We aim to find a rule to commute the delay operation with the decimation stages to pull $\mathbf{S}$ in front of the expression. We find that this commutation gives raise to a commutator.

$$\bar{\mathbf{D}}\bar{\phi}(t) = \bar{\mathbf{D}}(\phi^o(t) + \mathbf{S}\phi^\epsilon(t)) \tag{3.75}$$
$$\simeq \mathbf{D}^o\phi^o(t) - \mathbf{S}d^\epsilon(t)\cdot\mathbf{D}^o\nu^o(t) + \mathbf{D}^o\mathbf{S}\phi^\epsilon(t) \tag{3.76}$$
$$\simeq \mathbf{S}\big(\mathbf{D}^o\phi^o(t) - d^\epsilon(t)\cdot\mathbf{D}^o\nu^o(t) + \mathbf{D}^o\phi^\epsilon(t)\big) - [\mathbf{S},\mathbf{D}^o]\phi^\epsilon(t) \tag{3.77}$$
$$\simeq \mathbf{S}\mathbf{D}\phi(t) - [\mathbf{S},\mathbf{D}^o]\phi^\epsilon(t) \tag{3.78}$$

Here, we made use of the fact that the decimation stages have no effect on the out-of-band part of the phase[10]. Furthermore, we have used the property given in eq. (2.20) to develop the delayed total phase into its in-band and out-of-band components. The operator $\mathbf{D}^o$ denotes a delay by the out-of-band component of $d(t) = d^o(t) + d^\epsilon(t)$.

To demonstrate the use of eq. (3.78) we derive the form of the intermediary variable η for left-handed and right-handed MOSAs. The former is defined as

$$\bar{\eta}_{ij} = \overline{\mathrm{isi}}_{ij} - \bar{\mathbf{D}}_{ij}\frac{\overline{\mathrm{rfi}}_{jk} - \overline{\mathrm{rfi}}_{ji}}{2} \tag{3.79}$$
$$= \mathbf{S}\big(\mathbf{D}_{ij}\phi_{ji} - \phi_{ij}\big) - \bar{\mathbf{D}}_{ij}\mathbf{S}\big(\phi_{ji} - \phi_{jk}\big) \tag{3.80}$$
$$= \mathbf{S}\big(\mathbf{D}_{ij}\phi_{jk} - \phi_{ij}\big) + [\mathbf{S},\mathbf{D}^o_{ij}]\big(\phi_{ji} - \phi_{jk}\big)^\epsilon. \tag{3.81}$$

We yield two terms. The first one has the same algebraic form as eq. (3.11) and the second resembles an additive term that will remain even after TDI. This demonstrates the general coupling mechanism of residual laser noise due to the non-commutativity of the decimation stages with the out-of-band delay operator.

The intermediary variable η for right-handed MOSAs does not pick up the commutator as there are no delay operators applied to form it. It is easy to verify that

$$\bar{\eta}_{ij} = \overline{\mathrm{isi}}_{ij} + \frac{\overline{\mathrm{rfi}}_{ik} - \overline{\mathrm{rfi}}_{ij}}{2} = \mathbf{S}\big(\mathbf{D}_{ij}\phi_{ji} - \phi_{ik}\big). \tag{3.82}$$

Adopting the single-index notation for left-handed laser ($\phi_1 = \phi_{12}$, $\phi_2 = \phi_{23}$ and $\phi_3 = \phi_{31}$) we find a general expression that holds for all η_{ij}.

$$\bar{\eta}_{ij} = \mathbf{S}\underbrace{\big(\mathbf{D}_{ij}\phi_j - \phi_i\big)}_{\eta_{ij}} + [\mathbf{S},\mathbf{D}^o_{ij}]\underbrace{\big(\phi_{ji} - \phi_j\big)^\epsilon}_{p_{ji}-p_j} \tag{3.83}$$

[10] For this to hold we require that the filters have vanishing group delay. This can be achieved by implementing acausal digital filters, where an integer group delay is compensated by reassigning shifted timestamps to the samples.

Here, we identify η_{ij} (without the bar) and the difference of the laser phases in the second term can be approximated by just their laser noise content. This is possible since laser noise is the dominant in-band contribution in beatnote phase.

Next, we want to give a more detailed description of the commutator. As already mentioned above, in the current baseline design of LISA the decimation procedure is performed in stages. Each stage consists of a digital filter to prevent aliasing and a decimator. Therefore, the entire decimation procedure can be represented by

$$\mathbf{S} = \prod_{i=N}^{1} \mathbf{S}_{M_i\downarrow}\mathbf{F}_i. \tag{3.84}$$

Commutator rules can be applied to study the effect of each stage individually. In this manuscript, to simplify the modeling we only consider a single stage. This also reflects the implementation of the state-of-the-art LISA simulators that we will use to verify our models. Therefore we redefine

$$\mathbf{S} = \mathbf{S}_{M\downarrow}\mathbf{F}. \tag{3.85}$$

and insert it into the commutator of eq. (3.78). Next, using commutator rule eq. (A.2) we split it up into two terms.

$$[\mathbf{S}_{M\downarrow}\mathbf{F}, \mathbf{D}^o] = \mathbf{S}_{M\downarrow}[\mathbf{F}, \mathbf{D}^o] + [\mathbf{S}_{M\downarrow}, \mathbf{D}^o]\mathbf{F}. \tag{3.86}$$

We find two contributions, the filter-delay commutator that is decimated, and the decimation-delay commutator of the filtered signal. In the following sections we will take a closer look at those and discuss the conditions for them to be non-vanishing.

Filtering-delay commutator

The magnitude of the filtering-delay commutator strongly depends on the time-dependence of the delay $d^o(t)$. Intuitively, the commutator becomes zero for a constant delay as then both, filtering and delay operation, represent LTI systems that commute by definition. However, in case of a time-dependent delay the commutator is non-vanishing. The first description can be found in Bayle et al. (2019) where it was dubbed "flexing-filtering effect".

In what follows, we rederive the result using the definitions established in section 1.3. We set off by expanding the expression

$$\begin{aligned}
\mathbf{F}\mathbf{D}^o\phi^\epsilon(t) &= \int_{\mathbb{R}} h_{\mathbf{F}}(\tau)\phi^\epsilon(t-\tau-d^o(t-\tau))\,\mathrm{d}t && \text{(3.87a)}\\
&= \int_{\mathbb{R}} h_{\mathbf{F}}(\tau)\phi^\epsilon(t-\tau-d^o(t)+\tau\dot{d}^o(t))\,\mathrm{d}t && \text{(3.87b)}\\
&\simeq \int_{\mathbb{R}} h_{\mathbf{F}}(\tau)\phi^\epsilon(t-d^o(t)-\tau)\,\mathrm{d}t + \int_{\mathbb{R}} h_{\mathbf{F}}(\tau)\tau\dot{d}^o(t)\dot{\phi}^\epsilon(t-d^o(t)-\tau)\,\mathrm{d}t && \text{(3.87c)}\\
&= \mathbf{D}^o\mathbf{F}\phi^\epsilon(t) + \dot{d}^o(t)\,\mathbf{D}^o\mathbf{G}\frac{\mathrm{d}}{\mathrm{d}t}\phi^\epsilon(t). && \text{(3.87d)}
\end{aligned}$$

Here, we assume a small delay derivative $\dot{d}^o \ll 1$. As we will later see $\dot{d}^o$ is dominated by the clock drifts $\dot{q}^o$ which are of the order of 5×10^{-7}. Relative inter-spacecraft velocities play a minor role as tens of $\mathrm{m\,s^{-1}}$ corresponds to $\dot{d}^o \sim 10^{-8}$. In the next step, we expand the laser phase to first order in $\tau\dot{d}^o$. This is appropriate as τ takes as its maximum value half the filter kernel length such that the product $\tau\dot{d}^o$ remains small. In the last line of eq. (3.87) we collect the two convolution integrals and identify two terms. The first one resembles the application of the operators in reverse order. The second term represents exactly the commutator we sought for, therefore, we write

$$[\mathbf{F}, \mathbf{D}^o]\phi^\epsilon(t) = \mathbf{F}\mathbf{D}^o\phi^\epsilon(t) - \mathbf{D}^o\mathbf{F}\phi^\epsilon(t) = \dot{d}^o(t)\,\mathbf{D}^o\mathbf{G}\frac{\mathrm{d}}{\mathrm{d}t}\phi^\epsilon(t) \tag{3.88}$$

Here, the operator $\mathbf{G}$ represents a filter operation with kernel $h_{\mathbf{G}}(\tau) = \tau \cdot h_{\mathbf{F}}(\tau)$. To express the PSD of eq. (3.88) we assume a constant delay derivative and find

$$S_{\delta\phi}^{[\mathbf{F},\mathbf{D}^o]}(f) = \left| \frac{\dot{d}^o}{2\pi} \frac{\mathrm{d}\tilde{h}_{\mathbf{F}}(f)}{\mathrm{d}f} \right|^2 S_\phi(t). \tag{3.89}$$

Consequently, the amplitude of the flexing-filtering effect is dependent on two factors. First, it is directly proportional to the delay derivative $\dot{d}^o$, and second, it relies upon a flat filter response. For a filter that is unity throughout the band the magnitude of $\frac{\mathrm{d}\tilde{h}_{\mathbf{F}}(f)}{\mathrm{d}f}$ would be exactly zero. However, realizing such a filter comes with high computational cost as many taps would be required. Therefore, in principle, one has to trade off number of filter taps against the level of flexing-filtering residual. Another solution is to correct the non-flat response of the anti-aliasing filters on ground by means of a compensation filter. This is discussed in more details at the end of the section.

Decimation-delay commutator

The non-commutation of the decimation and the delay operation also affects the residual in eq. (3.78). As explained in section 1.3 decimation describes the process of reducing the sampling rate of a discrete-time signal from $M \cdot f_s$ to f_s. Here, f_s denotes the sampling rate after decimation. For the decimation-delay commutator applied to a general phase noise we write

$$[\mathbf{S}_{M\downarrow}, \mathbf{D}^o]\phi^\epsilon(t) = \mathbf{S}_{M\downarrow}\mathbf{D}^o\phi^\epsilon(t) - \mathbf{D}^o\mathbf{S}_{M\downarrow}\phi^\epsilon(t). \tag{3.90}$$

We can directly infer that the condition for a vanishing commutator is that $\mathbf{D}^o$ corresponds to an integer shift (after decimation, so $d^o \cdot f_s$ equals to an integer k). In discrete time we write

$$\mathbf{S}_{M\downarrow}\mathbf{D}^o\phi_n^\epsilon = \mathbf{S}_{M\downarrow}\phi_{n-M\cdot k}^\epsilon = \phi_{M\cdot(n-k)}^\epsilon, \tag{3.91}$$

$$\mathbf{D}^o\mathbf{S}_{M\downarrow}\phi_n^\epsilon = \mathbf{D}^o\phi_{M\cdot n}^\epsilon = \phi_{M\cdot(n-k)}^\epsilon. \tag{3.92}$$

As both expressions yield the same result we conclude that the statement above is correct. For non-integer delays we cannot rely on the discrete formulation of the expression but have to make use of the Whittaker-Shannon interpolation formula (see eq. (1.29)) to transform the problem into continuous time. The derivation of the commutator of decimation and the application of a general LTI system is given in appendix B.1.

To express the PSD of equation eq. (3.90) we use eq. (B.18) of appendix B and plugin the transfer function of a constant delay $\tilde{h}(f) = e^{-2\pi i f d^0}$. We find

$$S_{\delta\phi}^{[\mathbf{S}_{M\downarrow},\mathbf{D}^o]}(f) = \mathrm{rect}\left(\frac{f}{f_s}\right) \sum_{n=1}^{M-1} 4 \cdot c_n(d^o) \cdot S_\phi^{(n)}(f) \tag{3.93}$$

where the weighting factors $c_n(d^o)$ are given by

$$c_n(d) = \begin{cases} \sin^2(\pi f_s \frac{n}{2} d^o) & \text{for } n \text{ even}, \\ \sin^2(\pi f_s \frac{n+1}{2} d^o) & \text{for } n \text{ odd}. \end{cases} . \tag{3.94}$$

As the delay d^o generally varies over time the amplitude of the residual is modulated. We find an upper bound of the PSD by setting all $c_n = 1$. On average, assuming that d^o covers many multiples of the sampling time T_s, c_n takes the value $\frac{1}{2}$.

Compensation filter

As mentioned above the aforementioned flexing-filtering effect can be suppressed by means of a compensation filter. This filter is placed after the last decimator and can even be moved to the on-ground processing pipeline to relax computational requirement on the spacecraft. It is used to "lift" the transfer function of the decimation stage to ensure unity gain in-band. We can model it as having a decimation stage operator

$$\mathbf{S} = \mathbf{F}^{+}\mathbf{S}_{M\downarrow}\mathbf{F}. \tag{3.95}$$

We model the compensation filter $\mathbf{F}^{+}$ as an FIR filter running at the decimated sampling rate f_s. Hence, for modeling we can commute it with the decimator by

$$\mathbf{F}\mathbf{S}_{M\downarrow}x_n = \mathbf{F}x_{M\cdot n} = \sum_k h_k x_{M\cdot(n-k)} = \sum_k \mathring{h}_k x_{M\cdot n-k} = \mathbf{S}_{M\downarrow}\mathring{\mathbf{F}}x_n. \tag{3.96}$$

Here, the filter kernel $\mathring{h}_n$ is defined as

$$\mathring{h}_k = \begin{cases} h_{k/M} & \text{if } k \bmod M = 0 \\ 0 & \text{else} \end{cases} \tag{3.97}$$

which is equivalent to the original filter kernel filled with $M-1$ zeros in between taps. The $[\mathbf{S}, \mathbf{D}^o]$ commutator is now given as

$$[\mathbf{F}^{+}\mathbf{S}\mathbf{F}, \mathbf{D}^o] = [\mathbf{S}\mathring{\mathbf{F}}^{+}\mathbf{F}, \mathbf{D}^o] \tag{3.98}$$

$$= \mathbf{S}[\mathring{\mathbf{F}}^{+}\mathbf{F}, \mathbf{D}^o] + [\mathbf{S}, \mathbf{D}^o]\mathring{\mathbf{F}}^{+}\mathbf{F}. \tag{3.99}$$

We have again proceeded as in eq. (3.86) and split the commutator into two contributions. The first one is responsible for the flexing-filtering effect and the second one for aliasing. Note that the level of flexing-filtering is reduced as the transfer function of $\mathring{\mathbf{F}}^{+}\mathbf{F}$ is closer to unity in-band. On the other hand, the effect of aliasing is amplified as the compensation filter lifts up the response in the stop band of the filter $\mathbf{F}$.

To demonstrate the effect of the compensation filter and validate the models derived for the filter-delay and decimation-delay commutators, we run numerical simulations and compare them against our models. In our setup, we simulate a time series of red phase noise with an ASD of

$$\sqrt{S_p(f)} = \sqrt{S_{\dot{p}}(f)} \cdot (2\pi f)^{-1} = 30\,\mathrm{Hz}/\sqrt{\mathrm{Hz}} \cdot (2\pi f)^{-1} = 4.77\,\mathrm{cycles}/\sqrt{\mathrm{Hz}} \cdot \frac{\mathrm{Hz}}{f}, \tag{3.100}$$

at a rate of 16 Hz. We use the optimized filter design for phase units described in appendix C as the anti-aliasing filter and suggest a compensation filter that uses 81 taps. The latter is computed via sampling of the impulse response of a continuous-time filter that has the reciprocal transfer function of the original anti-aliasing filter in-band.

To investigate frequencies down to 10^{-4} Hz we choose 250 000 s as the duration. Then, we simulate two commutators. The first one involves the simple decimation stage presented in eq. (3.85). The second simulation additionally uses a compensation filter to suppress the flexing-filtering effect.

$$\delta\phi^{[\mathbf{S}_{4\downarrow}\mathbf{F}, \mathbf{D}^o]}(t) \simeq [\mathbf{S}_{4\downarrow}\mathbf{F}, \mathcal{D}^o]p(t) = \mathbf{S}_{4\downarrow}\mathbf{F}\mathcal{D}^o p(t) - \mathcal{D}^o\mathbf{S}_{4\downarrow}\mathbf{F}p(t) \tag{3.101a}$$

$$\delta\phi^{[\mathbf{F}^{+}\mathbf{S}_{4\downarrow}\mathbf{F}, \mathbf{D}^o]}(t) \simeq [\mathbf{F}^{+}\mathbf{S}_{4\downarrow}\mathbf{F}, \mathcal{D}^o]p(t) = \mathbf{F}^{+}\mathbf{S}_{4\downarrow}\mathbf{F}\mathcal{D}^o p(t) - \mathcal{D}^o\mathbf{F}^{+}\mathbf{S}_{4\downarrow}\mathbf{F}p(t) \tag{3.101b}$$

In both cases we decimate by a factor of four. The calligraphic $\mathcal{D}$ indicates that we are using a fractional delay filter to numerically approximate the delay operation for discrete time series. The impact of that is further discussed in detail in section 3.3.2. To suppress interpolation

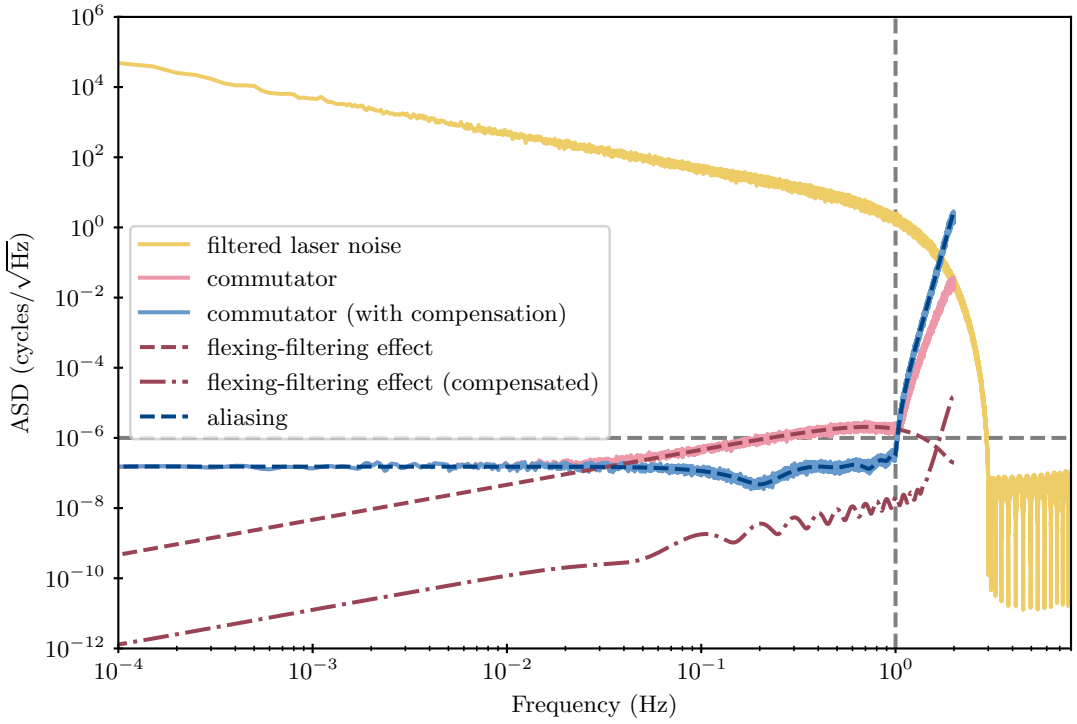

Figure 3.7: Commutator residuals due to the flexing-filtering effect and aliasing. The numerical ASDs of the filtered laser phase noise is shown in yellow, and the commutator residuals with (blue) and without (red) compensation filter are plotted. For more details on the models see text.

residuals sufficiently we choose the Lagrange interpolation method with a high interpolation order of 101 which is implemented in the Python package PyTDI (Staab et al., 2023a). As the simplest time-varying delay we choose a linear dependence of the delay

$$d^o(t) = d_0 + \dot{d} \cdot t \tag{3.102}$$

with $d_0 = 8\,\mathrm{s}$ and $\dot{d} = 5 \times 10^{-7}$. With those parameters the delay will scan from 8 s through 8.125 s which correspond to an integer delay and a mid-sample delay ($\epsilon = 0.5$), respectively.

The numerical ASDs of the simulation outlined in eq. (3.101) are shown in fig. 3.7. The yellow line represents the level of laser phase noise after filtering. In solid blue and red the results of the commutator with and without compensation filter is plotted. For comparison, we also show models for the flexing-filtering effect (with compensation in dashed-dotted red and without compensation in dashed red) and aliasing effect (dashed blue). They are given as

$$S_{\delta\phi}^{\mathbf{S}_{4\downarrow}[\mathbf{F},\mathbf{D}^o]}(f) = \tilde{\mathbf{S}}_{4\downarrow}\left(\left|\frac{\dot{d}^o}{2\pi}\frac{\mathrm{d}\tilde{h}_{\mathbf{F}}(f)}{\mathrm{d}f}\right|^2 S_{\dot{p}}(f)\right), \tag{3.103}$$

$$S_{\delta\phi}^{\mathbf{S}_{4\downarrow}[\mathbf{F}^+\mathbf{F},\mathbf{D}^o]}(f) = \tilde{\mathbf{S}}_{4\downarrow}\left(\left|\frac{\dot{d}^o}{2\pi}\frac{\mathrm{d}\left(\tilde{h}_{\mathbf{F}^+}(f)\cdot\tilde{h}_{\mathbf{F}}(f)\right)}{\mathrm{d}f}\right|^2 S_{\dot{p}}(f)\right), \tag{3.104}$$

$$S_{\delta\phi}^{[\mathbf{S}_{4\downarrow},\mathbf{D}^o]\mathbf{F}^+\mathbf{F}}(f) = \mathrm{rect}\left(\frac{f}{f_s}\right)\sum_{n=1}^{M-1} 4\cdot c_n(\bar{d}^o)\cdot\left(\tilde{\mathbf{F}}^+\tilde{\mathbf{F}}S_p(f)\right)^{(n)}(f). \tag{3.105}$$

Here, we note that the flexing-filtering contributions residing at $f > 2\,\mathrm{Hz}$ are potentially aliased into band. Therefore, the not only the flatness in-band is relevant for this coupling but also

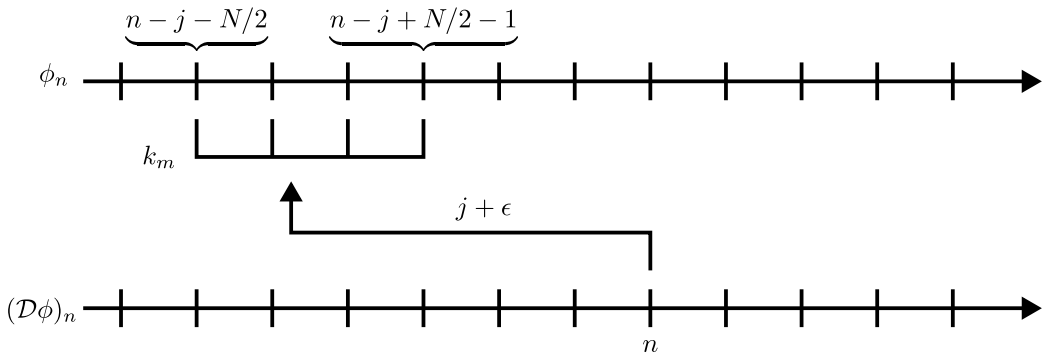

Figure 3.8: Illustration of the discrete convolution of the fractional delay filter kernel k_m (the comb-shaped structure) with the time series ϕ_n. As an example we choose a kernel length $N = 4$, an integer shift $j = -5$ and a fractional shift $\epsilon = 0.25$.

out-of-band. The last equation represent aliased noise that dominates the on-board processing residual after appropriately compensating for the non-flatness.

In fig. 3.7 we indeed observe that without compensation the flexing-filtering effect dominates the residual for frequencies higher than 3×10^{-2} Hz. With compensation, on the other hand, it is pushed below the residual due to aliasing which cannot be further reduced by any means.

3.3.2 TDI residuals

The post-processed implementation of TDI requires an independent measurement of the propagation delays between the satellites and an appropriate interpolation method to time-shift the discretely sampled data. Errors in the ranges and inaccurate interpolation will introduce residual laser and timing noise in the resulting combinations.

Therefore, we introduce the post-processing delay operation $\hat{\mathcal{D}}$ that is subject to ranging noise in the ranging estimates. As an example we observe its action when forming the intermediary variable η on left-handed MOSAs.

$$\hat{\eta}_{ij} = \mathrm{isi}_{ij} + \hat{\mathcal{D}}_{ij}\frac{\mathrm{rfi}_{ji} - \mathrm{rfi}_{jk}}{2} \tag{3.106}$$

$$= \mathrm{isi}_{ij} + \left(\mathbf{D}_{ij} + \hat{\mathcal{D}}_{ij} - \mathbf{D}_{ij}\right)\frac{\mathrm{rfi}_{ji} - \mathrm{rfi}_{jk}}{2} \tag{3.107}$$

$$= \eta_{ij} + \left(\hat{\mathcal{D}}_{ij} - \mathbf{D}_{ij}\right)\frac{\mathrm{rfi}_{ji} - \mathrm{rfi}_{jk}}{2} \tag{3.108}$$

We recover the "true" variable and an additional residual that is produced by the difference between the post-processing delay operation and the actual delay operation. Let us further split

$$(\hat{\mathcal{D}} - \mathbf{D})\phi(t) = (\hat{\mathcal{D}} - \hat{\mathbf{D}})\phi(t) + (\hat{\mathbf{D}} - \mathbf{D})\phi(t). \tag{3.109}$$

Here, we distinguish between the residual caused by interpolation errors (first term) and ranging errors (second term). Let us now study both effects individually.

Interpolation error

In order to time-shift the discretely sampled beatnotes by arbitrary delays we require an interpolation method. In practice, this operation is carried out by a fractional delay filter which is represented by an FIR system. In fig. 3.8 we illustrate this operation. For optimal performance the filter kernel k_m is centered around the time of evaluation. We split the delay into an integer shift j and a fractional shift ϵ such that we can write $-d = (j + \epsilon)T_s$ where T_s denotes the sampling time. This is convenient because a time-shift by an integer amount of samples is trivial

and can be performed beforehand. Furthermore, the filter kernel k_m is then only dependent on the fractional shift ϵ. We can formally represent the fractional delay filter by

$$(\mathcal{D}\phi)_n = \sum_{m=-N/2}^{N/2-1} k_m(\epsilon) \cdot \phi_{n-j-m}. \tag{3.110}$$

Here, ϕ_n are the discrete-time samples of the beatnote phase and N is the length of the length of the kernel. Here, we only work with even length kernels but a similar expression for odd N can be easily derived.

Let us now apply the rule for transforming this discrete-time operation into a continuous LTI system. We find the continuous-time kernel

$$h_{\mathcal{D}}(\tau) = \sum_{m=-N/2}^{N/2-1} k_m(\epsilon) \cdot \delta(\tau - (j+m)T_s). \tag{3.111}$$

with a transfer function of

$$\tilde{h}_{\mathcal{D}}(f) = \sum_{m=-N/2}^{N/2-1} k_m(\epsilon) \cdot e^{-2\pi i f(j+m)T_s}. \tag{3.112}$$

Using those definitions we write the interpolation residual as

$$\delta\phi^{\mathcal{D}}(t) = (\mathcal{D} - \mathbf{D})\phi(t) = \mathbf{D}\underbrace{(\mathbf{D}^{-1}\mathcal{D} - 1)}_{\mathbf{\Delta}}\phi(t) \tag{3.113}$$

Here, the operator $\mathbf{\Delta}$ effectively describes the dissimilarity of $\mathbf{D}^{-1}\mathcal{D}$ from unity. We use eq. (1.28) to derive the PSD of the residual and find

$$S^{\mathcal{D}}_{\delta\phi}(f) = \underbrace{\left|\tilde{h}_{\mathcal{D}}(f) \cdot e^{2\pi i f d} - 1\right|^2}_{\tilde{\mathbf{\Delta}}} S_\phi(f). \tag{3.114}$$

In general, the propagation delays in LISA vary slowly over time. As the interpolation error is dependent on the value of the fractional shift ϵ the amplitude of the residual is modulated over the year. It is easy to verify that it vanishes for $\epsilon = 0, 1$ as an integer shift is trivially implemented. For any other fractional value the delay filter can be designed such that the interpolation residual stays below some requirement.

Classically, Lagrange interpolation is used to interpolate LISA data (Shaddock et al., 2004). This method fits a Lagrange polynomial of order $N-1$ to the data which is centered around the time of evaluation. It can be shown that this method produces a maximal flat response at DC. Therefore, it is well suited to interpolate LISA data at low frequencies. However, the optimal response at low frequencies comes at the cost of slow convergence at high frequencies close to the Nyquist frequency.

To relax this behavior we introduce a new class of fractional delay filters in appendix D. They are based on the design of FIR type II filters which have an even number of coefficients and are symmetric. As a result, the transfer function of this filter naturally exhibits a fractional group delay of 0.5. An arbitrary fractional delay filter can be derived from this with a similar magnitude response. Therefore, we can tailor the frequency response over the LISA band to fulfill a specific frequency-dependent requirement and at the same time minimize the number of coefficients of the interpolation kernel.

To test the performance of the two interpolation methods we run a simple numerical simulation using PyTDI (Staab et al., 2023a). As in section 3.3.1 we generate a time series of red

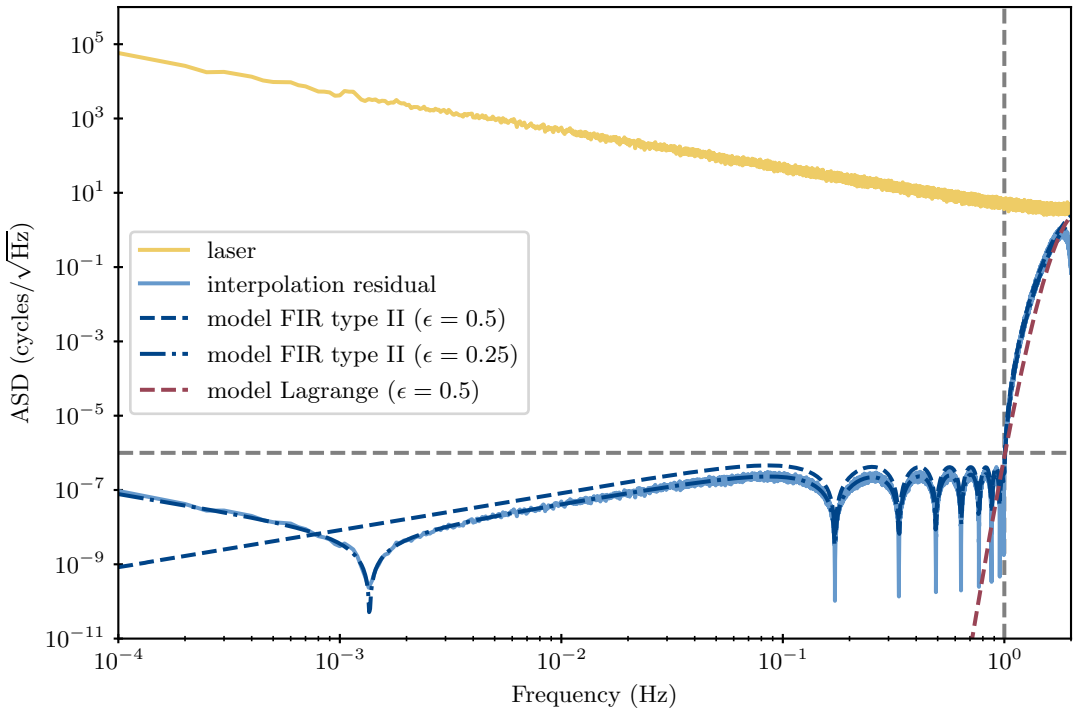

Figure 3.9: Interpolation residual of fractional delay filters. The ASD of raw laser phase noise is shown in yellow and the solid blue line represents the ASD of the resulting interpolation residual for $\epsilon = 0.25$ using the FIR type II design with $N = 28$. For comparison the dashed lines represent models for $\epsilon = 0.5$ for the FIR type II design (blue) and Lagrange interpolation (red) with $N = 42$. For reference we indicate the upper bound of the LISA band and the 1 μcycle/$\sqrt{\text{Hz}}$ requirement with grey dashed lines.

laser phase noise with the ASD given in eq. (3.100). Then we choose a constant delay d and apply it to the time series. For one copy we use the fractional delay filter we want to test and for another we use Lagrange interpolation of very high order ($N = 102$) that serves as the "true reference". The difference of the two should then be an approximate numerical representation of eq. (3.113).

The result of this experiment is shown in fig. 3.9. The level of raw laser phase noise is shown in yellow. For both interpolation methods we choose the minimum number of coefficients to push the interpolation residual below the $1\,\mu\text{cycle}/\sqrt{\text{Hz}}$ requirement in the LISA band. For the FIR type II design (blue) we find $N = 28$ and for the Lagrange interpolation method (red) $N = 42$. The superior performance of the latter at low frequencies is obvious as the red dashed line quickly drops to very small number not resolved in the graph. However, the FIR type II design only uses two thirds of the number of coefficients and trades off low-frequency performance for drop rate close to the Nyquist frequency to still fulfill the requirement. To demonstrate the effect of leakage (non-zero at DC) in the design procedure of this kernel type we choose $\epsilon = 0.25$ ($d = 8.1975\,\text{s}$ at $f_s = 4\,\text{Hz}$) for the numerical simulation. The model represented by the blue dashed-dotted line perfectly explains the residual.

Ranging error

The second contribution in eq. (3.109) is due to ranging errors. We define the estimated delay operator as $\hat{\mathbf{D}}$ which applies a delay of $\hat{d}(t) = d(t) + r(t)$. Here, $r(t)$ describes any deviation from the true delay $d(t)$. As we assume a small delay error we can expand to first order and find

$$\delta\phi^{\hat{\mathbf{D}}}(t) = (\hat{\mathbf{D}} - \mathbf{D})\phi(t) \simeq -r(t)\mathbf{D}\nu(t). \tag{3.115}$$

We note that the delay error couples to the beatnote frequency $\nu(t) = \dot{\phi}(t)$. From section 3.2.4 we know that $r(t)$ contains nano-second slowly drifting offsets and femto-second in-band noise. Therefore, analogously to the beatnote frequency we distinguish between $r^o(t)$ and $r^\epsilon(t)$. Let us develop eq. (3.115).

$$r(t)\mathbf{D}\nu(t) = \underbrace{r^o(t)\mathbf{D}\nu^o(t)}_{\text{out-of-band}} + \underbrace{r^o(t)\mathbf{D}\nu^\epsilon(t)}_{\text{residual laser noise}} + \underbrace{r^\epsilon(t)\mathbf{D}\nu^o(t)}_{\text{ranging noise coupling}} + \underbrace{r^\epsilon(t)\mathbf{D}\nu^\epsilon(t)}_{\text{second order}} \tag{3.116}$$

The ranging residual splits into four terms. The product of the two out-of-band components is itself out-of-band and therefore irrelevant for us[11]. The second term represents the coupling of laser frequency noise to slow varying ranging offsets. Similarly, any timing jitter in the ranging error couples to the mega-hertz beatnote frequency. Lastly, the product of the two in-band component is second order in small quantities and can therefore be safely dropped.

To model the PSDs of the two relevant terms above we assume a constant ranging bias B for the out-of-band component of the ranging error and constant beatnote frequency a. Then, the PSD of eq. (3.115) is trivially given by

$$S_{\delta\phi}^{\hat{\mathbf{D}}}(f) = B^2 S_\nu(f) + a^2 S_r(f). \tag{3.117}$$

To numerically validate theses findings we have to also consider the quickly increasing phase ramp in the simulation of the beatnote phase. As this produces large numbers that reduce the numerical precision of the floating point representation we switch to frequency units. The beatnote frequency is easier to handle as it does not grow arbitrarily large but stays within certain bounds. Therefore, we simulate it as the sum of the beatnote offset $a = 10\,\text{MHz}$ and laser frequency noise $\dot{p}(t)$.

$$\nu(t) = a + \dot{p}(t) \tag{3.118}$$

[11] We will later see that it is further suppressed by TDI that acts like a derivative at low frequencies.

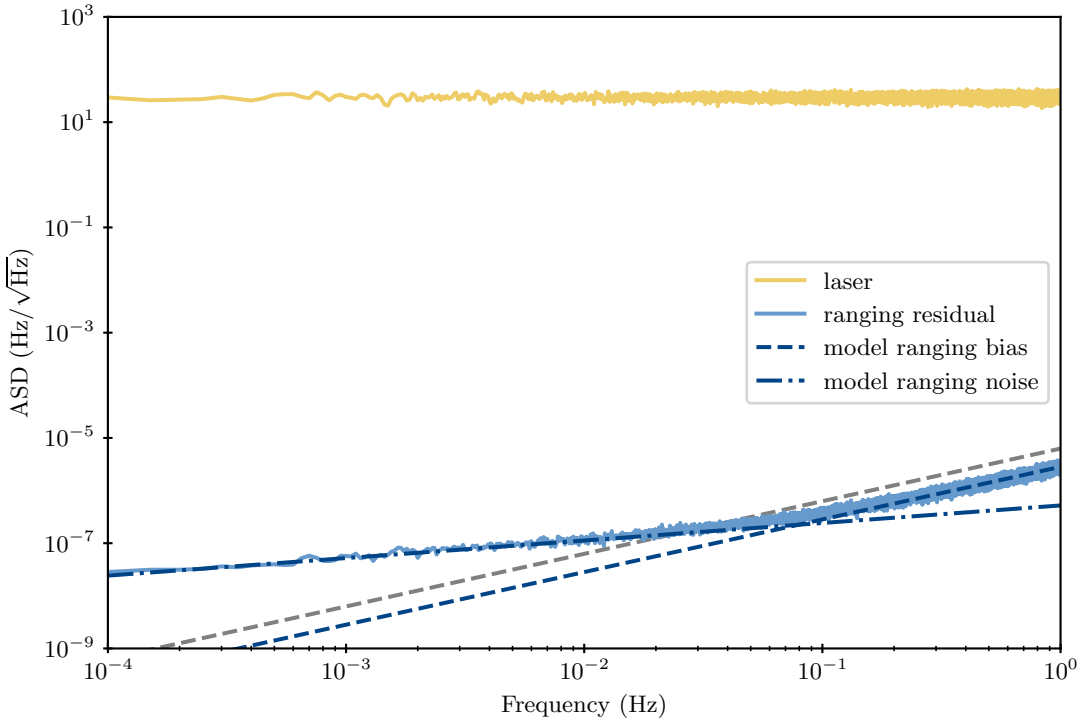

Figure 3.10: Ranging residual from ranging error. In yellow the level of raw laser frequency noise with ASD of $30\,\mathrm{Hz}/\sqrt{\mathrm{Hz}}$ is shown. The solid blue line represents the result of the difference given in eq. (3.119) alongside with models for the contribution caused by the ranging bias (dashed blue) and ranging noise (dashed-dotted blue). Again, we show the $1\,\mu\mathrm{cycle}/\sqrt{\mathrm{Hz}}$ requirement in dashed grey.

We express eq. (3.115) in frequency units by taking the derivative

$$\delta\nu^{\hat{\mathbf{D}}}(t) = \left(\dot{\hat{\mathbf{D}}} - \dot{\mathbf{D}}\right)\nu(t), \tag{3.119}$$

where $\dot{\mathbf{D}}$ is the Doppler delay that also includes the Doppler shift (cf. section 3.2.5). As the dominant ranging noise in LISA we assume modulation noise with an ASD given in eq. (1.22).

The PSD of eq. (3.119) follows by multiplying eq. (3.115) by the factor $(2\pi f)^2$. We find

$$S_{\delta\nu}^{\hat{\mathbf{D}}}(f) = (2\pi f)^2\left(B^2 S_{\dot{p}}(f) + a^2 S_M(f)\right). \tag{3.120}$$

The numerical results of eq. (3.119) for a bias of $B = 5\times10^{-8}\,\mathrm{s} \simeq 15\,\mathrm{m}$ are presented in fig. 3.10. The ASD of the ranging residual (blue) is well explained by the model. At low frequencies the contribution from modulation noise coupling to the beatnote frequency dominates, while at high frequencies the laser noise coupling with the ranging bias takes over.

3.3.3 Michelson combinations

In this section we apply the formalism we have derived in the previous sections to the second generation Michelson variable. In the first step we bring together the results on the effect of on-board processing and the post-processing delay operator for the intermediary variable η. We use the definition given in eq. (3.56) and replace each occurrence of the propagation delay $\mathbf{D}$ by the corresponding decimated post-processing delay $\hat{\bar{\mathcal{D}}}$. Furthermore, we operate on the decimated interferometric measurement as they are produced by the spacecraft. Using eqs. (3.83)

and (3.108) we find

$$\hat{\bar{\eta}}_{ij} = \begin{cases} \overline{\mathrm{isi}}_{ij} + \hat{\bar{\mathcal{D}}}_{ij}\frac{\overline{\mathrm{rfi}}_{ji}-\overline{\mathrm{rfi}}_{jk}}{2} & \text{if } \epsilon_{ijk}=1 \\ \overline{\mathrm{isi}}_{ij} + \frac{\overline{\mathrm{rfi}}_{ij}-\overline{\mathrm{rfi}}_{ij}}{2} & \text{if } \epsilon_{ijk}=-1 \end{cases} \tag{3.121}$$

$$= \mathbf{S}\eta_{ij} - [\mathbf{S}, \mathbf{D}^o_{ij}]p_j + \underbrace{[\mathbf{S}, \mathbf{D}^o_{ij}]p_{ji}}_{\delta\eta^{[\mathbf{S},\mathbf{D}]}_{ij}} + \underbrace{\big(\hat{\bar{\mathcal{D}}}_{ij} - \bar{\mathbf{D}}_{ij}\big)(\bar{\phi}_{ji} - \bar{\phi}_j)}_{\delta\eta^{\hat{\mathcal{D}}}_{ij}}, \tag{3.122}$$

where ϵ_{ijk} denotes the Levi-Civita symbol which equals to 1 for even permutations of $i, j, k = 1, 2, 3$ and -1 for odd permutations. The first two terms in the last line are grouped together as they will form the fundamental laser noise residual in the final TDI combination. We identify the other two as the residual due to on-board processing and the use of the post-processing delay.

TDI relies on constructing more and more complex beam paths. For illustration we form the intermediary variable $\eta_{ijk} = \mathbf{D}_{ijk}\phi_k - \phi_i$ that represents an interferometer which combines the local beam with a beam that has traveled from spacecraft k over j to i. We construct it from the single-link intermediary variables defined in eq. (3.122).

$$\hat{\bar{\eta}}_{ijk} = \hat{\bar{\eta}}_{ij} + \hat{\bar{\mathcal{D}}}_{ij}\hat{\bar{\eta}}_{jk} \tag{3.123}$$

$$= \mathbf{S}\eta_{ijk} - [\mathbf{S}, \mathbf{D}^o_{ijk}]p_k + \delta\eta^{[\mathbf{S},\mathbf{D}]}_{ijk} + \delta\eta^{\hat{\mathcal{D}}}_{ijk} \tag{3.124}$$

Again, we collect residuals related to fundamental laser noise residual in the first two terms and the remaining ones in the last two terms.

Finally, we build the second generation Michelson variable X_2 via several intermediary variables to save up on computational cost. This is possible as X_2 possesses a high degree of symmetry as it is composed of two beams taking several round-trips of increasing complexity. Results for Y_2 and Z_2 can be obtained by circular permutation of the indices. We have

$$\hat{\bar{\eta}}_{iji} = \hat{\bar{\eta}}_{ij} + \hat{\bar{\mathcal{D}}}_{ij}\hat{\bar{\eta}}_{ji} \tag{3.125a}$$

$$\hat{\bar{\eta}}_{ijiki} = \hat{\bar{\eta}}_{iji} + \hat{\bar{\mathcal{D}}}_{iji}\hat{\bar{\eta}}_{iki} \tag{3.125b}$$

$$\hat{\bar{\eta}}_{ijikikiji} = \hat{\bar{\eta}}_{ijiki} + \hat{\bar{\mathcal{D}}}_{ijiki}\hat{\bar{\eta}}_{ikiji} \tag{3.125c}$$

$$\hat{\bar{X}}_2 = \hat{\bar{\eta}}_{131212131} - \hat{\bar{\eta}}_{121313121} \tag{3.125d}$$

We apply the rule given in eq. (3.124) repeatedly and find

$$\hat{\bar{X}}_2 = \mathbf{S}X_2 - \big[\mathbf{S}, [\mathbf{D}^o_{13121}, \mathbf{D}^o_{12131}]\big]p_1 + \delta X_2^{[\mathbf{S},\mathbf{D}]} + \delta X_2^{\hat{\mathcal{D}}}. \tag{3.126}$$

Let us first develop the terms that produce the fundamental laser noise residual and out-of-band drifts due to time-varying delays. Therefore, we expand the decimated Michelson variable X_2. Here we need to specify the time reference frame all measurements and delay operators are naturally given in, the spacecraft on-board time $\hat{\tau}_i$.

$$\mathbf{S}X_2^{\hat{\tau}_1} = \mathbf{S}[\mathbf{D}^{\hat{\tau}_1}_{13121}, \mathbf{D}^{\hat{\tau}_1}_{12131}]\phi_1^{\hat{\tau}_1} \tag{3.127}$$

$$= \mathbf{S}\mathbf{T}^{\hat{\tau}_1}_{\tau_1}[\mathbf{D}^{\tau_1}_{13121}, \mathbf{D}^{\tau_1}_{12131}]\phi_1^{\tau_1} \tag{3.128}$$

$$= \mathbf{S}\mathbf{T}^{\hat{\tau}_1,o}_{\tau_1}\big([\mathbf{D}^{\tau_1}_{13121}, \mathbf{D}^{\tau_1}_{12131}]\phi_1^{\tau_1,o} + [\mathbf{D}^{\tau_1}_{13121}, \mathbf{D}^{\tau_1}_{12131}]p_1^{\tau_1}\big) \tag{3.129}$$

$$= \mathbf{T}^{\hat{\tau}_1,o}_{\tau_1}[\mathbf{D}^{\tau_1}_{13121}, \mathbf{D}^{\tau_1}_{12131}]\phi_1^{\tau_1,o} + \mathbf{S}[\mathbf{D}^{\hat{\tau}_1,o}_{13121}, \mathbf{D}^{\hat{\tau}_1,o}_{12131}]p_1^{\hat{\tau}_1} \tag{3.130}$$

In the second line we transform the commutator into the proper time of spacecraft 1. Then, the laser phase $\phi_1^{\tau_1,o}$ now given with respect to its proper time is free of clock noise. Therefore,

we can split it up into slow drifts $\phi_1^{\tau_1,o}$ and in-band laser noise $p_1^{\tau_1}$. Furthermore, all time-shift operators can be reduced to their out-of-band version as they are applied to small quantities, such that the coupling of the in-band component is negligible. Here, the delay operator $\mathbf{D}_{ij}^{\tau_i}$ accounting for the proper pseudo-range is naturally free of in-band components since we neglect the effect of GW signals. Let us now combine the decimated and the second-order commutator in eq. (3.126).

$$\mathbf{S}X_2^{\hat{\tau}_1} - \left[\mathbf{S}, [\mathbf{D}_{13121}^{\hat{\tau}_1,o}, \mathbf{D}_{12131}^{\hat{\tau}_1,o}]\right] p_1^{\hat{\tau}_1} = \underbrace{\mathbf{T}_{\tau_1}^{\hat{\tau}_1,o}[\mathbf{D}_{13121}^{\tau_1}, \mathbf{D}_{12131}^{\tau_1}]\phi_1^{\tau_1,o}}_{X_2^o} + \underbrace{[\mathbf{D}_{13121}^{\hat{\tau}_1,o}, \mathbf{D}_{12131}^{\hat{\tau}_1,o}]\mathbf{S}p_1^{\hat{\tau}_1}}_{\delta X_2} \tag{3.131}$$

We obtain two terms. The first one collects the out-of-band drifts of the TDI combination and the second one represents the fundamental laser noise residual due to arm length mismatch. With this, we summarize the contents of $\hat{\tilde{X}}_2$ as

$$\hat{\tilde{X}}_2 = X_2^o + \delta X_2 + \delta X_2^{[\mathbf{S},\mathbf{D}]} + \delta X_2^{\hat{\mathcal{D}}}. \tag{3.132}$$

The remaining terms are discussed in the respective section. We collect the laser noise residual due to on-board processing $\delta X_2^{[\mathbf{S},\mathbf{D}]}$ and TDI residuals that we further distinguish as interpolation residuals $\delta X_2^{\mathcal{D}}$, bias residuals δX_2^{B} and modulation noise residuals δX_2^{M}.

$$\delta X_2^{\hat{\mathcal{D}}} = \delta X_2^{\mathcal{D}} + \delta X_2^{B} + \delta X_2^{M} \tag{3.133}$$

We verify the models developed above by running numerical simulations using the LISA Instrument simulator. This simulator generates the LISA interferometric measurements (see chapter 2) in units of total frequency for the reasons discussed in section 3.2.5. To obtain the most realistic LISA setup but at the same time observe the residuals we include only laser and clock related effects. We choose six laser sources locked to a cavity such that they are independent and have the same level of laser frequency noise

$$\sqrt{S_{\dot{p}}(f)} = 30\,\mathrm{Hz}/\sqrt{\mathrm{Hz}}. \tag{3.134}$$

The central frequency of each laser is offset from the nominal value $\nu_0 = 281.6\,\mathrm{THz}$ by a constant amount of a few megahertz to obtain valid absolute beatnote frequencies in range from 5 MHz to 25 MHz. As the baseline mission design of LISA foresees locked lasers, we discuss the impact of laser locking later.

For the clocks we consider the most complete model available in the simulator. Their deviations from the nominal frequency is described in terms of a fractional frequency shift $y(t)$. It includes a random jitter component represented by a flicker noise with an ASD of

$$\sqrt{S_{\dot{q}}(f)} = 6.32 \times 10^{-14}\,\sqrt{\mathrm{Hz}} \cdot \left(\frac{f}{\mathrm{Hz}}\right)^{-\frac{1}{2}}, \tag{3.135}$$

and an out-of-band drift that is modeled by a second order polynomial

$$y_{0,i} + y_{1,i} \cdot t + y_{2,i} \cdot t^2. \tag{3.136}$$

We summarize the individual numerical values of $y_{n,i}$ in table 3.1. As described in section 2.1.1 the spacecraft timer is derived by integrating the fractional clock frequency. If we assume synchronized timers at launch and a transfer time of 400 d we find that the timers will be desynchronized by a few seconds. Therefore, we consider initial timer offsets $\delta\hat{\tau}_{0,i}$ in the simulation.

Prior to any processing we convert the data type of each simulation output from a double precision float (64 bit) to an extended precision float (equivalent to 80 bit for the machine used in this study). This measure avoids adding numerical noise that potentially limits the result

	$\delta\hat{\tau}_{0,i}$ (s)	$y_{0,i}$ (s s^{-1})	$y_{1,i}$ (s^{-1})	$y_{2,i}$ (s^{-2})
clock 1	-	5×10^{-8}	1.6×10^{-15}	9×10^{-24}
clock 2	-	6.25×10^{-7}	2×10^{-14}	6.75×10^{-23}
clock 3	-	-3.75×10^{-7}	-1.2×10^{-14}	-1.125×10^{-22}

Table 3.1: Summary of the numerical values used in the LISA Instrument simulator for the initial timer offsets $\delta\hat{\tau}_i$ and the polynomial coefficients $y_{n,i}$ that parameterize the out-of-band fractional clock frequency deviations defined in eq. (2.11).

when operating on the megahertz-beatnotes in TDI. We then process the simulation output in two steps. First, we combine the sideband beatnotes and the PRN ranges to form a high accuracy, high precision estimate of the measured pseudo-ranges. Then, we use the Python package PyTDI (Staab et al., 2023a) to evaluate the second generation Michelson variable X_2. Ultimately, to check the validity of the derived models and the level of residual laser noise we evaluate the ASDs.

Let us define a nominal configuration of the secondary instrumental noises, the on-board processing and the implementation of TDI. The goal of the nominal configuration is to well suppress any laser noise residuals. To analyze the individual residual laser noise contributions we change certain parameters in the simulation and processing chain. The nominal on-board processing consists of a strong anti-aliasing filter and decimation from 16 Hz to 4 Hz. To account for the flexing-filtering effect the filter is very flat in the pass-band. More details on the filter can be found in appendix C. Furthermore, ranging biases are set to zero and modulation noise that acts as ranging noise in TDI is turned off. For the interpolation method used in TDI we use high order Lagrange interpolation ($N = 62$) which leaves negligible interpolation error in-band.

In the following sections we discuss the individual residual laser and timing noise contributions. Each experiment modifies some relevant parameters in the simulation and processing. We will discuss those and demonstrate that we can relax the nominal configuration to use less stringent filter and interpolation kernel design and allow for ranging errors. We compare the resulting PSDs to the microcycle-requirement which is propagated through TDI and reads

$$S^{\mathrm{req}}_{\delta X_2}(f) = 64 \cdot \sin^2(2\pi f \bar{d}) \sin^2(4\pi f \bar{d}) \cdot S^{\mathrm{req}}_{\delta\phi}(f), \tag{3.137}$$

where $\bar{d}$ represents an average arm length over all arms. The additional factor of four accounts for the number of inter-spacecraft interferometers involved in the Michelson combination.

For brevity we omit specifying the time reference frame of physical quantities and delay operators and implicitly assume that they are given in the spacecraft on-board time and $\mathbf{D}_{ij}$ denotes the delay by the out-of-band component of the measured pseud-range $d_{ij}^{\hat{\tau}_i}$. Furthermore, for the coupling of laser noise residuals we assume constant arms in the models for simplifying the expressions and enabling us to express their PSDs (which requires stationary processes).

Onboard processing residual

Let us first discuss the laser noise residuals in X_2 that are caused by the non-commutativity of the decimation stage and the propagation delay. To "turn on" this residual we modify the nominal configuration defined above by introducing a more relaxed anti-aliasing filter. We use the optimized design for frequency units described in appendix C.

As the optimized anti-aliasing filter design amplifies the flexing-filtering coupling, we also include a compensation filter that we design similarly to the procedure outlined in section 3.3.1. For comparison we process two sets of data; with and without the compensation filter.

The laser noise residual in X_2 due to a general decimation stage $\mathbf{S}$ is given as

$$\begin{aligned}\delta X_2^{[\mathbf{S},\mathbf{D}]} = &-(1-\mathbf{D}_{131})(1-\mathbf{D}_{12131})\Big([\mathbf{S},\mathbf{D}_{12}]p_{21}+\mathbf{D}_{12}[\mathbf{S},\mathbf{D}_{21}]p_{12}\Big)\\ &+(1-\mathbf{D}_{121})(1-\mathbf{D}_{12131})\Big([\mathbf{S},\mathbf{D}_{13}]p_{31}+\mathbf{D}_{13}[\mathbf{S},\mathbf{D}_{31}]p_{13}\Big).\end{aligned} \tag{3.138}$$

We substitute $\mathbf{S}$ by $\mathbf{S}_{4\downarrow}\mathbf{F}$ for the simple decimation stage and by $\mathbf{F}^{+}\mathbf{S}_{4\downarrow}\mathbf{F}$ for the decimation stage including the compensation filter. Furthermore, we split up the contributions coming from the flexing-filtering coupling and aliasing an find the following analytical models for their PSDs

$$\begin{aligned}S_{\delta X_2}^{\mathbf{S}_{4\downarrow}[\mathbf{F},\mathbf{D}^o]}(f) = 16\sin^2(\pi f d_{12131})\Big(&\sin^2(\pi f d_{131})\big(S_{\delta\phi_{21}}^{\mathbf{S}_{4\downarrow}[\mathbf{F},\mathbf{D}_{12}^o]}(f)+S_{\delta\phi_{12}}^{\mathbf{S}_{4\downarrow}[\mathbf{F},\mathbf{D}_{21}^o]}(f)\big)\\ &+\sin^2(\pi f d_{121})\big(S_{\delta\phi_{31}}^{\mathbf{S}_{4\downarrow}[\mathbf{F},\mathbf{D}_{13}^o]}(f)+S_{\delta\phi_{13}}^{\mathbf{S}_{4\downarrow}[\mathbf{F},\mathbf{D}_{31}^o]}(f)\big)\Big)\end{aligned} \tag{3.139}$$

$$\begin{aligned}S_{\delta X_2}^{[\mathbf{S}_{4\downarrow},\mathbf{D}^o]\mathbf{F}}(f) = 16\sin^2(\pi f d_{12131})\Big(&\sin^2(\pi f d_{131})\big(S_{\delta\phi_{21}}^{[\mathbf{S}_{4\downarrow},\mathbf{D}_{12}^o]\mathbf{F}}(f)+S_{\delta\phi_{12}}^{[\mathbf{S}_{4\downarrow},\mathbf{D}_{21}^o]\mathbf{F}}(f)\big)\\ &+\sin^2(\pi f d_{121})\big(S_{\delta\phi_{31}}^{[\mathbf{S}_{4\downarrow},\mathbf{D}_{13}^o]\mathbf{F}}(f)+S_{\delta\phi_{13}}^{[\mathbf{S}_{4\downarrow},\mathbf{D}_{31}^o]\mathbf{F}}(f)\big)\Big)\end{aligned} \tag{3.140}$$

where the individual contributions of each laser is given by

$$S_{\delta\phi_{ji}}^{\mathbf{S}_{4\downarrow}[\mathbf{F},\mathbf{D}_{ij}^o]}(f) = \tilde{\mathbf{S}}_{4\downarrow}\left(\left|\frac{\dot{d}_{ij}^o}{2\pi}\frac{\mathrm{d}\tilde{h}_{\mathbf{F}}(f)}{\mathrm{d}f}\right|^2 S_{\dot{p}}(f)\right) \tag{3.141}$$

$$S_{\delta\phi_{ji}}^{[\mathbf{S}_{4\downarrow},\mathbf{D}_{ij}^o]\mathbf{F}}(f) = \mathrm{rect}\left(\frac{f}{f_s}\right)\sum_{n=1}^{M-1} 4\cdot c_n(\bar{d}_{ij}^o)\cdot\big(\tilde{\mathbf{F}}S_p(f)\big)^{(n)}(f) \tag{3.142}$$

To reproduce models including the compensation filter each occurrence of $\mathbf{F}$ has to be replaced by $\mathring{\mathbf{F}}^{+}\mathbf{F}$ (and $\tilde{h}_{\mathbf{F}}(f)$ must be replaced by $\tilde{h}_{\mathring{\mathbf{F}}^{+}}(f)\cdot\tilde{h}_{\mathbf{F}}(f)$) in the expressions above.

As the simulations are performed in units of frequency we have to slightly modify the PSD models. To transfer the models to frequency units it is not sufficient to multiply by a factor of $(2\pi f)^2$ as the decimation operation is non-linear and does not commute with the derivative. Therefore, we have to proceed more thoroughly and replace each occurrence of p_{ij} by $\dot{p}_{ij}$. The effect of this is that all PSDs of laser noise $S_p(f)$ (or $S_{\dot{p}}(f)$) collect an additional $(2\pi f)^2$ factor in the expressions above.

Next, we compare the analytical models to numerical simulations. In fig. 3.11 we show the results for the Michelson combination X_2 computed with (blue) and without (red) the compensation filter. The analytical models match well and demonstrate that indeed the compensation is required for this particular filter design to not violate the microcycle-requirement. When applying the compensation filter the flexing-filtering effect is reduced below the residual due to aliasing. Between $10^{-4}\,\mathrm{Hz}$ and $10^{-2}\,\mathrm{Hz}$ the numerical residual is dominated by numerical noise in the simulation. We verify this by running a noise-free simulation that only includes the megahertz-offsets of the beatnotes and the deterministic clock drifts. The result is shown in light grey and determines the numerical noise floor of any simulation.

Interpolation residual

The interpolation residual stems from the deviation of the interpolation kernel's transfer function from an ideal time-shift. We implement an interpolation method that uses a 28-coefficient kernel which is based off of an FIR type II low-pass filter design (for more details see appendix D). Otherwise, we adopt the nominal simulation and data processing setup.

The coupling of interpolation errors to the TDI variables is dependent on the particular implementation of the algorithm. Nested delays can be realized either by successively applying fractional delay filters $\mathcal{D}_{ij}\mathcal{D}_{jk}$ to a measurement or, alternatively, by shifting the measurement

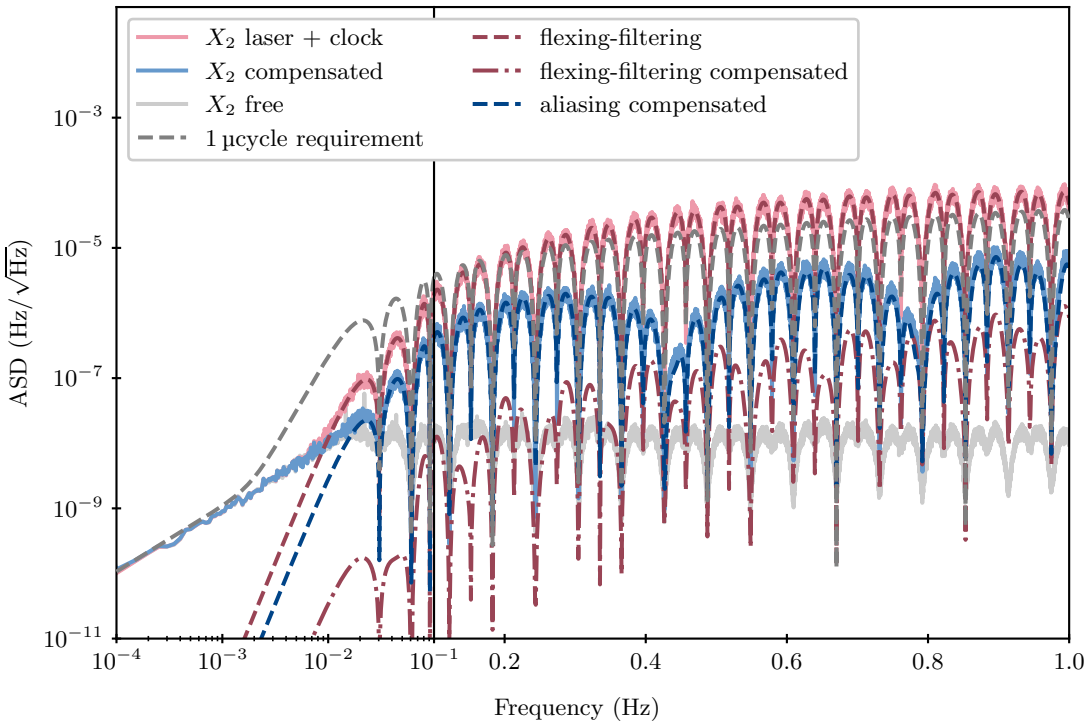

Figure 3.11: Commutator residuals due to on-board processing. The numerical results for the Michelson combination X_2 with and without compensation filter are shown in solid blue and solid red. We superimpose models for the flexing-filtering effect (dashed red and dotted red) and aliasing (dashed blue). Additionally, we plot the microcycle-requirement in dashed grey and the numerical noise floor of the simulation in leight grey.

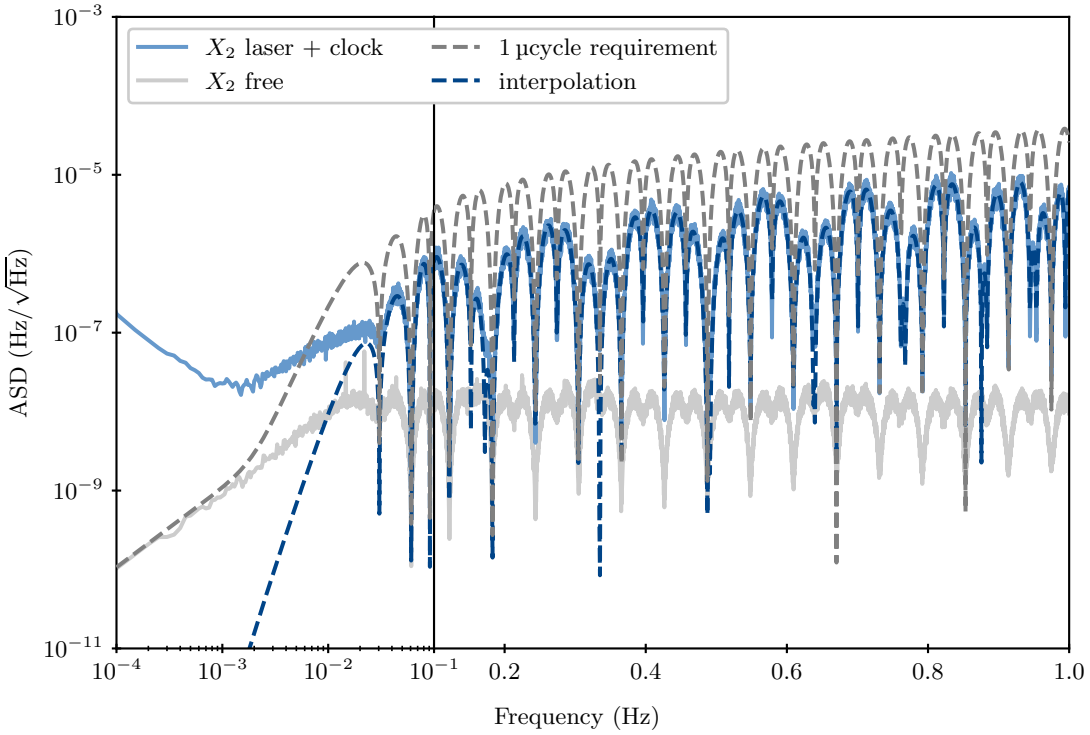

Figure 3.12: Interpolation residual in TDI. The solid blue line shows the numerical result using the FIR type II interpolation method which is well described by the model in dashed blue with the exception of the numerical noise floor arising at frequencies below 10^{-2} Hz.

in one go by using $\mathcal{D}_{ijk}$ that delays it by the effective delay $d_{ijk}(t) = d_{ij}(t) + d_{jk}\big(t - d_{ij}(t)\big)$. From a computational stand-point, collecting all delays in a single time-shift operation is often less expensive as delay operations can be factored such that they can be reused (e.g., $\mathbf{D}_{ijiki} = \mathbf{D}_{iji}\mathbf{D}_{iki}$ in eq. (3.125)). Whether atomic delay operations $\mathcal{D}_{ij}\mathcal{D}_{jk}$ or contracted ones $\mathcal{D}_{ijk}$ perform better depends on the numerical value of the delays. As a general rule, delaying time series by a small fractional delay is favorable as the interpolation error tends to zero for an integer time-shift.

To simplify the coupling and modeling of the residual we decide to use atomic delay operations for the evaluation of eq. (3.125) ($\hat{\mathcal{D}}_{ijk} \to \hat{\mathcal{D}}_{ij}\hat{\mathcal{D}}_{jk}$). Then, the interpolation residual appearing in eq. (3.132) is given as

$$\begin{aligned}\delta X_2^{\mathcal{D}} = (1 - \mathbf{D}_{131})(1 - \mathbf{D}_{12131})\big(\boldsymbol{\Delta}_{12}\bar{p}_{21} + \mathbf{D}_{12}\boldsymbol{\Delta}_{21}\bar{p}_{12}\big) \\ - (1 - \mathbf{D}_{121})(1 - \mathbf{D}_{12131})\big(\boldsymbol{\Delta}_{13}\bar{p}_{31} + \mathbf{D}_{13}\boldsymbol{\Delta}_{31}\bar{p}_{13}\big).\end{aligned} \tag{3.143}$$

Here, the bar on top of p_{ij} indicates laser frequency that was passed through the decimation stage $\mathbf{S}$. The PSD of this expressions reads

$$\begin{aligned}S_{\delta X_2}^{\mathcal{D}}(f) = 16\sin^2(\pi f d_{12131})\Big(\sin^2(\pi f d_{131})\big(\tilde{\boldsymbol{\Delta}}_{12} + \tilde{\boldsymbol{\Delta}}_{21}\big) \\ + \sin^2(\pi f d_{121})\big(\tilde{\boldsymbol{\Delta}}_{13} + \tilde{\boldsymbol{\Delta}}_{31}\big)\Big)\tilde{\mathbf{S}}S_p(f),\end{aligned} \tag{3.144}$$

with $\tilde{\boldsymbol{\Delta}}_{ij}$ as defined in eq. (3.114).

We show the results of the numerical simulation (solid blue) alongside with the analytical model (dashed blue) converted to frequency units in fig. 3.12. The model explains the residual well above 10^{-2} Hz. Below this frequency numerical effects take over which are not covered by the numerical noise floor of the simulation (light grey) but have another origin. At the time of

	B_{ij} (s)	a_{ij} (MHz)	b_{ij} (MHz)
MOSA 12	-1.1×10^{-8}	16.5	10.0
MOSA 23	1.5×10^{-8}	17.9	20.0
MOSA 31	1.6×10^{-8}	17.9	8.00
MOSA 13	-6.5×10^{-9}	-6.09	-10.0
MOSA 32	2.5×10^{-8}	-10.0	-8.00
MOSA 21	9.5×10^{-9}	-7.85	-20.0

Table 3.2: Overview of ranging biases B_{ij}, mean inter-spacecraft interferometer beatnote frequencies a_{ij} and mean reference interferometer beatnote frequencies b_{ij} for each MOSA.

writing, for the FIR type II interpolation method the kernel that is convolved with the data is only available in double precision (64 bit). Therefore, the result is limited by a white noise floor with an amplitude of approximately $3 \times 10^{-8}\,\mathrm{Hz}/\sqrt{\mathrm{Hz}}$. We estimate that the level scales with the number of coefficients in the interpolation kernel, that are all subject to numerical noise, and the megahertz-beatnote frequency. This additional noise floor can be mitigated by updating the interpolation kernel to extended precision. However, the calculation involves Numpy routines that are only available in double precision. In the future we will seek for suitable alternatives.

Ranging residuals

Lastly, we discuss the ranging residual that is caused by biases in the absolute ranging measurement and modulation noise in the sidebands. For studying this residual we add both effects to the simulation. The ranging biases are chosen randomly and their values are given in table 3.2. The level of modulation noise is assumed to be ten times higher in the right-handed MOSAs as compared to the left-handed ones. However, after ranging processing (see section 3.2.4) only left-handed modulation noise remains and we can model the ranging error per MOSA as

$$r_{ij}(t) = B_{ij} - \mathbf{D}_{ij} M_j(t) + M_i(t) \tag{3.145}$$

where we define $M_1 = M_{12}$, $M_2 = M_{23}$ and $M_3 = M_{31}$. The ASD of left-handed modulation noise has the usual level as given eq. (1.22).

Inserting eq. (3.145) into eq. (3.132) yields the following residuals due to the ranging bias and modulation noise, respectively.

$$\begin{aligned} \delta X_2^B = &-(1-\mathbf{D}_{131})(1-\mathbf{D}_{12131})\big(\mathbf{D}_{12}B_{12}\dot{\bar{p}}_{21} + \mathbf{D}_{121}B_{21}\dot{\bar{p}}_{12}\big) \\ &+ (1-\mathbf{D}_{121})(1-\mathbf{D}_{12131})\big(\mathbf{D}_{13}B_{13}\dot{\bar{p}}_{31} + \mathbf{D}_{131}B_{31}\dot{\bar{p}}_{13}\big) \end{aligned} \tag{3.146}$$

$$\begin{aligned} \delta X_2^M = &-(1-\mathbf{D}_{131})(1-\mathbf{D}_{12131})\big(a_{12}\bar{M}_1 + \mathbf{D}_{12}a_{21}\bar{M}_2\big) \\ &+ (1-\mathbf{D}_{121})(1-\mathbf{D}_{12131})\big(a_{13}\bar{M}_1 + \mathbf{D}_{13}a_{31}\bar{M}_3\big) \\ &+ (1-\mathbf{D}_{121})(1-\mathbf{D}_{131})(1-\mathbf{D}_{12131})b_1\bar{M}_1 \end{aligned} \tag{3.147}$$

The mean beatnote frequencies of the inter-spacecraft interferometer a_{ij} and the reference interferometer b_{ij}[12] appearing in the simulation are listed in table 3.2. Their values range between 5 MHz to 25 MHz and are relevant for the coupling of modulation noise. Again, the bar on top of laser frequency noise and modulation noise terms mark the decimation process applied to them.

[12] As reference interferometers are symmetric we use the short-hand notation $b_1 = b_{12} = -b_{21}$, $b_2 = b_{23} = -b_{32}$ and $b_3 = b_{31} = -b_{13}$.

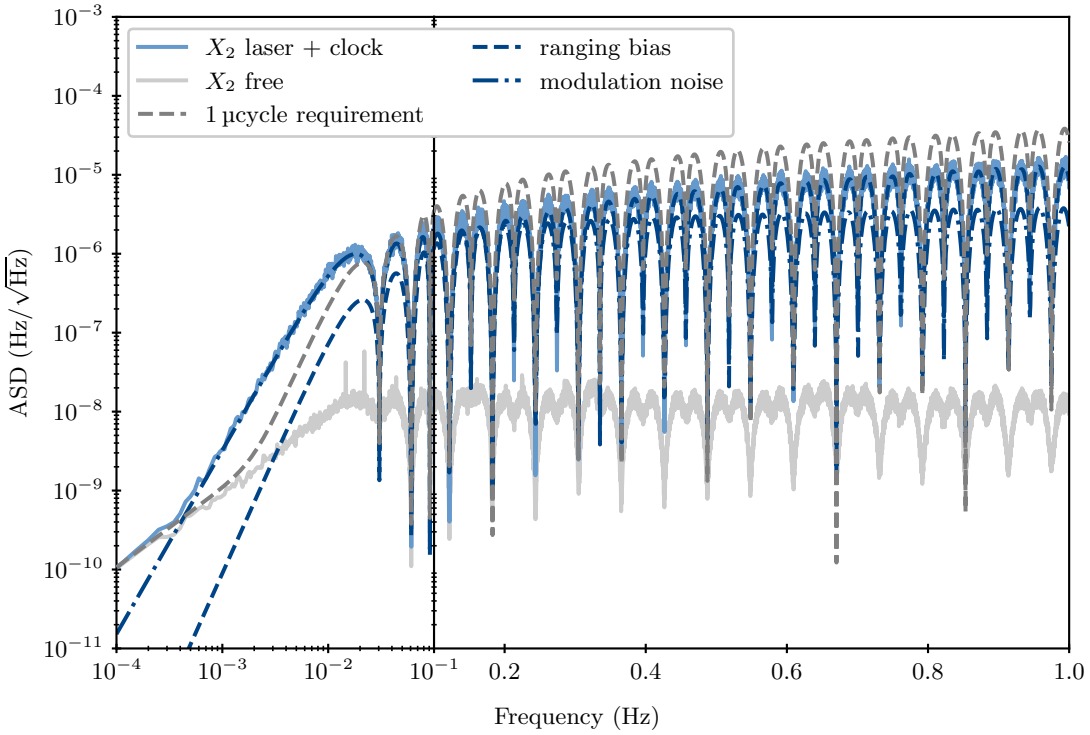

Figure 3.13: Laser and timing residuals due to ranging errors. The solid blue line represents the ASD of the simulated data including ranging biases and modulation noise. We model both effects in dashed blue and dashed-dotted blue, respectively.

The PSDs of the residuals are given by

$$\begin{aligned} S^{B}_{\delta X_2}(f) = 16\sin^2(\pi f d_{12131})\Big(&\sin^2(\pi f d_{131})\big(B^2_{12}+B^2_{21}\big) \\ &+\sin^2(\pi f d_{121})\big(B^2_{13}+B^2_{31}\big)\Big)(2\pi f)^2\tilde{\mathbf{S}}S_p(f), \end{aligned} \tag{3.148}$$

$$\begin{aligned} S^{M}_{\delta X_2}(f) = 16\sin^2(\pi f d_{12131})\Big(&\sin^2(\pi f d_{131})a^2_{21}+\sin^2(\pi f d_{121})a^2_{31} \\ &+\Big|\big(1-e^{-2\pi i f d_{121}}\big)a_{13}-\big(1-e^{-2\pi i f d_{131}}\big)a_{12} \\ &+\big(1-e^{-2\pi i f d_{121}}\big)\big(1-e^{-2\pi i f d_{131}}\big)b_1\Big|^2\Big)\tilde{\mathbf{S}}S_M(f). \end{aligned} \tag{3.149}$$

They agree with the expressions given in the literature assuming equal arms (Hartwig et al., 2022; Staab et al., 2023b). To properly account for the fact that the decimation stage is applied to data in frequency units we need to replace each occurrence of $S_p(f)$ and $S_M(f)$ by $S_{\dot{p}}(f)$ and $S_{\dot{M}}(f)$, respectively.

As before we compare the models to numerical simulations. In fig. 3.13 we show the results of the simulation (solid blue) superimposed with the models for the coupling of laser noise to the ranging bias (dashed blue) and modulation noise coupling to the beatnote frequencies (dashed dotted blue). We see that the models explain the excess noise very well (apart from frequencies below 4×10^{-4} Hz where the numerical noise floor dominates). Furthermore, we note that the microcycle-requirement is violated by the modulation noise coupling at low frequencies. As a consequence, the planning of the noise budget has to allocate more than the conservative $1\,\mu\text{cycle}/\sqrt{\text{Hz}}$ to this particular source of noise.

3.3.4 Discussion

In this chapter we have demonstrated the performance of TDI for realistic LISA measurements. We show how the sideband beatnotes and PRN measurements can be combined to accurately determine a precise estimate of the measured pseudo-range. We then study the different coupling mechanisms of laser and timing jitter to the final TDI combination. We identify three main channels; the standard laser noise residual caused by an arm length mismatch, residuals due to on-board processing and residuals that arise during TDI.

To check the validity of the derived models we run numerical simulations. Prior to processing of the data we convert it two a higher precision data type (in our case an 80 bit long double). This is required as the computation of second generation TDI variables reproduces a transfer function that looks like a double derivative at low frequencies with a dependency of f^2. Evaluating the microcycle-requirement in frequency units propagated through TDI yields $10^{-10}\,\mathrm{Hz}/\sqrt{\mathrm{Hz}}$ which is 17 orders of magnitudes below the nominal values of the beatnote frequency and hence double-precision float is not sufficient. As the use of extended precision requires more computational resources we propose a similar treatment as in the simulation of the LISA data; decomposing the total frequency into slow varying offsets and small in-band fluctuations. As a result, the variable with the fluctuations has a reduced dynamic range as it is dominated by laser frequency noise at levels of hundreds of $\mathrm{Hz}/\sqrt{\mathrm{Hz}}$. This would allow us to return back to double-precision which is supported more widely in today's CPU architectures.

The fundamental laser noise residual due the arm length mismatch dictates the choice of the generation of TDI combinations. In this chapter, we only discuss combinations up to the $\dot{L}$ closed property as this reduces the fundamental laser noise residual sufficiently for LISA. However, in theory, there is no limit to the "closureness" of virtual interferometers. The third generation of TDI combinations would cancel laser noise up to second order in the inter-spacecraft velocities, and up to first order in accelerations. The study of higher generation combinations might be relevant for future LISA-like missions that are challenged with more constraining requirements, higher level of laser noise or more dynamic relative motion of the stations.

The on-board design of the decimation process reducing the sampling rate of the interferometric data from 80 MHz to 4 Hz induce laser noise residuals due to non-flatness of the overall filter response of the decimation stages and the aliasing effect. We demonstrate the ability of compensation filters to lift the pass-band droop and make the in-band response sufficiently unity. This results in a reduction of the flexing-filtering effect. The compensation filters can run on ground to relax the computational requirement on board. On the other hand, the aliasing effect must be dealt with already on the spacecraft as it is irreducible after the fact. To keep residuals below the microcycle-requirement we suggest an appropriate FIR filter design for the last stage of the decimation process; decimating the sampling rate from 16 Hz to 4 Hz. We show that a filter with 29 coefficients suppresses the aliasing effect sufficiently which reduces the number of coefficients by a factor of five compared to previous filter designs which are currently used as the default in the LISA simulators.

The last category of laser noise residuals are introduced in TDI processing. The TDI algorithm relies on the implementation of discrete fractional delay filters and estimates of the inter-spacecraft ranges. To interpolate the data in between samples we design an appropriate interpolation kernel that uses a minimum set of coefficients. With that we reduce the computational cost[13] and the number of samples that need to be truncated where the filter kernel does not fully overlap with the data. As the computation of the filter kernel has to be repeated for every value of the time-shift we propose to evaluate it on a grid beforehand for selected fractional shifts. The grid has to be dense enough to interpolate linearly between them. This look-up table can then be used for computing interpolation kernels for arbitrary fractional shifts.

[13] Reducing the computational cost for on ground processing might be beneficial for the early alert pipeline. However, we generally expect TDI not to be the computational bottleneck of the processing chain.

Furthermore, errors in the ranges estimated from the PRN ranges and the sideband-sideband beatnotes introduce laser and timing jitter residuals in the final TDI combination. The former couples to slowly evolving biases in the ranging estimates which have to be below a couple of meters. The limiting in-band noise of the ranges is given by modulation noise that enters in the frequency distribution and modulation chain of the sidebands. We demonstrate that modulation noise couples to the megahertz beatnote frequencies and surpasses the microcycle-requirement at low frequencies. Therefore, this has to be appropriately reflected in the instrument noise budget.

As opposed to secondary noises the transfer function of laser noise residuals in TDI is dependent on laser locking (Nam et al., 2022; Staab et al., 2023b). Intuitively, this makes sense as laser locking introduces strong correlations among the six laser sources. This needs to be considered in the conclusions drawn above. However, Staab et al. (2023b) find that laser locking changes the overall transfer function only slightly. We suggest a follow-on study that evaluates a worst case over all locking configurations (Heinzel, 2018) under consideration for LISA.

Chapter 4

Time-delay Interferometric Ranging

Time-delay interferometric ranging (TDI-R) is a method to determine the propagation delays in LISA from the carrier-carrier beatnotes. It was first discussed in the literature by Tinto et al. (2005) and tested experimentally by Mitryk et al. (2012) in a table-top experiment as well as proposed for the GRACE-FO mission (Francis et al., 2015). The basic concept behind TDI-R is that TDI combinations are rather sensitive to ranging errors. As a consequence, if slightly wrong estimates of the ranges are used, the power in the TDI combinations will increase. In TDI-R we seek those ranges that minimize the residual laser noise power in the TDI combinations. The classical TDI-R estimator that was introduced by Tinto et al. (2005) reads

$$\hat{\boldsymbol{\theta}}_{\mathrm{LS}} = \arg\min_{\hat{\boldsymbol{\theta}}} \frac{1}{T} \int_0^T \left| X(t \,|\, \hat{\boldsymbol{\theta}}) \right|^2 \mathrm{d}t. \tag{4.1}$$

Here, the parameter vector $\boldsymbol{\theta}$ contains the delays d_{12}, d_{21}, d_{13} and d_{31} as the Michelson combination X only depends on the arms adjacent to the central spacecraft. The integral on the right-hand side of the expression calculates the power of the combination. The arg min-function finds the delays that minimize the power. The index LS stands for "least squares".

This heuristic approach to estimate the delays can be easily extended to all six arms including Y and Z in the calculation of the power. Analogously, any other set of TDI combinations can be used, e.g., the orthogonal set of A, E and T (Page and Littenberg, 2021). It has been shown that for an "optimal" TDI-R estimator the secondary noise in the TDI combinations has to be "whitened" (and "de-correlated") before calculating their power (Baghi et al., 2021b). In this chapter, we conduct a thorough analysis of the stated problem; how to optimally estimate the propagation delays required for TDI from the carrier-carrier beatnotes. We give analytical estimates of the lower bound on the estimation variance using the Fisher information matrix formalism.

4.1 Mathematical Foundation

The aim of this section is to derive from first principals an optimal estimator of the inter-satellite ranges appearing in the definition of the inter-spacecraft interferometer. We start by formulating the likelihood function of the available data streams and then study the Fisher information matrix (FIM) in the limit of dominant laser frequency noise.

4.1.1 Basics of statistical inference

In probability theory a random variable X describes the results of an experiment with an uncertain outcome. *Before* conducting the experiment one can only describe the probability of a particular result. As an example we consider the toss of a coin. We know that the outcome of this experiment is either heads or tails with a probability of 0.5. After repeating the experiment

ten times we yield seven times heads and three times tails. How can we be sure that it was a fair coin with equal probability for both, heads and tails? What is the significance of the result? And what might be the most probable probability for heads and tails?

Those questions are the concern of the theory of statistical inference which makes certain statements about the outcome of an experiment *after* it was performed. To do this we have to choose a sampling distribution that describes the joint probability distribution of the observations. In the example above we assume that each coin toss can be regarded as a Bernoulli experiment repeated $n = 10$ times. The probability to observe k times heads is given by the binomial distribution. It is given by

$$f(k \,|\, p, n) = \binom{n}{k} p^k (1-p)^{n-k}, \tag{4.2}$$

where the parameter p denotes the probability to toss heads.

A reasonable question to ask after observing $k = 7$ is: What if the coin is biased ($p \neq 0.5$)? What is the most probable value of the probability p? Evaluating the sampling distribution given in eq. (4.2) for the outcome of the experiment yields the *likelihood function* $\mathcal{L}(p)$. It is a function of the parameter p and allows one to test different values. The value p that maximizes the likelihood is called *maximum likelihood estimate*. It is defined as

$$\hat{p}_{\mathrm{MLE}} = \arg\max_{\hat{p}} \mathcal{L}(\hat{p}). \tag{4.3}$$

Here, we have introduced the hat-notation that indicates that $\hat{p}$ is not the true value of p but just an estimate. If we evaluate the maximum likelihood estimator by demanding $\frac{\mathrm{d}\mathcal{L}(p)}{\mathrm{d}p} = 0$ we find that $\hat{p}_{\mathrm{MLE}} = \frac{k}{n}$ which is 0.7 in our case. This result might not be surprising at first but it relies strongly on the assumption we made before on the sampling distribution and the choice of the estimator.

Properties of estimators

Estimators are objects that infer a set of parameters $\boldsymbol{\theta}$ from measured data $\boldsymbol{d}$. They are themselves random variables with a probability density function $f(\hat{\boldsymbol{\theta}})$. The maximum likelihood estimator introduced above is just one example but in general there exists infinitely many estimators to do the job. However, only some will perform well with regards to some optimality criterion. To illustrate this point let us look at a classical example, the sample variance.

We intend to infer the variance σ^2 of an unknown distribution. Therefore, we draw a finite number of samples $(x_i)_{i=1}^N$ from this distribution and estimate the *sample variance*. Let us consider two estimators

$$\hat{\sigma}_1^2 = \frac{1}{N} \sum_{i=1} (x_i - \bar{x})^2 \tag{4.4a}$$

$$\hat{\sigma}_2^2 = \frac{1}{N-1} \sum_{i=1} (x_i - \bar{x})^2 \tag{4.4b}$$

Here, $\bar{x}$ denotes yet another estimator, in this case, for the *sample mean*. It is defined as $\bar{x} = 1/N \sum_{i=1}^N x_i$.

Which of the estimators for the sample variance given in eq. (4.4) performs better? In an attempt to answer this question let us take a look at their expected value and their variance (for reference see, e.g., Jenkins and Watts (1968)). For $\hat{\sigma}_1^2$ we find

$$\mathrm{E}\{\hat{\sigma}_1^2\} = \frac{N-1}{N} \sigma^2, \tag{4.5a}$$

$$\mathrm{Var}\{\hat{\sigma}_1^2\} = \frac{2(N-1)}{N^2} \sigma^4, \tag{4.5b}$$

and for $\hat{\sigma}_2^2$

$$\mathrm{E}\{\hat{\sigma}_2^2\} = \sigma^2, \tag{4.6a}$$

$$\mathrm{Var}\{\hat{\sigma}_2^2\} = \frac{2}{N-1}\sigma^4. \tag{4.6b}$$

As we see there is no definitive answer. Estimator $\hat{\sigma}_1^2$ has a lower variance which is a measure of the spread of its distribution. However, estimator $\hat{\sigma}_2^2$ is said to be unbiased as on average it will determine the true variance σ^2 of the distribution in question. Therefore, whether to use either of the estimators depends on the criteria one is interested in.

In summary, the two fundamental measures of the performance of an estimator $\hat{\boldsymbol{\theta}}$ is its bias $\mathrm{B}\{\hat{\boldsymbol{\theta}}\}$ and its variance $\mathrm{Var}\{\hat{\boldsymbol{\theta}}\}$ defined as

$$\mathrm{B}\{\hat{\boldsymbol{\theta}}\} = \mathrm{E}\{\hat{\boldsymbol{\theta}}\} - \boldsymbol{\theta} \tag{4.7}$$

$$\mathrm{Var}\{\hat{\boldsymbol{\theta}}\} = \mathrm{E}\{(\hat{\boldsymbol{\theta}} - \mathrm{E}\{\hat{\boldsymbol{\theta}}\})^2\} \tag{4.8}$$

The maximum likelihood estimator

In section 4.1.1 we have introduced the likelihood function $\mathcal{L}(\boldsymbol{\theta})$. It is equal to the probability to observe data $\boldsymbol{d}$ for given parameters $\boldsymbol{\theta}$.

$$\mathcal{L}(\boldsymbol{\theta}) = f(\boldsymbol{d}\,|\,\boldsymbol{\theta}) \tag{4.9}$$

The likelihood function should not be confused with the probability distribution of the parameters $\boldsymbol{\theta}$. The latter can be expressed using Bayes' theorem which assumes a prior distribution of the parameters that is informed by the likelihood function to yield the posterior distribution.

The *maximum likelihood estimator* is defined yield the parameters $\boldsymbol{\theta}$ that maximizes the likelihood function.

$$\hat{\boldsymbol{\theta}}_{\mathrm{MLE}} = \arg\max_{\hat{\boldsymbol{\theta}}} \mathcal{L}(\hat{\boldsymbol{\theta}}) \tag{4.10}$$

Similarly, it is sometimes more convenient to work with the *log-likelihood* that is defined as

$$l(\boldsymbol{\theta}) = \log(\mathcal{L}(\boldsymbol{\theta})). \tag{4.11}$$

Since the logarithm is a strictly increasing function maximizing the likelihood function is equivalent to maximizing the log-likelihood. Often the latter is easier to handle numerically as it has reduced dynamical range. Furthermore, the logarithm of normal likelihood functions becomes a quadratic form which is convenient to evaluate on a computer.

The maximum likelihood estimator has two properties that are very useful in our application. First, it is a *consistent* estimator. Consistency mean that increasing the sample size (i.e., integration time) will result in a more precise estimate without limit. Second, it is an *efficient* estimator. The variance of the maximum likelihood estimate approaches the Cramér-Rao lower bound in the limit of an infinite sample size. The Cramér-Rao lower bound is the lower bound for the variance of any unbiased estimator and is defined as the inverse of the Fisher information matrix with entries

$$I_{i,j}(\boldsymbol{\theta}) = -\,\mathrm{E}\left\{\frac{\partial^2 l(\boldsymbol{\theta})}{\partial\theta_i \partial\theta_j}\right\}. \tag{4.12}$$

For a multivariate estimator $\hat{\boldsymbol{\theta}}$ the Cramér-Rao bound on the covariance matrix Σ is expressed as the matrix inequality

$$\Sigma \geq \mathrm{I}(\boldsymbol{\theta})^{-1}, \tag{4.13}$$

which means that the difference of the left-hand side and right-hand side is a positive semidefinite matrix.

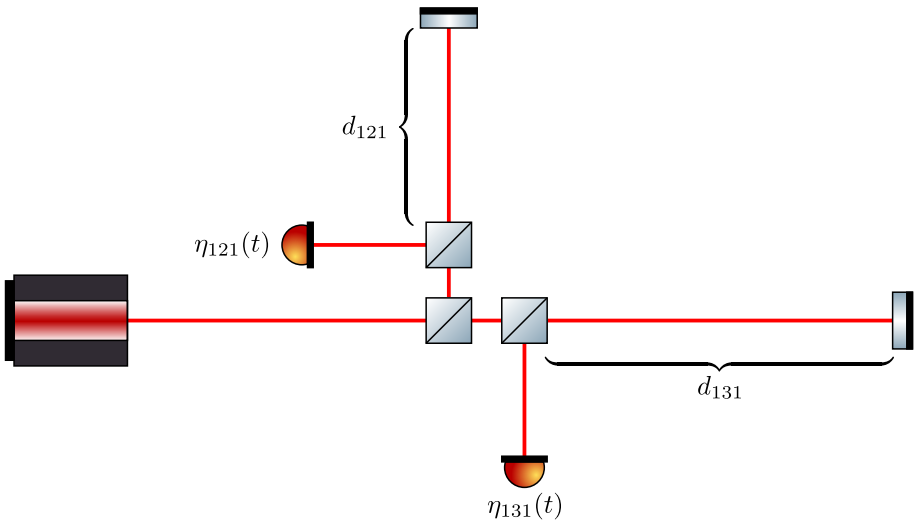

Figure 4.1: Toy model setup with two long-arm readouts $\eta_{121}(t)$ and $\eta_{131}(t)$ given in eq. (4.14). The round-trip delays are given by d_{121} and d_{131}.

In the following we use this formalism to statistically describe the LISA beatnote phases to extract the inter-satellite ranges. The beatnote phases contain large deterministic drifts and Gaussian distributed noise[1]. Therefore, we will start of by using a Gaussian likelihood function that represents the distribution of the data. Then, we use the Fisher information matrix formalism to find the lower bound on the delay estimates. In the last step, we verify our analytical findings numerically with simulations.

4.2 Toy Model

Let us start off by considering a simplified LISA setup to discuss the basic properties of the analysis. As a toy model we assume a static unequal-arm Michelson interferometer where both arms are read out separately. The setup is shown in fig. 4.1 and consists of a single laser source that is split at the central beam splitter. The beams pick up constant delays d_{121} and d_{131}, respectively, and recombine with an original copy at their corresponding beam splitter. Hence, the photodetector track the beatnote phases

$$\eta_{121}(t) = (\mathbf{D}_{121} - 1)p(t) + N^{\mathrm{ro}}_{121}(t), \tag{4.14a}$$
$$\eta_{131}(t) = (\mathbf{D}_{131} - 1)p(t) + N^{\mathrm{ro}}_{131}(t). \tag{4.14b}$$

Here, $N^{\mathrm{ro}}_{iji}(t)$ denotes the readout noise of the photodetectors and $p(t)$ the in-band laser frequency noise of the laser. The photodiodes detect a homodyne signal as the interfering beams are not subject to Doppler shifts and thus the terahertz optical laser frequency drops out. Furthermore, we intentionally make use of the LISA notations as indeed this setup can be reproduced by assuming a locking configuration where spacecraft 1 hosts the primary laser and spacecraft 2 and 3 act as transponders. Then the inter-spacecraft interferometers on spacecraft 1 effectively measure the beatnotes in eq. (4.14).

The goal of TDI-R is to estimate the round-trip delays encoded in those beatnotes. The traditional approach (Tinto et al., 2005) minimizes the residual power in the laser noise canceling

[1]This is a rather strong assumption which is found typically wrong in real-world experiments. Those usually comprise non-stationarities and glitches which violate the previous assumption.

TDI combination. For this setup it is given as

$$X(t) = (1 - \hat{\mathbf{D}}_{121})\eta_{131}(t) - (1 - \hat{\mathbf{D}}_{131})\eta_{121}(t) \tag{4.15}$$

$$\simeq (1 - \hat{\mathbf{D}}_{121})N^{\mathrm{ro}}_{131}(t) - (1 - \hat{\mathbf{D}}_{131})N^{\mathrm{ro}}_{121}(t). \tag{4.16}$$

Here, the hat on top of the delay operators indicates that we use estimates of the round-trip delays as the true values are not accessible. We formulate the traditional least-squares estimate as the parameter set $\hat{\boldsymbol{\theta}} = (\hat{d}_{121} \quad \hat{d}_{131})^{\mathrm{T}}$ that minimizes the power in the TDI combination $X(t)$.

$$\hat{\boldsymbol{\theta}}_{\mathrm{LS}} = \arg\min_{\hat{\boldsymbol{\theta}}} P(\hat{\boldsymbol{\theta}}) = \arg\min_{\hat{\boldsymbol{\theta}}} \frac{1}{T}\int_0^T \left|X(t\,|\,\hat{\boldsymbol{\theta}})\right|^2 \mathrm{d}t \tag{4.17}$$

As an alternative, we propose the maximum likelihood estimator

$$\hat{\boldsymbol{\theta}}_{\mathrm{MLE}} = \arg\max_{\hat{\boldsymbol{\theta}}} \mathcal{L}(\hat{\boldsymbol{\theta}}) = \arg\max_{\hat{\boldsymbol{\theta}}} f(\boldsymbol{d}\,|\,\hat{\boldsymbol{\theta}}), \tag{4.18}$$

where $\boldsymbol{d} = (\eta_{121} \quad \eta_{131})^{\mathrm{T}}$. Here, the challenge is to find a convenient parameterization of the data $\boldsymbol{d}$ to express its probability distribution $f(\boldsymbol{d}\,|\,\boldsymbol{\theta})$. Ultimately, from this we can derive the likelihood function $\mathcal{L}(\boldsymbol{\theta})$ to seek the Cramér-Rao lower bound on the covariance matrix of the estimates of any unbiased estimator.

4.2.1 The reduced likelihood function

The aim of this section is to derive the likelihood function for the toy model setup to compute the Cramér-Rao lower bound. In our analysis the data $\boldsymbol{d}$ is represented by a discretely sampled time-series of duration $T = NT_s$ where N is the number of samples and T_s the sampling time. As we assume zero-mean colored Gaussian noise the probability distribution of the measurements in eq. (4.14) is given by

$$f(\boldsymbol{d}\,|\,\boldsymbol{\theta}) = \frac{e^{-\frac{1}{2}\boldsymbol{\eta}^{\mathrm{T}}\Sigma^{-1}\boldsymbol{\eta}}}{\sqrt{(2\pi)^{MN}\det(\Sigma)}}. \tag{4.19}$$

The data vector has elements $\boldsymbol{\eta} = \big(\eta_{121}(t_0) \quad \eta_{131}(t_0) \quad \eta_{121}(t_1) \quad \ldots\big) \in \mathbb{R}^{M\cdot N}$. Here, M denotes the number of channels and is equal to two for the toy model. The covariance matrix $\Sigma \in \mathbb{R}^{M\cdot N\times M\cdot N}$ is quite a big matrix and numerically expensive to operate on.

Therefore, it is convenient to describe the data in the Fourier domain. In appendix E we derive the statistics of the Fourier coefficients of zero-mean Gaussian time series. More specifically, the calculations below hold for multivariate T-periodic time series in the limit $T \to \infty$. Conveniently, Fourier coefficients $\tilde{\boldsymbol{\eta}}_k$ are independent for different k and complex multivariate normal. Therefore, the joint distribution is given by the product of distributions of the individual components.

$$f(\boldsymbol{d}\,|\,\boldsymbol{\theta}) \simeq \prod_{k=1}^{K} f(\tilde{\boldsymbol{\eta}}_k\,|\,\boldsymbol{\theta}) = \prod_{k=1}^{K} \frac{e^{-\tilde{\boldsymbol{\eta}}_k^{\dagger}\Gamma_k^{-1}\tilde{\boldsymbol{\eta}}_k}}{\pi^M \det\Gamma_k} \tag{4.20}$$

Here, the dagger denotes the conjugate transpose. We use common Fourier transform rules to express the Fourier coefficients and find

$$\tilde{\boldsymbol{\eta}}_k = \underbrace{\begin{pmatrix} e^{-2\pi i k\Delta f d_{121}} - 1 \\ e^{-2\pi i k\Delta f d_{131}} - 1 \end{pmatrix}}_{\mathrm{M}_k} \tilde{p}_k + \tilde{\boldsymbol{n}}_k. \tag{4.21}$$

The delay operations in eq. (4.14) become multiplicative factors and such much easier to handle in further calculations. The scalar $\tilde{p}_k$ and vector $\tilde{\boldsymbol{n}}_k$ denote the Fourier coefficients of the laser

noise $p(t)$ and the readout noises $\boldsymbol{n}(t) = \begin{pmatrix} N^{\mathrm{ro}}_{121}(t) & N^{\mathrm{ro}}_{131}(t) \end{pmatrix}^{\mathrm{T}}$. Consequently, using eq. (4.21) we can express the covariance matrix Γ_k as

$$\Gamma_k = \mathrm{E}\{\tilde{\boldsymbol{\eta}}_k \tilde{\boldsymbol{\eta}}_k^\dagger\} = \mathrm{M}_k \underbrace{\mathrm{E}\{|\tilde{p}_k|^2\}}_{P_k} \mathrm{M}_k^\dagger + \underbrace{\mathrm{E}\{\tilde{\boldsymbol{n}}_k \tilde{\boldsymbol{n}}_k^\dagger\}}_{\mathrm{N}_k} \tag{4.22}$$

where we identify the variance of $\tilde{p}_k$ and the covariance matrix of $\tilde{\boldsymbol{n}}_k$ which are given by

$$P_k = \frac{S_p(k\Delta f)}{2T}, \tag{4.23}$$

$$\mathrm{N}_k = \frac{S_N^{\mathrm{ro}}(k\Delta f)}{2T} \begin{pmatrix} 1 & 0 \\ 0 & 1 \end{pmatrix}. \tag{4.24}$$

Here, we assume that the readout noises are uncorrelated such that N_k becomes diagonal.

Similar to eq. (4.20) the log-likelihood function of the data can be written as the sum of the individual log-likelihood functions $l_k(\boldsymbol{\theta})$ of the vector of k-th Fourier coefficients.

$$l(\boldsymbol{\theta}) = \sum_{k=1}^{K} l_k(\boldsymbol{\theta}) = \sum_{k=1}^{K} -\log(\pi^M \det \Gamma_k) - \tilde{\boldsymbol{\eta}}_k^\dagger \Gamma_k^{-1} \tilde{\boldsymbol{\eta}}_k \tag{4.25}$$

In the next step, we attempt to simplify this expression further by introducing the unitary transformation $\mathrm{U}_k^\dagger \tilde{\boldsymbol{\eta}}_k = \begin{pmatrix} \mathrm{E}_k & \mathrm{F}_k \end{pmatrix}^\dagger \tilde{\boldsymbol{\eta}}_k$ of the Fourier coefficients. The matrix E_k is chosen such that it spans the null space of $\mathrm{M}_k^\dagger$, i.e., the subspace $\mathrm{E}_k^\dagger \tilde{\boldsymbol{\eta}}_k$ represents laser noise free channels.

We insert U_k into $l_k(\boldsymbol{\theta})$ defined in eq. (4.25) and yield

$$l_k(\boldsymbol{\theta}) = -\log(\pi^M \det \Gamma_k) - \tilde{\boldsymbol{\eta}}_k^\dagger \underbrace{\mathrm{U}_k \mathrm{U}_k^\dagger}_{\mathbb{1}} \Gamma_k^{-1} \underbrace{\mathrm{U}_k \mathrm{U}_k^\dagger}_{\mathbb{1}} \tilde{\boldsymbol{\eta}}_k, \tag{4.26}$$

$$= -\log(\pi^M \det \Gamma) - (\mathrm{U}^\dagger \tilde{\boldsymbol{\eta}})^\dagger (\mathrm{U}^\dagger \Gamma \mathrm{U})^{-1} (\mathrm{U}^\dagger \tilde{\boldsymbol{\eta}}). \tag{4.27}$$

For better readability, we have dropped the subscript k. The last term in eq. (4.27) can be further expanded into four terms adopting the blocked definition of the matrix $\mathrm{U} = \begin{pmatrix} \mathrm{E} & \mathrm{F} \end{pmatrix}$[2]. The blocked entries of $(\mathrm{U}^\dagger \Gamma \mathrm{U})^{-1}$ are approximately given by

$$(\mathrm{U}^\dagger \Gamma \mathrm{U})^{-1} = \begin{pmatrix} \mathrm{E}^\dagger(\mathrm{MPM}^\dagger + \mathrm{N})\mathrm{E} & \mathrm{E}^\dagger(\mathrm{MPM}^\dagger + \mathrm{N})\mathrm{F} \\ \mathrm{F}^\dagger(\mathrm{MPM}^\dagger + \mathrm{N})\mathrm{E} & \mathrm{F}^\dagger(\mathrm{MPM}^\dagger + \mathrm{N})\mathrm{F} \end{pmatrix}^{-1} \tag{4.28}$$

$$= \begin{pmatrix} \mathrm{E}^\dagger \mathrm{NE} & \mathrm{E}^\dagger \mathrm{NF} \\ \mathrm{F}^\dagger \mathrm{NE} & \mathrm{F}^\dagger(\mathrm{MPM}^\dagger + \mathrm{N})\mathrm{F} \end{pmatrix}^{-1} \tag{4.29}$$

$$\approx \begin{pmatrix} \mathrm{E}^\dagger \mathrm{NE} & \mathrm{E}^\dagger \mathrm{NF} \\ \mathrm{F}^\dagger \mathrm{NE} & \mathrm{F}^\dagger \mathrm{MPM}^\dagger \mathrm{F} \end{pmatrix}^{-1} \tag{4.30}$$

$$\approx \begin{pmatrix} (\mathrm{E}^\dagger \mathrm{NE})^{-1} & -(\mathrm{E}^\dagger \mathrm{NE})^{-1} \mathrm{E}^\dagger \mathrm{NF} (\mathrm{F}^\dagger \mathrm{MPM}^\dagger \mathrm{F})^{-1} \\ -(\mathrm{F}^\dagger \mathrm{MPM}^\dagger \mathrm{F})^{-1} \mathrm{F}^\dagger \mathrm{NE} (\mathrm{E}^\dagger \mathrm{NE})^{-1} & (\mathrm{F}^\dagger \mathrm{MPM}^\dagger \mathrm{F})^{-1} \end{pmatrix} \tag{4.31}$$

Here, we make use of the inversion formula for block matrices and the fact that the laser noise PSD is dominating across the entire band such that $P \gg \mathrm{N}$. If we insert this into eq. (4.27) we find that out of the four terms only one is relevant for maximum likelihood estimation of the delay parameters as the remaining terms are only weakly dependent on those. Maximizing the log-likelihood with respect to the parameters is therefore approximately equivalent to only maximizing this single term. We write the maximum likelihood estimator as

$$\hat{\boldsymbol{\theta}}_{\mathrm{MLE}} = \arg\max_{\hat{\boldsymbol{\theta}}} l(\hat{\boldsymbol{\theta}}) \simeq \arg\max_{\hat{\boldsymbol{\theta}}} \bar{l}(\hat{\boldsymbol{\theta}}), \tag{4.32}$$

[2]Here, the matrix E should not be confused with the expectation value operator $\mathrm{E}\{\cdot\}$.

where $\bar{l}(\boldsymbol{\theta})$ is the reduced log-likelihood function defined as

$$\bar{l}(\boldsymbol{\theta}) = \sum_k \underbrace{-\tilde{\boldsymbol{\eta}}_k^\dagger \mathrm{E}_k (\mathrm{E}_k^\dagger \Gamma \mathrm{E}_k)^{-1} \mathrm{E}_k^\dagger \tilde{\boldsymbol{\eta}}_k}_{\bar{l}_k(\boldsymbol{\theta})} . \tag{4.33}$$

Similarly, in the definition of the Fisher information matrix (see eq. (4.12)) we can readily replace $l(\boldsymbol{\theta})$ by $\bar{l}(\boldsymbol{\theta})$ as parameter independent terms drop out after taking the derivatives. As the Fourier component are statistically independent we can calculate their Fisher information matrices individually and sum them up in the end. The Fisher information matrix for the k-th contribution is given by

$$I_{i,j}(f_k) = -\,\mathrm{E}\left\{\frac{\partial^2 l_k(\boldsymbol{\theta})}{\partial\theta_i \partial\theta_j}\right\} \simeq -\,\mathrm{E}\left\{\frac{\partial^2 \bar{l}_k(\boldsymbol{\theta})}{\partial\theta_i \partial\theta_j}\right\} \tag{4.34}$$

$$= \mathrm{E}\left\{\tilde{\boldsymbol{\eta}}_k^\dagger\, \partial_i \partial_j (\mathrm{E}_k (\mathrm{E}_k^\dagger \mathrm{N}_k \mathrm{E}_k)^{-1} \mathrm{E}_k^\dagger) \tilde{\boldsymbol{\eta}}_k\right\} \tag{4.35}$$

$$\simeq 2P_k\, \mathrm{Re}\left\{\,\mathrm{Tr}\{\mathrm{M}_k^\dagger (\partial_i \mathrm{E}_k)(\mathrm{E}_k^\dagger \mathrm{N}_k \mathrm{E}_k)^{-1} (\partial_j \mathrm{E}_k)^\dagger \mathrm{M}_k\}\right\}. \tag{4.36}$$

In the last line we use the identity $\mathrm{E}\{\tilde{\boldsymbol{x}}^\dagger \mathrm{A} \tilde{\boldsymbol{x}}\} = \mathrm{Tr}\{\Gamma \mathrm{A}\}$ where $\Gamma = \mathrm{E}\{\tilde{\boldsymbol{x}}\tilde{\boldsymbol{x}}^\dagger\}$ and again the limit $P_k \gg \mathrm{N}_k$. Furthermore, we can see that the columns of E_k do not have to be orthonormal as required for the unitary transform introduced above. To demonstrate this we can define $\mathrm{E}'_k = \mathrm{E}_k \mathrm{A}$ where A is full rank and mixes the orthonormal basis vectors to forms a new non-orthonormal but complete basis. If we plug this into eq. (4.36) we find that the transformation matrix A drops out and we have effectively substituted E_k with E'_k. Consequently, we redefine E_k requiring that its column vectors represent some basis of the null space of $\mathrm{M}_k^\dagger$.

For the toy model the null space has dimension one and we choose

$$\mathrm{E}_k = \begin{pmatrix} -1 + e^{2\pi f_k d_{131}} \\ 1 - e^{2\pi f_k d_{121}} \end{pmatrix}, \tag{4.37}$$

such that it coincides with the definition of the laser noise canceling TDI combination $X(t)$ in eq. (4.16).

In the next step we plug eq. (4.37) into eq. (4.36) and find

$$\mathrm{I}(f) = \frac{S_{\dot{p}}(f)}{S_N^{\mathrm{ro}}(f)} \begin{pmatrix} \frac{4\sin^2(\pi f d_{131})}{2-\cos(2\pi f d_{121})-\cos(2\pi f d_{131})} & -\frac{4\cos(\pi f \Delta d)\sin(\pi f d_{121})\sin(\pi f d_{131})}{2-\cos(2\pi f d_{121})-\cos(2\pi f d_{131})} \\ -\frac{4\cos(\pi f \Delta d)\sin(\pi f d_{121})\sin(\pi f d_{131})}{2-\cos(2\pi f d_{121})-\cos(2\pi f d_{131})} & \frac{4\sin^2(\pi f d_{121})}{2-\cos(2\pi f d_{121})-\cos(2\pi f d_{131})} \end{pmatrix}. \tag{4.38}$$

Interestingly, the information at frequency f is proportional to the "signal-to-noise" ratio $\frac{S_{\dot{p}}(f)}{S_N^{\mathrm{ro}}(f)}$. In this context, the signal is represented by laser noise. Conversely, TDI requires better knowledge of the delays for higher levels of laser noise. So increasing the laser noise power in the LISA band to improve the performance of TDI-R is self-defeating.

To derive the full Fisher information matrix over all Fourier components we take the discrete sum over the individual contributions. In the limit of long observation times T the sum can be approximated by an integral.

$$\mathrm{I} = \sum_{k=1}^{K} \mathrm{I}(f_k) \simeq T \int_0^\infty \mathrm{I}(f)\, \mathrm{d}f \tag{4.39}$$

We find that the information grows proportional with the "integration time" T.

In the special case of equal arms ($d_{121} = d_{131}$) the full Fisher information matrix becomes singular as we find

$$\mathrm{I} = T \int_0^\infty \frac{S_{\dot{p}}(f)}{S_N^{\mathrm{ro}}(f)}\, \mathrm{d}f \cdot \begin{pmatrix} 1 & -1 \\ -1 & 1 \end{pmatrix}, \tag{4.40}$$

which has a determinant of zero. Therefore, we reparameterize the parameter vector $\boldsymbol{\theta}$ to represent the sum Σd and difference Δd of the two round-trip delays.

$$\boldsymbol{\theta'} = \begin{pmatrix} \Sigma d \\ \Delta d \end{pmatrix} = \begin{pmatrix} d_{121} + d_{131} \\ d_{121} - d_{131} \end{pmatrix} = \underbrace{\begin{pmatrix} 1 & 1 \\ 1 & -1 \end{pmatrix}}_{\mathrm{V}} \boldsymbol{\theta}. \tag{4.41}$$

Indeed, the transformed Fisher information matrix of the parameters $\boldsymbol{\theta'}$ has only one non-zero entry, the Fisher information on the delay difference Δd.

$$\mathrm{I}' = \mathrm{V}^{-1}\mathrm{I}\mathrm{V}^{-\mathrm{T}} = T \int_0^\infty \frac{S_{\dot{p}}(f)}{S_N^{\mathrm{ro}}(f)}\,\mathrm{d}f \cdot \begin{pmatrix} 0 & 0 \\ 0 & 1 \end{pmatrix} \tag{4.42}$$

The interpretation of this is that for equal round-trip delays it is impossible to infer information on the sum of the delays Σd as the likelihood function is completely degenerate in this parameter. On the other hand, the difference can be estimated and we find the Cramér-Rao bound on the variance

$$\sigma^2_{\Delta d} \geq \frac{1}{T}\left(\int_0^\infty \frac{S_{\dot{p}}(f)}{S_N^{\mathrm{ro}}(f)}\,\mathrm{d}f\right)^{-1}. \tag{4.43}$$

In the next step, we verify our finding in this section by using numerical simulations.

4.2.2 Numerical simulations

Unfortunately, the reduced likelihood function in eq. (4.33) is not valid for short integration times T and non-periodic data. Therefore, we seek a better representation by formulating the reduced likelihood function in time-domain. As introduced in eq. (4.19) the time-domain representation makes use of the time-discrete nature of the data $\boldsymbol{\eta} = \begin{pmatrix} \eta_{121}(t_0) & \eta_{131}(t_0) & \eta_{121}(t_1) & \dots \end{pmatrix}^{\mathrm{T}} \in \mathbb{R}^{2N}$ with covariance matrix $\Sigma \in \mathbb{R}^{2N\times 2N}$. We can apply the same reasoning as in the previous section and project the measurements onto two subspaces, one laser noise dominated and the other laser noise free, both roughly of dimension N (cf. Vallisneri et al., 2021). We assume the following reduced likelihood function analogous to eq. (4.33)

$$\bar{l}(\boldsymbol{\theta}) = -\frac{1}{2}\boldsymbol{X}^{\mathrm{T}}\Sigma_X^{-1}\boldsymbol{X}. \tag{4.44}$$

Here, the vector of laser noise free TDI variables is defined as $\boldsymbol{X} = \begin{pmatrix} X(t_0) & X(t_1) & \dots \end{pmatrix}$ and Σ_X is its covariance matrix. The maximum likelihood estimator in time-domain is then given by

$$\hat{\boldsymbol{\theta}}_{\mathrm{MLE}} = \arg\max_{\hat{\boldsymbol{\theta}}} \bar{l}(\hat{\boldsymbol{\theta}}). \tag{4.45}$$

The (negative) cost function presented in eq. (4.44) is equivalent to a cost function used in weighted least-squares estimation. Here, the covariance matrix Σ_X accounts for correlations among the samples and weights them according to their noise variance.

To evaluate the reduced likelihood function we need to model the entries of the covariance matrix Σ_X. We assume independent and identically distributed readout noises in the two beatnote measurements and find

$$\begin{aligned}
\left(\Sigma_X\right)_{i,j} &= \mathrm{E}\{X(t_i)\cdot X(t_j)\} && (4.46)\\
&= \mathrm{E}\left\{(1-\mathbf{D}_{131})N^{\mathrm{ro}}_{121}(t)\Big|_{t=t_i}(1-\mathbf{D}_{131})N^{\mathrm{ro}}_{121}(t)\Big|_{t=t_j}\right\} \\
&\quad + \mathrm{E}\left\{(1-\mathbf{D}_{121})N^{\mathrm{ro}}_{131}(t)\Big|_{t=t_i}(1-\mathbf{D}_{121})N^{\mathrm{ro}}_{131}(t)\Big|_{t=t_j}\right\} && (4.47)\\
&= 2R^{\mathrm{ro}}_N(t_j-t_i) - R^{\mathrm{ro}}_N(t_j-t_i+d_{131}) - R^{\mathrm{ro}}_N(t_j-d_{131}-t_i) \\
&\quad + 2R^{\mathrm{ro}}_N(t_j-t_i) - R^{\mathrm{ro}}_N(t_j-t_i+d_{121}) - R^{\mathrm{ro}}_N(t_j-d_{121}-t_i) && (4.48)\\
&= R^{\mathrm{ro}}_X(\tau). && (4.49)
\end{aligned}$$

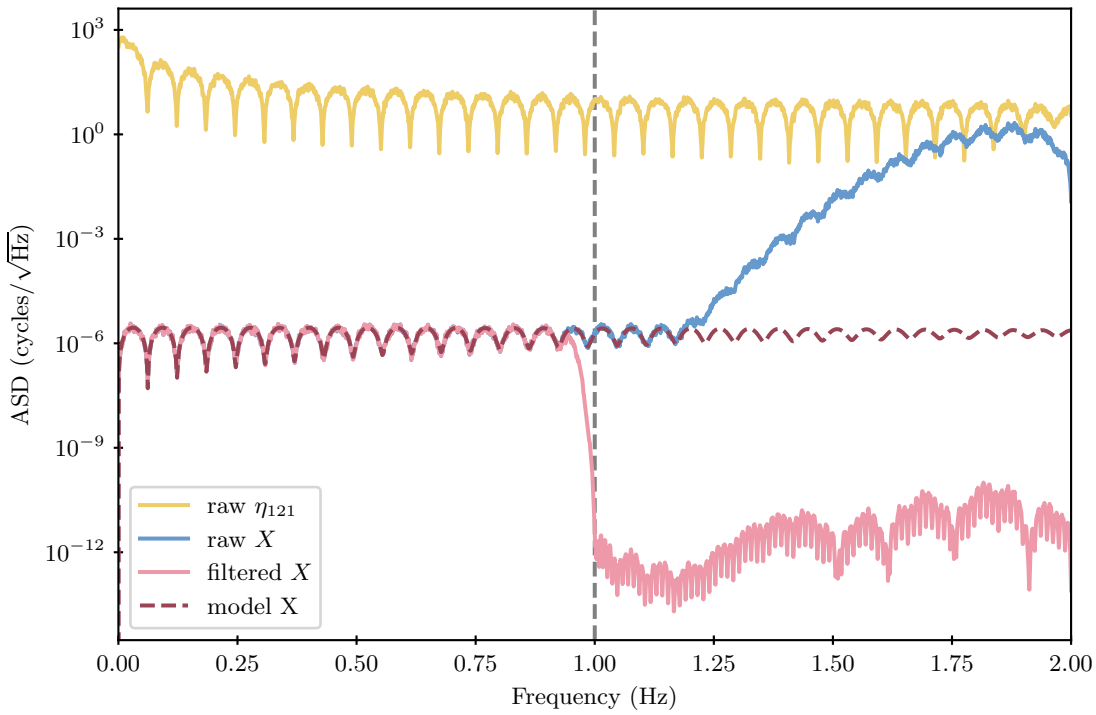

Figure 4.2: ASDs of toy model channels. The yellow line shows the numerical ASD of η_{121} which is dominated by laser phase noise modulated by the round-trip transfer function. In solid blue and red we represent the numerical ASDs of the TDI variable X prior to and after filtering. Residual laser phase noise in X at frequencies above 1.2 Hz are well suppressed by the filter. Furthermore, We superimpose the model for the ASD in X (dashed red).

As the arms are static the covariance matrix is composed of constant diagonals and we can write $\tau = t_j - t_i$. Furthermore, R_N^{ro} denotes the auto-correlation function of the readout noise. As we consider a white shape that is naturally band-limited up to the Nyquist frequency, the auto-correlation function is proportional to the sinc-function

$$R_N^{\text{ro}}(\tau) = \frac{A^2}{2} f_s \,\text{sinc}(f_s \tau), \tag{4.50}$$

where f_s denotes the sampling frequency and $A = 6\,\mu\text{cycles}/\sqrt{\text{Hz}}$ is the level in units of ASD.

To check how well the model fits the numerical simulations we simulate the one-way measurements η for 25 000 s and compute the variable X with the true delays ($d_{121} = 16.332$ s and $d_{131} = 16.145$ s) using PyTDI (Staab et al., 2023a). Then, we compare the numerical ASD of the resulting laser noise free variable with the model $S_X^{\text{ro}}(f)$ by taking the Fourier transform of eq. (4.49). For the simulation of the one-way beatnote phase measurement defined in eq. (4.14) we generate red laser phase noise eq. (3.100) and readout noise with a level of 1 µcycle/$\sqrt{\text{Hz}}$. The simulation is performed directly at a sampling rate of 4 Hz and no filters or decimators are used. To apply the propagation delays we use Lagrange interpolation of very high order (= 131).

In fig. 4.2 we plot the numerical ASD of X in blue and superimpose the model in dashed red. It agrees well up to a frequency of approximately 1.2 Hz. For higher frequency residual laser noise is limiting the combination that is introduced by interpolation errors. To suppress those effects and emulate the fact that we obtain reliable data only in the LISA band (10^{-4} Hz to 1 Hz) we use an FIR filter with a cut-off frequency at the band-edge. As a consequence, the model overestimates the ASD of the filtered combination (red) by around four orders of magnitude at frequencies higher than 1 Hz. This is acceptable as overestimation of the power only results in less weighting of those frequencies in the cost function.

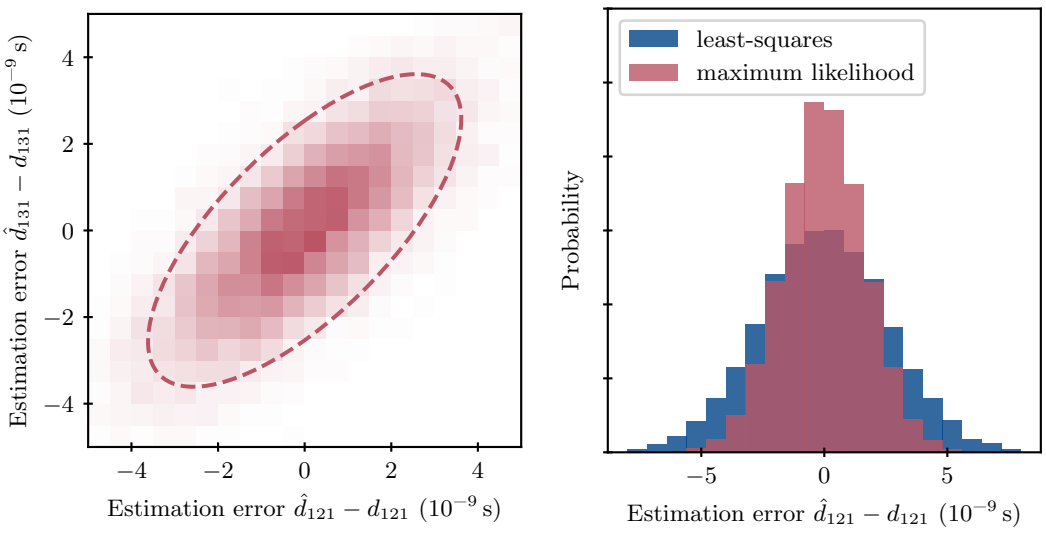

Figure 4.3: Histograms of estimation errors. In the left panel we show the two dimensional joint sample distribution of the maximum likelihood estimates. The ellipse (dashed line) traces a line of equal probability and encloses 68 % probability assuming a bivariant normal distribution with a covariance matrix given by the Cramér-Rao bound. The right panel demonstrates the advantage of the maximum likelihood method r(red) over the traditional least-squares method (blue). As an example we only plot the estimation error of arm d_{121}.

In the next step we want to validate the lower bound for the covariance matrix of the delay estimates d_{121} and d_{131}. We perform a Monte-Carlo simulation to sample the probability distribution of the maximum likelihood estimate given in eq. (4.45). Therefore, we choose the integration time $T = 1000\,\mathrm{s}$ and run $N = 10\,000$ simulations with independent noise realisations. Then, for each run we calculate the maximum likelihood estimate $\hat{\boldsymbol{\theta}}_{\mathrm{MLE}}$. To minimize the reduced log-likelihood function we use the conjugate gradient method as implemented by SciPy (Virtanen et al., 2020).

The calculation of the reduced log-likelihood function in eq. (4.44) is performed in two steps. First, the TDI combination $\boldsymbol{X}$ is calculated using fractional delay filters using the Lagrange interpolation method (of order 61). Second, the product $\boldsymbol{X}^{\mathrm{T}}\Sigma_X^{-1}\boldsymbol{X}$ is evaluated. To safe computational time we precompute the Cholesky decomposition of the covariance matrix Σ_X. It is defined from the auto-correlation function of the readout noise and the delays estimates which we do not know beforehand. However, the result is not sensitive to small errors[3] in the delays used for the computation of the covariance matrix. To simplify we assume the true delays in this calculation. Once we have obtained the Cholesky decomposition of the covariance matrix we can calculate the product $\boldsymbol{X}^{\mathrm{T}}\Sigma_X^{-1}\boldsymbol{X}$ in two steps. First, $\Sigma_X^{-1}\boldsymbol{X}$ is interpreted as an equivalent linear system of equations $\Sigma_X\boldsymbol{Y} = \boldsymbol{X}$. The solution $\boldsymbol{Y}$ is exactly the result of the earlier expression. In the last step, we only have to take the scalar product $\boldsymbol{X}^{\mathrm{T}}\boldsymbol{Y}$. This concludes the calculation of the log-likelihood function.

The results of the Monte-Carlo simulation are shown in fig. 4.3. The left panel shows the sampled distribution of the maximum likelihood estimate. We find a strong correlation between the two arms as predicted in the analytical work before; in the limit of equal arms the sum of the arms cannot be determined as it the likelihood function is fully degenerate in this variable and only the arm difference is available.

[3]We ran some quick numerical checks to confirm this assumption. The estimator yields the same result for delay errors over many standard deviations of the final estimate. In practice, the covariance matrix and its Cholesky decomposition can be recomputed in each iteration, however, which would result in a vast increase of computational cost.

For our particular choice of arm length and integration time T let us explicitly state the lower bound on the covariance matrix $\Sigma_{\boldsymbol{\theta}}$. It is given by the inverse of the Fisher information matrix (see eq. (4.40)) and evaluates to

$$\Sigma_{\boldsymbol{\theta}} \geq \begin{pmatrix} 2.52 & 1.79 \\ 1.79 & 2.51 \end{pmatrix} \cdot 10^{-18}\,\mathrm{s}^2. \tag{4.51}$$

Here, we can clearly see the correlated property of the parameters d_{121} and d_{131} as the off-diagonal terms are positive. For visual inspection we superimpose the line of equal probability of a normal distribution (which has the shape of an ellipse) with the covariance above (red dashed line in left panel of fig. 4.3). The probability is chosen such that the resulting ellipse encloses approximately 68 % which is equivalent to the one-sigma confidence interval in the univariate normal case. To validate the result we count the number of samples of the Monte-Carlo simulation that resides inside the 68 %-confidence ellipse and find a slightly lower fraction of 67 %. This is in good agreement with the theoretical lower bound as the lower percentage indicate the real distribution is slightly broader then the theoretical limit.

In the right panel of fig. 4.3 we compare the traditional least-squares estimator with our maximum likelihood estimator (see eq. (4.17)). The calculation of the power of the TDI variable X is much simpler as we can just use a discrete sum to approximate the integral. We can clearly see that the distribution function of the least-squares estimates is broader and, therefore, a less optimal estimator of the delays. To compare the performance we estimate the width of the distributions in the sensitive direction (in the case of equal arms) which is given by the arm length difference. We find sample standard deviations of $\sigma_{\Delta d}^{\mathrm{LS}} = 1.38 \times 10^{-9}\,\mathrm{s}$ and $\sigma_{\Delta d}^{\mathrm{MLE}} = 1.18 \times 10^{-9}\,\mathrm{s}$. This results in an improvement of 14 % of the maximum likelihood method over the least-squares method.

4.3 Full LISA

In this section we want to return to the full LISA case by generalizing the results we have obtained for the toy model in the precious section. The setup becomes more complex as the split interferometry setup produces long arm and local reference measurements. Furthermore, we need to consider six arms that are time-dependent. As Doppler shifts in the beams become relevant, the interferometric measurements must be defined in terms of total phase (instead of just laser phase noise as in eq. (4.14))

$$\mathrm{isi}_{ij}(t) = \mathbf{D}_{ij}\phi_{ji}(t) - \phi_{ij}(t) + N_{ij}^{\mathrm{ro}}(t) \tag{4.52a}$$

$$\mathrm{rfi}_{ij}(t) = \phi_{ik}(t) - \phi_{ij}(t) \tag{4.52b}$$

where $\phi_{ij}(t)$ denotes the laser phases that we model as $\phi_{0,ij} + \nu_{0,ij} \cdot t + p_{ij}(t)$. Here, $\phi_{0,ij}$ is the initial phase of the laser, $\nu_{0,ij}$ its nominal central frequency and $p_{ij}(t)$ any phase deviations from the nominal phase. Moreover, the only noise apart from the latter is readout noise in the inter-spacecraft interferometer.

As before, we collect all measurements in a single vector ordered as

$$\boldsymbol{y} = \left(\left\{ \left\{ \mathrm{isi}_{ij}(t_k) \right\}_{ij=12,23,31,13,32,21} \quad \left\{ \mathrm{rfi}_{ij}(t_k) \right\}_{ij=12,23,31} \right\}_{k=0}^{N-1} \right)^{\mathrm{T}} \in \mathbb{R}^{9N}. \tag{4.53}$$

Here, we take the six inter-spacecraft interferometers in standard order and append the three reference interferometers on left-handed MOSAs. This is sufficient as we do not model the influence of fiber noise which necessitates the extra step described in section 3.2.2.

In section 3.1.2 we argue that in a static but rotating constellation of three spacecraft the number of independent laser noise free variables is three (we discuss this in more detail in

section 4.3.2). The classical choice is the three Michelson variables defined from the intermediary variables η_{ij} as

$$\begin{aligned} X_1 = &(1 - \mathbf{D}_{121})(\eta_{13} + \mathbf{D}_{13}\eta_{31}) \\ &- (1 - \mathbf{D}_{131})(\eta_{12} + \mathbf{D}_{12}\eta_{21}), \end{aligned} \tag{4.54}$$

$$\begin{aligned} X_2 = &(1 - \mathbf{D}_{121} - \mathbf{D}_{12131} + \mathbf{D}_{1312121})(\eta_{13} + \mathbf{D}_{13}\eta_{31}) \\ &- (1 - \mathbf{D}_{131} - \mathbf{D}_{13121} + \mathbf{D}_{1213131})(\eta_{12} + \mathbf{D}_{12}\eta_{21}). \end{aligned} \tag{4.55}$$

The remaining combinations Y and Z follow by cyclic permutation. The first generation Michelson variable cancels laser noise for six constant arms. Therefore, it is well suited for the analytical computation of the Fisher information matrix to compute the Cramér Rao lower bound (see section 4.3.2). On the other hand, we require the second generation Michelson variables to apply the TDI-R algorithm to a realistic LISA setup with flexing arms where the first generation suppresses laser noise insufficiently.

The intermediary variables η_{ij} in eqs. (4.54) and (4.55) can be computed as

$$\eta_{ij} = \mathrm{isi}_{ij} \begin{cases} -\mathbf{D}_{ij}\mathrm{rfi}_{jk} & \text{if } \epsilon_{ijk} = 1, \\ +\mathrm{rfi}_{ik} & \text{if } \epsilon_{ijk} = -1. \end{cases} \tag{4.56}$$

Before we set off to formulate the likelihood function of the data let us investigate the implications of considering total phase instead of only the in-band phase fluctuations.

4.3.1 Absolute laser frequency estimation

For a flexing LISA constellation the absolute laser frequency couples to the interferometric measurements and even persists after TDI[4]. The reason for this is that the slow-drifting Doppler shifts caused by the time-dependent arms shift the terahertz-frequency by a few megahertz. This results in megahertz-beatnotes in the inter-spacecraft interferometers. As a result we can directly monitor the lasers' optical frequencies and their Doppler shifts. Let us investigate the inter-spacecraft interferometer in units of frequencies. By taking the derivative of eq. (4.52) we obtain

$$\dot{\mathrm{isi}}_{ij}(t) = \big(1 - \dot{d}_{ij}(t)\big)\mathbf{D}_{ij}\big(\nu_{0,ji} + \dot{p}_{ji}(t)\big) - \big(\nu_{0,ij} + \dot{p}_{ij}(t)\big) \tag{4.57a}$$

$$\simeq (\nu_{0,ji} - \nu_{0,ij}) - \dot{d}_{ij}(t) \cdot \nu_{0,ji} + \dot{\mathbf{D}}_{ij}\dot{p}_{ji}(t) - \dot{p}_{ij}(t) \tag{4.57b}$$

$$\dot{\mathrm{rfi}}_{ij}(t) = (\nu_{0,ik} - \nu_{0,ij}) + \dot{p}_{ik}(t) - \dot{p}_{ij}(t). \tag{4.57c}$$

We note that the measurements are indeed sensitive to the relative laser frequencies $\nu_{0,ji} - \nu_{0,ij}$ and the Doppler shift $\dot{d}_{ij}(t) \cdot \nu_{0,ji}$. The "common mode" nominal laser frequency couples only via the Doppler shift which is nominally around 10^{-8}. In the limit of vanishing inter-spacecraft velocities the Doppler term cancels and the inter-spacecraft interferometer becomes insensitive to the absolute laser frequency.

To disentangle the relative laser frequency and the Doppler shift in eq. (4.57) we require an independent sensor for the Doppler factors $\dot{d}_{ij}$. Those are provided by the sideband beatnotes (see section 3.2.4) with high accuracy. If we assume constant inter-spacecraft velocities and constant laser frequencies (integration times T that are much smaller than the dynamics of the system) we can set a figure on the estimation performance. As we consider white laser frequency noise with a level of $30\,\mathrm{Hz}/\sqrt{\mathrm{Hz}}$ we can simply use the average of the time series to yield a good estimate of the dc component of the signals in eq. (4.57). We follow that the variance of the dc

[4]This coupling is not to be confused with the need of a scale factor to convert the relative phase measurement back to a relative distance measurement. This scale factor is given by the laser wavelength which must be properly calibrated beforehand or estimated online (e.g., using the method proposed here).

component estimate depends on the integration time T and reads $\sigma^2_{\Delta\nu_0} = 2\frac{S_{\dot{p}}}{T}$ where the factor two accounts for the independent laser noise contributions in each interferometer. Therefore, we conclude that the relative laser frequency $\nu_{0,ji} - \nu_{0,ij}$ can be determined with a precision of $\sigma_{\Delta\nu_0}$. The determination of the absolute laser frequency requires knowledge of the Doppler shift $\dot{d}$. Its estimation precision σ_{ν_0} is worse by a factor $\dot{d}^{-1}$. If we choose an integration time of one day we find $\sigma_{\Delta\nu_0} \simeq 0.1\,\mathrm{Hz}$ and $\sigma_{\nu_0} \simeq 10\,\mathrm{MHz}$.

4.3.2 Delay estimation

In this section we want to apply the Fisher information matrix formulation developed in section 4.2.1 to the LISA constellation with six independent lasers. Furthermore, we consider six static delays d_{ij} which define the parameter vector $\boldsymbol{\theta}$ that we seek to estimate. Under the condition of dominating laser frequency noise we can analogously follow that the likelihood function can be simplified and restricted to the space of laser noise free combinations. Then, it is sufficient to only consider the reduced likelihood function in the Fisher information analysis which yields an lower bound of the estimation variance.

As for the toy model we work in Fourier space to make the calculation tractable. This requires circular noise time-series such that the Fourier coefficients of the time series are statistically independent (see appendix E). Therefore, the joint probability distribution of the data can be written as a product of the individual probability distributions of the Fourier coefficients. Let us redefine the variables that are used in the simplified calculation of the Fisher information matrix in Fourier space (see eq. (4.36)).

The Fourier coefficients that describes the vector of measured time series $\boldsymbol{y}(t)$ is given by

$$\tilde{\boldsymbol{y}}_k = \underbrace{\begin{pmatrix} -1 & 0 & 0 & 0 & 0 & e^{-2\pi i k \Delta f d_{12}} \\ 0 & -1 & 0 & 0 & e^{-2\pi i k \Delta f d_{23}} & 0 \\ 0 & 0 & -1 & e^{-2\pi i k \Delta f d_{31}} & 0 & 0 \\ 0 & 0 & e^{-2\pi i k \Delta f d_{13}} & -1 & 0 & 0 \\ 0 & e^{-2\pi i k \Delta f d_{32}} & 0 & 0 & -1 & 0 \\ e^{-2\pi i k \Delta f d_{21}} & 0 & 0 & 0 & 0 & -1 \\ -1 & 0 & 0 & 1 & 0 & 0 \\ 0 & -1 & 0 & 0 & 0 & 1 \\ 0 & 0 & -1 & 0 & 1 & 0 \end{pmatrix}}_{\mathrm{M}_k} \tilde{\boldsymbol{p}}_k + \tilde{\boldsymbol{n}}_k. \tag{4.58}$$

Here, the matrix M_k mixes the laser sources to form the inter-spacecraft and reference interferometers. The vectors $\tilde{\boldsymbol{p}}_k$ and $\tilde{\boldsymbol{n}}_k$ collect the Fourier coefficients of the laser noise and readout noise in standard order

$$\boldsymbol{p}(t) = \begin{pmatrix} p_{12}(t) & p_{23}(t) & p_{31}(t) & p_{13}(t) & p_{32}(t) & p_{21}(t) \end{pmatrix}^{\mathrm{T}}, \tag{4.59}$$

$$\boldsymbol{n}(t) = \begin{pmatrix} N^{\mathrm{ro}}_{12}(t) & N^{\mathrm{ro}}_{23}(t) & N^{\mathrm{ro}}_{31}(t) & N^{\mathrm{ro}}_{13}(t) & N^{\mathrm{ro}}_{32}(t) & N^{\mathrm{ro}}_{21}(t) & 0 & 0 & 0 \end{pmatrix}^{\mathrm{T}}. \tag{4.60}$$

The trailing zeros in the definition of $\boldsymbol{n}(t)$ indicate that we only consider readout noise in the inter-spacecraft interferometer and neglect any other secondary noise processes (especially readout noise in the reference interferometer as it couples only subdominantly in the final TDI variables).

The complex covariance matrix of the k-th Fourier coefficient follows analogously as

$$\Gamma_k = \mathrm{E}\{\tilde{\boldsymbol{y}}_k \tilde{\boldsymbol{y}}_k^\dagger\} = \mathrm{M}_k \underbrace{\mathrm{E}\{\tilde{\boldsymbol{p}}_k \tilde{\boldsymbol{p}}_k^\dagger\}}_{\mathrm{P}_k} \mathrm{M}_k^\dagger + \underbrace{\mathrm{E}\{\tilde{\boldsymbol{n}}_k \tilde{\boldsymbol{n}}_k^\dagger\}}_{\mathrm{N}_k}, \tag{4.61}$$

where we identify the covariance matrices of $\tilde{\boldsymbol{p}}_{\boldsymbol{k}}$ and $\tilde{\boldsymbol{n}}_k$ which are given by

$$\mathrm{P}_k = \frac{S_p(k\Delta f)}{2T} \begin{pmatrix} 1 & 0 & 0 & 0 & 0 & 0 \\ 0 & 1 & 0 & 0 & 0 & 0 \\ 0 & 0 & 1 & 0 & 0 & 0 \\ 0 & 0 & 0 & 1 & 0 & 0 \\ 0 & 0 & 0 & 0 & 1 & 0 \\ 0 & 0 & 0 & 0 & 0 & 1 \end{pmatrix}, \tag{4.62}$$

$$\mathrm{N}_k = \frac{S_N^{\mathrm{ro}}(k\Delta f)}{2T} \begin{pmatrix} 1 & 0 & 0 & 0 & 0 & 0 & 0 & 0 & 0 \\ 0 & 1 & 0 & 0 & 0 & 0 & 0 & 0 & 0 \\ 0 & 0 & 1 & 0 & 0 & 0 & 0 & 0 & 0 \\ 0 & 0 & 0 & 1 & 0 & 0 & 0 & 0 & 0 \\ 0 & 0 & 0 & 0 & 1 & 0 & 0 & 0 & 0 \\ 0 & 0 & 0 & 0 & 0 & 1 & 0 & 0 & 0 \\ 0 & 0 & 0 & 0 & 0 & 0 & 0 & 0 & 0 \\ 0 & 0 & 0 & 0 & 0 & 0 & 0 & 0 & 0 \\ 0 & 0 & 0 & 0 & 0 & 0 & 0 & 0 & 0 \end{pmatrix}. \tag{4.63}$$

As the laser noises are independent but identically distributed their covariance matrix is (constant) diagonal. On the other hand the covariance matrix of the readout noise reproduces the zeros in the lower right corner.

In the next step let us analyze the mixing matrix M_k in more detail. It has rank 6 which indicates the number of linearly independent rows. The null space of M_k that is spanned by the columns of E_k projects the laser noise dominated interferometric measurements onto a set of three TDI combinations. We choose the set of first generation Michelson combinations and define the combination in two steps. First, we construct the intermediary variables with the matrix E_k^{η} and only then projects those onto the laser noise free subspace using E_k^{X}.

$$\mathrm{E}_k^{\eta} = \begin{pmatrix} 1 & 0 & 0 & 0 & 0 & 0 \\ 0 & 1 & 0 & 0 & 0 & 0 \\ 0 & 0 & 1 & 0 & 0 & 0 \\ 0 & 0 & 0 & 1 & 0 & 0 \\ 0 & 0 & 0 & 0 & 1 & 0 \\ 0 & 0 & 0 & 0 & 0 & 1 \\ 0 & 0 & -e^{2\pi i\Delta f d_{31}} & 1 & 0 & 0 \\ -e^{2\pi i\Delta f d_{12}} & 0 & 0 & 0 & 0 & 1 \\ 0 & -e^{2\pi i\Delta f d_{23}} & 0 & 0 & 1 & 0 \end{pmatrix} \tag{4.64}$$

$$\mathrm{E}_k^{X} = \begin{pmatrix} -\left(1-e^{2\pi i\Delta f(d_{13}+d_{31})}\right) & \left(1-e^{2\pi i\Delta f(d_{23}+d_{32})}\right)e^{2\pi i\Delta f d_{21}} & 0 \\ 0 & -\left(1-e^{2\pi i\Delta f(d_{21}+d_{12})}\right) & \left(1-e^{2\pi i\Delta f(d_{31}+d_{13})}\right)e^{2\pi i\Delta f d_{32}} \\ \left(1-e^{2\pi i\Delta f(d_{12}+d_{21})}\right)e^{2\pi i\Delta f d_{13}} & 0 & -\left(1-e^{2\pi i\Delta f(d_{32}+d_{23})}\right) \\ 1-e^{2\pi i\Delta f(d_{12}+d_{21})} & 0 & -\left(1-e^{2\pi i\Delta f(d_{32}+d_{23})}\right)e^{2\pi i\Delta f d_{31}} \\ 0 & -\left(1-e^{2\pi i\Delta f(d_{21}+d_{12})}\right)e^{2\pi i\Delta f d_{23}} & 1-e^{2\pi i\Delta f(d_{31}+d_{13})} \\ -\left(1-e^{2\pi i\Delta f(d_{13}+d_{31})}\right)e^{2\pi i\Delta f d_{12}} & 1-e^{2\pi i\Delta f(d_{23}+d_{32})} & 0 \end{pmatrix} \tag{4.65}$$

To perform both steps at once we must multiply the two matrices

$$\mathrm{E}_k = \mathrm{E}_k^{\eta} \cdot \mathrm{E}_k^{X}. \tag{4.66}$$

At first the order seems counter-intuitive, however, to project the measurement $\tilde{\boldsymbol{y}}_k$ into the laser noise free space we have to perform $\tilde{\boldsymbol{X}}_k = \mathrm{E}_k^{\dagger}\tilde{\boldsymbol{y}}_k = \mathrm{E}_k^{X\,\dagger}\mathrm{E}_k^{\eta\,\dagger}\tilde{\boldsymbol{y}}_k$. Additionally, we can check whether we have captured the entire null space by calculating the rank of $\mathrm{E}_k^{\dagger}$; it is full rank.

We then proceed with the calculation of the Fisher information matrix. For a single Fourier coefficient the result is equivalent to eq. (4.36) with $P_k = \frac{S_p(k\Delta f)}{2T}$ (the identity matrix in

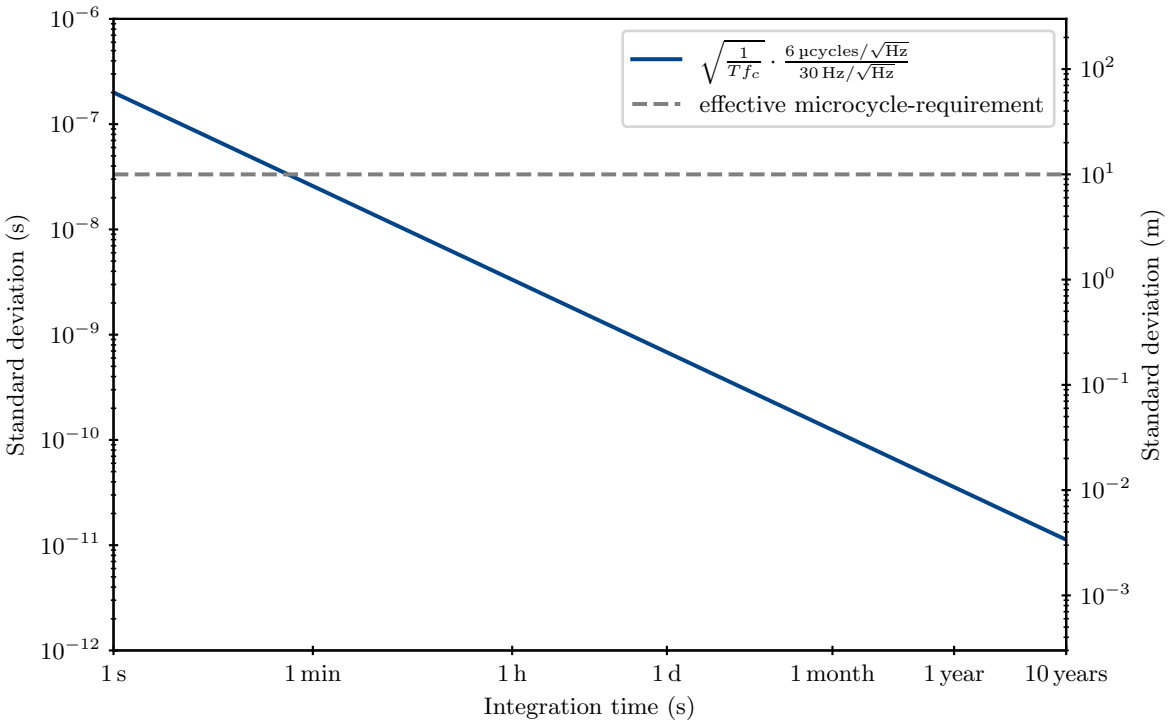

Figure 4.4: Cramér-Rao bound σ_d as a function of integration time T (blue). For comparison the horizontal dashed line in grey represent the maximum allowed bias to limit the laser noise residual in the Michelson variable below the microcycle-requirement.

eq. (4.62) vanishes during calculations). To obtain the full Fisher information we take the sum over all single information matrices that can be approximated by an integral (cf. eq. (4.39)). To simplify the expression we directly assume the case of equal arm length. We find that the Fisher information matrix is independent of the arm length. It reads

$$\mathrm{I} = T \int_0^\infty \frac{S_{\dot{p}}(f)}{S_N^{\mathrm{ro}}(f)}\,\mathrm{d}f \cdot \begin{pmatrix} 1 & 0 & 0 & 0 & 0 & 0 \\ 0 & 1 & 0 & 0 & 0 & 0 \\ 0 & 0 & 1 & 0 & 0 & 0 \\ 0 & 0 & 0 & 1 & 0 & 0 \\ 0 & 0 & 0 & 0 & 1 & 0 \\ 0 & 0 & 0 & 0 & 0 & 1 \end{pmatrix}. \tag{4.67}$$

Furthermore, we do not encounter any degeneracies as it was the case for the toy model in the equal arms limit. They are broken by the fact that all six lasers must cancel (as opposed to one) in three (as opposed to one) TDI combination. As the Fisher information matrix is (constant) diagonal the delay estimates are mutually uncorrelated and we can readily write down their individual Cramér-Rao bound. It is given by

$$\sigma_d^2 \geq \frac{1}{T}\left(\int_0^\infty \frac{S_{\dot{p}}(f)}{S_N^{\mathrm{ro}}(f)}\,\mathrm{d}f\right)^{-1} \tag{4.68}$$

Analogously to eq. (4.43) we find that the lower bound on the estimation variance of the delays is inversely proportional to the integration time T and the integrated PSD of laser frequency noise weighted by the PSD of readout noise.

In fig. 4.4 we evaluate the Cramér-Rao bound given in eq. (4.68) for different integration times T. We assume the usual level of $30\,\text{Hz}/\sqrt{\text{Hz}}$ for laser frequency noise and $6\,\mu\text{cycles}/\sqrt{\text{Hz}}$ for the readout noise in the inter-spacecraft interferometer. The evaluation of the integral becomes

trivial and we set the upper integration limit to 1 Hz (the high frequency end of the LISA band). We see that after about a minute of integration the standard deviation of the delay estimate falls below 10 m which represents the maximum allowed arm length error to limit the laser noise residual in the Michelson combination below the microcycle-requirement.

4.3.3 Bias calibration

As already hinted towards in section 3.2.4 TDI-R can be used to calibrate ranging biases in the PRN ranges. Therefore, we set up a numerical experiment where we use TDI-R to calculate independent estimates of the ranges that are by definition free of any ranging bias. We run numerical simulations using LISA Instrument (Bayle et al., 2022a). Here, for the sake of realism, we choose numerical orbits provided by ESA (Martens and Joffre, 2021) generated by LISA Orbits (Bayle et al., 2022b). The simulation is performed over a duration of 20 000 s in units of frequency fluctuations. For convenience, we omit total frequency units to avoid trends in the TDI variables that have to be properly modeled and removed prior to evaluation of the reduced likelihood function. Furthermore, for all numerical calculations we can rely on double precision floats (as opposed to extended precision) which speeds up the computation. Similar to the toy model simulations, we only include laser noise and readout noise in the inter-spacecraft interferometer with the following white levels

$$\sqrt{S_{\dot{p}}} = 30\,\mathrm{Hz}/\sqrt{\mathrm{Hz}}, \tag{4.69}$$

$$\sqrt{S_N^{\mathrm{ro}}} = 6\,\mu\mathrm{cycles}/\sqrt{\mathrm{Hz}}. \tag{4.70}$$

Furthermore, we also simulate ranging biases in the PRN ranges that we attempt to estimate in this experiment. They are chosen as given in table 3.2.

As the arms are flexing we have to parameterize them appropriately. Therefore, we use splines to model them. We choose polynomial order three and five knots such that there is one knot every 5000 s. The rationale behind it is that we want to avoid overfitting any noise or signal in the LISA band. With a "sampling rate" of 2×10^{-4} Hz the delay models contain only frequency components up to the Nyquist rate of 10^{-4} Hz by construction. As a consequence, the parameter vector $\boldsymbol{\theta}$ is of dimension $6 \times 5 = 30$.

As in section 4.2.2 we need to formulate the likelihood function in time-domain as the frequency-domain representation is only valid for periodic noises and long integration times T. Furthermore, in the realistic LISA setup considered here, the arm lengths are time-dependent which makes the measurements non-stationary for which the Fourier series representation does not exist. Therefore, we formulate the reduced likelihood as in eq. (4.44) where

$$\boldsymbol{X} = \begin{pmatrix} \dot{X}_2(t_0) & \dot{Y}_2(t_0) & \dot{Z}_2(t_0) & \dot{X}_2(t_1) & \dots \end{pmatrix} \in \mathbb{R}^{3\cdot N} \tag{4.71}$$

now collects the second generation Michelson variables $\dot{X}_2$, $\dot{Y}_2$ and $\dot{Z}_2$ in frequency units for all times. We require second generation variables as those sufficiently approximate the null space for flexing arms. We calculate them numerically using PyTDI (Staab et al., 2023a).

The entries of the covariance matrix Σ_X consists of $N \times N$ (where $N = 80\,000$ is the number of samples) blocks of dimension 3×3 that describe the covariance between the three combination at times t_i and t_j

$$(\Sigma_X)_{i,j} = \mathrm{E}\left\{ \begin{pmatrix} \dot{X}(t_i)\cdot\dot{X}(t_j) & \dot{X}(t_i)\cdot\dot{Y}(t_j) & \dot{X}(t_i)\cdot\dot{Z}(t_j) \\ \dot{Y}(t_i)\cdot\dot{X}(t_j) & \dot{Y}(t_i)\cdot\dot{Y}(t_j) & \dot{Y}(t_i)\cdot\dot{Z}(t_j) \\ \dot{Z}(t_i)\cdot\dot{X}(t_j) & \dot{Z}(t_i)\cdot\dot{Y}(t_j) & \dot{Z}(t_i)\cdot\dot{Z}(t_j) \end{pmatrix} \right\}. \tag{4.72}$$

Plugging in the definition of the second generation Michelson combinations (eq. (4.55)) and taking into account readout noise in the inter-spacecraft interferometer yields a rather lengthy expression that is left out here for the sake of brevity. It is composed of terms involving the

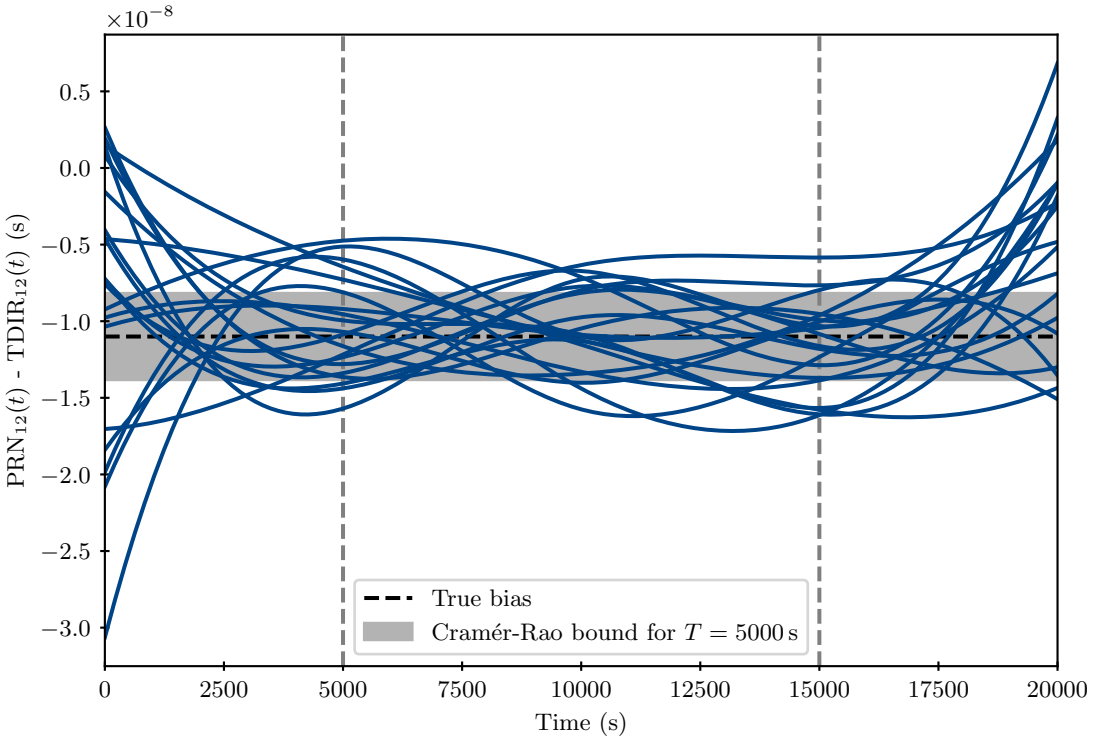

Figure 4.5: Differences between PRN range and TDI-R range for delay d_{12}. Each blue line represents a single realization. The horizontal dashed line in black indicates the true value of the bias $B_{12} = -1.1 \times 10^{-8}\,\mathrm{s}$. The grey area indicates the region covered by the Cramér-Rao bound evaluated for $T = 5000\,\mathrm{s}$. The interval that we consider in our analysis is marked by the vertical dashed lines in grey.

auto-correlation function of the readout noise (derivative) $R_{\dot{N}}^{\mathrm{ro}}(\tau)$ evaluated at different times $\tau = \big(t_j - d_{\mathrm{I}}(t_j)\big) - \big(t_i - d_{\mathrm{II}}(t_i)\big)$. Here, the roman indices I and II indicate nested time-delays. We make use of the rule that the auto-correlation function of the time derivative of a process is given by the negative second derivative of the auto-correlation function of the process itself.

$$R_{\dot{N}}^{\mathrm{ro}}(\tau) = -\frac{\mathrm{d}^2}{\mathrm{d}\tau^2} R_N^{\mathrm{ro}}(\tau) = \frac{A^2}{2} f_s (\pi f_s)^2 \cdot \left(\mathrm{sinc}(f_s \tau) - 2 \frac{\mathrm{sinc}(f_s \tau) - \cos(\pi f_s \tau)}{(\pi f_s \tau)^2} \right) \tag{4.73}$$

Here, $R_N^{\mathrm{ro}}(\tau)$ represents the auto-correlation function of readout noise in phase units which we assume to be band-limited and white with a level of $A = 6\,\mu\mathrm{cycles}/\sqrt{\mathrm{Hz}}$ (analogues to eq. (4.50)).

When calculating the matrix Σ_X we run into computational problems. Storing the full matrix requires roughly 50 GB which exceeds the memory of the machine we run our simulations on. Fortunately, the matrix Σ_X arranged in the order we have defines in eq. (4.72) is concentrated around the diagonal. The reason for this is that the ACF of the readout noise quickly decays for large τ. Therefore, we only store a finite band of the matrix along the diagonal with maximum $|\tau| = |t_j - t_i|$ of 100 s (those account for a maximum delay of $8 \times 10\,\mathrm{s}$ and margin for the finite width of the ACF). To achieve actual zeros outside of the band we use a Kaiser window to smoothly taper off the ACF with a total width of 40 s and an attenuation of 240 dB. The windowing results in a mismodeling of the noise process. As we have chosen quite a conservative window, the effect will only be visible at very low frequencies which are lifted by the window. This results in overestimating the PSD which is acceptable as it only leads to less weighting at those frequencies (as discussed already in section 4.2.2)

To investigate the statistics of the reduced maximum likelihood estimator described here and check consistency with the Cramér-Rao bound estimated in section 4.3.2 we run an ensemble of

20 simulations. For each realization we individually calculate the maximum likelihood estimate $\hat{\boldsymbol{\theta}}^{(i)}_{\mathrm{MLE}}$ (here, i indicates the run) using the conjugate gradient method. The results are presented in fig. 4.5. Each blue line represents the difference between the PRN range and the TDI-R range for one realization. Here, we only show the results for the delay d_{12}. The horizontal dashed line in black shows the true value of the bias we set in the simulation. We can observe that the TDI-R estimate is unbiased as the range difference fluctuates around the true bias. The grey area represents the expected minimal uncertainty given by the Cramér-Rao bound evaluated for $T = 5000\,\mathrm{s}$. The reason for using the knot separation of the splines is that it determines the degrees of freedom of the model. By allowing a high number of the latter the model will "overfit" the data. Furthermore, we can see that TDI-R performs poorly at the boundaries. Therefore, in our further analysis, we only consider the central $10\,000\,\mathrm{s}$ indicated by the vertical dashed lines in grey. We denote this interval in the following by the symbol P.

Ranging performance

To assess the ranging performance of TDI-R we consider the metric

$$\sigma^2_{\hat{d}^{(i)}_{ij}} = \frac{1}{P}\int_P \left(\mathrm{PRN}_{ij}(t) - \mathrm{TDIR}^{(i)}_{ij}(t) - B_{ij}\right)^2 \mathrm{d}t. \tag{4.74}$$

It represents the mean squared error of the TDI-R estimate from the true range. We construct the true range by subtracting the true bias from the PRN estimate. We calculate this metric for every realization i and take the mean over all arms and realizations. The square root of the result represents the root mean squared of the ranging error of TDI-R. We yield $\bar{\sigma}_{\hat{d}} = 2.81 \times 10^{-9}\,\mathrm{s}$ which is consistent with the analytical Cramér-Rao bound given in eq. (4.68) for $T = 5000\,\mathrm{s}$ which reads $2.83 \times 10^{-9}\,\mathrm{s}$. We therefore conclude that we have formulated a minimum variance and unbiased estimator of the six ranges d_{ij}. The result can be further improved by smoothing the result using a Kalman-like filter (Reinhardt et al., 2023) or models with less degrees of freedom.

Bias calibration performance

In the last step of our analysis, we estimate the six biases B_{ij} using the results from TDI-R. To estimate those we subtract the TDI-R ranges from the PRN ranges which are contaminated with the bias. Then, we take the temporal mean by integrating the difference and dividing by the length of the time series P. Formally we yield estimates of the six biases

$$\hat{B}^{(i)}_{ij} = \frac{1}{P}\int_P \left(\mathrm{PRN}_{ij}(t) - \mathrm{TDIR}^{(i)}_{ij}(t)\right) \mathrm{d}t, \tag{4.75}$$

for the i-th realisation. We analyze them by calculating the squared error from the true biases

$$\sigma^2_{\hat{B}^{(i)}_{ij}} = \left(\hat{B}^{(i)}_{ij} - B_{ij}\right)^2. \tag{4.76}$$

To reduce the variance of the latter we take the average over all arms and realizations. The square root of the result yields a mean estimation error of $2.07 \times 10^{-9}\,\mathrm{s}$ which is consistent with the analytical Cramér-Rao bound for $T = P = 10\,000\,\mathrm{s}$ which reads $2.00 \times 10^{-9}\,\mathrm{s}$. Again, we conclude that we have found the optimal estimator for the ranging bias in the PRN ranges using TDI-R. To improve the performance further the integration time P must be increased (see fig. 4.4).

4.3.4 Discussion

In this chapter, we have presented a thorough analysis of an optimal TDI-R estimator by formulating the likelihood function of the LISA carrier-carrier beatnotes. We calculate the Fisher information matrix in the limit of dominating laser noise and find simple expressions for the limit of equal arms. Then, we derive the Cramér-Rao bound that is defined as the inverse of the Fisher information matrix. It determines the lower bound on the estimation uncertainty of any unbiased estimator of the parameters of the likelihood function, i.e., the delays in LISA. We validate those analytical limits by running numerical simulations and demonstrate that we are able to formulate optimal estimators that reach the Cramér-Rao bound. Ultimately, we show that TDI-R can be used to calibrate biases present in the PRN ranges.

In the studies presented in this manuscript, we concentrate more on the analytical understanding of TDI-R. As a next step it is important to implement this method in the ranging processing pipeline for LISA. In a ranging sensor fusion study by Reinhardt et al. (2023), the traditional TDI-R estimator (Tinto et al., 2005) has been already successfully applied to resolve the ambiguity of the PRN ranges and calibrate their bias. To implement the optimal TDI-R estimator introduced here in state-of-the-art LISA processing pipelines it has to be adapted for more realistic data.

Realistic LISA data comprises beatnote phases or frequencies in total units. Due to Doppler shifts and the Frequency plan the central frequency of the lasers is time-varying. Consequently, we need to appropriately model both the Doppler shifts and drifting absolute laser frequencies to remove the deterministic trend present in the TDI variables to properly express their likelihood function. Furthermore, more realistic models for the lasers have to be assumed. First, the ASD of realistic laser frequency noise deviates from white noise below a few mHz. However, we expect that this adjustment will only have a negligible effect on the results. Second, the baseline design of LISA foresees locked lasers. Those effect the correlation properties of the six lasers as they are not independent anymore but follow each other with a time lag. The consequences of laser locking are currently investigated in dedicated studies.

To make the TDI-R algorithm more robust against instrumental glitches and the impact of GWs it can be beneficial to artificially amplify laser frequency noise in a frequency band that is free of any disturbances. The simplest scheme is to modulate a tone at around 1 Hz (Francis et al., 2015). Then, only the power at a single frequency has to be analyzed which makes this method more robust. Furthermore, the amplitude of the tone can be tuned such to achieve a particular ranging precision.

Overall, the run time of the algorithm and its memory demands can be improved. Therefore, we propose to reformulate the likelihood function in the Frequency domain. For finite-length time series that are not periodic and non-stationary the Fourier coefficients will be correlated. Therefore, their covariance matrix will have off-diagonal terms and require a similar treatment as we do in the time domain. However, assuming appropriate windowing of the time series, the covariance matrix of the Fourier coefficients will be much more concentrated around its diagonal.

Chapter 5

Summary and Conclusion

In this thesis, we have discussed various aspects of the initial noise reduction pipeline for the Laser Interferometer Space Antenna (LISA); a space mission led by ESA to measure gravitational waves (GWs) in the 10^{-4} Hz to 1 Hz frequency band. Time-delay interferometry (TDI) represents an integral part of the initial noise reduction pipeline to suppress laser frequency noise by synthesizing virtual equal-arm interferometers. We provide an overview of various TDI combinations suitable for LISA and discuss their operational advantages. To numerically compute TDI combinations we have developed the Python package PyTDI (Staab et al., 2023a) that is extensively used in this thesis and also widely adopted in the LISA consortium. It can handle interferometric data given in either phase or frequency units. Prior to performing TDI, precise estimates of the inter-spacecraft pseudo-ranges have to be calculated. We present a ranging processing pipeline that combines ranging information from the sideband-sideband beatnotes and the PRN ranging measurements to yield femtosecond-stable propagation delays that serve as an input for TDI. Furthermore, we demonstrate the ability to calibrate biases in the PRN ranges using a technique named time-delay interferometric ranging (further discussed below). To validate the performance of the ranging processing pipeline and the TDI algorithm, we analytically model laser and timing residuals and compare them to numerical simulations using the LISA simulation suite developed by the consortium. The residuals arise due to on-board processing of the interferometric data and errors introduced by the post-processing implementation of TDI. We demonstrate good agreement between the PSD of the numerical results and the models that describe the coupling of the residuals to the final TDI output analytically.

From the modeling of laser and timing noise residuals, we have identified direct implications for the design of the LISA instrument. First, modulation noise that is introduced when deriving the phase modulation signal from the pilot tone and modulating it on the laser beam represents the limiting in-band ranging noise. It has to be appropriately accounted for in the LISA noise budget as it exceeds the microcycle-requirement, which serves as benchmark in our investigations. Second, the design of the on-board decimation stages reducing the sampling rate of the interferometric data from initially 80 MHz down to the telemetry rate of 4 Hz requires careful design of anti-aliasing filters. We suggest the use of FIR type I filters, which have an odd number of coefficients and therefore an integer group delay which can be easily compensated. Furthermore, they exhibit zero phase distortion. The design of these filters is trading-off the amount of aliased laser noise and computational effort. Therefore, we propose filter designs for the final decimation stage (16 Hz to 4 Hz) that use a minimum number of coefficient and, at the same time, produce a laser noise residual below the microcycle requirement. Previously, it was assumed that the so-called flexing-filtering effect also poses requirements on the filter design. However, we show that this effect can be mitigated by applying a compensation filter on ground that flattens the response of the decimation stage in the LISA band. Lastly, we investigate different interpolation methods used to implement time shifts in post-processed TDI. We present a novel method to design minimum length interpolation kernels that fulfill the microcycle-requirement.

In the second part of this thesis, we present our advances on the statistical description of time-delay interferometric ranging. TDI-R is a post-processing technique to extract ranging information from the carrier-carrier beatnotes. We derive the optimal TDI-R estimator by formulating the likelihood function of the interferometric data that contains the inter-spacecraft propagation delays as parameters. Using the Fisher information formalism we express the Cramér-Rao bound which sets the theoretical limit on the estimation variance of the delays. We then demonstrate prototype TDI-R pipelines. We run Monte-Carlo simulations to test their performance and characterize their estimation statistics. Ultimately, we show that our implemented algorithms perform very close to the theoretical limit we have calculated analytically before. Hence, we conclude that we have found the optimal TDI-R estimator.

For future studies, we propose to combine the presented data processing pipelines and increase the complexity of the LISA data that is analyzed. Especially, the TDI-R algorithm needs to be prepared for data in total phase or frequency units which requires estimation of the absolute laser frequency to detrend the TDI variables. Furthermore, the effect of laser locking, which is foreseen in the baseline design of LISA, on the performance of the various pipelines has to be studied. Staab et al. (2023b) already investigated the coupling of laser noise residuals in the second generation Michelson variable X_2 for the N1-12 locking topology. This study has to be extended to the remaining locking topologies that are considered for LISA. In turn, this also means that the ability of TDI-R to estimate biases in the PRN measurements is dependent on the locking topology used. Therefore, we should evaluate the performance of TDI-R for the various locking topologies. Furthermore, the performance of TDI-R can be enhanced by modulating a low frequency tone around 1 Hz on the frequency of the primary laser. This artificially increases the laser noise power in a narrow frequency band and would make the TDI-R algorithm more robust against in-band disturbances like glitches, non-stationary instrumental noise or even GWs.

Appendix A

Commutator Algebra

In this manuscript we make extensive use of the notion of commutators. They express whether it is allowed to interchange the order of two operators $\mathbf{A}$ and $\mathbf{B}$ applied to a timer series $x(t)$. We define the commutator of $\mathbf{A}$ and $\mathbf{B}$ as

$$[\mathbf{A}, \mathbf{B}]x(t) = \mathbf{AB}x(t) - \mathbf{BA}x(t). \tag{A.1}$$

which itself defines an operator again. If $[\mathbf{A}, \mathbf{B}] = 0$ the operators $\mathbf{A}$ and $\mathbf{B}$ are said to commute.

Commutators possess a set of identities that we use to simplify expressions and split them up into individual contributions. Relevant for our calculations are

$$[\mathbf{A} + \mathbf{B}, \mathbf{C}] = (\mathbf{A} + \mathbf{B})\mathbf{C} - \mathbf{C}(\mathbf{A} + \mathbf{B}) = [\mathbf{A}, \mathbf{C}] + [\mathbf{B}, \mathbf{C}] \tag{A.2a}$$

$$[\mathbf{A}, \mathbf{B}] = -(\mathbf{BA} - \mathbf{AB}) = -[\mathbf{B}, \mathbf{A}] \tag{A.2b}$$

$$[\mathbf{A}, \mathbf{BC}] = \mathbf{ABC}\underbrace{-\mathbf{BAC} + \mathbf{BAC}}_{=0}-\mathbf{BCA} = [\mathbf{A}, \mathbf{B}]\mathbf{C} + \mathbf{B}[\mathbf{A}, \mathbf{C}] \tag{A.2c}$$

$$[\mathbf{AB}, \mathbf{C}] = \mathbf{ABC}\underbrace{-\mathbf{ACB} + \mathbf{ACB}}_{=0}-\mathbf{CAB} = \mathbf{A}[\mathbf{B}, \mathbf{C}] + [\mathbf{A}, \mathbf{C}]\mathbf{B} \tag{A.2d}$$

Appendix B

Aliasing for Stochastic Processes

Aliasing occurs when decimating the sampling rate of a discrete time series. The resulting time series has a reduced band-limit and therefore any power that resides at higher frequencies will be folded into band. To mitigate this, it is important to implement appropriate anti-aliasing filters before decimation that act as low-pass filters which remove any signal content above the new Nyquist frequency.

Here, we describe the effect of aliasing on stochastic processes. As introduced earlier, due to their random nature they are best characterized by their ACF or PSD. We follow the definitions given in section 1.3.

Let y_n be a discrete time series with sampling rate f_s that is derived from x_n by decimating it by a factor M. Formally we write

$$y_n = x_{nM} \tag{B.1}$$

$$y(t) = \sum_{n=-\infty}^{\infty} \mathrm{sinc}(f_s t - n) \cdot x_{nM} \tag{B.2}$$

In the second line we use the Whittaker-Shannon interpolation formula (see eq. (1.29)) to represent the discrete time series as a continuous one.

In the next step, we use the definition in eq. (1.24) to write down the ACF of $y(t)$. We

develop

$$\mathrm{ACF}\{y(t)\}(\tau) = \mathrm{E}\{y(t)y(t+\tau)\} \tag{B.3}$$

$$= \mathrm{E}\left\{\left(\sum_{m=-\infty}^{\infty} \operatorname{sinc}\left(f_s t - m\right)\cdot x_{mM}\right)\left(\sum_{n=-\infty}^{\infty} \operatorname{sinc}\left(f_s(t+\tau) - n\right)\cdot x_{nM}\right)\right\} \tag{B.4}$$

$$= \sum_{m,n=-\infty}^{\infty} \operatorname{sinc}\left(f_s t - m\right)\operatorname{sinc}\left(f_s(t+\tau) - n\right)\mathrm{ACF}\{x(t)\}\big((n-m)T_s\big) \tag{B.5}$$

$$= \sum_{m,n=-\infty}^{\infty} \operatorname{sinc}\left(f_s t - m\right)\operatorname{sinc}\left(f_s(t+\tau) - n\right)\int_{\mathbb{R}} \mathrm{PSD}\{x(t)\}(f)\, e^{2\pi i f(n-m)T_s}\,\mathrm{d}f \tag{B.6}$$

$$= \int_{\mathbb{R}} \mathrm{PSD}\{x(t)\}(f)\left(\sum_{m=-\infty}^{\infty} \operatorname{sinc}\left(f_s t - m\right)e^{-2\pi i f m T_s}\right)\left(\sum_{n=-\infty}^{\infty} \operatorname{sinc}\left(f_s(t+\tau) - n\right)e^{2\pi i f n T_s}\right)\mathrm{d}f \tag{B.7}$$

$$= \int_{\mathbb{R}} \mathrm{PSD}\{x(t)\}(f) \sum_{m,n=-\infty}^{\infty} \operatorname{rect}\left(\frac{f - m f_s}{f_s}\right) e^{-2\pi i(f-mf_s)t} \operatorname{rect}\left(\frac{f - n f_s}{f_s}\right) e^{2\pi i(f-nf_s)(t+\tau)}\,\mathrm{d}f \tag{B.8}$$

$$= \int_{\mathbb{R}} \mathrm{PSD}\{x(t)\}(f) \sum_{n=-\infty}^{\infty} \operatorname{rect}\left(\frac{f - n f_s}{f_s}\right) e^{2\pi i(f-nf_s)\tau}\,\mathrm{d}f \tag{B.9}$$

$$= \int_{\mathbb{R}} \operatorname{rect}\left(\frac{f}{f_s}\right)\left(\sum_{n=-M}^{M} \mathrm{PSD}\{x(t)\}(f + n f_s)\right) e^{2\pi i f\tau}\,\mathrm{d}f. \tag{B.10}$$

In eq. (B.6) we replace the ACF by the inverse Fourier transform of the PSD. This enables us to factor terms containing m and n, respectively. Then, in eq. (B.8) we use common discrete-time Fourier transformation laws which convert the sinc-functions into rect-functions which are defined by

$$\operatorname{sinc}(x) = \frac{\sin(\pi x)}{\pi x} \tag{B.11}$$

$$\operatorname{rect}(x) = \begin{cases} 0, & \text{if } |x| > \frac{1}{2} \\ \frac{1}{2}, & \text{if } |x| = \frac{1}{2} \\ 1, & \text{if } |x| < \frac{1}{2}. \end{cases} \tag{B.12}$$

In the next line, we observe that the constituents of the sum are only non-vanishing if $m = n$ which leave us with a single sum running over index n. Finally, in eq. (B.10), we perform the substitution $f \to f + n f_s$ and identify the PSD of $y(t)$ as the Fourier Transform of the ACF which is given by

$$\mathrm{PSD}\{y(t)\}(f) = \operatorname{rect}\left(\frac{f}{f_s}\right)\sum_{n=-M}^{M} \mathrm{PSD}\{x(t)\}(f + n f_s). \tag{B.13}$$

B.1 Decimation-Filtering Commutator

In this section we derive the PSD of the commutator of the decimation and filtering operations. In general, the filtering operation represents any LTI system, e.g. also a constant time-shift. Formally, the commutator is given by

$$y(t) = [\mathbf{S}_{M\downarrow}, \mathbf{F}]x(t) = \mathbf{S}_{M\downarrow}\mathbf{F}x(t) - \mathbf{F}\mathbf{S}_{M\downarrow}x(t). \tag{B.14}$$

One has to make sure that the operator $\mathbf{F}$ is well defined for both sampling rates, before decimation and after decimation.

As eq. (B.14) represents a difference of two time series, its PSD can be expanded into

$$\begin{aligned}\mathrm{PSD}\{y\}(f) &= \mathrm{PSD}\{\mathbf{S}_{M\downarrow}\mathbf{F}x(t) - \mathbf{F}\mathbf{S}_{M\downarrow}x(t)\}(f) && \text{(B.15)}\\ &= \mathrm{PSD}\{\mathbf{S}_{M\downarrow}\mathbf{F}x(t)\}(f) + \mathrm{PSD}\{\mathbf{F}\mathbf{S}_{M\downarrow}x(t)\}(f) \\ &\quad - \mathrm{CSD}\{\mathbf{S}_{M\downarrow}\mathbf{F}x(t), \mathbf{F}\mathbf{S}_{M\downarrow}x(t)\}(f) - \mathrm{CSD}\{\mathbf{F}\mathbf{S}_{M\downarrow}x(t), \mathbf{S}_{M\downarrow}\mathbf{F}x(t)\}(f). && \text{(B.16)}\end{aligned}$$

The first two terms are already explained in the previous section. The cross spectral densities (CSDs) can be derived in a similar manner and we find that

$$\mathrm{CSD}\{\mathbf{S}_{M\downarrow}\mathbf{F}x(t), \mathbf{F}\mathbf{S}_{M\downarrow}x(t)\}(f) = \tilde{h}(f)\,\mathrm{rect}\left(\frac{f}{f_s}\right)\sum_{n=-M}^{M}\tilde{h}^*(f+nf_s)\,\mathrm{PSD}\{x(t)\}(f+nf_s) \quad \text{(B.17)}$$

Therefore, the PSD of the commutator is given by

$$\mathrm{PSD}\{y(t)\}(f) = \mathrm{rect}\left(\frac{f}{f_s}\right)\sum_{\substack{n=-M\\ n\neq 0}}^{M}\left|\tilde{h}(f) - \tilde{h}(f+nf_s)\right|^2\mathrm{PSD}\{x(t)\}(f+nf_s). \quad \text{(B.18)}$$

Appendix C

Filter Design

In this work we use three different filter designs for anti-aliasing before decimation. The first design is used as the default in the LISA simulators as it is very flat in the pass-band and has high suppression in the stop-band. As it is a rather conservative design using $N = 145$ filter taps we seek a less stringent design for phase and for frequency units. Here, we require that aliased noise resides below the microcycle-requirement. We find that 29 taps for phase units and 33 for frequency units are sufficient. This is a vast improvement compared to 145 taps. We show the transfer function and its derivative of each design in fig. C.1. Furthermore, a more detailed investigation on the aliased noise for the two optimized designs is presented in fig. C.2.

C.1 LISA Instrument design

The calculation of the filter taps for LISA Instrument's default implementation relies on the windowing method (see e.g. Oppenheim et al., 1999). We use the `firwin`-funtion from the `scipy.signal` Python package (Virtanen et al., 2020). We choose a Kaiser window with an attenuation of 240 dB which amounts to a stop-band suppression of 12 orders of magnitude. To allow for some margin the transition-band starts at 1.1 Hz and the stop-band at 2.9 Hz. In fig. C.1 we see the transfer function in blue. It exhibits high flatness in the LISA band and high suppression in the stop-band.

C.2 Optimized design for phase units

To relax the filter design and use fewer filter taps we introduce another design method. We *image*[1] the microcycle-requirement (that only holds in-band) up until the Nyquist rate before decimation. Then, we design a filter such that it has unity gain at dc and fulfills the following optimality criterion. We require that the filter design minimized the absolute maximum weighted error of the transfer function in the stop-band. Here, the weighted error is given as

$$E(f) = W(f)\big(\tilde{h}(f) - \tilde{h}_d(f)\big). \tag{C.1}$$

Here, we restrict ourselves to FIR type I filters that have an odd number of taps and even symmetry such that their transfer function $\tilde{h}(f)$ is real up to a linear phase. The desired transfer function $h_d(f)$ is zero in the stop-band such that the error function simplifies.

To find the filter taps that minimize the maximum weighted error in the stop-band there exists a number of quickly converging algorithms (Parks and McClellan, 1972; McClellan et al., 1973). We adopt the Parks-McClellan algorithm also discussed in Oppenheim et al. (1999). To account for the red shape of the laser phase noise $\sqrt{S_p(f)} = 30\,\mathrm{Hz}/\sqrt{\mathrm{Hz}}\cdot(2\pi f)^{-1}$ we put a lower

[1] *Imaging* denotes the inverse process to aliasing. Instead of folding aliases into band upon decimation we fold in-band power out-of-band to determine the maximal allowed power of the aliases.

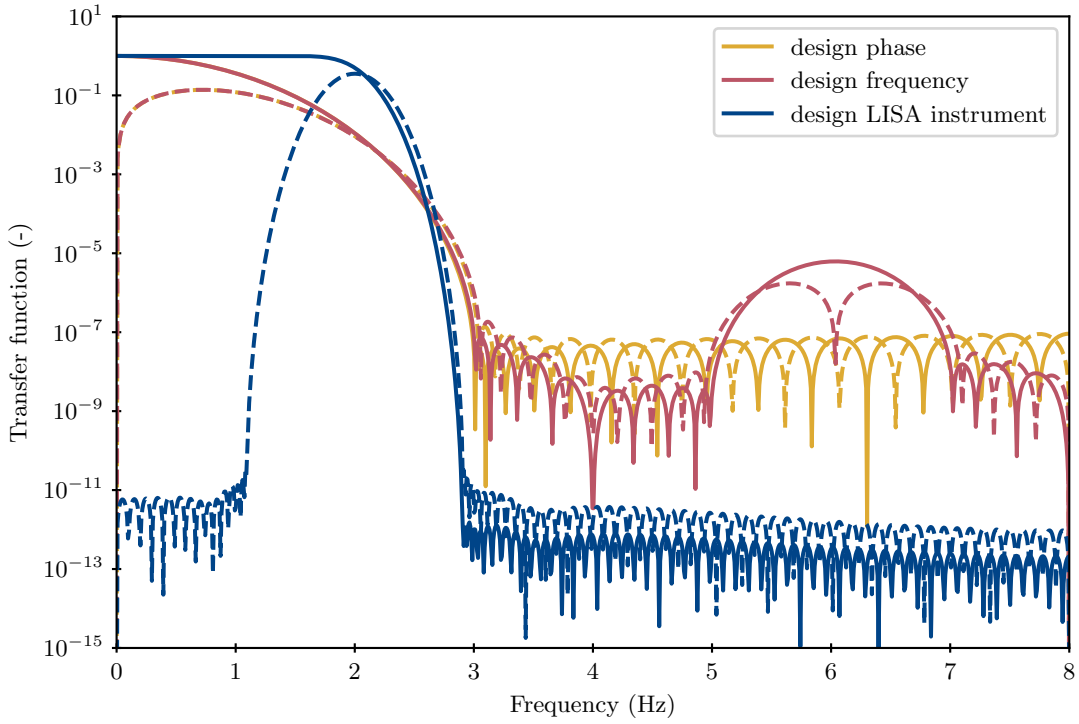

Figure C.1: Transfer functions (solid) and derivatives (dashed) of various filter designs.

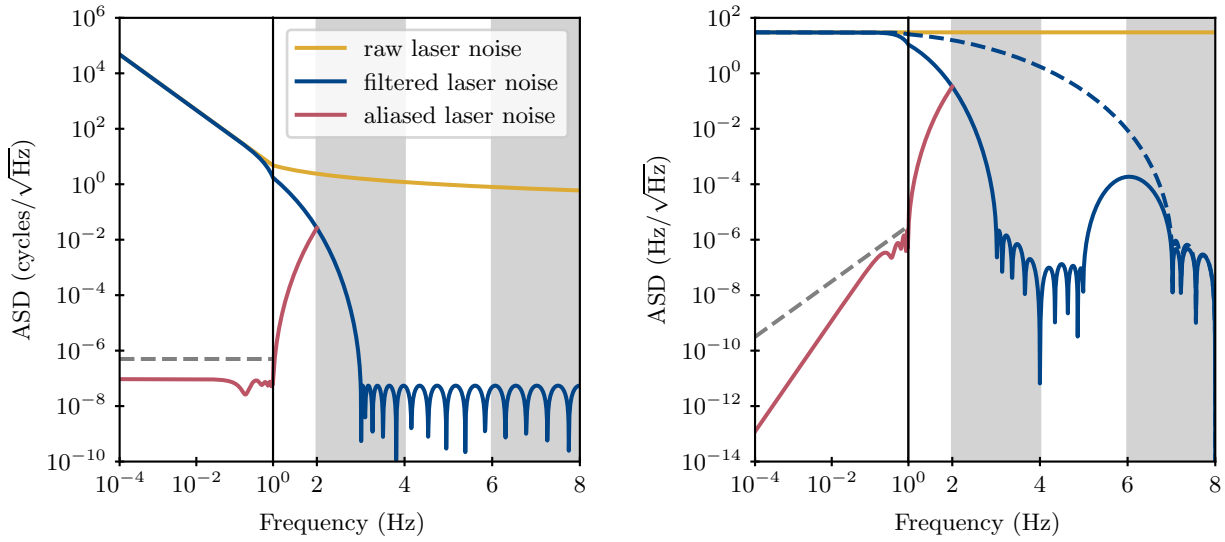

Figure C.2: Effect of anti-aliasing filter designs on laser noise for phase units (left panel) and frequency units (right panel). The raw laser noise is shown in yellow. It has a red shape in phase units and is white in frequency units. The ASD after anti-aliasing is shown in blue and the aliased contribution after decimation to 4 Hz is shown in red. The grey and white bands in the frequency range 2 Hz to 8 Hz indicate orientation of the sub-bands after folding. Grey sub-bands are mirrored before they are added to the 0 Hz to 2 Hz band. As the filter for frequency units is compiled from two filter we show the effect of the first filter in blue dashed (for more details see the text).

weighting on higher frequencies. Therefore, the weighting function is given by $W(f) = f^{-1}$. As a result the transfer function (yellow) plotted in fig. C.1 slowly increases in the stop-band (which is hard to see). In fig. C.2 (left panel) we show the effect of the transfer function on the red laser phase noise. Here, we observe that after filtering (blue line) the phase noise is equi-ripple in the stop-band. This is as intended since folding the frequency range 2 Hz to 8 Hz into band produces aliased noise (red line) that stays below the flat microcycle-requirement.

C.3 Optimized design for frequency units

The design of the anti-aliasing filter in frequency is more complicated as the microcycle-requirement appears now as $\sqrt{S_{\delta\nu}^{\mathrm{req}}(f)} = 1\,\mu\mathrm{cycle}/\sqrt{\mathrm{Hz}} \cdot (2\pi f)$. Imaging this requirement to frequencies up to 8 Hz produces zeros at 4 Hz and 8 Hz. To automatically impose zeros in the transfer function of the anti-aliasing filter at those frequencies we construct a composite filter from two FIR type I filters, one running at 16 Hz and the other one running at 8 Hz. As each of those filter has a definite zero at their respective Nyquist frequency we fulfill the above requirement.

The stop-band of the first filter starts at 7 Hz and we use a weighting function that is equivalent to the imaged microcycle-requirement. To stay below it we require 9 taps. The ASD of laser noise after the application of the first filter is shown as the dashed blue line in fig. C.2 (right panel). In the next step we design the second filter that runs at 8 Hz with a stop-band ranging from 3 Hz to 4 Hz. We choose the same weighting function and find that 11 taps suffice. We combine the two filter designs into a single filter by discrete convolution of the coefficients which gives in total $9 + 2 \cdot 11 - 2 = 31$ taps. The total transfer function of this filter is shown in fig. C.1 as the red line. Characteristically, the transfer function has a bump between 5 Hz and 7 Hz. This is allowed and only relaxes the number of required taps as this band is aliased to the interval 1 Hz to 2 Hz which is not part of the LISA band.

Appendix D

Fractional Shift Filters Based on FIR Type II Filters

In section section 3.3.2 we discuss about interpolation residuals and propose a new kernel design that relaxes the required number of coefficients. As consequence the interpolation error increases at low frequencies. Therefore, we carefully derive an interpolation kernel based off of a FIR type II low-pass filter design that respects the microcycle-requirement at all frequencies.

We start by designing an FIR type II filter that has even number of taps and even symmetry. We proceed with a similar algorithm as already introduced in appendix C. We seek the filter taps that minimize the maximum weighted error in the domain of interest. Here, we desire a response of unity up to a frequency of 1 Hz. As an additional constraint we fix the response at dc to exactly one. This procedure yields equi-ripples in the pass-band of the filter.

The interpolation error is formulated in frequency domain as the deviation of the interpolation kernel transfer function from a pure delay which is represented as a complex linear phase (cf. eq. (3.114)). To fulfill the microcycle-requirement we demand

$$\tilde{\mathbf{\Delta}} S_p(f) < S_{\delta\phi}^{\mathrm{req}}(f) \qquad \Rightarrow \qquad \tilde{\mathbf{\Delta}} < \frac{S_{\delta\phi}^{\mathrm{req}}(f)}{S_p(f)}, \tag{D.1}$$

which yields a constraint on the maximal allowed interpolation error. In fig. D.1 we plot the right-hand side of the equation above as the black dashed line. Here, we assume a laser phase noise ASD of $30\,\mathrm{Hz}/\sqrt{\mathrm{Hz}} \cdot (2\pi f)^{-1}$. Therefore, the requirement picks up a slope of one which dictates a weighting function of $W(f) = f^{-1}$ for the weighted error function such that the response is closer to unity at low frequencies. Using the Parks-McClellan algorithm we solve for the filter coefficients and find that 18 taps are sufficient to push the absolute error of the transfer function (dashed red line in fig. D.1) below the requirement.

The transfer function of the resulting FIR type II filter designs naturally possesses a group delay of half a sample. Therefore, it already represents a fractional shift filter for the special case of $\epsilon = 0.5$. Next, we seek to generalize this approach for all ϵ between 0 and 1. To achieve this we first come up with a continuous-time representation of the interpolation kernel $k(t)$. By discretely sampling a shifted version of it we yield the coefficients of any fractional shift filter. As an integer shift is equivalent to convolving by a Dirac-delta pulse we already identify the values of $k(t)$ for times that are integer multiples of the sampling time T_s. We summarize this in fig. D.2 where we show in the left panel the FIR type II filter coefficients in blue and the Dirac pulse in grey. The red line represents $k(t)$ that smoothly interpolates between the fixed values.

$$v(t) = w(t) \cdot \mathrm{sinc}(2 f_s t) \tag{D.2}$$

$$k(t) = \sum_n v\left(t - n \cdot \frac{T_s}{2}\right) \cdot \mathring{h}_n = v(t) + \sum_{n=-N/2}^{N/2-1} v\left(t - (n+1/2) \cdot \frac{T_s}{2}\right) \cdot h_n \tag{D.3}$$

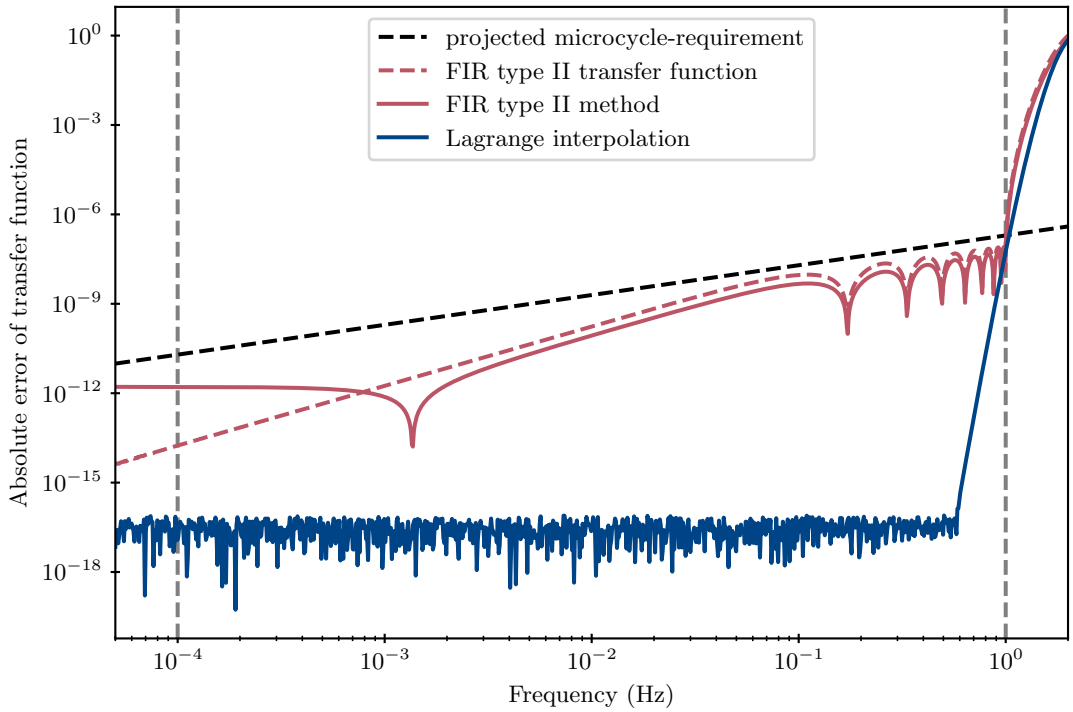

Figure D.1: Comparison of the interpolation error of different kernel designs with the projected microcycle-requirement in dashed black. For a fractional shift of $\epsilon = 0.25$ the performance of the newly proposed FIR type II method (solid red) and the standard Lagrange interpolation method (solid blue) is shown. Additionally, the magnitude response of the FIR filter the interpolation kernel is based off of is plotted in dashed red. For more details on the design parameters see the text.

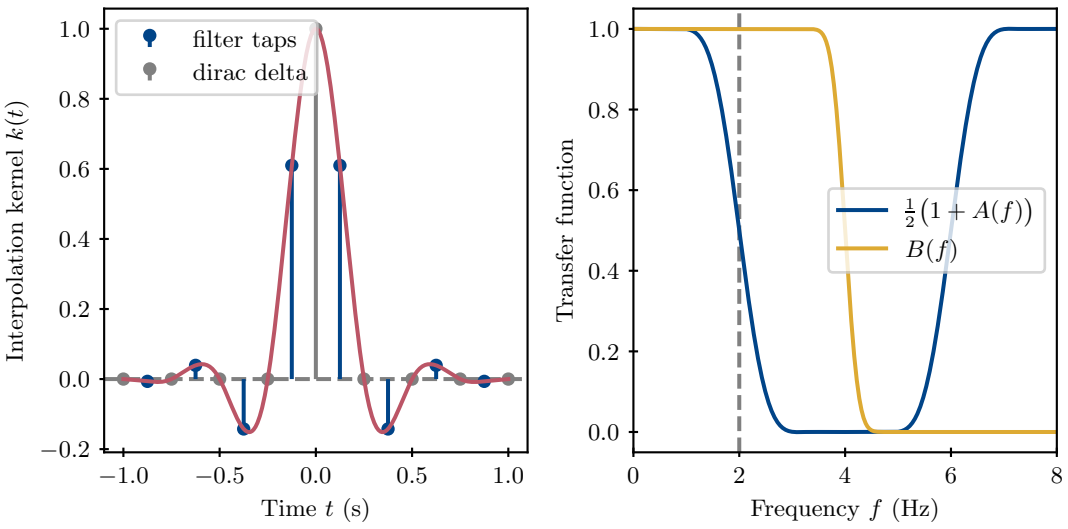

Figure D.2: Illustration of the design procedure of the interpolation kernel using the FIR type II method for $N = 8$ and $f_s = 4\,\mathrm{Hz}$. The left panel shows the continuous-time kernel function $k(t)$ that smoothly interpolates the filter taps that are interleaved with a Dirac pulse. In the right panel we show the shape of the constituent of the Fourier transform of $\tilde{k}(f)$ that defines the frequency response of the interpolation kernel.

Here, $\mathring{h}_n$ are all supports including the Dirac pulse and h_n denotes only the filter coefficients. We choose a window function $w(t)$ such that $k(t)$ has a finite length. The Fourier transform of the kernel defines the frequency response. We find

$$\tilde{k}(f) = \frac{1}{f_s} \underbrace{\left(\tilde{w}(f') * \mathrm{rect}\left(\frac{f'}{2f_s}\right)\right)(f)}_{B(f)} \cdot \frac{1}{2}\left(1 + \underbrace{\sum_{n=0}^{\frac{N}{2}-1} 2\cos\left(2\pi f(n+1/2)\frac{T_s}{2}\right) \cdot h_n}_{A(f)}\right) \tag{D.4}$$

where $A(f)$ denotes the amplitude response of the FIR filter and $B(f)$ the frequency response of the windowed sinc-function.

In the right panel of fig. D.2 we plot both the periodic response of the term $\frac{1}{2}\big(1 + A(f)\big)$ in blue and the effect of the windowed sinc which acts like a low pass filter with magnitude response $B(f)$ in yellow. A proper choice of the window function $w(t)$ is crucial for the performance of the filter as it reduces the effect of aliasing when discretely sampling the interpolation kernel $k(t)$ again. The coefficients of the interpolation kernel follow as

$$k_m(\epsilon) = k\big((m + 1 - \epsilon) \cdot T_s\big) \tag{D.5}$$

Finally, let us describe the parameters we choose to interpolate the beatnote measurements sampled at 4 Hz. We follow the algorithm above to calculate FIR filter taps that fulfill the microcycle-requirement which yields 18 taps. Then, we choose a Kaiser window (Nuttall, 1981) given as

$$w(t) = \begin{cases} \frac{I_0\left(\beta\sqrt{1-(2t/L)^2}\right)}{I_0(\beta)} & \text{if } |t| \leq \frac{L}{2}\ , \\ 0 & \text{else}\ . \end{cases} \tag{D.6}$$

Here, the parameter β determines the suppression of the sidelobes and we choose $\beta = 26.6$ which is equivalent to an attenuation of 250 dB. Furthermore, the length of the window L determines the number of coefficients of the interpolation kernel. We set $L = (10 + 1)T_s$ such that the resulting kernel has length $M = 18 + 10 = 28$. To compare the performance of the proposed

method with the standard Lagrange interpolation method, we plot the interpolation error for $\epsilon = 0.25$ in fig. D.1. We observe that the interpolation error of the proposed method (red line) generally performs better than the FIR filter amplitude response. However, at low frequencies we can see the effect of aliasing which is suppressed down to a level of roughly 10^{-12} by the windowing. On the other hand, Lagrange interpolation (blue line) requires 42 coefficients to achieve the microcycle-requirement in the entire LISA band.

Appendix E

Statistics of the Fourier Transform

Let $x(t)$ be a real zero-mean Gaussian process (for its rigorous definition see, e.g., Rasmussen and Williams, 2006). We assume it to be band-limited and periodic in time with period T such that we can represent it with a finite number of Fourier coefficients. The Fourier series representation is given as

$$x(t) = \sum_{k=-K}^{K} \tilde{x}_k e^{2\pi i k \Delta f t}. \tag{E.1}$$

Here, Δf is given by the inverse of T and K determines the number of frequency components such that $K\Delta f$ surpasses the band limit. As the Gaussian process is real the Fourier coefficients $\tilde{x}_k$ are not independent. It can easily be verified that $\tilde{x}_k = \tilde{x}_k^*$. Therefore, $x(t)$ is uniquely described by K coefficients $(\tilde{x}_k)_{k=1}^K$ (the $k = 0$ component vanishes because of the zero-mean property).

In the next step we seek to express the probability density function of the Fourier coefficients which are defined as

$$\tilde{x}_k = \frac{1}{T} \int_{-\frac{T}{2}}^{\frac{T}{2}} x(t) e^{-2\pi i k \Delta f t} \, \mathrm{d}t. \tag{E.2}$$

Our first observation is that $\tilde{x}_k$ must be Gaussian distributed as the Fourier transform is a linear operation on the Gaussian process $x(t)$. Furthermore, $\tilde{x}_k$ is circular symmetric (its distribution is invariant under adding a deterministic complex phase) so we follow that the vector $\tilde{\boldsymbol{x}}$ collecting all K Fourier coefficients is jointly distributed as

$$p(\tilde{\boldsymbol{x}}) = (\pi^K \det \Sigma)^{-1} e^{-\tilde{\boldsymbol{x}}^\dagger \Sigma^{-1} \tilde{\boldsymbol{x}}}. \tag{E.3}$$

Here, the complex-valued covariance matrix is defined as

$$\Sigma = \mathrm{E}\{\tilde{\boldsymbol{x}} \tilde{\boldsymbol{x}}^\dagger\}. \tag{E.4}$$

It expresses the covariance between different Fourier components. We find that it is approximately diagonal for large T. Let us demonstrate this by using the definitions given in eqs. (E.2)

and (E.4).

$$\mathrm{E}\{\tilde{x}_k\tilde{x}_l^*\} = \frac{1}{T^2}\int_{-\frac{T}{2}}^{\frac{T}{2}}\int_{-\frac{T}{2}}^{\frac{T}{2}} \underbrace{\mathrm{E}\{x(t)\cdot x(t')\}}_{\mathrm{ACF}\{x\}(t-t')} \cdot e^{-2\pi i k\Delta f t}\cdot e^{2\pi i l\Delta f t'}\,\mathrm{d}t\,\mathrm{d}t' \tag{E.5}$$

$$= \frac{1}{T^2}\int_{-\frac{T}{2}}^{\frac{T}{2}}\int_{-\frac{T}{2}}^{\frac{T}{2}}\int_{\mathbb{R}} \mathrm{PSD}\{x\}(f)\cdot e^{2\pi i f(t-t')}\cdot e^{-2\pi i k\Delta f t}\cdot e^{2\pi i l\Delta f t'}\,\mathrm{d}f\,\mathrm{d}t\,\mathrm{d}t' \tag{E.6}$$

$$= \frac{1}{T^2}\int_{\mathbb{R}} \mathrm{PSD}\{x\}(f)\int_{-\frac{T}{2}}^{\frac{T}{2}} e^{2\pi i(f-k\Delta f)t}\,\mathrm{d}t\int_{-\frac{T}{2}}^{\frac{T}{2}} e^{-2\pi i(f-l\Delta f)t'}\,\mathrm{d}t'\,\mathrm{d}f \tag{E.7}$$

$$= \frac{1}{T^2}\int_{\mathbb{R}} \mathrm{PSD}\{x\}(f)\cdot\mathrm{sinc}(Tf-k)\cdot\mathrm{sinc}(Tf-l)\,\mathrm{d}f \tag{E.8}$$

In the first line we have identified the ACF of $x(t)$ defined in eq. (1.24) that we replace by the Fourier transform of the PSD. To develop this further we assume the PSD appears approximately constant within a frequency interval of the characteristic width of the sinc-function in eq. (E.8) which is of the order $\frac{1}{T}$. Then we can write

$$\mathrm{E}\{\tilde{x}_k\tilde{x}_l^*\} \simeq \begin{cases} \frac{\mathrm{PSD}\{x\}(k\Delta f)}{T} & \text{if } k=l,\\ 0 & \text{else.}\end{cases} \tag{E.9}$$

Here, we have used the fact that the integral over the product of sinc-functions that are displaced by an integer evaluates to

$$\int_{\mathbb{R}}\mathrm{sinc}(Tf-k)\cdot\mathrm{sinc}(Tf-l)\,\mathrm{d}f = \frac{\delta_{kl}}{T}, \tag{E.10}$$

where δ_{kl} is the Kronecker delta. In the limit $T\to\infty$ the expression eq. (E.9) becomes exact.

Let us now consider a vector of real zero-mean Gaussian processes $\boldsymbol{z}(t)$ of dimension M that share the same properties as before. Similarly, we express them in terms of their Fourier coefficients $(\tilde{\boldsymbol{z}}_k)_{k=1}^K$. Following the derivation above it is easy to verify that in the limit $T\to\infty$ the vector of Fourier coefficients is statistically independent among different frequencies. Therefore, we follow that $\tilde{\boldsymbol{z}}_k$ is jointly complex Gaussian and we write for its joint probability density function

$$p(\tilde{\boldsymbol{z}}_k) = (\pi^M\det\Sigma_k)^{-1}e^{-\tilde{\boldsymbol{z}}_k^\dagger\Sigma_k^{1-}\tilde{\boldsymbol{z}}_k}, \tag{E.11}$$

where $\Sigma_k\in\mathbb{C}^{M\times M}$ is the covariance matrix for the k-th Fourier coefficient of the different channels with entries

$$(\Sigma_k)_{i,j} = \frac{\mathrm{CSD}\{z_i,z_j\}(k\Delta f)}{T}. \tag{E.12}$$

Bibliography

Abbott, B. P. et al. (2017). "GW170817: Observation of Gravitational Waves from a Binary Neutron Star Inspiral". In: *Physical Review Letters* 119.16, p. 161101. ISSN: 0031-9007, 1079-7114. DOI: 10.1103/PhysRevLett.119.161101.

Abbott, B. P. et al. (2019). "GWTC-1: A Gravitational-Wave Transient Catalog of Compact Binary Mergers Observed by LIGO and Virgo during the First and Second Observing Runs". In: *Physical Review X* 9.3, p. 031040. ISSN: 2160-3308. DOI: 10.1103/PhysRevX.9.031040.

Abbott, R. et al. (2021). "GWTC-2: Compact Binary Coalescences Observed by LIGO and Virgo during the First Half of the Third Observing Run". In: *Physical Review X* 11.2, p. 021053. ISSN: 2160-3308. DOI: 10.1103/PhysRevX.11.021053.

Abich, K. et al. (2019). "In-Orbit Performance of the GRACE Follow-on Laser Ranging Interferometer". In: *Physical Review Letters* 123.3, p. 031101. ISSN: 0031-9007, 1079-7114. DOI: 10.1103/PhysRevLett.123.031101.

Agazie, G. et al. (2023). "The NANOGrav 15 Yr Data Set: Evidence for a Gravitational-Wave Background". In: *The Astrophysical Journal Letters* 951.1, p. L8. DOI: 10.3847/2041-8213/acdac6.

Akiyama, K. (2019). "First M87 Event Horizon Telescope Results. I. The Shadow of the Supermassive Black Hole". In: *Astrophys. J. Lett.* 875, p. L1. DOI: 10.3847/2041-8213/ab0ec7.

Amaro Seoane, P. (2021). "The Gravitational Capture of Compact Objects by Massive Black Holes". In: *Handbook of Gravitational Wave Astronomy*. Ed. by C. Bambi, S. Katsanevas, and K. D. Kokkotas. Singapore: Springer Singapore, pp. 1–79. ISBN: 9789811547027. DOI: 10.1007/978-981-15-4702-7_17-1.

Amaro-Seoane, P. et al. (2017). *Laser Interferometer Space Antenna*. arXiv: 1702.00786 [astro-ph].

Amaro-Seoane, P. et al. (2023). "Astrophysics with the Laser Interferometer Space Antenna". In: *Living Reviews in Relativity* 26.1, p. 2. ISSN: 1433-8351. DOI: 10.1007/s41114-022-00041-y.

Armano, M. et al. (2016). "Sub-Femto- g Free Fall for Space-Based Gravitational Wave Observatories: LISA Pathfinder Results". In: *Physical Review Letters* 116.23, p. 231101. ISSN: 0031-9007, 1079-7114. DOI: 10.1103/PhysRevLett.116.231101.

Armano, M. et al. (2018). "Beyond the Required LISA Free-Fall Performance: New LISA Pathfinder Results down to 20 μ Hz". In: *Physical Review Letters* 120.6, p. 061101. ISSN: 0031-9007, 1079-7114. DOI: 10.1103/PhysRevLett.120.061101.

Armstrong, J. W., F. B. Estabrook, and M. Tinto (1999). "Time-Delay Interferometry for Space-based Gravitational Wave Searches". In: *The Astrophysical Journal* 527.2, pp. 814–826. ISSN: 0004-637X, 1538-4357. DOI: 10.1086/308110.

Baghi, Q., J. Baker, J. Slutsky, and J. I. Thorpe (2021a). "Model-Independent Time-Delay Interferometry Based on Principal Component Analysis". In: *Physical Review D* 104.12, p. 122001. ISSN: 2470-0010, 2470-0029. DOI: 10.1103/PhysRevD.104.122001.

Baghi, Q., J. G. Baker, J. Slutsky, and J. I. Thorpe (2023). "Fully Data-Driven Time-Delay Interferometry with Time-Varying Delays". In: *Annalen der Physik*, p. 2200447. ISSN: 0003-3804, 1521-3889. DOI: 10.1002/andp.202200447.

Baghi, Q., J. I. Thorpe, J. Slutsky, and J. Baker (2021b). "Statistical Inference Approach to Time-Delay Interferometry for Gravitational-Wave Detection". In: *Physical Review D* 103.4, p. 042006. ISSN: 2470-0010, 2470-0029. DOI: 10.1103/PhysRevD.103.042006.

Bañados, E. et al. (2014). "DISCOVERY OF EIGHT $z \sim 6$ QUASARS FROM Pan-STARRS1". In: *The Astronomical Journal* 148.1, p. 14. ISSN: 0004-6256, 1538-3881. DOI: 10.1088/0004-6256/148/1/14.

Bayle, J.-B. and O. Hartwig (2023). "Unified Model for the LISA Measurements and Instrument Simulations". In: *Physical Review D* 107.8, p. 083019. ISSN: 2470-0010, 2470-0029. DOI: 10.1103/PhysRevD.107.083019.

Bayle, J.-B., O. Hartwig, and M. Staab (2022a). *LISA Instrument*. Zenodo. DOI: 10.5281/ZENODO.6447389.

Bayle, J.-B., A. Hees, M. Lilley, and C. Le Poncin-Lafitte (2022b). *LISA Orbits*. Zenodo. DOI: 10.5281/ZENODO.6412992.

Bayle, J.-B., M. Lilley, A. Petiteau, and H. Halloin (2019). "Effect of Filters on the Time-Delay Interferometry Residual Laser Noise for LISA". In: *Physical Review D* 99.8, p. 084023. ISSN: 2470-0010, 2470-0029. DOI: 10.1103/PhysRevD.99.084023.

Brown, W. R. et al. (2020). "The ELM Survey. VIII. Ninety-eight Double White Dwarf Binaries". In: *The Astrophysical Journal* 889.1, p. 49. ISSN: 1538-4357. DOI: 10.3847/1538-4357/ab63cd.

Caprini, C. et al. (2016). "Science with the Space-Based Interferometer eLISA. II: Gravitational Waves from Cosmological Phase Transitions". In: *Journal of Cosmology and Astroparticle Physics* 2016.04, pp. 001–001. ISSN: 1475-7516. DOI: 10.1088/1475-7516/2016/04/001.

Cornish, N. J. and R. W. Hellings (2003). "The Effects of Orbital Motion on LISA Time Delay Interferometry". In: *Classical and Quantum Gravity* 20.22, pp. 4851–4860. ISSN: 0264-9381, 1361-6382. DOI: 10.1088/0264-9381/20/22/009.

Cutler, C. (1998). "Angular Resolution of the LISA Gravitational Wave Detector". In: *Physical Review D* 57.12, pp. 7089–7102. ISSN: 0556-2821, 1089-4918. DOI: 10.1103/PhysRevD.57.7089.

Dhurandhar, S. V., K. R. Nayak, and J.-Y. Vinet (2002). "Algebraic Approach to Time-Delay Data Analysis for LISA". In: *Physical Review D* 65.10, p. 102002. ISSN: 0556-2821, 1089-4918. DOI: 10.1103/PhysRevD.65.102002.

EPTA Collaboration et al. (2023). "The Second Data Release from the European Pulsar Timing Array - III. Search for Gravitational Wave Signals". In: *Astronomy & Astrophysics* 678, A50. DOI: 10.1051/0004-6361/202346844.

Estabrook, F. B., M. Tinto, and J. W. Armstrong (2000). "Time-Delay Analysis of LISA Gravitational Wave Data: Elimination of Spacecraft Motion Effects". In: *Physical Review D* 62.4, p. 042002. ISSN: 0556-2821, 1089-4918. DOI: 10.1103/PhysRevD.62.042002.

Esteban Delgado, J. J. (2012). "Laser Ranging and Data Communcation for the Laser Interferometer Space Antenna". PhD thesis. University of Granada, Spain.

Fakhouri, O., C.-P. Ma, and M. Boylan-Kolchin (2010). "The Merger Rates and Mass Assembly Histories of Dark Matter Haloes in the Two Millennium Simulations: Merger Rates". In: *Monthly Notices of the Royal Astronomical Society* 406.4, pp. 2267–2278. ISSN: 00358711. DOI: 10.1111/j.1365-2966.2010.16859.x.

Flauger, R., N. Karnesis, G. Nardini, M. Pieroni, A. Ricciardone, and J. Torrado (2021). "Improved Reconstruction of a Stochastic Gravitational Wave Background with LISA". In: *Journal of Cosmology and Astroparticle Physics* 2021.01, pp. 059–059. ISSN: 1475-7516. DOI: 10.1088/1475-7516/2021/01/059.

Fleddermann, R., C. Diekmann, F. Steier, M. Tröbs, G. Heinzel, and K. Danzmann (2018). "Sub-Pm$\{\{\sqrt\{\{\rm Hz\}\}\hat\{-1\}\}\}$ Non-Reciprocal Noise in the LISA Backlink Fiber". In: *Classical and Quantum Gravity* 35.7, p. 075007. ISSN: 0264-9381, 1361-6382. DOI: 10.1088/1361-6382/aaa276.

Francis, S. P., D. A. Shaddock, A. J. Sutton, G. de Vine, B. Ware, R. E. Spero, W. M. Klipstein, and K. McKenzie (2015). "Tone-Assisted Time Delay Interferometry on GRACE Follow-On". In: *Physical Review D* 92.1, p. 012005. ISSN: 1550-7998, 1550-2368. DOI: 10.1103/PhysRevD.92.012005.

Gaia Collaboration et al. (2018). "*Gaia* Data Release 2: Summary of the Contents and Survey Properties". In: *Astronomy & Astrophysics* 616, A1. ISSN: 0004-6361, 1432-0746. DOI: 10.1051/0004-6361/201833051.

García-Bellido, J., M. Peloso, and C. Unal (2016). "Gravitational Waves at Interferometer Scales and Primordial Black Holes in Axion Inflation". In: *Journal of Cosmology and Astroparticle Physics* 2016.12, pp. 031–031. ISSN: 1475-7516. DOI: 10.1088/1475-7516/2016/12/031.

Genzel, R., F. Eisenhauer, and S. Gillessen (2010). "The Galactic Center Massive Black Hole and Nuclear Star Cluster". In: *Reviews of Modern Physics* 82.4, pp. 3121–3195. ISSN: 0034-6861, 1539-0756. DOI: 10.1103/RevModPhys.82.3121.

Hartwig, O. (2021). "Instrumental Modelling and Noise Reduction Algorithms for the Laser Interferometer Space Antenna". PhD thesis.

Hartwig, O., J.-B. Bayle, M. Staab, A. Hees, M. Lilley, and P. Wolf (2022). "Time-Delay Interferometry without Clock Synchronization". In: *Physical Review D* 105.12, p. 122008. ISSN: 2470-0010, 2470-0029. DOI: 10.1103/PhysRevD.105.122008.

Hees, A., S. Bertone, and C. Le Poncin-Lafitte (2014). "Relativistic Formulation of Coordinate Light Time, Doppler, and Astrometric Observables up to the Second Post-Minkowskian Order". In: *Physical Review D* 89.6, p. 064045. ISSN: 1550-7998, 1550-2368. DOI: 10.1103/PhysRevD.89.064045.

Heinzel, G. (2018). *LISA Frequency Planning*.

Inchauspé, H., M. Hewitson, O. Sauter, and P. Wass (2022). "New LISA Dynamics Feedback Control Scheme: Common-mode Isolation of Test Mass Control and Probes of Test-Mass Acceleration". In: *Physical Review D* 106.2, p. 022006. ISSN: 2470-0010, 2470-0029. DOI: 10.1103/PhysRevD.106.022006.

Jenkins, G. M. and D. G. Watts (1968). *Spectral Analysis and Its Applications*. Holden-Day Series in Time Series Analysis. San Francisco: Holden-Day. ISBN: 978-0-8162-4464-5.

Kaplan, G. H. (2006). *The IAU Resolutions on Astronomical Reference Systems, Time Scales, and Earth Rotation Models*. arXiv: astro-ph/0602086.

Kormendy, J. and L. C. Ho (2013). "Coevolution (Or Not) of Supermassive Black Holes and Host Galaxies". In: *Annual Review of Astronomy and Astrophysics* 51.1, pp. 511–653. ISSN: 0066-4146, 1545-4282. DOI: 10.1146/annurev-astro-082708-101811.

LISA Performance Working Group (2021). *LISA Performance Model and Error Budget (LISA-LCST-INST-TN-003)*. Tech. rep.

Martens, W. and E. Joffre (2021). "Trajectory Design for the ESA LISA Mission". In: *The Journal of the Astronautical Sciences* 68.2, pp. 402–443. ISSN: 0021-9142, 2195-0571. DOI: 10.1007/s40295-021-00263-2. arXiv: 2101.03040 [gr-qc].

Max Rohr, J., S. Ast, O. Gerberding, J. Reiche, and G. Heinzel (2020). "Fiber Backscatter under Increasing Exposure to Ionizing Radiation". In: *Optics Express* 28.23, p. 34894. ISSN: 1094-4087. DOI: 10.1364/OE.404139.

McClellan, J., T. Parks, and L. Rabiner (1973). "A Computer Program for Designing Optimum FIR Linear Phase Digital Filters". In: *IEEE Transactions on Audio and Electroacoustics* 21.6, pp. 506–526. ISSN: 0018-9278. DOI: 10.1109/TAU.1973.1162525.

Mitryk, S. J., G. Mueller, and J. Sanjuan (2012). "Hardware-Based Demonstration of Time-Delay Interferometry and TDI-ranging with Spacecraft Motion Effects". In: *Physical Review D* 86.12, p. 122006. ISSN: 1550-7998, 1550-2368. DOI: 10.1103/PhysRevD.86.122006.

Moore, C. J., R. H. Cole, and C. P. L. Berry (2015). "Gravitational-Wave Sensitivity Curves". In: *Classical and Quantum Gravity* 32.1, p. 015014. ISSN: 0264-9381, 1361-6382. DOI: 10.1088/0264-9381/32/1/015014.

Muratore, M., D. Vetrugno, and S. Vitale (2020). "Revisitation of Time Delay Interferometry Combinations That Suppress Laser Noise in LISA". In: *Classical and Quantum Gravity* 37.18, p. 185019. ISSN: 0264-9381, 1361-6382. DOI: 10.1088/1361-6382/ab9d5b.

Muratore, M., D. Vetrugno, S. Vitale, and O. Hartwig (2022). "Time Delay Interferometry Combinations as Instrument Noise Monitors for LISA". In: *Physical Review D* 105.2, p. 023009. ISSN: 2470-0010, 2470-0029. DOI: 10.1103/PhysRevD.105.023009.

Nam, D. Q., Y. Lemiere, A. Petiteau, J.-B. Bayle, O. Hartwig, J. Martino, and M. Staab (2022). *TDI Noises Transfer Functions for LISA*. arXiv: 2211.02539 [astro-ph, physics:gr-qc].

Nayak, K. R. and J.-Y. Vinet (2004). "Algebraic Approach to Time-Delay Data Analysis for Orbiting LISA". In: *Physical Review D* 70.10, p. 102003. ISSN: 1550-7998, 1550-2368. DOI: 10.1103/PhysRevD.70.102003.

Nelemans, G., L. R. Yungelson, and S. F. Portegies Zwart (2001). "The Gravitational Wave Signal from the Galactic Disk Population of Binaries Containing Two Compact Objects". In: *Astronomy & Astrophysics* 375.3, pp. 890–898. ISSN: 0004-6361, 1432-0746. DOI: 10.1051/0004-6361:20010683.

Nissanke, S., M. Vallisneri, G. Nelemans, and T. A. Prince (2012). "GRAVITATIONAL-WAVE EMISSION FROM COMPACT GALACTIC BINARIES". In: *The Astrophysical Journal* 758.2, p. 131. ISSN: 0004-637X, 1538-4357. DOI: 10.1088/0004-637X/758/2/131.

Nuttall, A. (1981). "Some Windows with Very Good Sidelobe Behavior". In: *IEEE Transactions on Acoustics, Speech, and Signal Processing* 29.1, pp. 84–91. ISSN: 0096-3518. DOI: 10.1109/TASSP.1981.1163506.

Oppenheim, A. V., R. W. Schafer, and J. R. Buck (1999). *Discrete-Time Signal Processing*. 2nd ed. Upper Saddle River, N.J: Prentice Hall. ISBN: 978-0-13-754920-7.

Page, J. and T. B. Littenberg (2021). "Bayesian Time Delay Interferometry". In: *Physical Review D* 104.8, p. 084037. ISSN: 2470-0010, 2470-0029. DOI: 10.1103/PhysRevD.104.084037.

Parks, T. and J. McClellan (1972). "Chebyshev Approximation for Nonrecursive Digital Filters with Linear Phase". In: *IEEE Transactions on Circuit Theory* 19.2, pp. 189–194. ISSN: 0018-9324. DOI: 10.1109/TCT.1972.1083419.

Périgois, C., C. Belczynski, T. Bulik, and T. Regimbau (2021). "Startrack Predictions of the Stochastic Gravitational-Wave Background from Compact Binary Mergers". In: *Physical Review D* 103.4, p. 043002. ISSN: 2470-0010, 2470-0029. DOI: 10.1103/PhysRevD.103.043002.

Prince, T. A., M. Tinto, S. L. Larson, and J. W. Armstrong (2002). "LISA Optimal Sensitivity". In: *Physical Review D* 66.12, p. 122002. ISSN: 0556-2821, 1089-4918. DOI: 10.1103/PhysRevD.66.122002.

Rasmussen, C. E. and C. K. I. Williams (2006). *Gaussian Processes for Machine Learning*. Adaptive Computation and Machine Learning. Cambridge, Mass: MIT Press. ISBN: 978-0-262-18253-9.

Reardon, D. J. et al. (2023). "Search for an Isotropic Gravitational-wave Background with the Parkes Pulsar Timing Array". In: *The Astrophysical Journal Letters* 951.1, p. L6. ISSN: 2041-8205, 2041-8213. DOI: 10.3847/2041-8213/acdd02.

Reinhardt, J. N., M. Staab, K. Yamamoto, J.-B. Bayle, A. Hees, O. Hartwig, K. Wiesner, and G. Heinzel (2023). *Ranging Sensor Fusion in LISA Data Processing: Treatment of Ambiguities, Noise, and On-Board Delays in LISA Ranging Observables*. arXiv: 2307.05204 [astro-ph, physics:gr-qc].

Reynaud, S., B. Lamine, L. Duchayne, P. Wolf, and M.-T. Jaekel (2008). "Bounds on Gravitational Wave Backgrounds from Large Distance Clock Comparisons". In: *Physical Review D* 77.12, p. 122003. ISSN: 1550-7998, 1550-2368. DOI: 10.1103/PhysRevD.77.122003.

Romano, J. D. and G. Woan (2006). "Principal Component Analysis for LISA: The Time Delay Interferometry Connection". In: *Physical Review D* 73.10, p. 102001. ISSN: 1550-7998, 1550-2368. DOI: 10.1103/PhysRevD.73.102001.

Rosado, P. A. (2011). "Gravitational Wave Background from Binary Systems". In: *Physical Review D* 84.8, p. 084004. ISSN: 1550-7998, 1550-2368. DOI: 10.1103/PhysRevD.84.084004.

Schneider, R., V. Ferrari, S. Matarrese, and S. F. Portegies Zwart (2001). "Low-Frequency Gravitational Waves from Cosmological Compact Binaries". In: *Monthly Notices of the Royal Astronomical Society* 324.4, pp. 797–810. ISSN: 00358711, 13652966. DOI: 10.1046/j.1365-8711.2001.04217.x.

Sesana, A. (2016). "Prospects for Multiband Gravitational-Wave Astronomy after GW150914". In: *Physical Review Letters* 116.23, p. 231102. ISSN: 0031-9007, 1079-7114. DOI: 10.1103/PhysRevLett.116.231102.

Sesana, A., F. Haardt, P. Madau, and M. Volonteri (2005). "The Gravitational Wave Signal from Massive Black Hole Binaries and Its Contribution to the *LISA* Data Stream". In: *The Astrophysical Journal* 623.1, pp. 23–30. ISSN: 0004-637X, 1538-4357. DOI: 10.1086/428492.

Shaddock, D. A., B. Ware, R. E. Spero, and M. Vallisneri (2004). "Postprocessed Time-Delay Interferometry for LISA". In: *Physical Review D* 70.8, p. 081101. ISSN: 1550-7998, 1550-2368. DOI: 10.1103/PhysRevD.70.081101.

Shaddock, D. A., M. Tinto, F. B. Estabrook, and J. W. Armstrong (2003). "Data Combinations Accounting for LISA Spacecraft Motion". In: *Physical Review D* 68.6, p. 061303. ISSN: 0556-2821, 1089-4918. DOI: 10.1103/PhysRevD.68.061303.

Staab, M., J.-B. Bayle, and O. Hartwig (2023a). *PyTDI*. Zenodo. DOI: 10.5281/ZENODO.6351736.

Staab, M., M. Lilley, J.-B. Bayle, and O. Hartwig (2023b). *Laser Noise Residuals in LISA from Onboard Processing and Time-Delay Interferometry*. arXiv: 2306.11774 [astro-ph, physics:gr-qc].

Stella, L., N. E. White, and W. Priedhorsky (1987). "The Discovery of a 685 Second Orbital Period from the X-ray Source 4U 1820 - 30 in the Globular Cluster NGC 6624". In: *The Astrophysical Journal* 312, p. L17. ISSN: 0004-637X, 1538-4357. DOI: 10.1086/184811.

Stroeer, A and A Vecchio (2006). "The LISA Verification Binaries". In: *Classical and Quantum Gravity* 23.19, S809–S817. ISSN: 0264-9381, 1361-6382. DOI: 10.1088/0264-9381/23/19/S19.

Taylor, J. H. (1994). "Binary Pulsars and Relativistic Gravity". In: *Reviews of Modern Physics* 66.3, pp. 711–719. ISSN: 0034-6861, 1539-0756. DOI: 10.1103/RevModPhys.66.711.

Tinto, M. and J. W. Armstrong (1999). "Cancellation of Laser Noise in an Unequal-Arm Interferometer Detector of Gravitational Radiation". In: *Physical Review D* 59.10, p. 102003. ISSN: 0556-2821, 1089-4918. DOI: 10.1103/PhysRevD.59.102003.

Tinto, M. and S. Dhurandhar (2023). "Higher-Order Time-Delay Interferometry". In: *Physical Review D* 108.8, p. 082003. ISSN: 2470-0010, 2470-0029. DOI: 10.1103/PhysRevD.108.082003.

Tinto, M., S. Dhurandhar, and D. Malakar (2023). "Second-Generation Time-Delay Interferometry". In: *Physical Review D* 107.8, p. 082001. ISSN: 2470-0010, 2470-0029. DOI: 10.1103/PhysRevD.107.082001.

Tinto, M., F. B. Estabrook, and J. W. Armstrong (2004). "Time Delay Interferometry with Moving Spacecraft Arrays". In: *Physical Review D* 69.8, p. 082001. ISSN: 1550-7998, 1550-2368. DOI: 10.1103/PhysRevD.69.082001.

Tinto, M., D. A. Shaddock, J. Sylvestre, and J. W. Armstrong (2003). "Implementation of Time-Delay Interferometry for LISA". In: *Physical Review D* 67.12, p. 122003. ISSN: 0556-2821, 1089-4918. DOI: 10.1103/PhysRevD.67.122003.

Tinto, M., M. Vallisneri, and J. W. Armstrong (2005). "Time-Delay Interferometric Ranging for Space-Borne Gravitational-Wave Detectors". In: *Physical Review D* 71.4, p. 041101. ISSN: 1550-7998, 1550-2368. DOI: 10.1103/PhysRevD.71.041101.

Vallisneri, M. (2005). "Geometric Time Delay Interferometry". In: *Physical Review D* 72.4, p. 042003. ISSN: 1550-7998, 1550-2368. DOI: 10.1103/PhysRevD.72.042003.

Vallisneri, M., J.-B. Bayle, S. Babak, and A. Petiteau (2021). "Time-Delay Interferometry without Delays". In: *Physical Review D* 103.8, p. 082001. ISSN: 2470-0010, 2470-0029. DOI: 10.1103/PhysRevD.103.082001.

Virtanen, P. et al. (2020). "SciPy 1.0: Fundamental Algorithms for Scientific Computing in Python". In: *Nature Methods* 17.3, pp. 261–272. ISSN: 1548-7091, 1548-7105. DOI: 10.1038/s41592-019-0686-2.

Wissel, L., O. Hartwig, J. Bayle, M. Staab, E. Fitzsimons, M. Hewitson, and G. Heinzel (2023). "Influence of Laser Relative-Intensity Noise on the Laser Interferometer Space Antenna". In: *Physical Review Applied* 20.1, p. 014016. ISSN: 2331-7019. DOI: 10.1103/PhysRevApplied.20.014016.

Xu, H. et al. (2023). "Searching for the Nano-Hertz Stochastic Gravitational Wave Background with the Chinese Pulsar Timing Array Data Release I". In: *Research in Astronomy and Astrophysics* 23.7, p. 075024. ISSN: 1674-4527. DOI: 10.1088/1674-4527/acdfa5. arXiv: 2306.16216 [astro-ph, physics:gr-qc].